

Department of Civil and Environmental Engineering

University of Strathclyde

Investigating strain localisation in clay
using mica markers and X-ray Computed
Tomography

*A Thesis presented for the Degree of Doctor of Philosophy
by*


Christopher U. Ibeh

JUNE 2021

Declaration

This thesis is the result of the author's original research. It has been composed by the author and has not been previously submitted for examination which has led to the award of a degree.

Due acknowledgement must always be made of the use of any material contained in, or derived from, this thesis.

Signed: 

Date: 10/09/2021

Dedication

To God almighty.

Acknowledgement

Firstly, I would like to express my sincere gratitude to my supervisors, Prof. Rebecca Lunn and Prof. Alessandro Tarantino for their invaluable support, mentorship, guidance, understanding and motivation throughout my PhD. I would also like to specially thank Dr. Matteo Pedrotti who also supported me and was always available to offer insights throughout the period of my research.

Secondly, I also wish to acknowledge the support of the University of Strathclyde for providing the funding for my research.

Thirdly, I appreciate the departmental admin staff and the technical staff at the laboratories for their assistance in numerous ways within the period of this work.

Finally, I would like to thank my family: my wife, daughter, parents and siblings for their understanding and support throughout this research period.

Table of Contents

Declaration.....	ii
Dedication.....	iii
Acknowledgement.....	iv
Publications.....	ix
Abstract.....	xi
1. Introduction.....	1
1.1. Background.....	1
1.2. Research Aim.....	2
1.3. Research Objectives.....	3
1.4. Structure of Thesis.....	3
1.5. Reference.....	5
2. Geomaterial Instability.....	8
2.1. Strain localisation.....	8
2.2. Continuum constitutive modelling.....	10
2.3. Geomaterial modelling spectrum.....	11
2.4. Constitutive model enrichment.....	14
2.5. Full field imaging of soil.....	15
2.5.1. X-ray Computed Tomography.....	16
2.5.2. Challenges to the use of X-ray CT for imaging clay.....	17
2.6. Particle Kinematic evaluation and strain quantification.....	19
2.7. Use of clay markers.....	23
2.7.1. Characterisation of mica.....	24
2.8. Existing miniature cells for soil mechanical testing.....	25
2.9. References.....	28
3. On the utilization of mica waste: the pore-fluid chemistry of mica soils and its implication for erosion susceptibility.....	36
Abstract.....	36
3.1. Introduction.....	37
3.1.1. Mica.....	39
3.2. Materials and Methods.....	40
3.2.1. Specimen Preparation.....	41
3.2.2. Experimental procedure.....	43
3.3. Results and Discussion.....	47
3.3.1. Sedimentation test.....	47
3.3.2. Liquid Limit test.....	51
3.3.3. Jet erosion test.....	52

3.3.4.	An electrochemical conceptual model for mica.....	58
3.3.5.	An electrochemical conceptual model for the erosion of mica.....	62
3.3.6.	Environmental considerations about the use of mica for agricultural applications	65
3.4.	Conclusion.....	66
3.5.	Acknowledgement.....	67
3.6.	Data Availability Statement	67
3.7.	Reference.....	67
4.	An experimental investigation into the use of mica as a material for the stabilisation of marginal clays in construction	75
Abstract	75
4.1.	Introduction	77
4.2.	Materials and specimen preparation.....	79
4.3.	Experimental procedure	81
4.3.1.	Direct Shear Tests	81
4.3.2.	One-dimensional (oedometer) compression tests	82
4.3.3.	X-ray Computed Tomography	83
4.4.	Results	84
4.4.1.	Shear strength behaviour of kaolin-mica composites	84
4.4.2.	1-D compression behaviour of kaolin-mica composites.....	88
4.4.3.	Hydraulic conductivity of kaolin-muscovite composites	92
4.4.4.	X-ray CT slices of consolidated and sheared samples.....	93
4.5.	Discussion	94
4.6.	4.6. Conclusions	99
4.7.	References	100
4.8.	Appendix I – Determination of void ratio change in oedometer compression.	104
4.9.	Appendix II – Determination of hydraulic conductivity from oedometer consolidation test	106
5.	An X-ray CT study of miniature clay sample preparation techniques	108
Abstract	108
5.1.	Introduction	109
5.1.1.	Miniature soil sample preparation techniques	110
5.2.	Material	111
5.3.	Sample Preparation	112
5.4.	Methodology	113
5.4.1.	X-CT imaging	114
5.4.2.	Stereographic projection	114
5.4.3.	Spatial statistical analysis (Fisher Spherical distribution.....	115

5.5.	Results and Discussion.....	116
5.5.1.	Tube and lathe derived Oedometer overconsolidated specimens	116
5.5.2.	Mould consolidated specimens (to lower stress)	119
5.6.	Conclusion.....	121
5.7.	Reference.....	121
6.	PLATYMATCH- A particle-matching algorithm for the analysis of platy particle kinematics using X-ray Computed Tomography	123
	Abstract.....	123
6.1.	Introduction	125
6.2.	Material and sample preparation	130
6.3.	Experimental Procedure	131
6.3.1.	Image Acquisition and processing	135
6.3.2.	Thresholding and Image classification	135
6.3.3.	Particle Property Measurement.....	135
6.4.	Implementation of matching algorithm by Druckrey and Alshibli, (2014)	137
6.4.1.	Initial Results for the compression test.....	138
6.5.	PLATYMATCH Framework	147
6.6.	PLATYMATCH Implementations.....	149
6.6.1.	Evaluation of particle matching attributes using the artificially rotated sample (Rotation Test) – Attribute Analysis.	149
6.6.2.	Evaluation of particle matching accuracy, using a sample that was scanned, removed, and replaced and re-scanned (Replacement Test).	154
6.6.3.	Particle tracking after unconfined uniaxial compression (Compression Test)	155
6.7.	Conclusion.....	159
6.8.	Acknowledgements	161
6.9.	Data Availability Statement	161
6.10.	References	161
6.11.	Appendix 1	166
7.	Investigating strain localisation in clay using “platy” mica particles and X-ray Computed tomography	168
	Abstract.....	168
7.1.	Introduction	169
7.2.	X-ray Computed Tomography	171
7.3.	Miniature Triaxial cell apparatus	172
7.3.1.	Schematic of triaxial apparatus.....	172
7.4.	Miniature Triaxial cell apparatus	175
7.4.1.	Materials and sample preparation:	175
7.4.2.	Testing procedure:	176

7.4.3.	Particle Matching	178
7.4.4.	Particle orientation	179
7.5.	Test result and discussion.....	180
7.5.1.	Triaxial test on Kaolin samples.....	180
7.5.2.	Triaxial test on kaolin with mica markers.....	182
7.6.	Particle kinematic analysis	184
7.6.1.	Particle Displacement	184
7.6.2.	Particle Rotation.....	187
7.6.3.	Particle Orientation	189
7.7.	Inferring mechanisms of initiation and propagation of strain localisation.....	193
7.8.	Conclusion.....	196
7.9.	Reference.....	198
7.10.	Appendix 1	202
7.10.1.	Pore -water pressure measurement device (Tensiometer).....	202
7.10.2.	Latex Membrane	206
7.10.3.	External Stress Application/Control System (Actuator and controller).....	207
7.10.4.	Load cell and displacement transducer	208
7.10.5.	Data acquisition/Process Control System	208
7.10.6.	Test Apparatus use procedure	209
7.11.	Appendix II.....	212
8.	Conclusion and Recommendation	213
8.1.	Introduction	213
8.1.1.	Chemical and mechanical characterisation of mica.....	214
8.1.2.	Influence of sampling method on disturbance of kaolin microstructure	215
8.1.3.	Platy particle matching Code	215
8.1.4.	Miniature triaxial cell with an in-built High Capacity Tensiometer.....	216
8.1.5.	Strain localisation investigated using mica markers and X-ray CT.....	217
8.2.	Proposed Future areas	218

Publications

1. Ibeh C. U., Pedrotti M., Tarantino A.; Lunn R. J. (2019) Initiation and propagation of strain localisation in cohesive soil using a novel miniature triaxial cell and X-ray computed Tomography; Book of Abstracts, InterPore 11th Annual Meeting, Valencia, Spain; 6 – 10th May 2019.
2. Ibeh C. U., Pedrotti M., Tarantino A., Lunn R. J. (2019) An X-ray CT study of miniature clay sample preparation techniques. *E3S Web of Conferences*, 92. 01004. ISSN 2267-1242. <https://doi.org/10.1051/e3sconf/20199201004>
3. Ibeh C. U., Pedrotti M., Tarantino A., Lunn R. J. (2021) On the utilization of mica waste: the pore-fluid chemistry of mica soils and its implication for erosion susceptibility. *Geoderma*, 403, 115256. <https://doi.org/10.1016/j.geoderma.2021.115256>
4. Ibeh C. U., Tarantino A., Pedrotti M., Lunn R. J. (2021) An experimental investigation into the use of mica soil for stabilisation of marginal clays. Accepted for publication in *Construction and building materials Journal* 299, 123971. <https://doi.org/10.1016/j.conbuildmat.2021.123971> .
5. Ibeh C. U., Pedrotti M., Tarantino A., Lunn R. J (2021) PLATYMATCH - a particle-matching algorithm for the analysis of platy particle kinematics using X-ray Computed Tomography. *Submitted to Computer and Geotechnics and under review.*

6. Ibeh C. U., Pedrotti M., Tarantino A., Lunn R. J. (2021) Investigating strain localisation in clay using mica markers and X-ray Computed tomography. *To be submitted to Geotechnique.*

Abstract

Mass movements in clay deposits result in damage to infrastructures and buildings with significant social, economic, and environmental consequences. These processes are characterised by strain localisation, a complex process to investigate experimentally and model. Strain localisation in clays is particularly worrisome and possess huge destructive capabilities because clay is characterised by low shear strength. Conventional laboratory tests are essentially a post-mortem destructive analysis of localised deformations, and do not account for the fundamental physics of soil behaviours. Hence the development of 4-dimensional (4-D) non-destructive imaging approaches to study soil mechanical behaviour. However, due to the small size of clay particles compared to achievable X-ray computed tomography (X-ray CT) resolution, it has not been possible to directly evaluate particle scale clay micromechanics non-destructively using 4-D imaging techniques.

This thesis presents a novel technique involving the use of plate-shaped (“platy”) muscovite mica marker for the evaluation of the initiation and propagation of strain localisation in kaolin. First, an investigation was carried out to understand the suitability of the use of mica particle markers for the study of clay by carrying out both chemical and mechanical characterization of mica. Subsequently, sample preparation techniques were experimented to understand the appropriate sampling approach with least microstructure disturbance. Furthermore, a novel miniature triaxial cell instrumented with a high capacity tensiometer and a novel platy particle matching algorithm were developed for the study of mica marker particle kinematics within kaolin. Kinematic analysis (displacement and rotation) of mica particle markers within the kaolin sample was then carried out.

The results presented in this thesis demonstrated that (i) The particle configuration of silt sized muscovite samples consistently varied (dispersive and non-dispersive) with pore-water chemistry, regardless of whether the samples being tested were suspension sediments or

compacted samples. (ii) By adding both silt sized muscovite or sand sized muscovite to kaolin for up to 30% sand sized muscovite or silt sized muscovite, the compressive behaviour is still clay-dominated. Similarly, the addition of mica (up to 30%) to kaolin does not significantly affect its hydraulic conductivity of kaolin. However, the shear strength characteristics of kaolin may significantly change by the addition of about 2.5-30% of silt sized muscovite or sand in the low normal stress (<100 kPa) but not at higher stress regime. (iii) PLATYMATCH (algorithm developed in this thesis) can effectively match platy particles in consecutive sample scans when adequately registered and the particles adequately segmented. (iv) A conceptual model of the initiation and propagation of strain localisation in kaolin was developed.

The findings of this thesis implies that there is the potential to use platy mica particle marker images for early (pre-peak shear strength) detection of the initiation and propagation of strain localisation in kaolin and this may possibly be useful in enhancing available constitutive models such as the double scale constitutive model for improved clay behaviour prediction.

1. Introduction

1.1. Background

Soil deformation in the form of landslides alone is more widespread than any other geological event and can occur anywhere in the world (WHO, 2021). Landslides contribute to about 17% of the fatalities due to natural hazards (CRED, 2021). Between 1998-2017, landslides affected an estimated 4.8 million people and caused more than 18 000 deaths (WHO, 2021). The cost of losses from landslide is also enormous for example annual landslide costs are estimated as USD 1–5 billion in Italy, Austria, Switzerland and France; annual losses in the United States exceed USD 3.5 Billion (Schuster, R.L. and Highland, 2001). The economic, environmental, and social impacts of landslide is worsened by climate change and rising temperature which are expected to trigger more landslides (WHO, 2021) as well as the increasing costs of development and investments in landslide-prone areas (Bandara, R.M.S., 2013; Petley, D.N., Dunning, S.A. and Rosser, 2005).

Deformation in geomaterials (soils, rocks, concrete, etc.) is often localized, *i.e.*, occurring in the form of shear bands or fractures (Viggiani et al., 2013). Landslide is a strain localisation phenomenon which involve three-dimensional shear bands (Oka et al., 2005). Strain localisation can occur in all types of geomaterial. However, strain localisation in clays is particularly worrisome and possess huge destructive capabilities because clay is prone to failure and is characterised by low shear strength, often have high water content, and known to induce failure when present in other soils (Yalcin, 2007). Hence, there is the need to better understand and predict strain localisation phenomena in clay. Examples of clay failure systems include: the Blue clay slope Spineto landslide system in Italy (Di Maio, and Vassallo, 2011);

the Agulu-Nanka landslide in west Africa (Ibeh, 2020) ; Black Ven mudslide complex in Dorset, UK (Chandler and Brunsten, 1995); and mudslide in Southern California (Ren et al. 2011).

More recently, significant work has been done to understanding the contribution of particle scale mechanism to the macroscopic behaviour of geomaterials- thanks to X-ray Computed Tomography (X-ray CT) technique which enable 3D non-destructive imaging of representative sample of particles large enough to be imaged at reasonable resolution (Andò et al., 2012; Cheng & Wang, 2018a; Druckrey & Alshibli, 2014; Fu et al., 2008). Although many achievements have been reported with the use of X-ray CT in the study of strain localisation in geomaterials such as sand and gravel, the study of strain localisation in clay remains challenging (Birmpilis et al., 2017).

Clay soils exhibit relatively more complex behaviour compared to sands and despite years of macroscale studies of clay behaviour, the underlying particle scale mechanisms have been largely unexplored. This is because clay particles are very small – with sizes in the order of microns/sub-microns and thickness in the order of tenths/hundredths of naometers, they are plate shaped, and they exhibit physico-chemical interactions in addition to mechanical interactions. However, considering that most of the rupture and deformation incidents in soil is widespread in clay soils, it is important to evaluate clay micromechanics to better understand localisation phenomenon in clay using 4-D X-ray imaging approach.

1.2. Research Aim

The overall aim of this PhD research was to investigate the initiation and propagation of strain localisation in kaolin clay, using mica marker and X-ray CT. It is hypothesized that if suitable sized plate shaped (mica) particle markers are used to study kaolin upon triaxial compression using an X-ray CT, the marker particle kinematics response will help elucidate the initiation and propagation of strain localisation in kaolin. Concepts and techniques from

kinematic analysis inspired in part by progress in the study of sand particle kinematics and localisation, obtained using X-ray CT, was employed. The central question we seek to answer in this study were: can we understand the mechanism of particle interaction in soft clay using mica markers? can measures of mica marker individual grain kinematics detect strain localisation in clay? If so, can such analysis provide early detection of failure and offer new and useful insights on clay micromechanics?

1.3. Research Objectives

The specific objectives of this research were:

- 1) To characterize mica chemically (in terms of its particle interaction and erodibility in different pore-fluid pH and electrolyte concentration) and mechanically (in terms of compressibility, shear strength, and hydraulic conductivity).
- 2) To determine the best approach for sampling miniature clay sample with minimum disturbance.
- 3) To develop a miniature triaxial cell suitable for X-ray Computed Tomography (X-ray CT) imaging of clay with markers and with an inbuilt High-Capacity Tensiometer for hydro-mechanical measurement.
- 4) To develop, implement and validate a particle matching algorithm to quantify particle kinematics -displacement and rotation- of plate-shaped particles using X-ray -CT data.
- 5) To develop a conceptual understanding of the initiation and propagation of strain localisation in kaolin by using X-ray CT and mica markers.

1.4. Structure of Thesis

This thesis is made up of eight chapters. Chapter 2 presents a review of the literature relevant to strain localisation in soil, mica characterisation, miniature triaxial cell equipment

design, and algorithm development for particle kinematics analysis upon loading in soil. Chapters 3 to 6 each contain either manuscript accepted for publication or manuscript under review for publication. Chapter 3 presents investigation into the characterisation of mica particle erosivity in different chemical environment conducted using a Jet Erosion Test (JET) apparatus, this was in part to characterise the chemical behaviour of mica. Chapter 4 contain the mechanical characterisation of mica and mica kaolin composite, using oedometer and direct shear tests. Chapter 5 presents investigation into miniature clay sample preparation techniques using X-ray CT and mica markers. Chapter 6 presents details of the development and validation of a “platy” particle matching algorithm PLATYMATCH, implemented in MATLAB. Chapter 7 is written in a journal article format to be submitted to Geotechnique but is still being worked on. The chapter presents details of the development of a miniature triaxial compression cell with an inbuilt high capacity tensiometer, designed for use within X-ray CT for undrained triaxial compression of clay. It also contains the evaluation of mica marker kinematics within kaolin for the evaluation of the initiation and propagation of strain localisation in kaolin, using the developed miniature triaxial compression cell, PLATYMATCH, and X-ray CT. Chapter 8 presents the main conclusions of this research as well as the limitations of this study and some recommendations for future work with a list of specific topics suggested for future research.

It is important to note that this research evolved through the PhD program and was impacted by restrictions due to Covid-19 in the following ways:

- in chapter 3, it was not possible to obtain additional scans of the mica only particles to enable a closer observation of their roughness.
- In chapter 4, due to time constraints, results of a previous shear test of the same kaolin was adapted for this study with a shear rate that was slightly different, but within the limit to avoid pore pressure build up during shear

- In chapter 4, additional X-ray CT scans of kaolin with relatively low concentration of muscovite were not obtainable due to covid-19 restrictions.

-In chapter 7, it was not possible to design a smaller tensiometer to enable enhanced image resolution. It was also not possible to perform additional triaxial tests in chapter 7 to explore the conditions that affect localisation behaviour in clays.

References cited are presented at the end of each chapter.

1.5. Reference

Andò, E., Hall, S.A., Viggiani, G., Desrues, J. and Bésuelle, P. (2012) ‘Grain-scale experimental investigation of localised deformation in sand: A discrete particle tracking approach’, *Acta Geotechnica*, 7(1), pp. 1–13. doi: 10.1007/s11440-011-0151-6.

Bandara, R.M.S., and K. M. W. (2013) ‘Overview of landslide risk reduction studies in Sri Lanka.’, in C. Margottini, P. Canuti, and K. S. (ed.) *Landslide science and practice*, ed. 1st edn. Berlin, Heidelberg: Springer International Journal of Landslide Inventory and Susceptibility and Hazard Zoning, pp. 345–352.

Birmpilis, G., Dijkstra, J., Tudisco, E. and Hall, S. (2017) ‘In-situ study of deformation mechanisms of soft clay using X-ray Computed Tomography and Digital Volumetric Correlation’, (June).

Chandler, J.H. and Brunsdon, D. (1995) ‘Steady state behaviour of the Black Ven mudslide: the application of archival analytical photogrammetry to studies of landform change.’, *Earth Surface Processes and Landforms*, 20(3), pp. 255–275.

Cheng, Z. and Wang, J. (2018) ‘A particle-tracking method for experimental investigation of kinematics of sand particles under triaxial compression’, *Powder Technology*, 328(September), pp. 436–451. doi: 10.1016/j.powtec.2017.12.071.

CRED (2021) *Natural disasters*, Centre for Research on the Epidemiology of Disasters. Available at: <http://www.cred.be/> (Accessed: 30 May 2021).

- Druckrey, A. M. and Alshibli, K. A. (2014) '3D Behavior of Sand Particles Using X-Ray Synchrotron Micro-Tomography', pp. 2814–2821. doi: 10.1061/9780784413272.272.
- Fu, Y., Wang, L., Tumay, M.T. and Li, Q. (2008) 'Quantification and Simulation of Particle Kinematics and Local Strains in Granular Materials Using X-Ray Tomography Imaging and Discrete-Element Method', *Journal of Engineering Mechanics*, 134(2), pp. 143–154. doi: 10.1061/(asce)0733-9399(2008)134:2(143).
- Ibeh, C. U. (2020) 'Effect of changing groundwater level on shallow landslide at the basin scale: A case study in the Odo basin of south eastern Nigeria', *Journal of African Earth Sciences*, 165(August 2019), p. 103773. doi: 10.1016/j.jafrearsci.2020.103773.
- Di Maio, C. and Vassallo, R. (2011) 'Geotechnical characterization of a landslide in a Blue Clay slope.', 8(1), pp. 17–32.
- Oka, F., Kodaka, T., Kimoto, S., Ichinose, T. and Higo, Y., 2005. Strain localization of rectangular clay specimen under undrained triaxial compression conditions. In *PROCEEDINGS OF THE INTERNATIONAL CONFERENCE ON SOIL MECHANICS AND GEOTECHNICAL ENGINEERING* (Vol. 16, No. 2, p. 841). AA BALKEMA PUBLISHERS.
- Petley, D.N., Dunning, S.A. and Rosser, N. J. (2005) 'The analysis of global landslide risk through the creation of a database of worldwide landslide fatalities', in *Landslide risk management*. CRC Press, pp. 377–384.
- Ren, D., Fu, R., Leslie, L.M. and Dickinson, R. E. (2011) 'Modeling the mudslide aftermath of the 2007 Southern California Wildfires', *Natural Hazards*, 57(2), pp. 327–343.
- Schuster, R.L. and Highland, L. (2001) *Socioeconomic and environmental impacts of landslides in the western hemisphere*. Denver (CO): US Department of the Interior, US Geological Survey.

Viggiani, G., Bésuelle, P. and Desrues, J. (2013) ‘X-ray Microtomography as a Tool for Studying Localized Damage / Deformation in Clay Rock’, Proceedings of the NEA Clay Club Workshop on Clay characterisation from nanoscopic to microscopic resolution, pp. 91–98.

WHO (2021) Landslides. Available at: https://www.who.int/health-topics/landslides#tab=tab_1 (Accessed: 30 May 2021).

Yalcin, A. (2007) ‘The effects of clay on landslides: A case study’, Applied Clay Science, 38(1–2), pp. 77–85.

2. Geomaterial Instability

Trends of climate change and global warming has increased landslide hazard over the last two decades. Mass movements in clay deposits result in damage to infrastructures and buildings (Figure 1) with significant social, economic, and environmental consequences (Yulong Chen et al., 2020; Huang & Dai, 2014; Liu et al., 2018; Pritchard et al., 2014)



Figure 1: a) Alta Landslide which occurred on the 3rd of June 2020 in a body of clay, destroys road in Northern Norway (adapted from www.lifeinnorway.net on the 30th of May 2021) b) Drone image showing the landslide site at Ask in Gjerdrum municipality, Norway after a deadly landslide on the 30th of December 2020 (adapted form www.world-today-news.com on the 30th of May 2021).

A common denominator of geomaterial instability process is that they most often involve multi-physical and non-linear processes at several length scales, this makes it challenging to predict them accurately. In addition, these processes are often characterized by strain localization, a sudden nonhomogeneous deformation phenomenon (ALERT, 2016). Strain localization is a complex process to investigate experimentally and model.

2.1. Strain localisation

Strain localisation is ubiquitous in geo-materials and occur over a vast range of scales, from the microscale of grains to faults extending over kilometres. A common form is shear banding, which is a narrow zone of intense shear straining. Most geomaterial fail by the formation and propagation of zones of localised shear deformation. Its formation is usually

accompanied by a softening response resulting in progressive failure. Strain localisation may be accompanied by dilatancy (inelastic volume increase) and/or compression (inelastic volume decrease) as well as by chemical alteration. Thus, they may exist as compaction bands, shear bands or dilation bands (Figure 2). Relatively small-scale shear zones and fractures can significantly compromise foundations and underground structures of all types and, at a larger scale, control the propagation of earthquakes. On the other hand, compaction bands may control both the mechanical and hydraulic transport behaviour of geomaterials for example the formation of trap (impermeable barrier) for hydrocarbon reservoir or bounded aquifers.

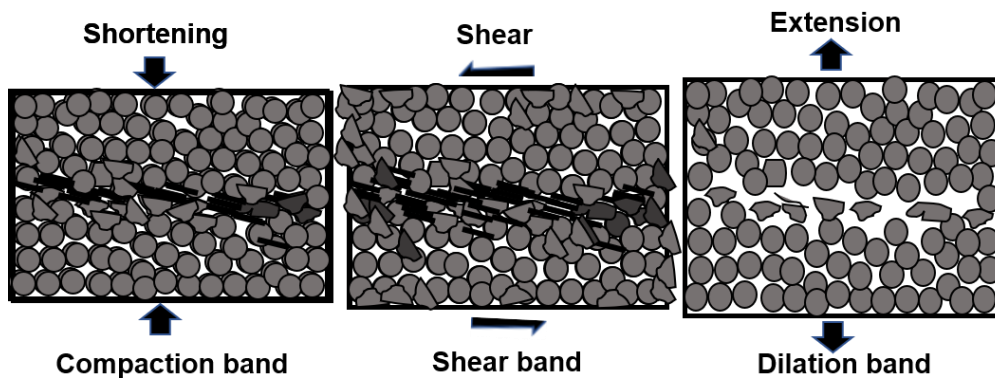


Figure 2: Localised deformation with compaction, shear and dilation band (modified from Du Bernard et al., 2002)

Considering that strain localization is a precursor to failure in geomaterials, it is one of the most important and rich but complex issue in geomechanics (ALERT, 2016). This has motivated numerous theoretical, experimental, and numerical works in geomechanics. However, numerous questions still exist about how strain localisation is initiated and propagated and how the formation and subsequent evolution of strain localisation are related to the hydraulic state, stress state including suction, deformation history, material properties, heat, and chemical alterations. The eventual precursors in the transition from homogeneous deformation to localised deformation is poorly understood. Therefore, it is important to clarify

the mechanism involved in their formation and propagation and enriching knowledge and understanding of strain localisation in clay geomaterials is key in the field of geomechanics.

2.2. Continuum constitutive modelling

Mechanical behavior of geomaterials is generally modelled within the framework of continuum mechanics and stress-strain constitutive models have been developed to represent different types of soil materials to aid the prediction of pre- and post-failure deformation of ground and embankment as well as displacement of structures which they interact with. A well-known example of such constitutive models is the modified Cam Clay model (Schofield, and Wroth, 1968). However, a major drawback of these models is their implicit assumption of material continuum and as such, at strain localisation regime, we deal with mathematically ill-posed governing equations (ALERT, 2016). Classical continuum models show significant limitation when trying to model strain localisation in geomaterials.

According to Mallikarachchi & Soga (2020) this results from the fact that conventional constitutive models do not contain material parameters with dimension of length and as such features such as shear band thickness is undetermined. Continuum mechanics approaches rely on macroscopic empirical data to characterize the stress-strain response of a material. It generally relies on measuring soil properties on sample boundaries, as such, the fundamental material physics is not represented. The discrete nature of granular materials does not make it easy to define the notion from a phenomenological point of view. Essentially, localization of deformation reduces the scale of the problem and phenomena occurring at the grain or near-grain scale cannot be left out in the modelling of the macroscopic behaviour of geomaterials. This was rightly put by Terzaghi when he stated that (Santamarina, 2001):

“Coulomb purposely ignored the fact that sand consists of individual grains and dealt with sand as if it were a homogeneous mass with certain mechanical properties. [The] idea proved very useful... but it developed into an obstacle as soon as its hypothetical character came to

be forgotten. The way out of this difficulty lies in dropping the old fundamental principles and starting again from elementary fact that sand consists of individual grains”.

An excellent understanding of the above concept led Sibille & Froiio, (2007) to say that *'This has led to the paradox of micromechanics of granular materials as a science based almost entirely on “virtual evidence”*. The importance and significance of micro-scale geomaterial study is well established in the literature (e.g., Andò et al., 2012; Druckrey & Alshibli, 2014; Hall et al., 2010; Hasan & Alshibli, 2012; Hill & Selvadurai, 2005; Iwashita K., Oda, 1998; Shire & O’Sullivan, 2013; Viggiani et al., 2013). As aptly stated by Viggiani et al., (2013), clay rocks, just as any other geomaterials, have a microstructure, although this is ignored in classical models. This has always come back to haunt us especially when deformation is localized in regions so small that the detail of the geomaterial structure cannot safely be ignored.

Continuum models with adequate material microstructure parameters will be better at describing and better predicting localisation phenomena which are the precursors of failure in geomaterials. Thus, particle and near-particle-scale investigation could represent an effective approach to address such drawbacks. Overall, the recognition of the above concept has seen a move from conventional continuum mechanics to discrete or mixed discrete and continuum methods.

2.3. Geomaterial modelling spectrum.

A broad spectrum of geomaterial modelling approach has been developed (Figure 3), ranging from the continuum end (e.g., FEM) to the discrete end (e.g., Discrete Element Method- DEM), with mesh free hybrid methods such as Smoothing Particle Hydrodynamics (SPH) at the middle. These methods complement each other and have their associated advantages and disadvantages.

The analysis of geostructures in geomechanics is often made based on finite element method (Bui & Nguyen, 2017). This is done either through the onset of kinematically admissible sliding by evaluation as solution evolves at mesh nodes (Hicks & Spencer, 2010) or through the detection of failure as a loss of global equilibrium seen as a lack of convergence of the solution identified by the lack of convergence within a certain iteration number (Griffiths & Lane, 1999; Taylor, and Zienkiewicz 2005). Unfortunately, FEM shows some limitations when dealing with localised deformation problems because due to their mesh size and the nature of constitutive models employed. While methods like FEM are suited for large scale geomaterial modelling, the mechanical constitutive models they are built upon may fail in capturing the effect of particle scale phenomena like strain localisation.

Hybrid mesh free modelling approach such as SPH, in which element size are point based, although overall a continuum-based method, does not require any background mesh and solve the strong-form governing differential equations, unlike FEM solving weak-form differential equations. Although mesh free, SPH requires large computational power and scaling this method to large scale geomechanically structures is non-trivial. Like FEM, they are also built on macroscopic constitutive models that may fail in capturing the effect of particle scale phenomena.

Discrete element model (DEM) is a numerical method in which the finite displacement and rotation of discrete bodies are simulated (O'Sullivan, 2011; Shire & O'Sullivan, 2013). It has long been known that the particulate nature of soil underlies its response characteristics and DEM simulations can help the development of constitutive models in understanding the complex behaviour of soils (O'Sullivan, 2011). In a DEM model, particle move and rotate relative to each other and during the movement, contacts between particles are formed and broken based on a defined contact law. The contact forces resulting from the interaction of particles and the inertia of the body are generated from which acceleration is computed and the

resultant displacement over a small-time step increment is determined. With several time steps, the evolution of the system is simulated. The micro scale result of the simulation is often used to enhance our understanding of fundamental mechanisms and to inform continuum models for use in practice.

The need to complement DEM simulations with experimental studies has been emphasised in the geotechnical literature. Although the development of discrete element model to capture the behaviour of clays have been attempted by several authors (Anandarajah & Yao, 2002; Pagano et al., 2017), there is a lack of experimental data to validate or calibrate these models. In addition, the 3D geometry of clay particles, the number of particles required to capture a representative Element Volume - REV, and realistic particle size distribution are not properly captured.

Other limitations include the complex geometry and contact law for clays requiring large computer memory and high processor speed. Real physical soils are 3D and to develop a DEM model that truly captures the 6 degrees of freedom and real geometry of soils 3D simulation is needed, but this comes with the challenge of large computational cost. High performance computers (HPC) associated with supercomputer are composed of multiple processors for higher performance than common personal computers and may help to solve this problem. While DEM is promising for evaluating strain localisation in soils as it involves particle scale modelling, it is limited in terms of parallelisation to tackle field-scale applications due to the enormous number of particles required to capture large scale features and the associated computational power required for such analysis.

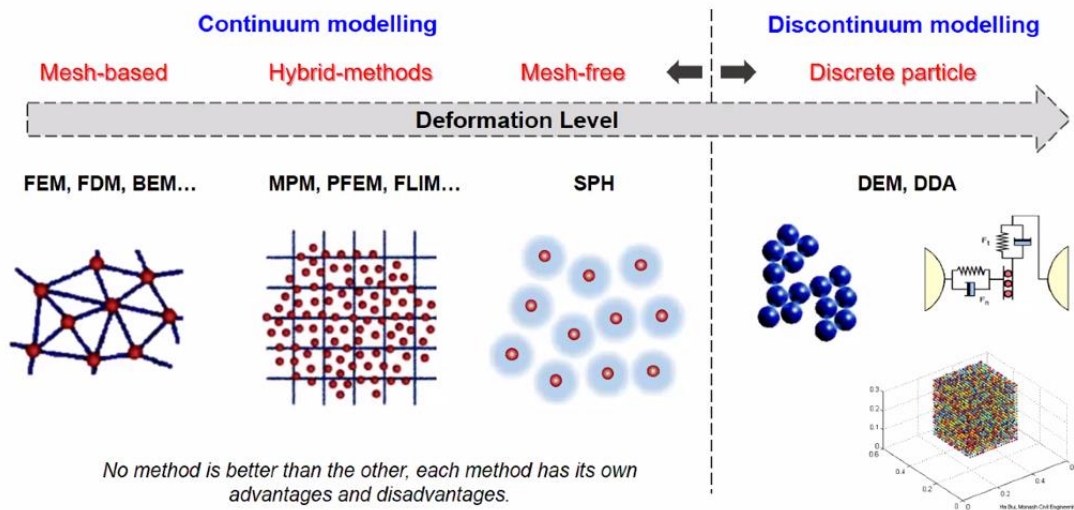


Figure 3: Geomaterial numerical modelling spectrum (adapted from ALERT, 2020)

2.4. Constitutive model enrichment

There needs to be some form of enrichment of conventional constitutive models by adding soil “genome” (particle scale soil properties) for any reasonable progress to be made with predicting deformation and instabilities in geomaterials. A new development is the emergence of the double scale approach to the study of instabilities in geomaterial. The double scale modelling approach defines and solves two numerical problems which must be linked— one at the small scale and the other at the large (continuum) scale. Linking the two scales require an understanding of the physics at the appropriate scale and ideally this comes directly from experiment (Viggiani et al., 2013).

In the double scale approach to modelling strain localisation, the structure of constitutive model is enriched to accommodate micro/meso-scale details of the localisation band, including its orientation, thickness, and behaviour. Recent developments of a double-scale approach to tackle material instability issues related to softening and localization has seen its application in SPH modelling (Bui & Nguyen, 2017). In this approach, length scales are

incorporated in the structure of the constitutive model (e.g., an effective size of an SPH particle) and allows scaling of the constitutive behaviour of the SPH particle to correctly describe post-localization stage of failure. As such, the behaviour of the volume element crossed by the localisation band is governed by behaviour of the localisation band, its orientation and size as well as the behaviour of the zone outside the band. A length scale related to the thickness of the localisation band is involved in the modelling of mechanical behaviour.

Further, DEM approach is used to understand the particle-to-particle interactions and how such interactions take place in a force-displacement space. Experience from these studies is then used to enrich constitutive models such as the double scale constitutive model. The nascent state of these methods require that they need to be calibrated and validated with experimental data. Details of thickness and orientation of localisation band, initiation and deactivation of localisation band, evolution of localisation band thickness need to be understood and validated with experimental results to enable proper enrichment of constitutive models for better prediction of geomaterial (Mallikarachchi & Soga, 2020).

2.5. Full field imaging of soil

Full-Field Imaging is any imaging technique in which all pixels of the image are collected at the same time. Full-field methods encompass several different techniques. Imaging has traditionally been conducted on post-mortem samples, which pose the challenge of alteration of soil microstructure associated with sample preparation technique. For example, the use of Cryo-SEM requires sample size less than 2-3 mm to avoid effects of non-uniform freezing and for Environmental SEM, and sample preparation process leads to remoulding and disturbance to original structures especially for sensitive clays (Emdal et al., 2016).

In a bid to study strain localization in soils, various micro-scale techniques involving imaging and distinct particle modelling have been employed. Many such techniques exist, including among others, image correlation, grid method, speckle interferometry and the Moiré

method (Vautrin et al., 2002). Through such study, particle kinematics is evaluated. Once particle displacement field is measured, the strain field can be deduced.

Lin, and Penumadu, (2006) recognized that the deformation and strain components at different positions of a deforming specimen are required to better address strain localization and its impact on the interpretation of test results. They studied strain localization using dots drawn on latex membrane covering Kaolin clay but only sample surface deformation information will not give comprehensive details of the internal soil behaviour.

Until recently, various full field measurement has been used to study strain localization in coarse-grained geomaterials (e.g., sand and gravel). Clay geomaterials are more difficult to image due to the higher spatial resolution required to resolve the small particle size and localization thickness of available full field measuring techniques such as X-ray CT. However, this has started to change with developments of micro- X-ray CT (Lenoir et al., 2007).

2.5.1. X-ray Computed Tomography

On an X-ray CT system, X-Ray is produced through a source with the sample to be imaged placed at a distance from the source. As the X-ray radiation passes through the sample, the beam is progressively attenuated due to interactions with material constituent atoms. The attenuation may be primarily because of three mechanisms: photoelectric adsorption, Compton scattering and coherent scattering (Simons et al., 1997; Taina et al., 2008). Bear's law describes the attenuation of a beam of monochromatic X-ray radiation:

$$\frac{I}{I_0} = \exp(-\mu h) \quad [1]$$

where I_0 and I are the incident and attenuated X-ray, μ is the linear attenuation coefficient, and h is the thickness of the scanned object. The linear attenuation coefficient depends on the

material bulk density (ρ), atomic number (Z) and energy (E) of the Xray beam (Taina et al., 2008) according to equation 2.

$$\mu = \rho \left(a + \frac{bZ^{3.8}}{E^{3.8}} \right) \quad [2]$$

where a and b are energy-dependent coefficients.

The acquired attenuation signatures are reconstructed through tomographic reconstruction which consist of linear integration of attenuation, using reconstruction techniques such as filtered back propagation (Singh et al., 2010). The images are then filtered to remove/suppress noise (unwanted signal) prior to segmentation. Thereafter, elements of the X-ray CT image are differentiated through a technique known as segmentation. The segmented images are then used to analyse sample properties.

2.5.2. *Challenges to the use of X-ray CT for imaging clay*

Although with the advent of X-ray CT in geomechanics relative progress has been made to understanding the micromechanics of sand at the particle scale (Desrues & Viggiani, 2004; Druckrey & Alshibli, 2014; Karatza et al., 2019; Mallikarachchi & Soga, 2020; P. Wang et al., 2019; P. Wang & Yin, 2020), such cannot be said for clays especially clay due to small size of their particles which cannot be imaged with available X-ray CT resolution. This has hampered our understanding of particle-scale mechanisms underlying fundamental aspects of clay mechanical behaviour. For example, it is well known that the shearing of a loose soil sample results in no peak shear stress whereas shearing of a dense soil sample results in peak stress (Terzaghi, K., Peck, R.B. and Mesri, 1996); for a dense quartz sand sample, the peak stress is generally attributed to the interlocking of particles but for soil samples such as overconsolidated clay, it is not well understood how clay particles interact to give rise to peak shear stress (see Figure 4).

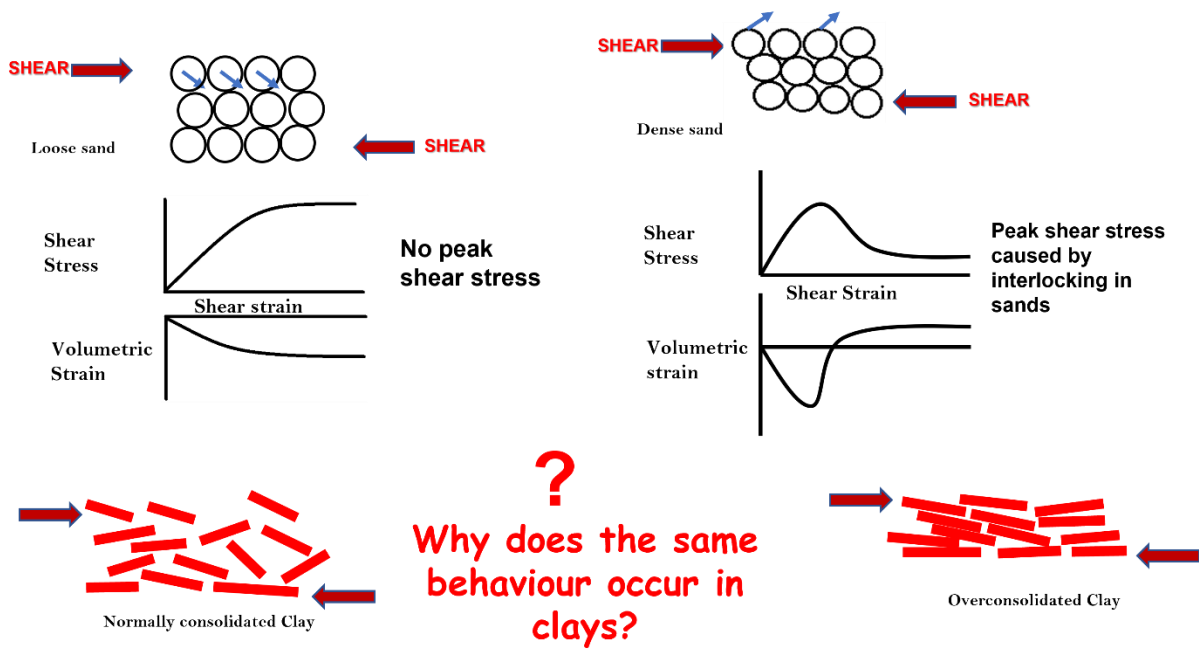


Figure 4: Sketch of the shear behaviour of dense sand compared to loose sand and the need to understand the difference between normally consolidated clay and overconsolidated clay.

The major challenges to understanding clay microstructure using the imaging approach are:

- i. The lack of imaging technology with adequate resolution to enable visualization of the spatial arrangement of clay particles and its associated pores at a representative element volume; in a time resolved process. Imaging a representative specimen from an X-ray CT is limited by resolution. Even with synchrotron Xray CT which can attain a resolution of 0.1 micrometer, difficulty persists in capturing a clear picture of the interfacial porosity that may encompass nano-pores (Cui et al. 2017).
- ii. Another challenge is how it might be possible to upscale imaging results to scales in space and time relevant in macroscopically observed soil properties. In addition, natural clays show structures such as bioturbation, sedimentary laminae diagenetic mineral growth and dissolution, but small samples may not capture such structure. Furthermore, image processing requires handling of large data volume and there is

a lack of standardized image processing protocol. Image processing like thresholding is essentially subjective.

- iii. Incorporating the physico-chemical microscopic interactions between particles (Pagano et al., 2017). Clay exhibit physico-chemical properties and capturing this through imaging is challenging.
- iv. The need to ensure that time dependent mechanical response, i.e., pore pressure dissipation and creep in clay sample does not affect image acquisition (Birmpilis et al., 2017). This may create additional challenges to obtaining accurate reconstructions from X-ray CT raw radiographs. Therefore, during clay sample image acquisition, the sample should ideally be kept stable without additional deformations or significant time dependent mechanical response.
- v. Adequately capturing the 3D platy shape of clay particles to effectively interpret soil microscopic behaviour for enriching discrete element models in non-trivial.
- vi. Evaluating particle kinematics using scans entail huge computational requirement for particle interactions between millions to billions of particles in a representative volume of clay sample.

There is currently no imaging technology capable of providing 4D visualization of clay sample of representative element volume at resolution high enough to visualize clay particle interaction.

2.6. Particle Kinematic evaluation and strain quantification

To better understand soil discrete mechanics, X-ray CT imaging technique are used to capture the particle scale features of granular soil subjected to some physical loading (mechanical, thermal, hydraulic etc.) over time. X-ray CT provides an effective approach for analysing microscopic deformation of geomaterials (Andò et al., 2012; Karatza et al., 2019;

Reijonen et al., 2020; Viggiani et al., 2013), because of the detailed and huge amount of information that can be obtained from acquired images. The analysis of such images usually requires particle matching algorithms for particle kinematic evaluation from one scan (before loading) to another scan (after loading). Although an approach called discrete digital image correlation -Discrete DIC (Andò et al., 2012; Hall et al., 2010) which recognises grains based on their image (numerous pixel grain scale information) can be used to produce full field strain measurement, the approach is computationally expensive (Andò et al., 2012). A more computationally simple approach to particle matching is the use of simple morphological particle attributes to match particle before and after loading, enabling the effective determination of sample kinematics.

As presented in Table 1, (Fu et al., 2008) implemented a particle matching algorithm to match crushed limestone particles (average size of $127\mu\text{m}$), using expected particle position reference and volume as matching parameters. Their algorithm searches for a particle in the initial sample scan with the closest location to where the particle should be in the second scan 2 (after loading) and then used the particle volume as an additional parameter if there are more than one particle in that location. This search approach may however break-down when searching for particles in a shear band (where particles may move in an unpredictable manner). (Andò et al., 2012) developed a particle matching algorithm -ID Track and used it to match carbonate and quartz sand (average size of $400\mu\text{m}$ and imaged at $15\mu\text{m}$ pixel size). ID Track searches for particles in two passes with the first pass using only volume difference and the second pass using both volume difference and difference of displacement of neighbouring particles. Particles with the closest feature as the one under consideration are matched. They pointed out their assumption that grains will tend to displace like their neighbours but also noted that this may cause problems when a neighbourhood overlaps a developed shear band. They used only one parameter with a wide enough distribution, i.e. volume, as the matching

parameter but this may be a challenge for particles with less-unique volume. (Cheng & Wang, 2018b) also implemented a similar algorithm as ID-Track to match quartz sand with an average size of 500 μ and imaged at 6.5 μ pixel size, but rather than using volume as the matching parameter they also used surface area in place of volume obtaining similar result. Further, (Druckrey & Alshibli, 2014) implemented an algorithm (to match quartz sand particles with an average size of 700 μ and 10.85 μ pixel size) that searches particles from one scan to another using particle features parameter including volume, surface area, length, and width. The parameters were considered in series (sequentially), and as such a particle must be within a set tolerance for the first parameter to be considered for check using the second parameter, and same as the third and fourth. Table 1 presents details of the samples studied, the imaging condition, the algorithm implementation approach used by the studies described above.

Table 1: available matching algorithm and their implementation

	Author	(Fu et al., 2008)	(Andò et al., 2012)	(Druckrey & Alshibli, 2014)	(Cheng & Wang, 2018b)
1	Material Tested and size	Crushed Limestone	Calcareous and quarzitic Sand	Quarzitic sand	Sand
2	Sample size (Diameter X Height)	103 mm X 100 mm	11 mm X 22 mm	9.5mm X 20.2 mm	8mm X 16 mm
3	Average Particle size	127 μ	400 μ	700 μ	500 μ
4	Pixel size	-	15 μ	10.85 μ	6.5 μ
5	Average ratio of particle major axis to pixel size		27	65	77
6	Average ratio of particle minor axis to pixel size		27	65	77
7	Particle segmentation approach	Thresholding	Watershed segmentation	Thresholding	-
8	Search box used	No	Yes	Yes	Yes
9	Particle feature used for matching	Particle proximity	Particle position and particle volume	Particle position with sequential filtering of particle features: Volume, Surface area; width and lengths	Particle position and particle Area or Volume
10	Matching criteria	Direct comparison	Iterative comparison	Sequential comparison	Iterative comparison

To our knowledge, there is currently no soil particle matching algorithm designed for platy particles and it is important to develop one for a robust matching of platy soil particle upon soil sample deformation.

2.7. Use of clay markers.

There is therefore the need to use alternative approach to image clays such as the use of marker which are large enough to be imaged with current technologies. (Fawad et al., 2010) have attempted to use silt sized quartz to quantify strain in clay during compression. Well graded quartz silt mixed with clay or gap graded soil may show transitional behaviour and equidimensional markers such as quartz silt may not reveal orientation and rotation information.

Mica is a phyllosilicate (platy shape) and mineralogically a clay. Its rotation and displacement may be easily detectable since it is platy in shape. Hence silt sized mica particles may be used as markers to estimate the kinematics of clays upon strain localization, provided the mica does not significantly alter the physical and electrochemical behaviour of the clay being studied. Mica is further described below.

Mica may occur as muscovite, lepidolite, phlogopite, biotite, and lepidomelane mineral forms (Hoseini et al., 2016). Muscovite mica is used in this study due to its ubiquitous nature. Mica is a phyllosilicate mineral, which may range in size from sand to silt and clay size platy particles, but it occurs mostly as a silt sized waste material in mine settings. It has the fundamental formula $\text{KAl}_2(\text{AlSi}_3\text{O}_{10})(\text{OH})_2$ and is a 2:1 clay mineral (Figure 5). The crystal structure is the one of active clays, it comprises a stack of unit layers of an Al–O–Al octahedral (O) layer sandwiched between two Si–O–Al tetrahedral (T) layers. Substitutions of lattice Si^{4+} by Al^{3+} in the tetrahedral layer and Fe^{3+} or Mg^{2+} and Ca^{2+} for Al^{3+} in the octahedral layer which invariably occur, result in a permanent net negative charge on the basal surfaces (Figure 1). The charge deficiency is compensated by interlayer cations such as K^+ and Na^+ adsorbed

between the T-O-T sheets, fitting closely into the hexagonal holes of the Si–O–Al sheet. The interlayer cations (e.g. K^+) strengthen the bonding between basal planes of TOT sheets, which are normally held by attractive van der Waals forces, through the attractive electrostatic interactions (Nosrati et al., 2009).

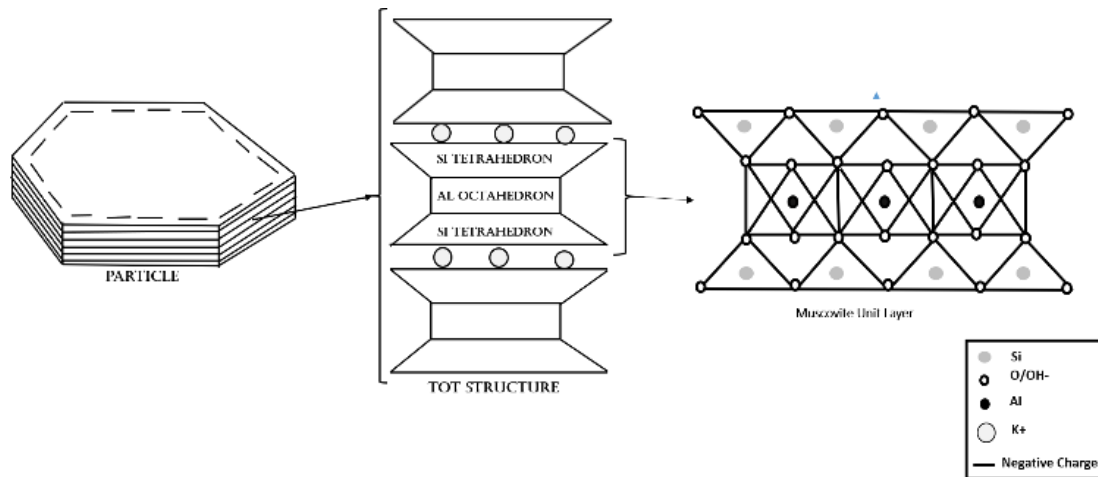


Figure 5: Muscovite mica structure

2.7.1. Characterisation of mica

For mica to be used as a clay marker, it needs to be characterised both in terms of its chemical behaviour and mechanical characteristics. This will give an understanding of mica characteristics, how mica markers interact with clay (for example kaolin) and what amount of mica marker could be used as clay markers without a significant compromise of the clay properties.

Mica occurs in all types of rocks: sedimentary, metamorphic and igneous and it also exist as mining waste in the mining industry, where its management (mica mine waste) has generated significant attention due to the large volume generated. About 10 million tonnes of mica waste is generated in a year and over 600 million tonnes of total industry stockpile is estimated to be available (Palumbo-Roe and Colman 2010). Mica waste is usually deposited in

large lagoons and abandoned in clay pits. It contains between 10% and 75% mica mineral and currently has seen very limited re-use; within flux for ceramic glazes and as a mild abrasive (Hojamberdiev, Eminov et al. 2011); (Zografou, Heath et al. 2014); Basak 2019). Such waste mica may be re-used in landscaping, low-volume paved roads and fill material for flood embankments or as potassium source in agricultural fields.

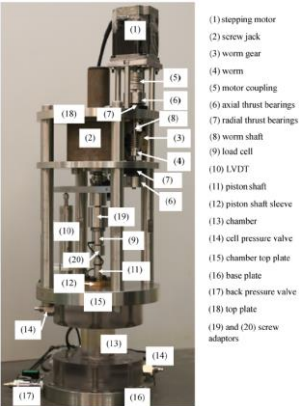

Characterising mica erodibility as part of its chemo-mechanical characterisation will be of an added advantage, considering that many of the proposed uses of mica waste require some level of erosion resistance. The charge on clay particles is well documented to be pH dependent (van Olphen 1977; Gratchev & Towhata, 2013; Mitchell & Soga, 2005; Nishimura et al., 1992) and affects their erodibility (Gupta, V. and Ahmed, 2007; Man & Graham, 2010; Momeni et al., 2020). Hence, to characterise the erodibility of mica it is important to consider a wide range of pore-water chemistries. Therefore, it will be important to better understand mica erosion susceptibility as part of its characterization.

2.8. Existing miniature cells for soil mechanical testing

Triaxial tests have been widely used to determine the strength characteristics of both saturated and unsaturated soil. Although, various miniature triaxial deformation devices have been developed for the study of soil using X-ray CT such as devices developed by: Cheng et al., 2020; Hall et al., 2010; Higo et al., 2013; Otani et al., 2002. Available miniature triaxial cells have a limiting design which restrict achievable resolution when used in industrial X-ray CT cone beam systems. For the X-ray CT system, higher resolution is achieved by taking the sample being imaged as close as possible to the X-ray source; thus, a triaxial device with relatively large diameter will restrict the achievable resolution. To better understand clay hydromechanics, it is important to develop a miniature triaxial cell, instrumented with a tensiometer for pore pressure measurement enabling triaxial compression of relatively soft clay with total and effective stress path evaluation. As confining effective stress is provided by

suction, the triaxial cell does not require the use of an external fluid to impose a total radial stress. In this way, the overall radial dimension of the cell can be reduced significantly and allow for the X-ray source to be very close to the sample. None of the existing triaxial cell was designed for soft clay, none of them is instrumented to measure both positive and negative pressure and non is designed for the peculiar nature of the Nikon XT H 225 LC X-ray computed tomography laboratory system Laboratory available at Strathclyde, hence the need to develop a new miniature triaxial cell. The device also has to be small enough to shear miniature clay sample, transparent to X-ray and allow for comparison between conventional soil boundary measuring devices and micro scale details obtainable with X-ray. Table 2a contains technical details of existing miniature triaxial cell and Table 2b contain details of research and result of the tests conducted with the respective miniature triaxial cells.

Table 2a: Technical details of existing miniature triaxial cells

Author	Image of device	Equipment dimension and weight	Pressure control / Negative pore pressure measurement	X-ray Source designed for	Limitation
(Cheng et al., 2020)		<p>-520 mm in height and 20 kg in weight.</p> <p>-The sample size required for the apparatus is 8mm X 16mm (diameter X height).</p>	Have pressure control/Not instrumented for negative pore pressure measurement	Laboratory	<p>- Not adapted for some -industrial X-CT device due to restriction preventing how close samples can get to the x-ray source and hence reduced image resolution for conventional laboratory CT.</p> <p>-Designed for triaxial testing of sand.</p>
(Hall et al., 2010)		Details not provided by author.	Have pressure control/Not instrumented for negative pore pressure measurement	Synchrotron radiation	<p>-Designed for Synchrotron radiation source</p> <p>-Designed for triaxial testing of rock or sand</p>


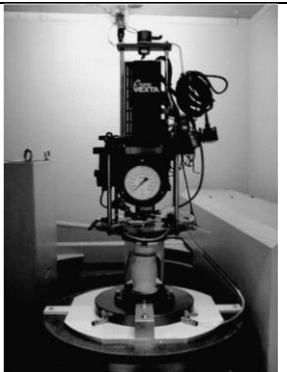
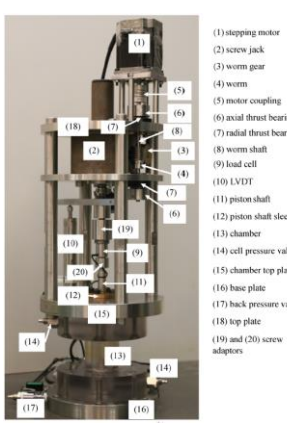


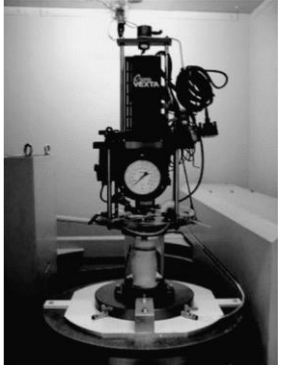
(Higo et al., 2013)		Details provided author.	not by	No pressure control/Not instrumented for negative pore pressure measurement	Laboratory	- Unable to measure Pore pressure or drain water during triaxial test -Designed for triaxial testing of sand
(Otani et al., 2002)		Details provided author.	not by	Have pressure control/Not instrumented for negative pore pressure measurement	Laboratory	-Designed for triaxial testing of sand

Table 2b: Research findings of tests conducted with existing miniature triaxial cells

Author	Image of device	Type of soil studied	What measured to visualise deformation	Image resolution	Result/Findings
(Cheng et al., 2020)		Leighton Buzzard sand 8 mm x 16 mm	Sand particles directly observed	6.5 μm	The sample, with nearly homogenous initial local porosities, starts to exhibit obvious inhomogeneity of local porosities and localization of particle kinematics and volumetric strain around the peak of deviatoric stress. Post-peak shear strength stage, large local porosities and volumetric dilation mainly occur in a localized band.
(Hall et al., 2010)		Callovo-Oxfordian argillite (Argillaceous Rock) 10mm *20mm	Digital volume correlation using natural particle inclusion in the rock.	14*14*14 μm ³	-Using mass density changes to detect shear strain localisation is limited and most often not effective. -The thickness of shear bands as it appears in DIC-based shear strain fields is largely over-evaluated, because it

					cannot be smaller than the subset size.
(Higo et al., 2013)		Tuyoura sand 70mm * 35 mm	Sand particles were directly observed	11*11*11 μm^3	-Voids in the shear bands was found to be much larger than those at the initial state or outside of the shear bands. -The stress-strain relations for partially saturated sand exhibit stronger softening behaviour than those for the fully saturated or the air-dried sand.
(Otani et al., 2002)		-Yamazuna Sand 100mm*50 mm	Sand particles directly observed	73*73*30 μm^3	-Shear band in the studied sand starts before the stress peak as a wide, diffuse zone, and then narrows into a concentrated shear zone after the peak

2.9. References

ALERT (2016) ‘ALERT Doctoral School 2016 Modelling of instabilities and bifurcation in Geomechanics’, Alert school book.

ALERT (2020) ‘ALERT Doctoral School 2020 Point based numerical methods in geomechanics’.

Anandarajah, A. and Yao, M. (2002) ‘Three-Dimensional Discrete Element Method of Analysis of Clays’, 129(June), pp. 237–241. doi: 10.1061/40647(259)42.

Andò, E., Hall, S.A., Viggiani, G., Desrues, J. and Bésuelle, P. (2012) ‘Grain-scale experimental investigation of localised deformation in sand: A discrete particle tracking approach’, Acta Geotechnica, 7(1), pp. 1–13. doi: 10.1007/s11440-011-0151-6.

- Du Bernard, X., Eichhubl, P. and Aydin, A. (2002) 'Dilation bands: A new form of localized failure in granular media', *Geophysical Research Letters*, 29(24), pp. 1–4. doi: 10.1029/2002GL015966.
- Birmpilis, G., Dijkstra, J., Tudisco, E. and Hall, S. (2017) 'In-situ study of deformation mechanisms of soft clay using X-ray Computed Tomography and Digital Volumetric Correlation', (June).
- Bui, H. H. and Nguyen, G. D. (2017) 'A coupled fluid-solid SPH approach to modelling flow through deformable porous media', *International Journal of Solids and Structures*, 125, pp. 244–264. doi: 10.1016/j.ijsolstr.2017.06.022.
- Chen, Y., Withanage, K.R., Uchimura, T., Mao, W. and Nie, W. (2020) 'Shear deformation and failure of unsaturated sandy soils in surface layers of slopes during rainwater infiltration', *Measurement: Journal of the International Measurement Confederation*, 149, p. 107001. doi: 10.1016/j.measurement.2019.107001.
- Cheng, Z., Wang, J., Coop, M.R. and Ye, G. (2020) 'A miniature triaxial apparatus for investigating the micromechanics of granular soils with in-situ X-ray microtomography scanning', *Frontiers of Structural and Civil Engineering*, 14(2), pp. 357–373. doi: 10.1007/s11709-019-0599-2.
- Cheng, Z. and Wang, J. (2018) 'A particle-tracking method for experimental investigation of kinematics of sand particles under triaxial compression', *Powder Technology*, 328, pp. 436–451. doi: 10.1016/j.powtec.2017.12.071.
- Cui, D., Sun, W., Wan, K. and Banthia, N. (2017) 'Porosity characterization in interfacial transition zone using dual CT scans', *Journal of Testing and Evaluation*, 45(2), pp. 408–418.
- Desrues, J. and Viggiani, G. (2004) 'Strain localization in sand: An overview of the experimental results obtained in Grenoble using stereophotogrammetry', *International*

- Journal for Numerical and Analytical Methods in Geomechanics, 28(4), pp. 279–321.
doi: 10.1002/nag.338.
- Druckrey, A. M. and Alshibli, K. A. (2014) ‘3D Behavior of Sand Particles Using X-Ray Synchrotron Micro-Tomography’, pp. 2814–2821. doi: 10.1061/9780784413272.272.
- Emdal, A., Gylland, A., Amundsen, H.A., Kåsin, K. and Long, M., 2016. Mini-block sampler. Canadian Geotechnical Journal, 53(8), pp.1235-1245.
- Fawad, M., Mondol, N.H., Jahren, J. and Bjørlykke, K., 2010. Microfabric and rock properties of experimentally compressed silt-clay mixtures. Marine and Petroleum Geology, 27(8), pp.1698-1712.
- Fu, Y., Wang, L., Tumay, M.T. and Li, Q. (2008) ‘Quantification and Simulation of Particle Kinematics and Local Strains in Granular Materials Using X-Ray Tomography Imaging and Discrete-Element Method’, Journal of Engineering Mechanics, 134(2), pp. 143–154. doi: 10.1061/(ASCE)0733-9399(2008)134:2(143).
- Gratchev, I. and Towhata, I. (2013) ‘Stress-strain characteristics of two natural soils subjected to long-term acidic contamination’, Soils and Foundations, 53(3), pp. 469–476. doi: 10.1016/j.sandf.2013.04.008.
- Griffiths, D. V. and Lane, P. A. (1999) ‘Slope stability analysis by finite elements’, Geotechnique, 49(3), pp. 387–403. doi: 10.1680/geot.1999.49.3.387.
- Gupta, V. and Ahmed, I. (2007) ‘Geotechnical characteristics of Surabhi Resort landslide in Mussoorie, Garhwal Himalaya, India’, Himalayan geology, 28(2), pp. 21–32.
- Hall, S.A., Bornert, M., Desrues, J., Pannier, Y., Lenoir, N., Viggiani, G. and Bésuelle, P., (2010) ‘Discrete and continuum analysis of localised deformation in sand using X-ray μ CT and volumetric digital image correlation’, Geotechnique, 60(5), pp. 315–322. doi: 10.1680/geot.2010.60.5.315.

- Hasan, A. and Alshibli, K. (2012) ‘Three-dimensional fabric evolution of sheared sand’, *Granular Matter*, 14(4), pp. 469–482. doi: 10.1007/s10035-012-0353-0.
- Hicks, M. A. and Spencer, W. A. (2010) ‘Influence of heterogeneity on the reliability and failure of a long 3D slope’, *Computers and Geotechnics*, 37(7–8), pp. 948–955. doi: 10.1016/j.compgeo.2010.08.001.
- Higo, Y., Oka, F., Sato, T., Matsushima, Y. and Kimoto, S. (2013) ‘Investigation of localized deformation in partially saturated sand under triaxial compression using microfocus X-ray CT with digital image correlation’, *Soils and Foundations*, 53(2), pp. 181–198. doi: 10.1016/j.sandf.2013.02.001.
- Hill, J. M. and Selvadurai, A. P. S. (2005) *Mathematics and mechanics of granular materials*, *Mathematics and Mechanics of Granular Materials*. doi: 10.1007/1-4020-4183-7.
- Hoseini, S. M. R., Bahrami, A. and Hosseinzadeh, M. (2016) ‘The reclamation of mica flakes from tailing disposal using gravity separators and flotation’, *International Journal of Mining and Geo-Engineering*, 50(1), pp. 61–76. Available at: https://ijmge.ut.ac.ir/article_57309.html%0Ahttps://ijmge.ut.ac.ir/article_57309_4424b4ab432302d7f80c8e180b7c029b.pdf.
- Huang, Y. and Dai, Z. (2014) ‘Large deformation and failure simulations for geo-disasters using smoothed particle hydrodynamics method’, *Engineering Geology*, 168, pp. 86–97. doi: 10.1016/j.enggeo.2013.10.022.
- Iwashita K., Oda, M. (1998) ‘Rolling Resistance At Contacts in Simulation of Shear Band’, *ASCE*, 124(March), pp. 285–292.
- Karatza, Z., Andò, E., Papanicolopoulos, S.A., Viggiani, G. and Ooi, J.Y. (2019) ‘Effect of particle morphology and contacts on particle breakage in a granular assembly studied using X-ray tomography’, *Granular Matter*, 21(3), pp. 1–13. doi: 10.1007/s10035-019-0898-2.

- Lenoir, N., Bornert, M., Desrues, J., Bésuelle, P. and Viggiani, G., (2007) ‘Volumetric digital image correlation applied to x-ray microtomography images from triaxial compression tests on argillaceous rock’, *Strain*, 43(3), pp. 193–205. doi: 10.1111/j.1475-1305.2007.00348.x.
- Lin, H. and Penumadu, D. (2006) ‘Strain localization in combined axial-torsional testing on kaolin clay’, *Journal of engineering mechanics*, 132(5), pp. 555–564.
- Liu, J., Gao, G., Wang, S., Jiao, L., Wu, X. and Fu, B. (2018) ‘The effects of vegetation on runoff and soil loss: Multidimensional structure analysis and scale characteristics’, *Journal of Geographical Sciences*, 28(1), pp. 59–78. doi: 10.1007/s11442-018-1459-z.
- Mallikarachchi, H. and Soga, K. (2020) ‘A two-scale constitutive framework for modelling localised deformation in saturated dilative hardening material’, *International Journal for Numerical and Analytical Methods in Geomechanics*, 44(14), pp. 1958–1982. doi: 10.1002/nag.3115.
- Man, A. and Graham, J. (2010) ‘Pore fluid chemistry, stress-strain behaviour, and yielding in reconstituted highly plastic clay’, *Engineering Geology*, 116(3–4), pp. 296–310. doi: 10.1016/j.enggeo.2010.09.011.
- Mitchell, J. K. and Soga, K. (2005) *Fundamentals of Soil Behavior*, Soil Science. doi: 10.1097/00010694-199407000-00009.
- Momeni, M., Bayat, M. and Ajalloeian, R. et al. (2020) ‘Laboratory investigation on the effects of pH-induced changes on geotechnical characteristics of clay soil’, *Geomechanics and Geoengineering*, 00(00), pp. 1–9. doi: 10.1080/17486025.2020.1716084.
- Nishimura, S., Tateyama, H., Tsunematsu, K. and Jinnai, K. (1992) ‘Zeta potential measurement of muscovite mica basal plane-aqueous solution interface by means of plane interface technique’, *Journal of Colloid And Interface Science*, 152(2), pp. 359–367. doi: 10.1016/0021-9797(92)90038-N.

- Nosrati, A., Addai-Mensah, J. and Skinner, W. (2009) 'pH-mediated interfacial chemistry and particle interactions in aqueous muscovite dispersions', *Chemical Engineering Journal*, 152(2–3), pp. 406–414. doi: 10.1016/j.cej.2009.05.001.
- O'Sullivan, C. (2011) 'Particle-Based Discrete Element Modeling: Geomechanics Perspective', *International Journal of Geomechanics*, 11(6), pp. 449–464. doi: 10.1061/(ASCE)gm.1943-5622.0000024.
- Otani, J., Mukunoki, T. and Obara, Y. (2002) 'Characterization of failure in sand under triaxial compression using an industrial X-ray CT scanner', *International Journal of Physical Modelling in Geotechnics*, 2(1), pp. 15–22. doi: 10.1680/ijpmg.2002.020102.
- Pagano, A.G., Tarantino, A., Pedrotti, M., Magnanimo, V., Windows-Yule, K. and Weinhart, T. (2017) 'Micromechanics of non-active clays in saturated state and DEM modelling', *EPJ Web of Conferences*, 140(1), pp. 1–4. doi: 10.1051/epjconf/201714015023.
- Pritchard, O. G., Hallett, S. H. and Farewell, T. S. (2014) 'Soil impacts on UK infrastructure: Current and future climate', *Proceedings of the Institution of Civil Engineers: Engineering Sustainability*, 167(4), pp. 170–184. doi: 10.1680/ensu.13.00035.
- Reijonen, H. M., Kuva, J. and Heikkilä, P. (2020) 'Benefits of applying X-ray computed tomography in bentonite-based material research focussed on geological disposal of radioactive waste', *Environmental Science and Pollution Research*, 27(31), pp. 38407–38421. doi: 10.1007/s11356-020-08151-2.
- Santamarina, J. C. (2001) 'Soil Behavior at the Microscale: Particle Forces J. Carlos Santamarina 1', *Proceedings Symposium Soil Behavior and Soft Ground Construction*, (October), pp. 1–32.
- Schofield, A. and Wroth, P. (1968) *Critical state soil mechanics*. McGraw-hill.
- Shire, T. and O'Sullivan, C., 2013. Micromechanical assessment of an internal stability criterion. *Acta Geotechnica*, 8(1), pp.81-90.

- Sibille, L. and Froiio, F. (2007) 'A numerical photogrammetry technique for measuring microscale kinematics and fabric in Schneebeli materials', *Granular Matter*, 9(3–4), pp. 183–193. doi: 10.1007/s10035-006-0032-0.
- Simons, F. J., Verhelst, F. and Swennen, R. (1997) 'Quantitative characterization of coal by means of microfocal X-ray computed microtomography (CMT) and color image analysis (CIA)', *International Journal of Coal Geology*, 34(1–2), pp. 69–88. doi: 10.1016/S0166-5162(97)00011-6.
- Singh, G., Biswas, D. R. and Marwaha, T. S. (2010) 'Mobilization of potassium from waste mica by plant growth promoting rhizobacteria and its assimilation by maize (*Zea mays*) and wheat (*Triticum aestivum* L.): A hydroponics study under phytotron growth chamber', *Journal of Plant Nutrition*, 33(8), pp. 1236–1251. doi: 10.1080/01904161003765760.
- Taina, I. A., Heck, R. J. and Elliot, T. R. (2008) 'Application of X-ray computed tomography to soil science: A literature review', *Canadian Journal of Soil Science*, 88(1), pp. 1–20. doi: 10.4141/cjss06027.
- Taylor, R.L; Zienkiewicz, O. C. and J.Z, Z. (2005) 'Finite Element Method for Solid and Structural Mechanics', (1), pp. 6–8.
- Terzaghi, K., Peck, R.B. and Mesri, G. (1996) *Soil mechanics in engineering practice*. John Wiley & Sons.
- Vautrin, A., Lee, J.R., Molimard, J. and Surrel, Y. (2002) 'Full-field optical techniques: Applications to strain measurement and mechanical identification', *10Th European Conference on Composite Materials*, (388), pp. 1–10.
- Viggiani, G., Bésuelle, P. and Desrues, J. (2013) 'X-ray Micro tomography as a Tool for Studying Localized Damage / Deformation in Clay Rock', *Proceedings of the NEA*

Clay Club Workshop on Clay characterisation from nanoscopic to microscopic resolution, pp. 91–98.

Wang, P., Karatza, Z. and Arson, C. (2019) ‘DEM modelling of sequential fragmentation of zeolite granules under oedometric compression based on X-ray CT observations’, *Powder Technology*, 347, pp. 66–75. doi: 10.1016/j.powtec.2019.02.050.

Wang, P. and Yin, Z. Y. (2020) ‘Micro-mechanical analysis of caisson foundation in sand using DEM’, *Ocean Engineering*, 203(February), p. 107240. doi: 10.1016/j.oceaneng.2020.107240.

3. On the utilization of mica waste: the pore-fluid chemistry of mica soils and its implication for erosion susceptibility

The same version of this chapter (with slight modification) has been published in: Ibeh C. U., Pedrotti M., Tarantino A., Lunn R. J. (2021) On the utilization of mica waste: the pore-fluid chemistry of mica soils and its implication for erosion susceptibility. *Geoderma*, 403, 115256. <https://doi.org/10.1016/j.geoderma.2021.115256>

Abstract

Soil is a vital resource which is limited in availability and must be adequately managed for sustainable development. Despite the importance of soil and its limited availability, a huge amount of soil is classified as waste. As one of the world's largest soil waste generators, the mining industry must transition to a circular economy model to meet sustainability requirements. As a readily available, large-volume waste material (about 10 million tonnes each year), waste mica has been considered for re-use as an alternative soil potassium source for plants, as landscaping material etc. One of the problems with mica waste is its susceptibility to erosion. To use mica as an agricultural or landscaping material, it is therefore important to understand the erodibility of mica and how its erodibility can be reduced. This study presents an experimental campaign to characterize mica erosion susceptibility. Mica particle-to-particle interaction forces and their effect on the macroscopic material behaviour were systematically investigated by changing pore fluid pH and ionic concentration. Sedimentation and liquid limit tests were first carried out to inform a conceptual model of the mica fabric. Triplets of 12 mica samples, compacted at different water contents and with different pore chemistry, were tested for erosion susceptibility using a Jet Erosion Test (JET) apparatus. The particle configuration of mica samples consistently varied with the pore water chemistry, regardless of whether the

samples being tested were suspension sediments or compacted samples. For mica samples formed with neutral water at low ionic concentration, the particles are in a dispersed configuration. This implies a relatively high erosion susceptibility, as particles are eroded one by one. For porewater samples formed with an increased ionic strength or within the acidic pH range, particles tend to cluster together and organize in a non-dispersed configuration. This results in a relatively less erosion susceptibility, as group of particles must be eroded as opposed to individual ones. Similarly, the Jet erosion test results reinforced these observations showing that mica erodibility varies with porewater chemistry. Considering that mica erodibility varies with pore fluid chemistry and mica waste derived from mining operations are often slightly acidic, this paper paves the way for tailored assessments of individual mica waste materials to determine the appropriateness of their use.

Key words: Muscovite-Mica, erosion, sedimentation, pore-fluid-chemistry, Jet erosion test, circular economy

3.1. Introduction

Soil is a vital resource which connects essential spheres such as food security, biodiversity, climate change and public health, as well as other social, economic, and environmental aspects of life. It is however limited in quality and availability and needs to be responsibly managed to meet the sustainable development goal (Keesstra et al., 2016; H. Wang & Zhang, 2021). Despite the importance of soil and its limited availability, huge amounts of soil are classified as waste. It is estimated that approximately 15 Gt/yr of waste soil is generated by the mining industry globally (Lottermoser 2010). As one of the world's largest waste generators, the mining industry must transition to a circular economy model to improve its sustainability.

Within the mining industry, the management of mica waste has generated significant attention due to the large volume generated. Mica waste originates from mining of relatively valuable materials such as gold, copper, uranium and platinum (Nosrati et al., 2009), from mining of coarse material such as granite (Hojamberdiev et al., 2011) from the mining of other phyllosilicates such as China clay (Zografou et al., 2014) and from the mining of mica itself (Basak, 2019). For instance, China clay extraction and processing involves the production of a very large quantity of mica waste, typically for every tonne of china clay, one tonne of residual mica is produced. About 10 million tonnes of mica waste is generated in a year and over 600 million tonnes of total industry stockpile is estimated to be available (Palumbo-Roe et al., 2014). Mica waste is usually deposited in large lagoons and abandoned in clay pits. It contains between 10% and 75% mica and currently has seen very limited re-use; within flux for ceramic glazes and as a mild abrasive (Basak, 2019; Hojamberdiev et al., 2011; Zografou et al., 2014). As a readily available, large-volume material, waste mica has been considered for use as backfill material and a landscaping material (Dudeney et al., 2013; Karlsson et al., 2017). Mica has also been considered for re-use as a component of construction materials, such as bricks or cement (Cresswell and Sims 2007) and in the agricultural industry as a source of important soil nutrients such as potassium which plays an important role in several physiological processes in plant nutrition (Meena et al., 2015; Singh et al., 2010).

A major problem with mica waste is that the material is susceptible to erosion as highlighted by Sinha et al. (2017). One of the key questions to be addressed in order to assess the suitability of mica as an agricultural or backfill material is how erodible the mica is and how its susceptibility to erosion can be reduced. This issue is addressed by this paper.

Mica is a class of clay mineral, with a layered or platy texture. The charge on mica particles is well documented to be pH dependent (van Olphen 1977, Nishimura *et al.*, 1992; Mitchell and Soga, 2005; Gratchev and Towhata, 2013; Liu *et al.*, 2018) and affects their erodibility (Man

and Graham, 2010; Momeni et al., 2020). Similarly, the use of mica waste for example, as an alternative source of potassium may require the addition of organic matter to promote the K mobilization to soil solution and its absorption by the plant (Bakken et al., 1997; Basak, 2019; Basak et al., 2017; A. Wang et al., 2015). This process gives rise to the production of organic acids (Biswas & Basak, 2014), which reduces the pH of the medium. Hence, to characterise the erodibility of mica waste it is important to consider a wide range of soil porewater chemistries.

This paper presents an experimental campaign to characterize mica erosion susceptibility for a range of porewater chemistries. Triplets of 12 mica samples, compacted at different water contents and with different pore chemistries, are tested for erosion susceptibility using a Jet Erosion Test (JET) apparatus and erodibility is found to vary with porewater pH. Results from sedimentation tests and liquid limit tests are used to inform development a conceptual model of particle-to-particle interactions. This model is able to explain the observed variations in the erosion resistance of mica under varying pore-water chemical conditions.

3.1.1. Mica

Mica may occur as muscovite, lepidolite, phlogopite, biotite, and lepidomelane mineral form (Hoseini et al., 2016). Muscovite mica is used in this study due to its ubiquitous nature. Mica is a phyllosilicate mineral, which may range in size from sand to silt and clay size platy particles, but it occurs mostly as a silt sized waste material in mine settings. It has the fundamental formula $\text{KAl}_2(\text{AlSi}_3\text{O}_{10})(\text{OH})_2$ and is a 2:1 clay mineral (Figure 1). The crystal structure is the one of active clays, it comprises a stack of unit layers of an Al–O–Al octahedral (O) layer sandwiched between two Si–O–Al tetrahedral (T) layers. Substitutions of lattice Si^{4+} by Al^{3+} in the tetrahedral layer and Fe^{3+} or Mg^{2+} and Ca^{2+} for Al^{3+} in the octahedral layer which invariably occur, result in a permanent net negative charge on the basal clay mineral (Figure 1). The charge deficiency is compensated by interlayer cations such as K^+ and Na^+ adsorbed

between the T-O-T sheets, fitting closely into the hexagonal holes of the Si–O–Al sheet. The interlayer cations (e.g. K^+) strengthen the bonding between basal planes of TOT sheets, which are normally held by attractive van der Waals forces, through the attractive electrostatic interactions (Nosrati et al., 2009).

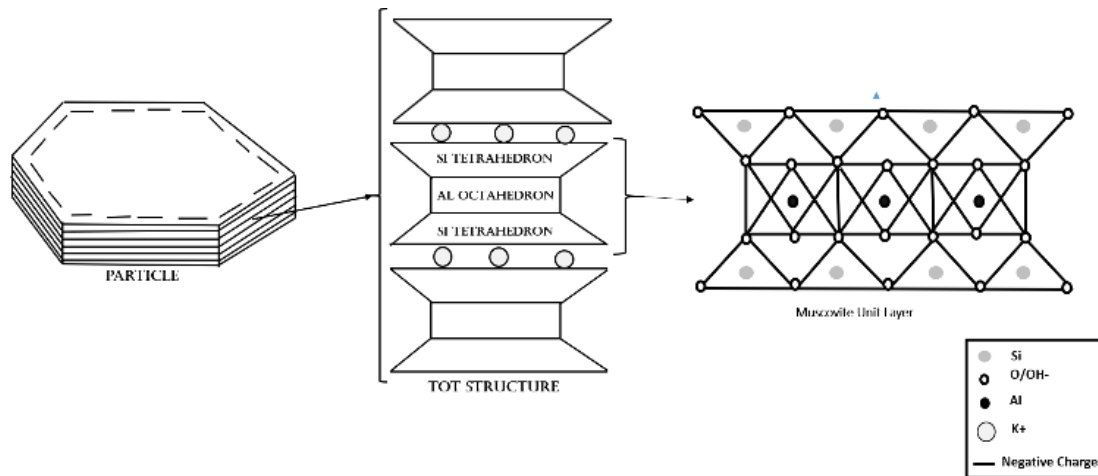


Figure 1: Muscovite mica structure

3.2. Materials and Methods

Muscovite silt sized muscovite purchased from LKAB minerals LTD, UK was used for this study. Laser diffraction analysis (Figure 2) showed the muscovite silt to have an equivalent average grain size of about 30 μm . The muscovite specific gravity is 2.8 (given by LKAB).

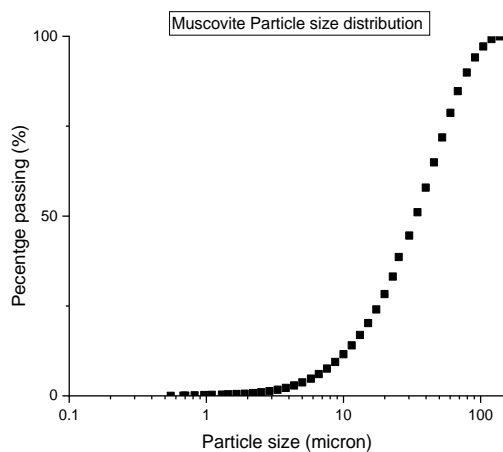


Figure 2: Particle size distribution of muscovite mica

To characterize the muscovite chemical composition, Micro-X-ray fluorescence (XRF) was performed at Bruker AXS, Germany using M4 Turnado Micro-XRF Spectrometer. The XRF analysis (Table 1) showed that the muscovite silt contains predominantly Al₂O₃ (32% wt.), SiO₂ (43% wt.), K₂O (13% wt.) Fe₂O₃ (8% wt.) and trace amounts of Na₂O and other compounds.

Table 1. Chemical composition of the muscovite silt used in this study.

Element	Atomic Number	Compound	Normalised Stoichiometric Composition (wt.%)
Mg	12	MgO	0.557
Al	13	Al ₂ O ₃	32.706
Si	14	SiO ₂	43.612
K	19	K ₂ O	13.01
Ti	22	TiO ₂	1.103
Mn	25	MnO	0.018
Fe	26	Fe ₂ O ₃	8.399
Co	27		0.022
Ni	28	NiO	0.002
Zn	30	ZnO	0.007
Ga	31		0.011
Rb	37		0.06
Sr	38	SrO	0.003
Y	39	Y ₂ O ₃	0
Zr	40		0.051
Nb	41		0.015
Ba	56	BaO	0.082
Rh	45		0

3.2.1. Specimen Preparation

Each sample of mica underwent a standard preparation procedure comprised of a washing stage and a pH correction stage.

Washing stage: As shown by the XRF analysis (Table 1), the dominant ion binding the muscovite sheet is potassium ion. The muscovite was rendered mono-ionic by using KCl. A

procedure similar to the one outlined by van Olphen (1977), and Palomino and Santamarina, (2005) was adopted. The muscovite was mixed with a 2 mol/L KCl solution at -3 mL of solution per gram of Muscovite. The suspension was left for 48 h, during which the clay particles were allowed to settle. Subsequently, its supernatant was siphoned and replaced with 1mol/L KCl. After 24 hours the supernatant was siphoned again and replaced with a fresh 1mol/L KCl and left to equalize for 96 hours. Thereafter, the excess salt was removed through 10 washing cycles with deionized water. The muscovite was then oven dried and ground into powder using a mortar and pestle and was eventually passed through a 425-micron sieve.

pH correction stage: when the muscovite is mixed with distilled water, the mixture result in a pH of ~8. Muscovite has the capacity to buffer the pH of acidic solutions. To have mica slurries or suspensions at a different pH, the pH needs to be corrected in the muscovite-water mixture, to neutralize the buffering effect of the mica. Depending on the target pH, the muscovite batches were corrected by adding drops of diluted HCl acid or KOH base to respectively increase or decrease the pH of the mixture. In the case of bases, a KOH solution was preferred to a NaOH solution to preserve the nature of the cations (K^+) dispersed in the mica mixture. In both cases (acidic or alkaline batch), the mixture was left to equilibrate for at least 24 hours and in case, the pH was corrected again.

For the sedimentation tests, samples at 4 different pH (e.g., 3, 5, 7, 9) were respectively prepared at 4 different KCl concentrations: 0 mol/L, 0.003 mol/L, 0.1 mol/L and 1.8 mol/L. A 2.54 cm diameter acrylic cylinder filled with the pore fluid and the Muscovite at a water content of ~1800 and total suspension volume of 78ml was used. The suspension was mixed and left to equilibrate overnight, after which it was remixed.

For liquid limit tests, samples at two different pH (5 and 8) were tested. The pH 8 sample was prepared using demineralized water and hence did not require any pH adjustment

since the muscovite mixed with demineralized water gave a pH of about 8. The sample at pH 5 was instead prepared as described above.

For the JET erosion test, two sets of samples, at pH 5 and pH 8, were prepared with different initial water contents (e.g., 0.2, 0.3 and 0.4) and statically compacted at 90 kPa in a cylindrical mould of 10cm in diameter by 10 cm in height. As compacted samples are partially saturated, adjusting the pH at low water content would result in improper mixing and heterogeneous areas within the sample. A different procedure than the one described above was implemented to reach the target pH for each sample. A slurry of mica ($w=1.5$) was initially prepared at either pH 5 or 8 following the same methodology described in the above paragraph pH correction stage. The pH-corrected slurry was then oven dried (24 hours at 105 °C) and then ground with a pestle and mortar. In this way, the dry clay was already in equilibrium, when exposed to water of the same pH, and the buffering effect of mica was neutralized. Therefore, the dry mica was mixed with a given amount of water at the target pH and then statically compacted. After compaction, each sample was subsequently kept in a sealed nylon bag for 48 hours to homogenize. Each sample was prepared in triplicate, resulting in a total of 18 samples (3 water contents * 2 pH * triplicates). The aim was to create samples at the same density, because soil density affects its erodibility; denser samples are expected to be more erosion resistant.

3.2.2. Experimental procedure

3.2.2.1. Sedimentation test

For the sedimentation tests, the following procedure was followed. First, the soil suspension with the target pH and electrolyte concentration was gently poured into the acrylic cylinder, and then it was covered, repeatedly inverted for 2 minutes, placed on a level surface and the time recorder simultaneously started. During the sedimentation test, the clear water-clay

suspension interface was recorded (ruler accuracy of 1mm), when visible, otherwise the sediment height was recorded instead. The height was recorded, starting from 2 seconds, and subsequently samples doubled the time, until there was no significantly measurable difference between three subsequent measurements. At the end of the test, the supernatant fluid was siphoned off, and the pH measured. As both the final volume of the sediment and the dry mass of the sample were recorded, the final void ratio of each sediment could be calculated.

3.2.2.2. *Liquid Limit test*

The liquid limit test was conducted with a penetrometer in accordance with BS Code (1990). However, as described in the previous section, the samples were prepared with different pore fluid chemistries (pH 8 and pH 5, no electrolyte added). Penetration measurements were obtained for five moisture contents and the moisture content corresponding to 20mm penetration was recorded as the liquid limit.

3.2.2.3. *Jet Erosion Test*

A schematic of the JET erosion apparatus used is shown in Figure 3. The custom-made JET erosion apparatus (Beber et al., 2019) was recently created in the Geomechanics laboratories at the University of Strathclyde and was designed according to Hanson & Cook, (2004) to investigate the erodibility and strength of compacted muscovite at varying porewater pH (pH 5 and pH 8) and moisture content (0.20, 0.30 and 0.40). The jet erosion test was performed using the following parameters: an initial nozzle height from the sample surface, J_E , of 80 mm and a nozzle diameter (d_0) of 6.4mm.

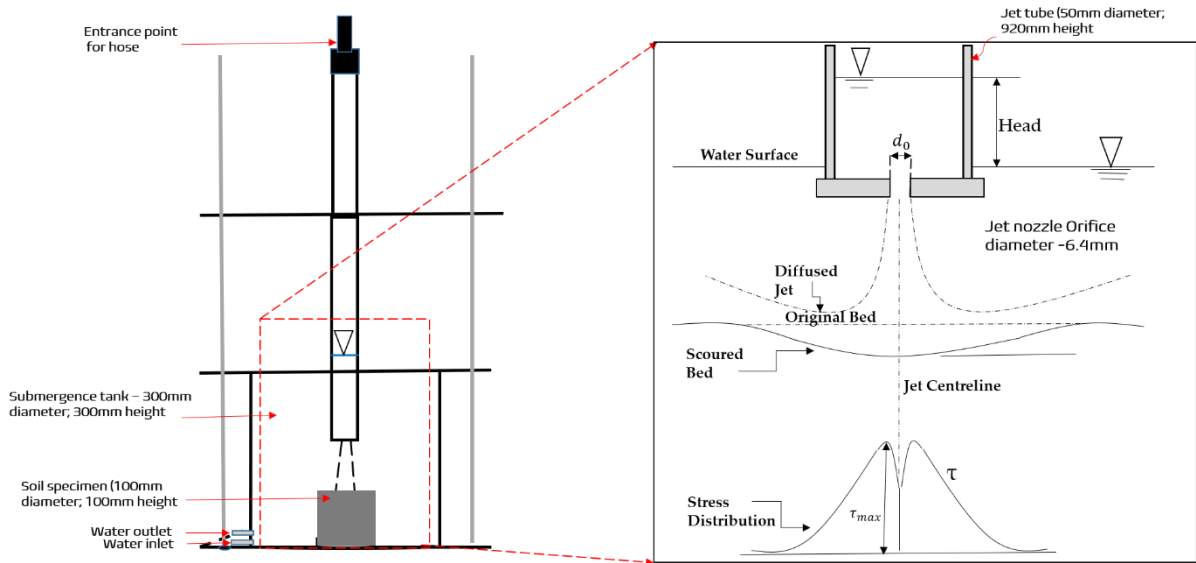


Figure 3: Schematic of jet erosion apparatus at the University of Strathclyde (modified from Hanson & Simon, (2001)).

In Figure 4 the workflow of the erosion test experimental procedure is reported.

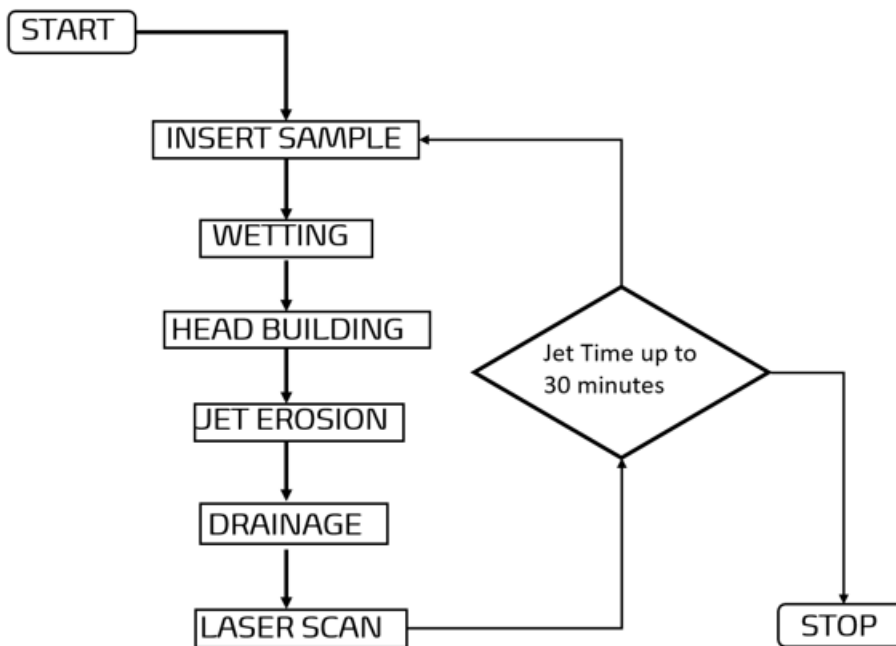


Figure 4: workflow showing the procedure for the conduct of the JET erosion test.

Stage 1: Sample insertion

The prepared cylindrical soil sample (labelled as soil sample mould in Figure 4) is tightly secured at the base of the tank onto a protruding ring.

Stage 2: Wetting

Water is piped into the tank through the water inlet positioned at the bottom (Figure 3) until the sample is submerged (~ 1 minute).

Stage3: Head building

The water head inside the “jet tube” (Figure 3) is increasingly raised, until a constant hydraulic head of 130 mm is reached.

Stage4: Jet Erosion

Once the target water head was reached, the jet tube was opened via a deflector and the jet test started. The jet was kept on for 5 minutes at a constant hydraulic head, after which, the jet tube was closed again.

Stage 5: Drainage

Once the jet tube was closed, the cell was drained (~2 minutes) from the outlet valve positioned at the bottom of the cell (Figure 3), in order to allow removal of the sample.

Stage 6: Laser scan

To allow for accurate determination of the scour depth, a 2D/3D scan control 2700-100/BL from Micro-Epsilon laser scanner was used. The scanner was mounted on a movable frame coupled with a software-timed motion controller OWIS PS-II. The scanner reference resolution is 15 microns. After scanning the sample surface, the whole procedure from stage 1 was then repeated, until a total elapsed erosion time of 30 minutes was reached. For each 5-minute step, the maximum scour depth and the total eroded volume was recorded. The critical stress, τ_c , was then determined in accordance with Hanson & Cook, (2004).

3.3. Results and Discussion

3.3.1. Sedimentation test

To investigate the microstructural behaviour of muscovite at low density, muscovite suspensions with different pore chemistries were tested. Among the different samples two clear patterns could be distinguished depending on the pore chemistry.

As illustrated in Figure 5, two types of behaviour were observed: one with a clear water-suspension interface (Figure 5a) and the other with a distinct sediment deposition height interface (Figure 5b). In the samples with clear water – suspension interface, once the sedimentation had started, the interface descends with time. Simultaneously, a sediment layer accumulates at the bottom of these samples, but the sediment interface height is not visible enough for measurement. These samples are said to be non-dispersive and only the visible clear water-suspension interface is measured and reported as shown in Figure 6 (the interface decreases with time).

By contrast, for samples with clear sediment deposition height interface (dispersive samples), their water -suspension interface is not visible enough for measurement. Only the distinct sedimentation deposition height interface was measured and reported. This interface increased with time as shown in Figure 6. In Figure 5a and b, the sediment deposition height interface is highlighted in blue and the clear water – suspension interface is highlighted in orange. The two interfaces converge into a single interface at the end of the sedimentation.

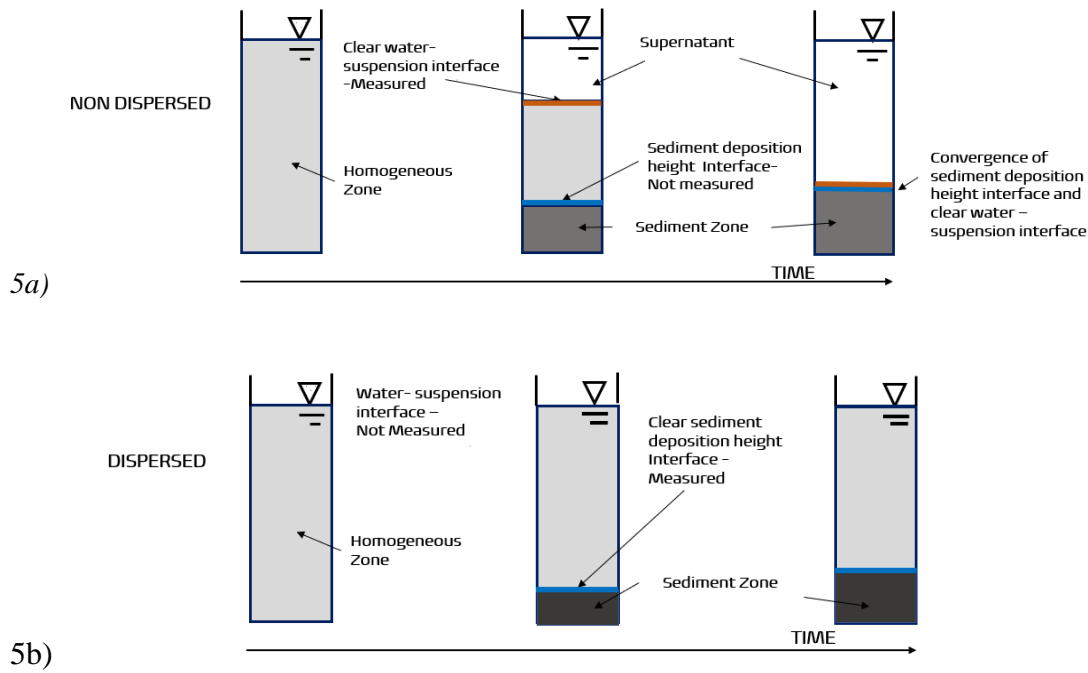


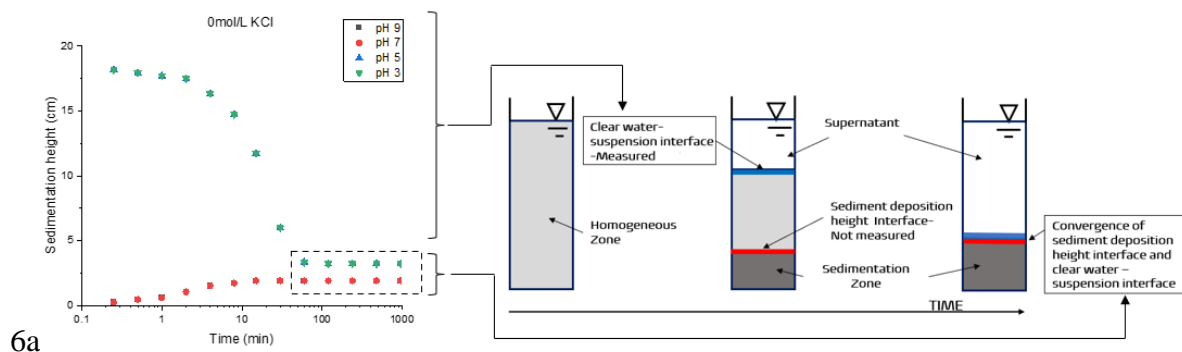
Figure 5: Illustration of different sedimentation patterns: a) non-dispersed sedimentation pattern showing two distinct interfaces, supernatant-suspension interface, and suspension-sedimentation zone interface; b) dispersed sedimentation pattern showing only the sedimentation zone-suspension interface.

In Figure 6, the data acquired from the sedimentation tests illustrated in Figure 5 (for pH 3, 5, 7 and 9 and KCl concentrations of 0 mol/l, 0.003 mol/l, 0.1 mol/l and 1.8 mol/l) are reported. Figure 6a shows two muscovite suspension sedimentation curves with no electrolyte concentration (0 mol/l KCl) at pH 3 and 9. The pH 3 sample showed a non-dispersed behaviour. The clear water – clay suspension interface was visible (Figure 6a) and decreased with time from 18cm to 3cm. A steep decline in the interface height is observed between 2 minutes and 15 minutes after the start time. Beyond 15 minutes, the interface height was stable at about 3 cm and did not change further (the final sedimentation height after 30 minutes is presented in Table 2 below). For the sample at pH 9, a dispersed behaviour was observed; there was no visible clear water - clay suspension interface. The sediment height interface increased from zero at the start, to about 2cm after 11 minutes after which it was relatively stable. At the end of the sedimentation, samples had final void ratios of 4.4 and 2.6, for pHs of 3 and 9 respectively.

Table 2: Final sedimentation height after 30 minutes

Final sedimentation height (cm)				
	pH 9	pH 7	pH 5	pH 3
1.8mol/l KCl	2.76	2.99	2.99	3.105
0.1mol/l KCl	2.99	2.99	2.99	3.105
0.003mol/l KCl	2.07	2.07	3.105	3.22
0mol/l KCl	1.84	1.91	3.2	3.22

Figure 6b shows the sedimentation curves of 4 samples with an electrolyte concentration of 0.003 mol/l KCl, but with different pH (3, 5, 7 and 9), the figure by the side of the plot describes the clear water-supernatant interface and the sediment deposit height. The pH 3 and pH 5 samples showed a non-dispersed behaviour (Figure 6b), with a similar trend to that of pH 3 with no electrolyte concentration (Figure 6a), while the pH 7 and pH 9 samples showed a dispersed behaviour (Figure 6b) similar to that of pH 9 with no electrolyte concentration (Figure 6a). Figure 6c shows the sedimentation curve for all four samples with an electrolyte concentration of 0.1 mol/l KCl and varying pH. In this case, regardless of pH, the behaviour is non-dispersed. Finally, Figure 6d shows the sedimentation curves for all samples with an electrolyte concentration of 1.8 mol/l KCl. Again, all samples show a non-dispersed behaviour, regardless the pH.



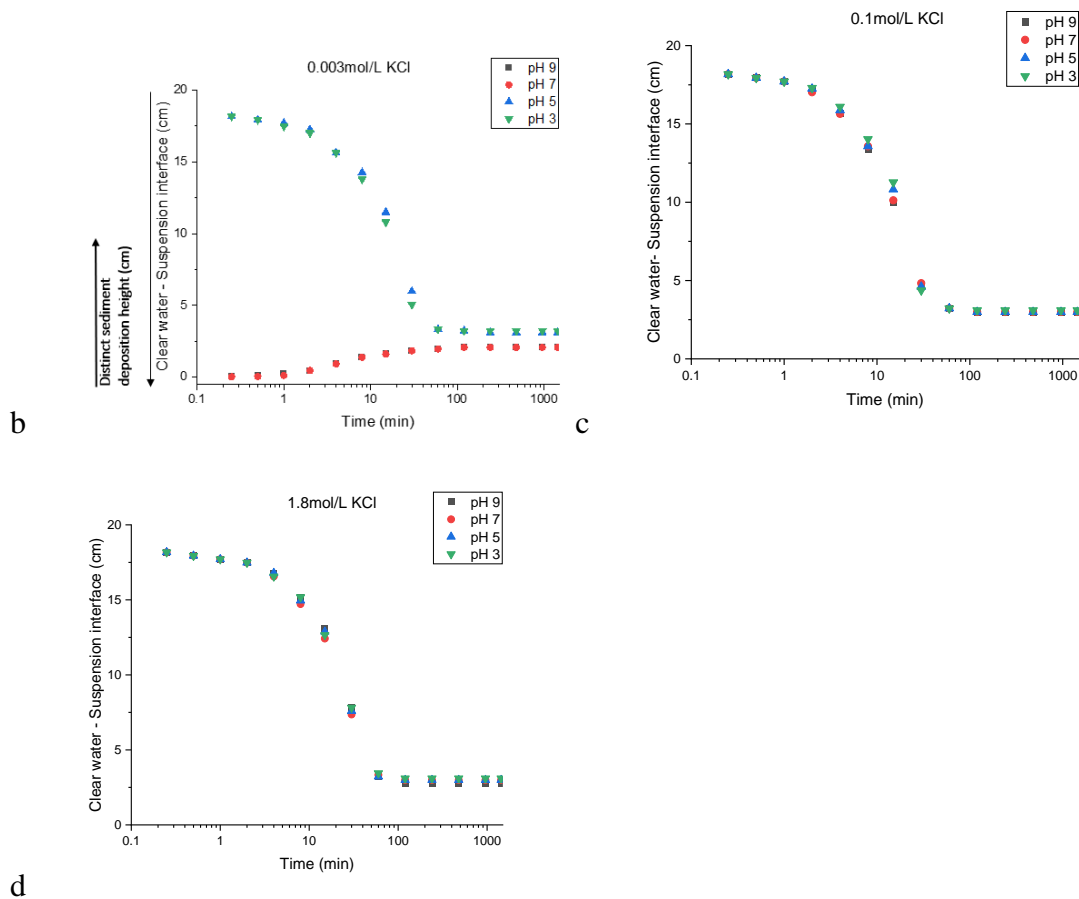


Figure 6: Muscovite sedimentation trend for different pH and ionic concentration at a) 0 mol/l KCl b) 0.003 mol/l KCl c) 0.1 mol/l KCl and d) 1.8 mol/l KCl

Appendix I show a photograph (Figure S1 in Appendix I) at the end of the sedimentation test of two mica samples, (a) with 0.1M KCl and pH 9 solution and (b) with 0 M KCl and pH 9 solution. Although the samples shown in the photograph are different from the ones presented in Fig. 5a (the initial concentration of the mica in the suspension and the cylinder size were different), the images clearly show the two modes of sedimentation observed in our tests, clear supernatant (convergence of sediment deposition height interface and clear water-suspension interface) and colloid-like supernatant. Supplementary information (S1) has been added which shows this photograph of the two-dominant sedimentation behaviour described in Figure 5.

3.3.2. Liquid Limit test

To estimate the mechanical strength of the muscovite under different particle configurations (dispersed or non-dispersed), the liquid limit of the muscovite was determined at two different pH. In Figure 7 the two liquid limit tests are reported. Mica prepared at pH 8 (dispersed particle configuration) had a liquid limit of 60% whereas the mica sample prepared at pH 5 had a liquid limit of 69%.

It is worth noting that during the determination of the liquid limit for the alkaline sample, it was not possible to have a level surface, as the samples tended to form a convex surface (Figure 8). Figure 8a, shows the alkaline sample, where a clear bulge is visible, whereas in Figure 8b, the top surface of the acidic sample is almost perfectly flat (Figure 8b). This phenomenon was associated with a tendency to swell in the alkaline sample, caused by a higher level of particle alignment when compared with the acidic sample.

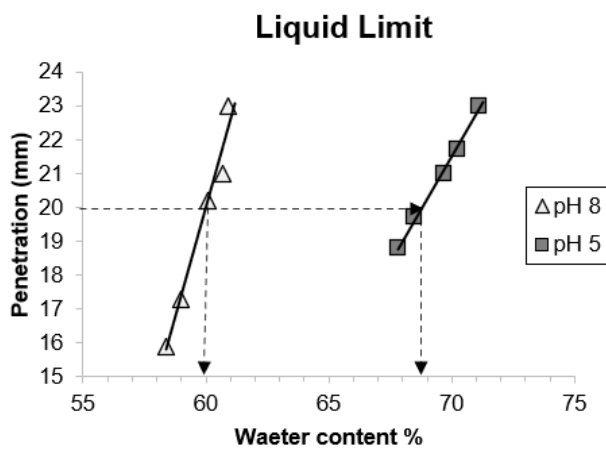


Figure 7: Liquid Limit of fine muscovite at a) pH 8 and b) pH 5



a

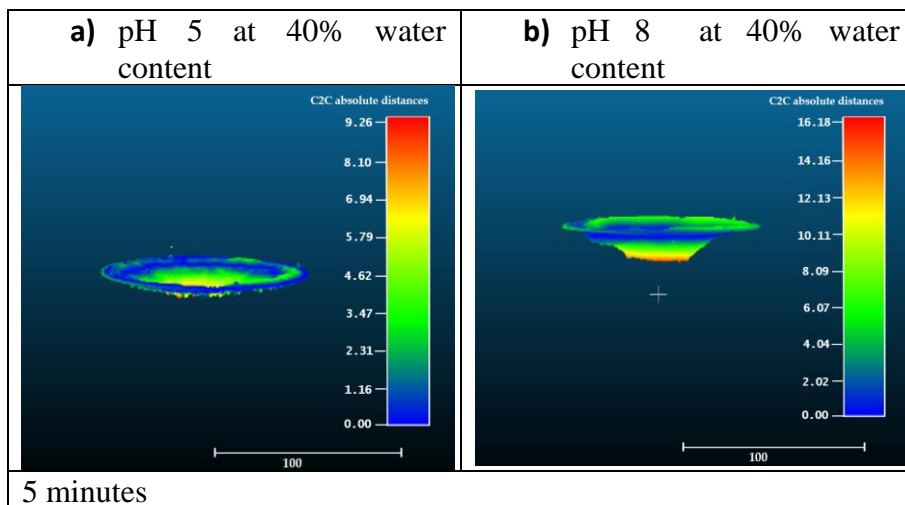


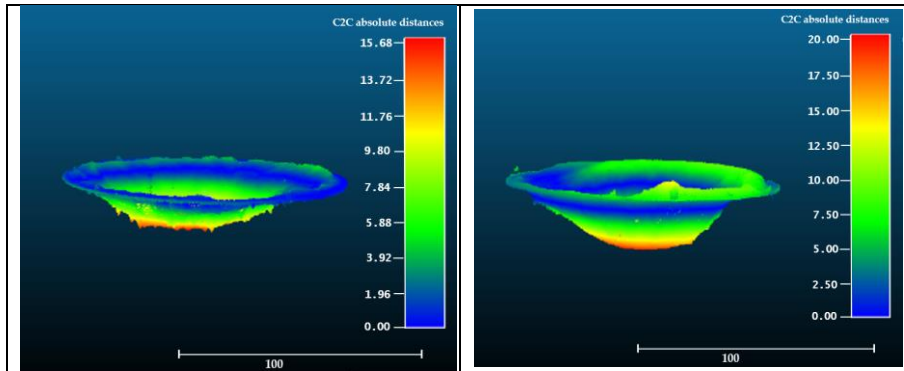
b)

Figure 8: a) Convex muscovite silt surface (pH 8) in a penetrometer cup b) silt sized muscovite mixed with acidified water (pH 5) with flat surface in a penetrometer cup.

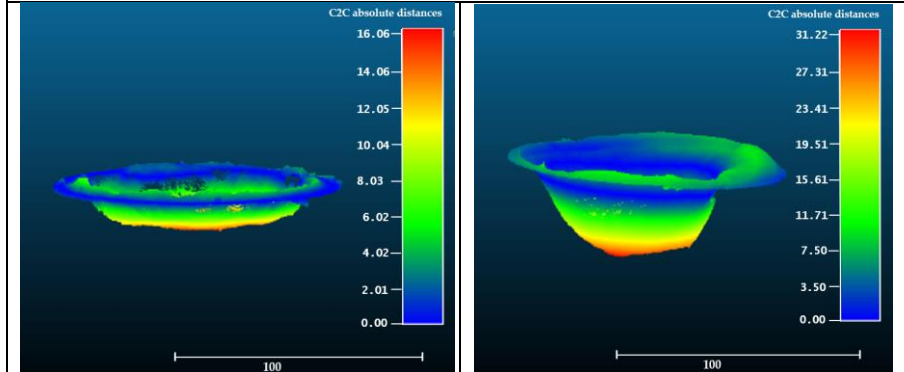
3.3.3. Jet erosion test

Two different sets of compacted mica samples prepared at differing pH (either pH 5 or 8) were tested for erosion susceptibility by means of the jet erosion test. Each set of samples was compacted at a different moisture content (e.g., 0.2, 0.3, and 0.4), and each sample was reproduced in triplicate, resulting in a total of 9 tests at pH 5 and 9 tests at pH 8.

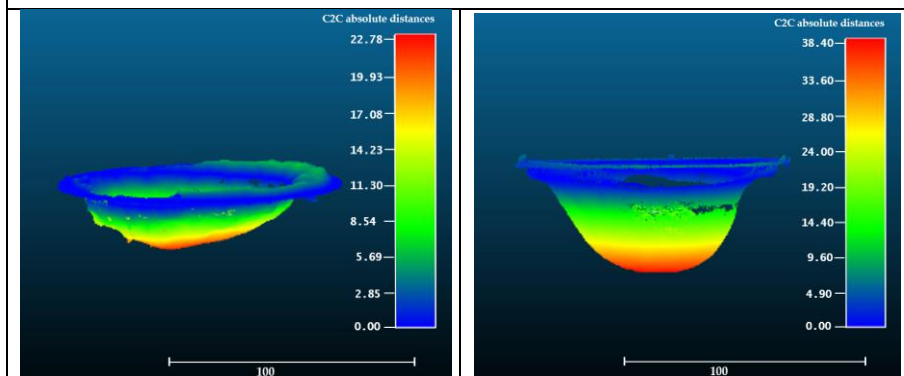




10 minutes



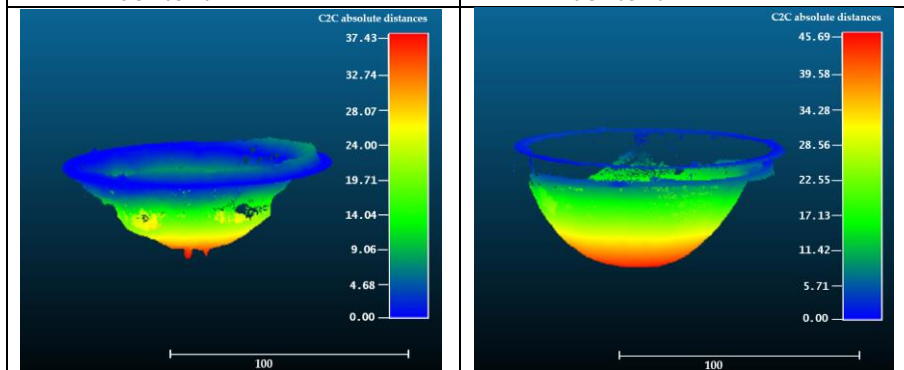
15 minutes



20- minutes

a. pH 5 at 40% water content

b. pH 8 at 40% water content



25 minutes

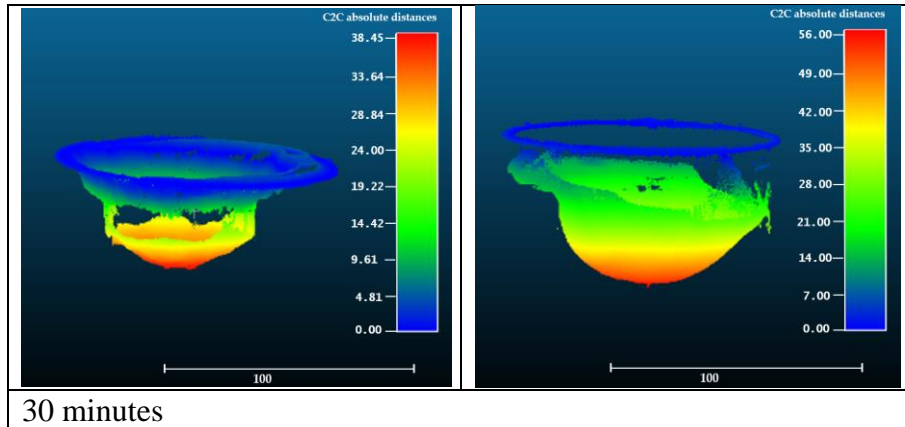
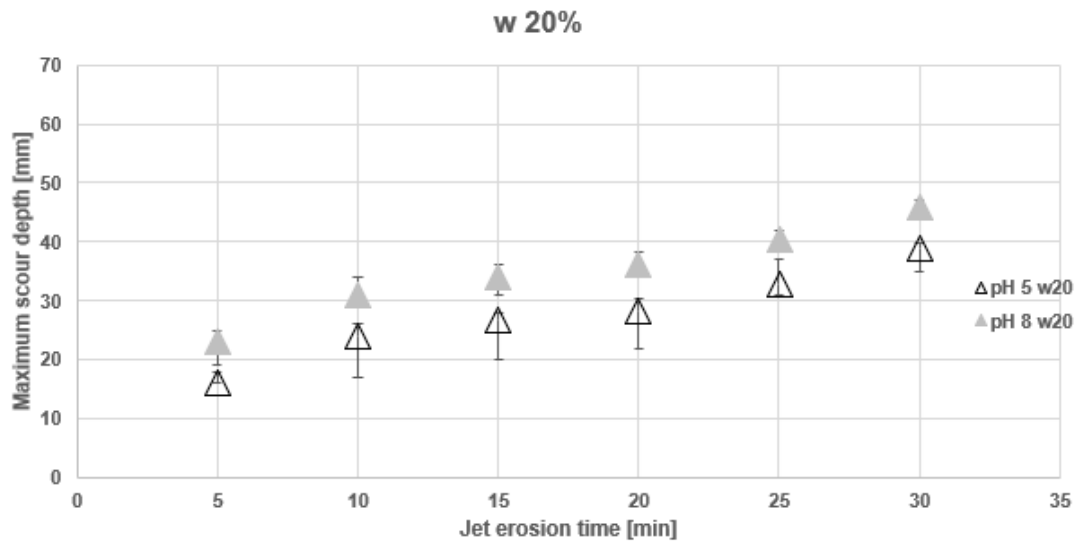


Figure 9: Jet erosion test eroded surfaces. a) pH 5 at 40% water content, b) pH 8 at 40% water content

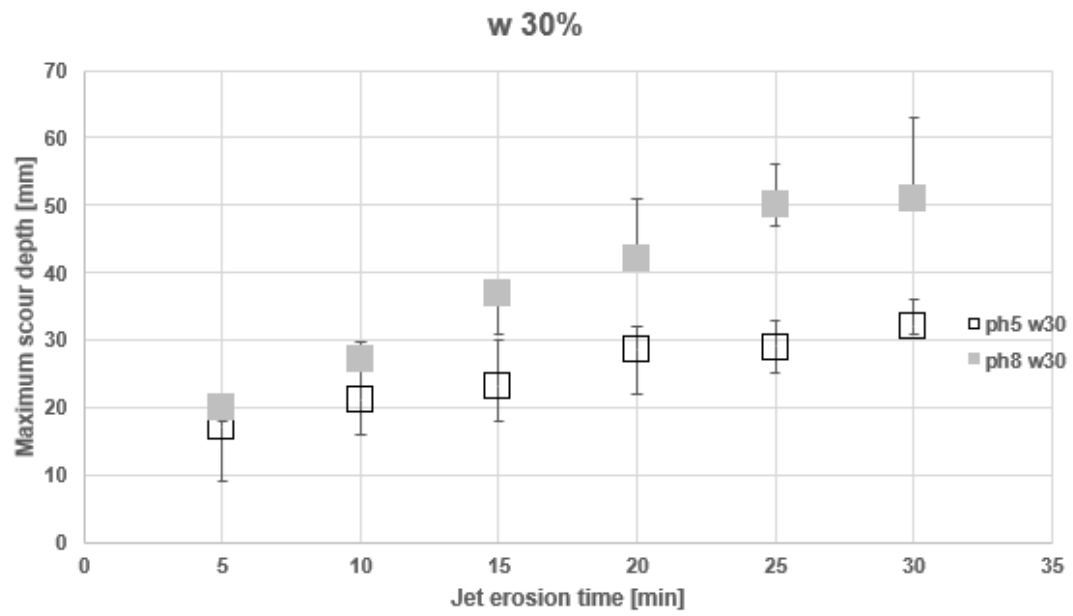
In Figure 9 the scans of the eroded surface at the end of each jet time interval (5 minutes) are shown for two samples compacted at a moisture content of 0.40. Figure 9a shows results for the sample prepared at pH 5 and Figure 9b at pH 8. Each row in Figure 9 contains the scans of the eroded surfaces, for jet erosion times of 5, 10, 15, 20, 25 and 30 minutes. The colour bars are blue for the shallowest scour depths, with a progressive increase through green – yellow and then red as the depth of scour increase (reported in millimetres).

For all the scans, the scour surface has a bell shape, that was centred under the nozzle of the jet. For both tests, as expected, the volume of scoured material increases, and the scour surface depth increases, with increasing time. For the same jet erosion time, the pH 5 sample (Figure 9a) has a consistently smaller scour depth than the pH 8 sample (Figure 9b). For example, after 5 minutes, the pH 5 sample has a maximum scour depth of 9 mm, whereas the pH 8 sample has a maximum scour depth of 16 mm.

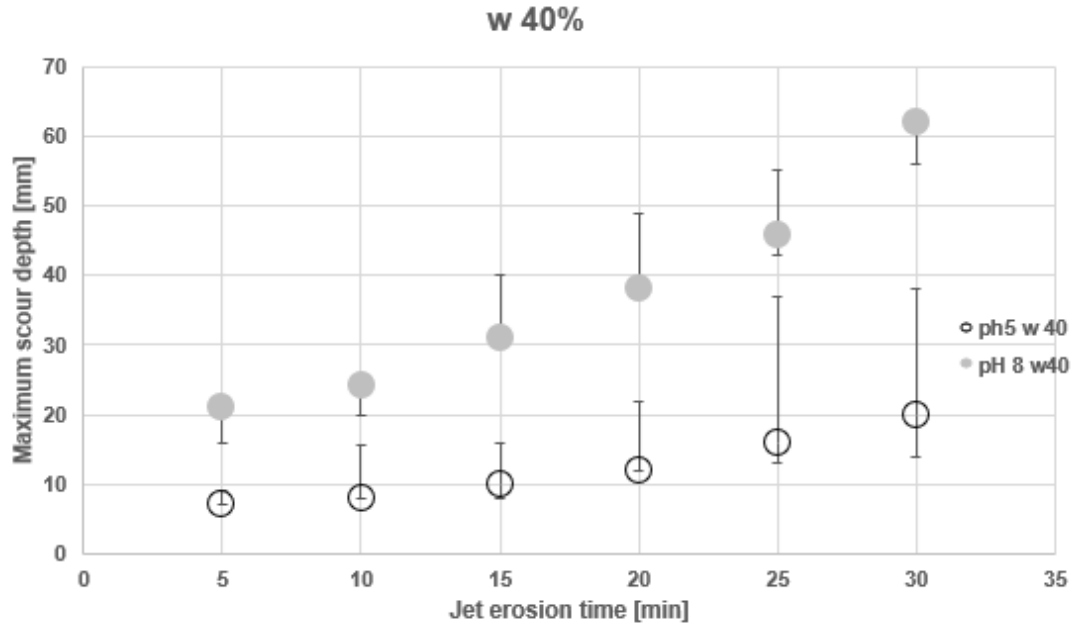
In Figure 10a, 10b and 10 c, the evolution of the maximum scour depth over time is reported for moisture contents of 0.2, 0.3 and 0.4, respectively. Each point corresponds to the median value of the triplicates and the error bars represent the range.



a)



b)



c)

Figure 10: Maximum scour depth. a) samples compacted at 20% moisture content, b) samples compacted at 30% moisture content and c) samples compacted at 40% moisture content

Samples compacted with alkaline water content are persistently more erodible (higher maximum scour depth) than samples compacted with acidic water content (Figure 10). Further, the higher the compaction moisture content the greater the difference in median scour depth between the acidic and the alkaline samples. For example, after 30 minutes of jet erosion, the difference in maximum median depth for the samples compacted at 0.20 was 7 mm, for the samples compacted at 0.30 was 19 mm and for the samples compacted at 0.40 was 42 mm.

The erosion data were elaborated by considering the model presented by Hanson & Cook, (2004), where the erosion rate ε [m/s] (equation 1) is assumed to be proportional to both the soil's erodibility coefficient k_D [m/s/Pa] and the excess of the applied shear stress τ at the surface at critical shear stress, τ_c [Pa] (Karamigolbaghi et al., 2017).

$$\varepsilon = k_D(\tau - \tau_c) \quad (1)$$

For each test, the critical shear stress, τ_c (equation 2), was calculated according to the theory exposed by Blaisdell in 1981, originally proposed for the scour depth of the bridge piers (Karamigolbaghi et al., 2017). In equation 2, τ_0 is the maximum shear stress of the jet, J_E is the

nozzle height from the scour surface and J_P is the potential core length where the mean centerline velocity of the jet remains the same as that exiting from the nozzle (calculated considering a friction coefficient of 6.3 and an iterative process). According to the presented theory, the critical shear stress, τ_c , is meant as the threshold shear stress at which the “*first detachment*” occurs, hence when erosion starts. In other words, below that threshold value, no erosion is occurring.

$$\tau_c = \tau_0 \left(\frac{J_P}{J_E} \right)^2 \quad (2)$$

(J_p is the potential core length = $C_d * d_0$, where C_d is the diffusion constant (6.3) and d_0 is the nozzle diameter; J_e is the equilibrium scour depth).

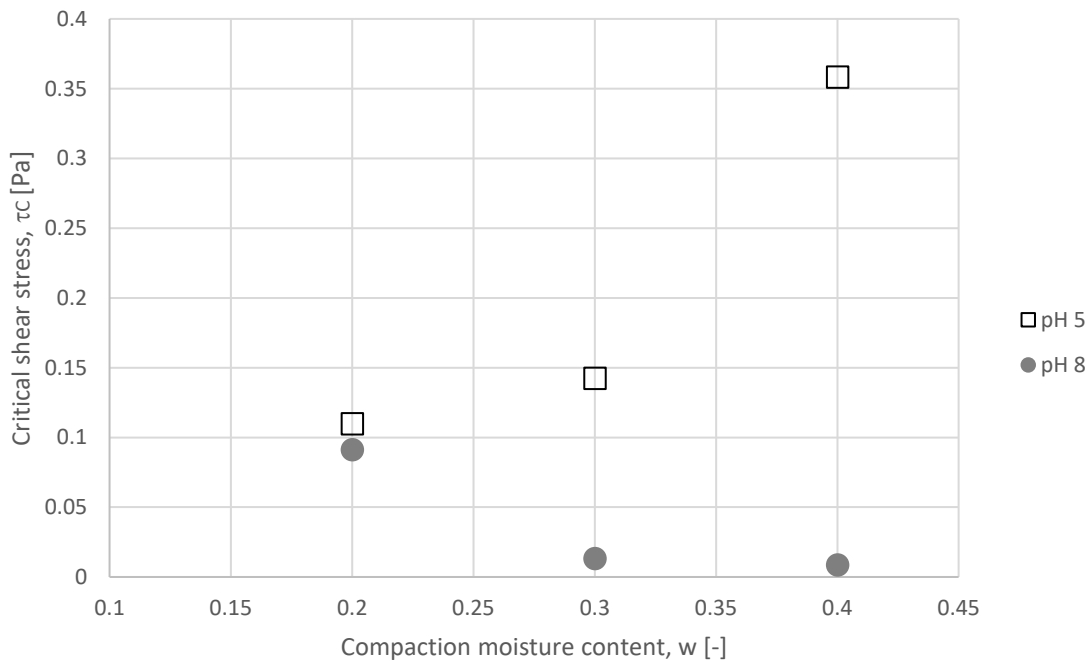


Figure 11. Critical shear stress

In Figure 11 the average value of the critical shear stress, τ_c , is plotted, as derived from the triplicate test, for each combination of pH and compaction moisture content. The critical shear stress of the alkaline samples decreases as the compaction moisture content increases. By contrast, the critical shear stress of the acidic samples increases as the compaction water content increases. At low values of the compaction moisture content, both the alkaline and the acidic

samples have a similar critical shear stress, of about 0.1 Pa. For the alkaline samples, this rapidly decreases to zero as the compaction moisture content increase. For the acidic samples, doubling the initial moisture content results in an increase in the critical shear stress of more than three times (from 0.11 Pa for a moisture content of 0.20 to 0.36 Pa for a moisture content of 0.40)

3.3.4. *An electrochemical conceptual model for mica*

Sedimentation tests show that particle configuration and interaction can be modified by changing the pore water chemistry. When mixed with distilled water, muscovite has an alkaline pH with relatively low sedimentation height and no clear water- suspension interface. This is indicative of a dispersive particle arrangement. On adjusting the pore fluid to acidic conditions (at low ionic concentrations – less than 0.1 mol/l) the particles show a clear water- suspension interface and the settling time reduces. This is indicative of a non-dispersive fabric (flocculated or aggregated). In addition, at a high ionic concentration, for all pHs considered non-dispersive behaviour was the dominant fabric mode.

The dispersive nature of fine muscovite at alkaline pH and low ionic concentration was further confirmed by the difficulty observed (the convex bulging surface of muscovite slurry in a penetrometer cup) in the determination of the muscovite liquid limit at low ionic concentration and high pH. A flat surface of muscovite slurry was only obtained for a moisture content that was close to the liquid limit when acidic pore fluid was used to prepare the slurry (non-dispersed, aggregated/flocculated fabric).

The aggregation of clay particles in colloidal suspension is generally controlled by the net balance between the mutual repulsion, due to the negative electrical charge of the surface, and the surface attraction due to the presence of surface forces such as Van der Waals forces. The repulsion between two charged surfaces is proportional to the electrical charge (or electric

potential) at the surface and inversely proportional to the dielectric constant of the medium between the surfaces.

Mica particles, when in suspension in water, are generally considered to have a negative charge distributed on their surface. This negative charge generates an electrical repulsion which depends on the physical properties of the dispersing media. Simultaneously, when a small distance exists between two facing surfaces, a Van der Waals attraction is instead generated, by the electron interaction of the two surfaces (Hamaker, 1937; Casimir and Polder, 1948) In a clay suspension, the interaction force existing between two particles at a given distance is given by the net energy resulting from the balance between the electrical repulsion and the Van der Waals attraction. For clays in suspension in water, this is generally assumed to be negative (repulsive) unless the chemistry of the suspension is altered. The aggregation rate between negatively charged particles is controlled by the repulsive interaction force and the kinetic energy resulting from their Brownian motion. If the repulsive barrier existing between two particles is high enough not to be overcome by the Brownian motion, the two particles will remain in a dispersed state, and settle individually. On the other hand, if by altering the chemistry of the suspension, and hence the charge of the particle surface, the negative repulsive barrier is depleted, the particles in suspension will have enough kinetic energy to overcome such a barrier, and aggregate/flocculate. These particles will therefore tend to settle as a cluster of one or more particles.

When dispersed in neutral water, mica tends to increase the pH of the solution toward a pH of around 8 or 9. It is reasonable to assume that this is the pH of pore water when in equilibrium with the mica, unless altered. In this condition, the surface of mica particles are highly negative: zeta (ζ) potential about -140 mV (Nishimura et al., 1992). When the pore water of mica is altered in order to decrease the pH below 5, the zeta potential decreases sharply. At pH 4 the ζ potential is about -70 mV (Nishimura et al., 1992). The change in the negative

potential at the particle surface and edge is directly proportional to the change in repulsion between two facing particles of mica. This change in the mica particle repulsion results in the observed change to the mica settling pattern when the pH drops from 9 to 5 (Figure 6a). It seems reasonable and consistent to assume that mica particles at pH 5 are settling in an aggregate/flocculated mode (non-dispersed). This hypothesis is strongly corroborated by the observations that: i) at pH 9 the water suspension never becomes clear, implying that smaller particles do not settle, and ii) the final volume of the sediment for the sample at pH 5 is higher than that at pH 9.

In addition, research by Zhao et al., (2008) and Yan et al., (2011) using direct colloid probe force measurement and atomic force microscope measurement respectively suggest that the basal plane of muscovite mica carry a permanent negative charge while the edge charge is pH dependent (with positive edge charge at lower pH and negative edge charge at higher pH range). This further supports additional interaction and flocculation between particles in the acidic pH range and dispersion in the alkaline pH range.

The energy barrier between particles can be also depleted by increasing the electrolyte concentration of the suspension. As explained by the well-known the DLVO theory (Guoy 1910, Deraguin and Landau 1941, Verwey and Overbeek 1948), the cations dissolved in water are shielding the electrical charge of the particle surface and therefore reducing its negative repulsion. Consequently, when the electrolyte concentration is increased, the particle repulsion becomes smaller and therefore the probability that two particles will aggregate/flocculate increases. Figure 6c and d, showed that, at 0.1M and 1.8 M concentration of KCl, the sedimentation times are all very similar, regardless of the pH and the KCl concentration. It seems reasonable to assume that at this electrolyte concentration, the shielding effect of the cations present in the double layer is so high that the charge (or potential) at the surface no

longer matters and the negative repulsion is entirely depleted. Hence, the Van der Waals attraction dominates.

Although distinguishing whether mica associates in flocs, or in aggregates made of parallel particles, is out of the scope of this research work it is worth noting that the sedimentation curves reported in Figure 6 for the non-dispersed samples are the same regardless of the way the suspension was destabilized (pH or ionic strength). This implies that the association mode is the same (i.e., either one or the other). Indeed, one might expect that aggregates and flocs with different sizes and densities would return a different final void ratio for the sediment and a different settlement velocity. The experimental evidence presented here is somehow in contrast with the common understanding that, for clay suspension, flocculation is generally attributed to acidic destabilization at low ionic strength, and aggregation to destabilization caused by high ionic strength. However, whatever the association process, the experimental evidence suggests that for the case of non-dispersed sedimentation, particles interaction is attractive.

The strength of mica samples in a dispersed configuration (pH 9 and low ionic strength) and a non-dispersed configuration (either pH 5 or high ionic strength) was compared using the liquid limit test. The non-dispersed samples were stronger, with a higher liquid limit, than the dispersed ones. These findings are consistent with the experimental results reported by Pedrotti, (2016) for kaolin clay at different particle configurations, where the liquid limit was found to increase with the average floc size within the sample. Again, these results suggest that the unit elements within the acidic mica samples are not single particles, but groups of particles clustered together.

In the 70s, Moore and Mitchell, (1974) first, and van Olphen (1977) after, showed that the shear strength of a clay sample is proportional to the net attraction existing between particles. Moore and Mitchell, (1974) proved it by measuring the undrained shear stress of clay

samples with differing van der Waals interaction, whereas van Olphen (1977) demonstrated it by measuring the Bingham stress of a suspension with different aggregate patterns. Accordingly, the results obtained here for the liquid limit (Figure 7), show that acidic samples, where particle interaction is attractive in nature, have a higher liquid limit than alkaline ones.

3.3.5. *An electrochemical conceptual model for the erosion of mica*

The increase in shear strength for the non-dispersed mica samples is also reflected in the erosion susceptibility tests.

Shields in 1936 performed a set of experimental tests on coarse soil, which for the following century has been considered as the benchmark dataset to develop theories and to characterize soil erosion susceptibility. As the soil tested by Shield was coarse and non-cohesive, the main assumption adopted in the many theories developed to interpolate his data, is that there is no electrochemical interaction forces between particles. When soil is eroded, single particles are detached from the soil mass by drag and lift forces, without creating any shear stress on the bed (Miedema, 2013). By contrast, a cohesive sediment, is subject to the phenomena where particles interact with each other. In Figure 12, the function developed by Soulsby and Whitehouse (1997), to interpolate Shields dataset for coarse material is shown (black solid line). The same curve has been extrapolated (black dashed line), using his equation in the range for smaller particle diameters (silt-size), in order to compare it with the experimental dataset presented in this research. In the same Figure, the function derived by **Lick et al. (2004)** is also reported for a reference compaction density of ~ 1.5 [g/cm³]. **Licket al. (2004)** developed this function (grey solid line in Figure 12) to account for the particle interaction that develops in finer materials. To allow a fit to the Shields dataset in the range of coarse material, a cohesive factor, inversely proportional with the particle size is introduced by **Lick et al. (2004)**. Soulsby and Whitehouse (1997) curves provide a reference behaviour for

the erosion mechanisms of interacting and non-interacting particles i.e., for soils with cohesion and for cohesionless behavior, respectively.

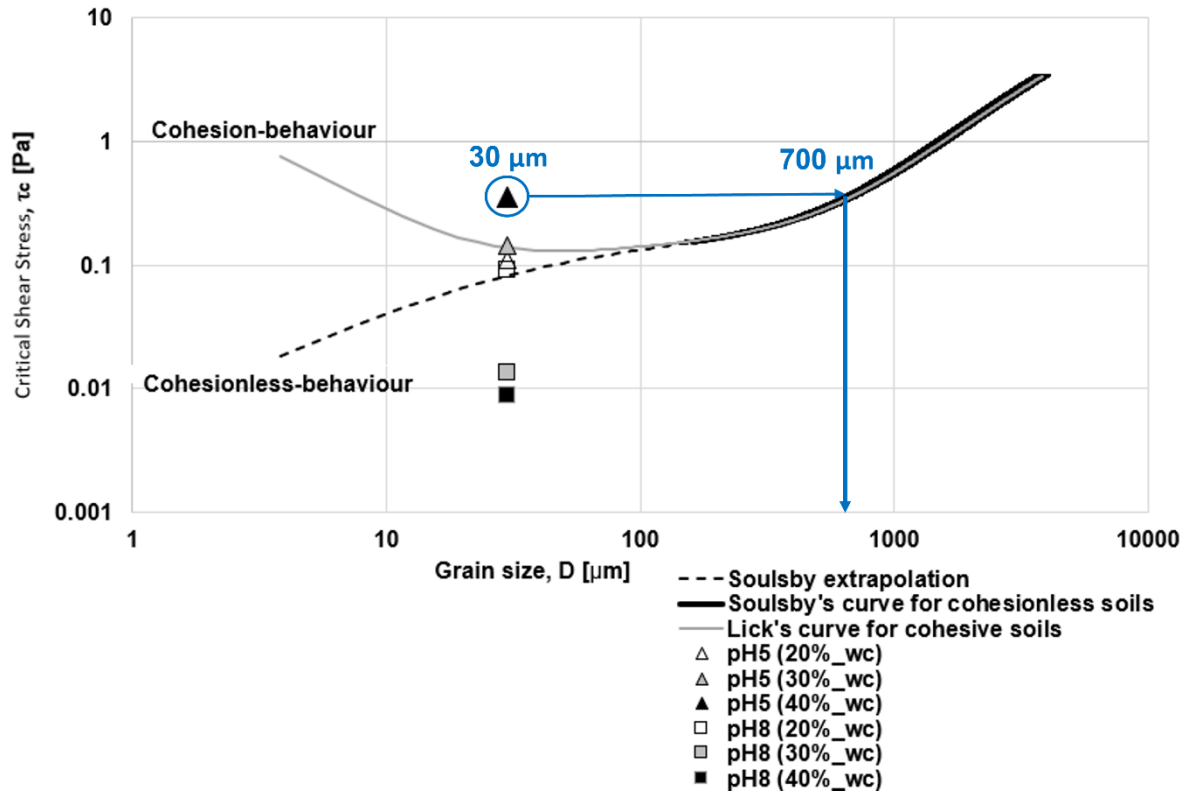


Figure 12: Shields's curve

In Figure 12, the two curves are plotted along with the six sets of erosion experimental data presented in Figure 10. It is interesting to note that at low compaction moisture contents, both the acidic and alkaline samples have a τ_c of about 0.1 Pa, and the two points lie quite close to Soulsby's curve for cohesionless soils. As the compaction moisture content is increased both datasets (e.g., acidic, and alkaline sample) move away from Soulsby's curve. As the alkaline water content at compaction is increased, the critical shear stress reduces, and the data points end up well below Soulsby's curve for cohesionless soils. As the number of particles in contact with alkaline water increases, the more particles are interacting in a dispersive fashion, the particles are therefore becoming more prone to erosion, hence less force is required to lift them. As shown in Figure 13a, it is suggested that for dispersed samples, erosion occurs in a particle-

by-particle fashion, as generally assumed for a cohesionless coarse material. By contrast, for the acidic samples, as the number of particles in contact with acidic water increases, the more particles are interacting in an attractive fashion, and the associated erosion critical shear stress moves towards and above Lick's curve for cohesive soils. Once the particle attraction is activated, the elementary unit within the soil is no longer a single particle, but a cluster of them (erosion of non-dispersed particle configuration in Figure 13b). This results in a higher shear stress at the surface. It is interesting to note that the critical shear stress of a sample of mica particle, with an average diameter of 30 μm when compacted with acidic water to a moisture content of 0.40, corresponds to a critical shear stress of a coarse material having a grain size of about 0.7 mm (700 μm), see blue line on Figure 12.



Figure 13: Conceptual model of mica particle erosion at a) dispersed particle configuration and b) non-dispersed particle configuration.

Although, the test conducted here is a small-scale laboratory test which will require further refinement, the result suggest that it may be possible to enhance muscovite silt stability through adequate pore-water acidification. This may be particularly useful in relatively low stress applications such as the use of mica as an alternative source of potassium (which plays an important role in several physiological processes in plant nutrition) or as a fill material for embankment.

The general formula for minerals of the mica group is $XY_{2-3}Z_4O_{10}(OH, F)_2$ with $X = K, Na, Ba, Ca, Cs, (H_3O), (NH_4)$; $Y = Al, Mg, Fe^{2+}, Li, Cr, Mn, V, Zn$; and $Z = Si, Al, Fe^{3+}, Be, Ti$. The alkaline nature of muscovite when mixed with neutral water is attributed to the replacement of an alkali earth metal by a hydrogen ion (Bakken et al. 1997). This implies that other mica types (Biotite, Lepidolite, Phlogopite, Paragonite and Glauconite) are likely to exhibit similar behaviour to muscovite with respect to their porewater chemistry. This study evaluated pure muscovite. Considering that acidic samples are less erodible than alkali samples and that mining waste is likely to be polymineralic, (laden with sulphate and heavy metals) resulting in acid systems, mine wastes may be less erodible than the pure muscovite. Additional studies are required to understand the polymineralic nature of mine wastes, as well as the presence of other forms of mica.

3.3.6. Environmental considerations about the use of mica for agricultural applications

This work suggests that acidification of pore-water contributes to stabilising the mica-based material against water-induced erosion. It is worth highlighting that the values of pH required to achieve stability falls within the range of pH values encountered in agricultural applications. Crop plants vary in their tolerance to acidity and plant nutrients have different optimal pH ranges (Goulding, 2016). For example, ericaceous (lime-hating) plants such as rhododendrons, camellias, heathers, azaleas, blueberries, white potatoes and conifer trees do well in acidic soil in the range of pH 5 to pH 6. Similarly, normal rain is usually slightly acidic, with a pH of between 5 and 5.6 (Goulding, 2016) due to the dissolution of carbon dioxide (CO_2) and the dissociation of the resulting carbonic acid (H_2CO_3). Soil usually attains the same equilibrium pH as that of the rain to which it is exposed. Hence, natural soil conditions will

generally provide a good environment for mica-enhanced erosion resistance as well as providing a source of potassium for ericaceous plants.

Considering mica as a source of potassium, there is a need to further evaluate the best possible environmental conditions for the release of potassium by mica. However, studies by Biswas & Basak, (2014); Meena et al. (2015); Singh et al. (2010) showed that potassium can be released favourably under a wide range of non-stringent environmental conditions, for example variation in temperature and moisture content did not affect the rate of mobilisation of K. They demonstrated that the addition of potassium solubilising rhizobacteria to waste mica for k mobilisation significantly enhanced the release of K ions and resulted in the release of organic acid, stabilising the pH of the system to a pH of between about 5 and 7. This is consistent with the desired pH range for enhanced erosion resistance.

3.4. Conclusion

This paper presents an experimental campaign to characterize mica erosion susceptibility. Mica particle-to-particle interaction forces and their effect on the macroscopic behaviour were systematically investigated by changing the pore fluid pH and ionic concentration. Results from sedimentation tests and liquid limit tests have informed a conceptual model of the mica fabric that is able to explain the enhanced erosion resistance under acidic and/or high ionic concentration pore-water conditions.

It is shown that the particle configuration of mica samples consistently varies with the pore water chemistry, regardless of whether the samples being tested were suspension sediments or compacted samples. For mica samples formed with neutral water at low ionic concentration, the particles are in a dispersed configuration. This implies relatively high erosion susceptibility, as particles are eroded one by one. When the mica pore chemistry is altered, however, either by acidification or by an increase in the ionic strength, particles tend

to cluster together and organize in a non-dispersed configuration. This results in a relatively less erosion susceptibility, as group of particles must be eroded as opposed to individual ones.

Although the water chemistry has been shown to change the particle configuration, the experimental findings suggest this may only occur when the water chemistry is altered at sample formation. The water used in the jet for all erosion tests was neutral water, but it did not result in a change to sample behaviour over time. To confirm the effect of infiltration water chemistry, further investigation is needed.

Considering that mica waste is derived from mining operations, which are often slightly acidic due to some metal content (e.g., iron sulphides which result in the leaching of sulphuric acid), the work presented in this paper paves the way for tailored assessments of individual mica waste materials to determine the appropriateness of their use.

3.5. Acknowledgement

The publication of this work was made possible through support from the University of Strathclyde Research Studentship.

3.6. Data Availability Statement

Some or all data, models, or code that support the findings of this study are available from the corresponding author upon reasonable request.

3.7. Reference

Bakken, A. K., Gautneb, H., & Myhr, K., 1997. The potential of crushed rocks and mine tailings as slow-releasing K fertilizers assessed by intensive cropping with Italian ryegrass in different soil types. *Nutrient Cycling in Agroecosystems*, 47, 41–48.

- Basak, B. B., 2019. Waste Mica as Alternative Source of Plant-Available Potassium: Evaluation of Agronomic Potential Through Chemical and Biological Methods. *Natural Resources Research*, 28(3), 953–965. <https://doi.org/10.1007/s11053-018-9430-3>
- Basak, B. B., Sarkar, B., Biswas, D. R., Sarkar, S., Sanderson, P., & Naidu, R., 2017. Bio-Intervention of Naturally Occurring Silicate Minerals for Alternative Source of Potassium: Challenges and Opportunities. *Advances in Agronomy*, 141, 115–145. <https://doi.org/10.1016/bs.agron.2016.10.016>
- Beber, R., Tarantino, A., Pedrotti, M., & Lunn, R. J., 2019. The effect of clay water content in the jet erosion test. *E3S Web of Conferences*, 92. <https://doi.org/10.1051/e3sconf/20199202016>
- Biswas, D. R., & Basak, B. B., 2014. Mobilization of potassium from waste mica by potassium-solubilizing bacteria (*Bacillus mucilaginosus*) as influenced by temperature and incubation period under in vitro laboratory conditions. *Agrochimica*, 58(4), 309–320. <https://doi.org/10.12871/0021857201442>
- BS, P., 1990. "7: 1990. British Standard Methods of Test for Soils for Civil Engineering Purposes, Part 7: Shear strength tests (total stress) tests." British Standards Institution, London.
- Casimir, H.B. and Polder, D., 1948. The influence of retardation on the London-van der Waals forces. *Physical Review*, 73(4), 360. <https://doi.org/10.1103/PhysRev.73.360>
- Cresswell, D. and Sims, V., 2007. "Characterisation of mineral wastes, resources and processing technologies—Integrated waste management for the production of construction material." Case Study: Green roof substrate using aerated concrete waste. Report WRT 177/WR0115 (October) issued by University of Leeds, Akristos, and Mineral Industry Research Organisation. DEFRA (Department for Environment, Food, and Rural Affairs), UK.

- Deraguin, B. and Landau L., 1941. "Theory of the stability of strongly charged lyophobic sols and of the adhesion of strongly charged particles in solution of electrolytes." *Acta Physicochim: USSR* 14: 633-662.
- Dudeny, A. W. L., Chan, B. K. C., Bouzalakos, S., & Huisman, J. L., 2013. Management of waste and wastewater from mineral industry processes, especially leaching of sulphide resources: State of the art. *International Journal of Mining, Reclamation and Environment*, 27(1), 2–37. <https://doi.org/10.1080/17480930.2012.696790>
- Goulding, K. W. T., 2016. Soil acidification and the importance of liming agricultural soils with particular reference to the United Kingdom. *Soil Use and Management*, 32(3), 390–399. <https://doi.org/10.1111/sum.12270>
- Guoy, G., 1910. "Constitution of the electric charge at the surface of an electrolyte." *J Physique* 9: 457-467.
- Gratchev, I., & Towhata, I., 2013. Stress-strain characteristics of two natural soils subjected to long-term acidic contamination. *Soils and Foundations*, 53(3), 469–476. <https://doi.org/10.1016/j.sandf.2013.04.008>
- Hamaker, H. C., 1937. The London-van der Waals attraction between spherical particles. *Physica*, 4(10), 1058–1072. [https://doi.org/10.1016/S0031-8914\(37\)80203-7](https://doi.org/10.1016/S0031-8914(37)80203-7)
- Hanson, G. J., & Cook, K. R., 2004. Apparatus, test procedures, and analytical methods to measure soil erodibility in situ. *Applied Engineering in Agriculture*, 20(4), 455–462.
- Hanson, G. J., & Simon, A., 2001. Erodibility of cohesive streambeds in the loess area of the Midwestern USA. *Hydrological Processes*, 15(1), 23–38. <https://doi.org/10.1002/hyp.149>
- Hojamberdiev, M., Eminov, A., & Xu, Y., 2011. Utilization of muscovite granite waste in the manufacture of ceramic tiles. *Ceramics International*, 37(3), 871–876. <https://doi.org/10.1016/j.ceramint.2010.10.032>

- Hoseini, S. M. R., Bahrami, A., & Hosseinzadeh, M., 2016. The reclamation of mica flakes from tailing disposal using gravity separators and flotation. *International Journal of Mining and Geo-Engineering*, 50(1), 61–76. <https://doi.org/10.22059/IJMGE.2016.57309>
- Karamigolbaghi, M., Ghaneizad, S. M., Atkinson, J. F., Bennett, S. J., & Wells, R. R., 2017. Critical assessment of jet erosion test methodologies for cohesive soil and sediment. *Geomorphology*, 295(March), 529–536. <https://doi.org/10.1016/j.geomorph.2017.08.005>
- Karlsson, T., Kauppila, P., & Lehtonen, M., 2017. Assessment of the effects of mine closure activities to waste rock drainage quality at the Hitura Ni-Cu mine, Finland. *Proceedings of the 13th International Mine Water Association Congress—“Mine Water & Circular Economy—A Green Congress”*, 80–87.
- Keesstra, S. D., Bouma, J., Wallinga, J., Tittonell, P., Smith, P., Cerdà, A., Montanarella, L., Quinton, J. N., Pachepsky, Y., Van Der Putten, W. H., Bardgett, R. D., Moolenaar, S., Mol, G., Jansen, B., & Fresco, L. O., 2016. The significance of soils and soil science towards realization of the United Nations sustainable development goals. *Soil*, 2(2), 111–128. <https://doi.org/10.5194/soil-2-111-2016>
- Lick, W., Jin, L., & Gailani, J., 2004. Initiation of Movement of Quartz Particles. *Journal of Hydraulic Engineering*, 130(8), 755–761. [https://doi.org/10.1061/\(asce\)0733-9429\(2004\)130:8\(755\)](https://doi.org/10.1061/(asce)0733-9429(2004)130:8(755))
- Liu, J., Gao, G., Wang, S., Jiao, L., Wu, X., & Fu, B., 2018. The effects of vegetation on runoff and soil loss: Multidimensional structure analysis and scale characteristics. *Journal of Geographical Sciences*, 28(1), 59–78. <https://doi.org/10.1007/s11442-018-1459-z>
- Lottermoser, B., 2010. *Mine Wastes: Characterization, treatment and environmental impacts*. Mine Wastes: Characterization, Treatment and Environmental Impacts.

- Man, A., & Graham, J., 2010. Pore fluid chemistry, stress-strain behaviour, and yielding in reconstituted highly plastic clay. *Engineering Geology*, 116(3–4), 296–310. <https://doi.org/10.1016/j.enggeo.2010.09.011>
- Meena, V. S., Maurya, B. R., Verma, J. P., Aeron, A., Kumar, A., Kim, K., & Bajpai, V. K., 2015. Potassium solubilizing rhizobacteria (KSR): Isolation, identification, and K-release dynamics from waste mica. *Ecological Engineering*, 81(August), 340–347. <https://doi.org/10.1016/j.ecoleng.2015.04.065>
- Miedema, S.A., 2011. Constructing the shields curve. *International Conference on Offshore Mechanics and Arctic Engineering*, 44397, 825-840. <https://doi.org/10.1115/OMAE2011-49232>
- Mitchell, J. K., & Soga, K., 2005. Fundamentals of Soil Behavior. In *Soil Science*, 158(1). <https://doi.org/10.1097/00010694-199407000-00009>
- Momeni, M., Bayat, M., & Ajalloeian, R., 2020. Laboratory investigation on the effects of pH-induced changes on geotechnical characteristics of clay soil. *Geomechanics and Geoengineering*, 1–9. <https://doi.org/10.1080/17486025.2020.1716084>
- Moore, C. A., & Mitchell, J. K., 1974. Electromagnetic Forces and Soil Strength. *Geotechnique*, 24(4), 627–640. <https://doi.org/10.1680/geot.1974.24.4.627>
- Nishimura, S., Tateyama, H., Tsunematsu, K., & Jinnai, K., 1992. Zeta potential measurement of muscovite mica basal plane-aqueous solution interface by means of plane interface technique. *Journal of Colloid And Interface Science*, 152(2), 359–367. [https://doi.org/10.1016/0021-9797\(92\)90038-N](https://doi.org/10.1016/0021-9797(92)90038-N)
- Nosrati, A., Addai-Mensah, J., & Skinner, W., 2009. pH-mediated interfacial chemistry and particle interactions in aqueous muscovite dispersions. *Chemical Engineering Journal*, 152(2–3), 406–414. <https://doi.org/10.1016/j.cej.2009.05.001>

- Palomino, A. M., & Santamarina, J. C., 2005. Fabric map for kaolinite: Effects of pH and ionic concentration on behavior. *Clays and Clay Minerals*, 53(3), 211–223. <https://doi.org/10.1346/CCMN.2005.0530302>
- Palumbo-Roe, B., Colman, T., Cameron, D. G., Linley, K., & Gunn, A. G., 2014. The nature of waste associated with closed mines in England and Wales. 82. <http://nora.nerc.ac.uk/id/eprint/10083/> (accessed 15 September 2020).
- Pedrotti, M., 2016. An experimental investigation on the micromechanisms of non-active clays in saturated and partially saturated states. PhD Thesis submitted to the Department of Civil and Environmental Engineering, University of Strathclyde.
- Singh, G., Biswas, D. R., & Marwaha, T. S., 2010. Mobilization of potassium from waste mica by plant growth promoting rhizobacteria and its assimilation by maize (*Zea mays*) and wheat (*Triticum aestivum* L.): A hydroponics study under phytotron growth chamber. *Journal of Plant Nutrition*, 33(8), 1236–1251. <https://doi.org/10.1080/01904161003765760>
- Sinha, N., Deb, D., & Pathak, K., 2017. Development of a mining landscape and assessment of its soil erosion potential using GIS. *Engineering Geology*, 216, 1–12. <https://doi.org/10.1016/j.enggeo.2016.10.012>
- Soulsby, R. and Whitehouse R., 1997. Threshold of sediment motion in coastal environments. *Pacific Coasts and Ports' 97: Proceedings of the 13th Australasian Coastal and Ocean Engineering Conference and the 6th Australasian Port and Harbour Conference*; Centre for Advanced Engineering, University of Canterbury. 1, 145-150.
- van Olphen, H., 1977. An introduction to clay colloid chemistry, for clay technologists, geologists, and soil scientists. 2nd Edition, Wiley, New York.

- Verwey, E. J. W., & Overbeek, J. T. G., 1948. Theory of the stability of lyophobic colloids. In *Journal of Colloid Science* (Vol. 10, Issue 2, pp. 224–225). [https://doi.org/10.1016/0095-8522\(55\)90030-1](https://doi.org/10.1016/0095-8522(55)90030-1)
- Wang, A., Li, X., Huang, Z., Huang, X., Wang, Z., & Wu, Q., 2015. Laboratory study on engineering geological characteristics and formation mechanism of altered rocks of Henan Tianchi pumped storage power station, China. *Environmental Earth*, 5063–5075. <https://doi.org/10.1007/s12665-015-4520-6>
- Wang, H., & Zhang, G. H., 2021. Temporal variation in soil erodibility indices for five typical land use types on the Loess Plateau of China. *Geoderma*, 381, 114695. <https://doi.org/10.1016/j.geoderma.2020.114695>
- Zografou, A., Heath, A., & Walker, P., 2014. China clay waste as aggregate in alkali-activated cement mortars. *Proceedings of the Institution of Civil Engineers - Construction Materials*, 167(6), 312–322. <https://doi.org/10.1680/coma.13.00037>

Appendix I

Supplementary material

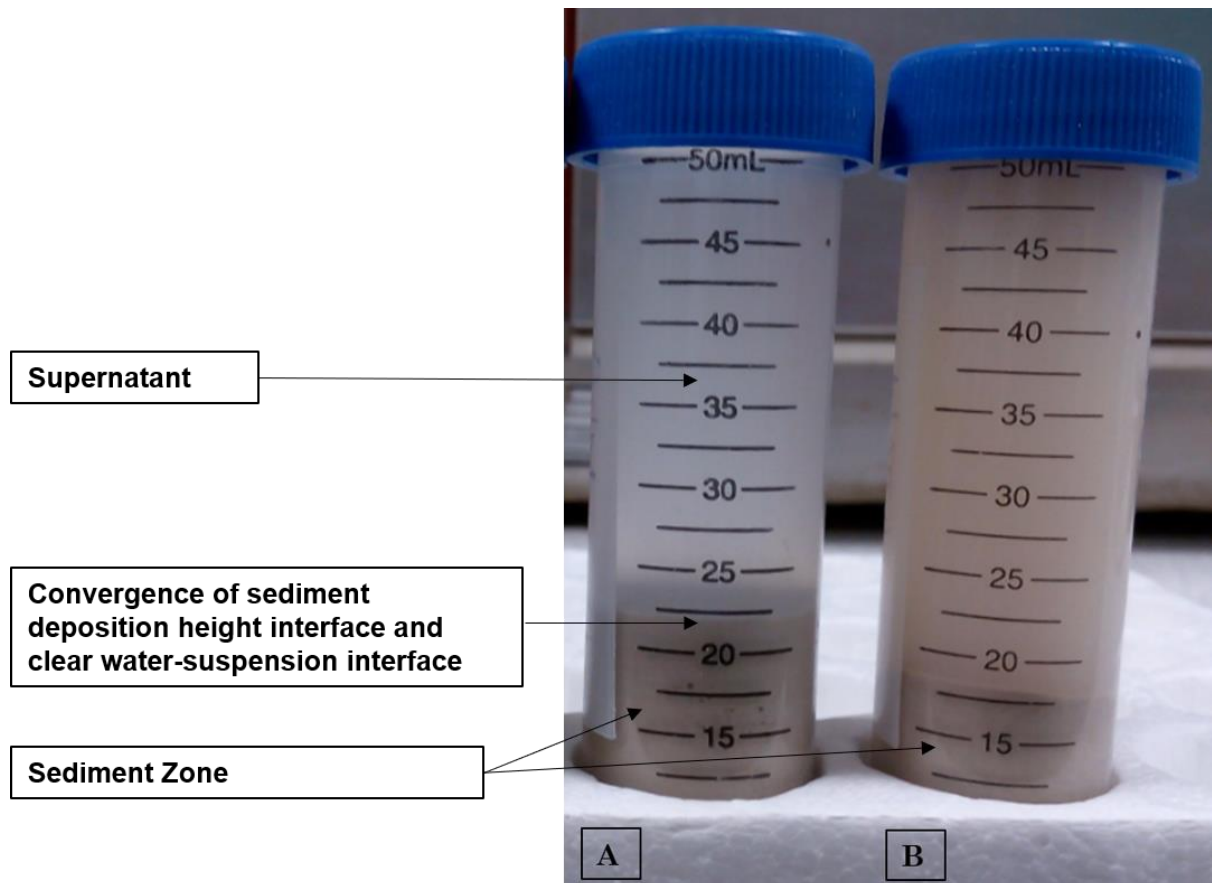


Figure S1: Photo of two columns at the end of the sedimentation test. Both samples were prepared with mica having average particle size of 37 μm , with an initial soil/water concentration of 90 g/L and were sedimented in a tube with a diameter of 29 mm (with a V base). The photo shows the 2 different sedimentation patterns: a) non-dispersed sedimentation (sample 0.1 mol/l KCl and pH 9) showing a supernatant-sediment zone interface and b) dispersed sedimentation (sample 0 mol/KCl and pH 9) showing a suspension-sediment zone interface.

4. An experimental investigation into the use of mica as a material for the stabilisation of marginal clays in construction

The same version of this chapter (with slight modification) has been published in: The same version of this chapter (with slight modification) has been published in: Ibeh C. U., Tarantino A., Pedrotti M., Lunn R. J. (2021) An experimental investigation into the use of mica soil for stabilisation of marginal clays. Accepted for publication in Construction and building materials Journal 299, 123971. <https://doi.org/10.1016/j.conbuildmat.2021.123971>

Abstract

The scarcity and cost of high-quality construction materials have resulted in their use being reserved for the construction of structures that experience relatively high stress, such as roads with high traffic volumes. Consequently, mechanically improved abundant marginal materials are common in relatively low stress construction applications such as landscaping, low-volume paved roads and fill material for flood embankments. In clays, mechanical improvement is commonly achieved through the addition of chemical stabilizers such as lime, bitumen, cement, and fly ash. However, these chemical stabilizers are associated with high cost and a large carbon footprint. Here, we present the first research demonstrating that clays can be mechanically improved through the addition of mica. Mica wastes are generated in significant volume as a by-product from the mining of relatively valuable materials. This paper explores the use of mica to improve the ultimate limit state of marginal clays for use as construction material. Kaolin clay was prepared with muscovite sand and muscovite silt in variable fractions (0%, 2.5%, 10% and 30% muscovite fraction). The hydraulic and mechanical response of the composite materials were investigated through one-dimensional compression

and direct shear testing. The most notable finding is that, at very low normal stresses (≤ 100 kPa), a relatively small fraction of mica is sufficient to shift the angle of shearing resistance of the composite, from the value for pure clay ($\phi' \sim 17^\circ$) towards the value for pure muscovite ($\phi' \sim 26^\circ$). X-ray computed tomography scans of the consolidated and sheared samples show that the relatively high strength of the mica clay composite at low normal stress is due to a fold-like mode of deformation observed in shearing. This mechanism appears to be suppressed at high stresses with the shear band likely developing through the clay matrix. As a result, the composite exhibits the same friction angle of the clay alone at high stresses.

Keywords: Mica, shear strength, hydraulic conductivity, marginal clay, kaolin, circular economy

4.1. Introduction

In recent years, the scarcity and cost of high-quality construction materials have resulted in their use being reserved for the construction of structures that will experience relatively high stress, such as roads with high traffic volumes (Liebenberg & Visser, 2003). Consequently, abundant marginal materials are common in relatively low stress geotechnical applications such as landscaping, low-volume paved roads and fill material for flood embankments. Further, the use of local marginal materials can result in significant carbon savings (Ameri & Behnood, 2012; Choi et al., 2020; Cook & Gourley, 2002; Kalinowska-Wichrowska et al., 2020; Liebenberg & Visser, 2003; Moreno et al., 2012) as well as enhancing the drive towards a circular economy (Kibert, 2001; Liebenberg & Visser, 2003; Soleimanbeigi & Edil, 2015).

Marginal materials are defined as materials that do not possess, in their present form, quality levels that meet current standards sufficient for their use as various structural components. Thus, their properties need to be mechanically improved. Chemical stabilizers such as lime, bitumen, cement, and fly ash have successfully been used in the past to improve the performance of some marginal clays (Coudert et al., 2019; Liebenberg & Visser, 2003; Obuzor et al., 2011; Phummiphon et al., 2016). However, these chemical stabilizers are associated with high cost and a large carbon footprint (Sargent et al., 2016). By-product mica could prove a valuable alternative to improve the mechanical performance of marginal clays.

A significant amount of mining by-product is mica generated both from the mining of relatively valuable materials such as gold, copper, uranium and platinum (Nosrati et al., 2009) and that of less valuable materials such as china clay (Zografou et al., 2014) and mica itself (Basak, 2019). About 10 million tons of mica waste is generated in a year and over 600 million tons of total industry stockpile are estimated to be available (Palumbo-Roe et al., 2014). Due to its abundance, researchers have begun to explore its use in construction. Mica has high

radiation resistance and good insulation properties (Shishelova & Zhitov, 2018) and has been shown to have good thermal and mechanical properties. For example, (Low, 1980; Mallik, 2020) observed that the mechanical and thermal properties of glass-mica composites are superior to those of conventional building materials, such as concrete, masonry products and cement mortar. Similarly, (Pacheco-Torgal et al., 2009), demonstrated the possibility of using a tungsten mine waste, containing mica and quartz, to produce alkali activated binders using a calcination process. To-date, the proposed applications for mica in construction use processes that expend relatively large amounts of energy (calcination and glass manufacture). Whilst highly valuable, these high energy applications may not be desirable for the full 600 million ton stockpile of mica waste. There is, therefore, scope to investigate lower-energy applications of waste mica in construction.

This paper explores the feasibility of using by-product mica for enhancing the mechanical properties of marginal clay for low stress applications in construction. The paper presents an evaluation of the shear strength, compressibility and hydraulic conductivity of muscovite and kaolin composites for geotechnical uses such as structural fills and landscaping. Speswhite kaolin clay was mixed with variable weight percentages of muscovite silt or sand, in the ratios 0%, 2.5%, 10% and 30% by weight of muscovite. The hydraulic and mechanical behaviour of these composite materials was then tested via one-dimensional compression and direct shear tests. Finally, sub-samples from the sheared specimens were imaged using X-ray computed tomography to enable an evaluation of the microscale mechanisms controlling the macroscopic behaviour of these composite materials.

4.2. Materials and specimen preparation

Three different materials were used in this study: Kaolin, Muscovite silt and Muscovite sand (Figure 1). Composite specimens made up of muscovite silt or sand mixed with kaolin in the ratios 2.5:97.5, 10:90, and 30:70 by weight were prepared and tested.



Figure 1. Images of (from left to right) kaolin, muscovite silt and muscovite sand used in this study.

Speswhite kaolin with a liquid limit $w_L = 0.64$ and a plastic limit $w_P = 0.32$ was used in the experiments. The grain size distribution, obtained through Laser diffraction analysis, is characterised by 80% clay-fraction (fraction < 2 micrometer) and 20% silt-fraction (fraction 2-63 micrometer). Muscovite silt used for this study was purchased from LKAB minerals Ltd. The muscovite silt has a median diameter $d_{50} = 30 \mu\text{m}$, particle sizes in the range 1 - 87 μm (obtained through Laser diffraction analysis) and a specific gravity of 2.8. Its chemical composition obtained with Micro- X-ray Fluorescent (Micro XRF) spectrometer performed at Bruker AXS is shown in Table 1. Muscovite sand was purchased from Specialist Aggregates Ltd. The muscovite sand has a median diameter, $d_{50} = 1.5 \text{ mm}$, particle sizes in the range 0.25—2.8 mm, and a specific gravity of 2.8 (see Figure 1c). Its chemical composition obtained through Micro XRF is shown in Table 1.

Table 1. Chemical composition of muscovite silt, muscovite sand and kaolin used in this study.

Element	Atomic Number	Compound	Normalized Stoichiometric Composition (wt.%)		
			Muscovite Silt	Muscovite Sand	Kaolin
Al	13	Al ₂ O ₃	32	30 – 36	38
Si	14	SiO ₂	43	43 – 50	47
K	19	K ₂ O	13	<9 -12	
Ti	22	TiO ₂	1	1	
Fe	26	Fe ₂ O ₃	8	1 – 5	-
Loss on ignition			Max 5%	Max 5%	

The kaolin and muscovite were supplied as dry powders/grains. We mixed the sample with a spatula until a homogeneous mixture was obtained, as determined by visual inspection since the colours of clay and mica particles are very different. To reconstitute kaolin clay and mica composite from slurry, distilled water was added to the dry powder up to a water content 1.5 times the liquid limit of kaolin ($w_L=0.64$) following the procedure suggested by (Burland, 1990). The reconstituted slurry preparation was used to better understand the intrinsic properties (devoid of field depositional conditions, ageing, cementation, and leaching) of the natural clay which is a robust frame of reference against which to assess the in-situ state of the clays. Slurry samples were used for both oedometer and direct shear tests. Samples were reconstituted from slurries prepared at the same initial water content to ensure that the different

compression behaviour of the composites is only associated with its intrinsic properties (and not biased by differences in the initial conditions)

4.3. Experimental procedure

4.3.1. Direct Shear Tests

Drained direct shear box tests were conducted using a digital direct shear apparatus (ELE International, Sheffield, UK) according to the BS1377 standard (1377-7 BS-CODE, 1990), see Figure 2 for typical setup for a direct shear test. The shear box has internal dimensions of 60×60 mm and accommodates specimens up to 20 mm height. The apparatus is equipped with a 5 kN capacity load cell and two displacement transducers to measure the shear force and both the vertical and shear (horizontal) displacements.

From the specimen consolidation data, it was determined that a shearing rate of 0.01 mm/min was sufficient to prevent pore water pressure build-up and thus maintain drained conditions during shearing. With the exception of the 100% kaolin sample, all specimens were sheared at this rate. For comparison with the composite materials, shear tests performed on the 100% kaolin clay, reconstituted from slurry and consolidated to 50, 100, and 150, are reported here taken from (Wong et al., 2018), with a shearing rate of 0.02 mm/min, and for a specimen consolidated to 300 kPa from (Galvani, 2003), with a shearing rate of 0.005 mm/min. From the calculated rate of consolidation using the consolidation curve for pure kaolin, the shear rate of 0.02 mm/min is within the limit to avoid pore pressure build up during shear. However, to be on the safe side, a shear rate of 0.01 mm/min was used.

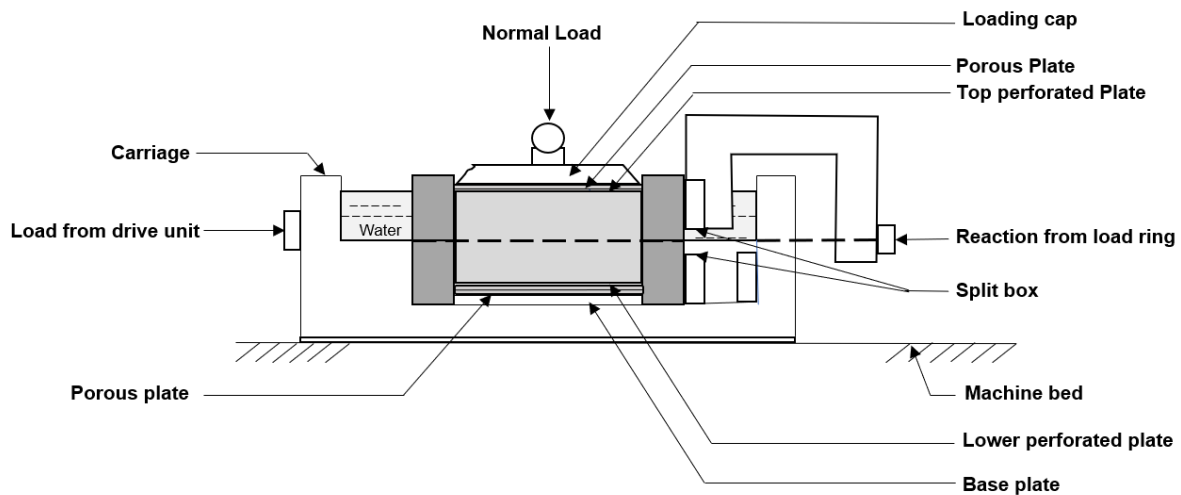


Figure 2: Typical setup for a direct shear test

4.3.2. One-dimensional (oedometer) compression tests

One dimensional oedometer compression tests were performed in a front-loading oedometer cell -diameter 75 mm (Controls Testing Equipment Ltd) according to (1377-5 BS-CODE, 1990), see Figure 3 for a typical setup of an oedometer cell. Prior to loading, all samples were submerged under water in the oedometer cell. Samples were compressed in incremental steps starting from 3kPa vertical stress and doubling the load up to 2230kPa vertical stress. Unloading was performed in five steps.

For each loading and unloading step, samples were allowed to consolidate, i.e. the subsequent loading step was only applied when the secondary compression branch of the consolidation curve was clearly visible. The change in void ratio associated with a given loading step was computed by taking into account the change in the void ratio accumulated in the current loading step, due to primary consolidation, and the change in void ratio accumulated in the previous loading step, due to secondary consolidation (see Appendix I).

For each loading step, the consolidation time t_{50} associated with 50% consolidation was calculated and this enabled estimation of the consolidation coefficient c_v and, hence, the hydraulic conductivity k as detailed in Appendix II.

The void ratio associated with each imposed vertical stress was calculated backwards from the final specimen water content, the dry mass, and the specimen cross sectional area.

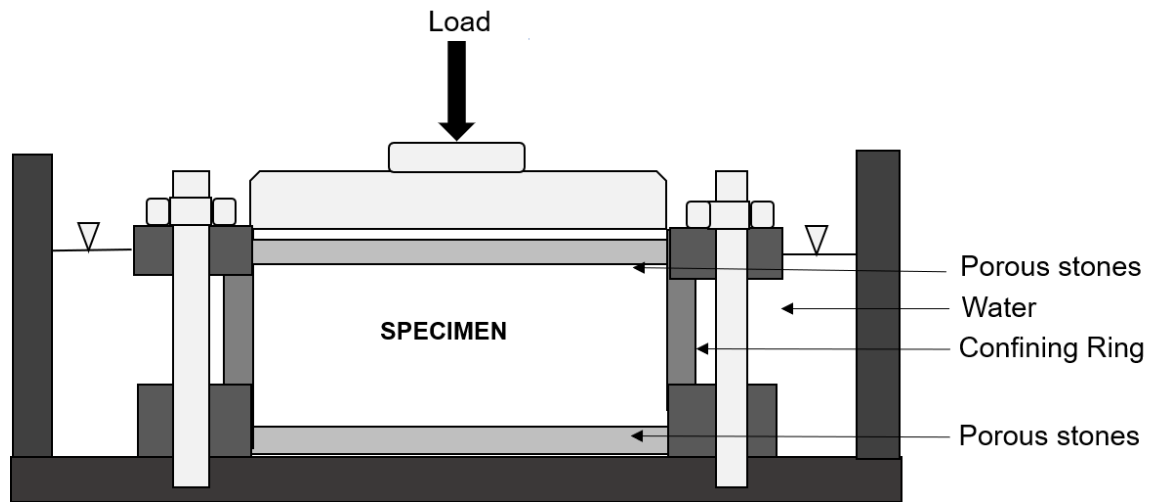


Figure 3: Typical setup of an oedometer cell

4.3.3. X-ray Computed Tomography

X-ray tomographies of the sample were performed with a Nikon XT H 320, see Figure 4 for details of the X-ray computed tomography setup. The scan was performed using 3141 projections during a single revolution at 125kV energy and 108 μ A current. The samples scanned were cylindrical samples cut out of consolidated or consolidated and sheared specimens with ~ 20 mm in diameter and the full sample height (after consolidation). The voxel size was $14.19 \times 14.19 \times 14.19 \mu\text{m}$. The samples were covered with Parafilm® to maintain a constant water content during the scan and the tomographies were reconstructed using Nikon metrology X-Tek software and visualised using Thermo Fisher Scientific Avizo software.

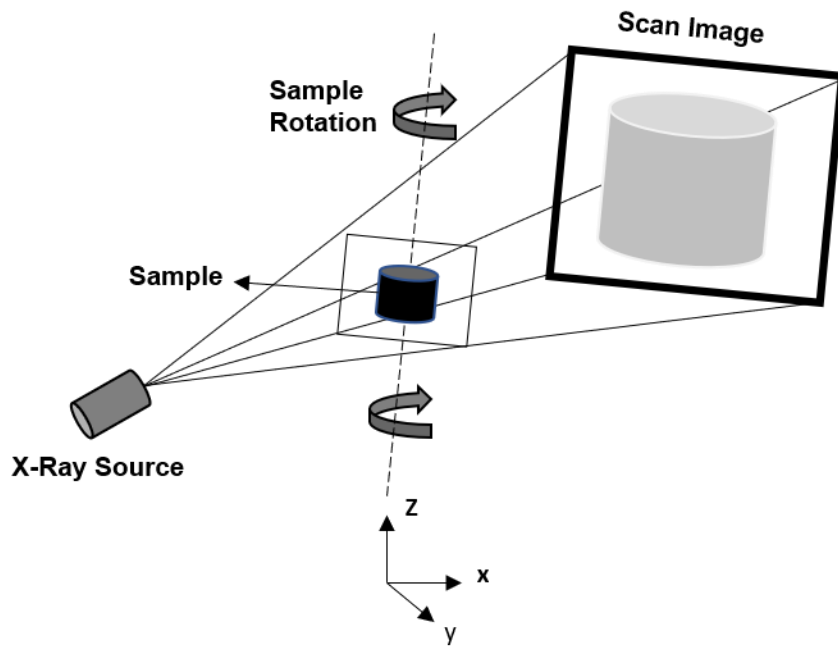
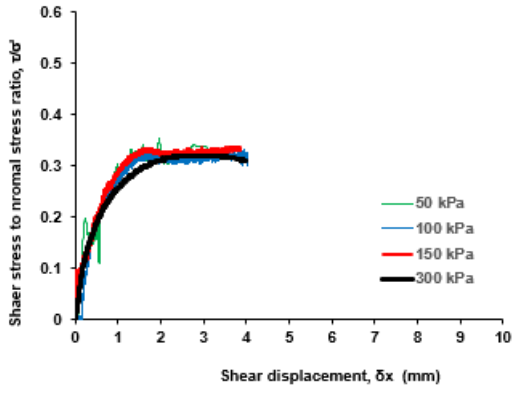


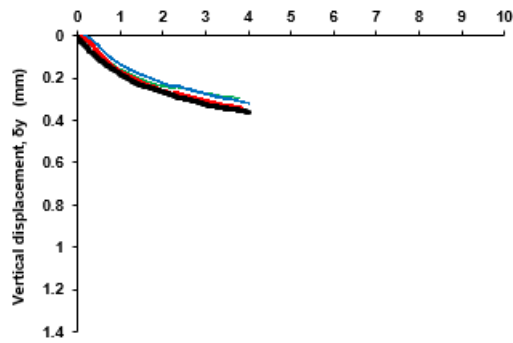
Figure 4: Typical X-ray computed tomography setup.

4.4. Results

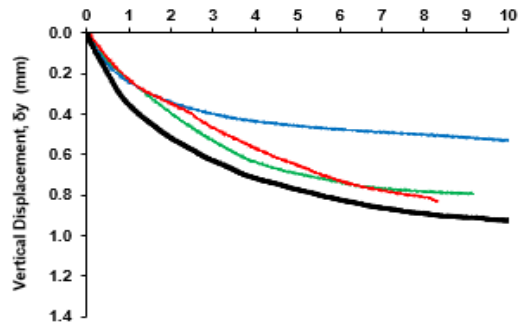
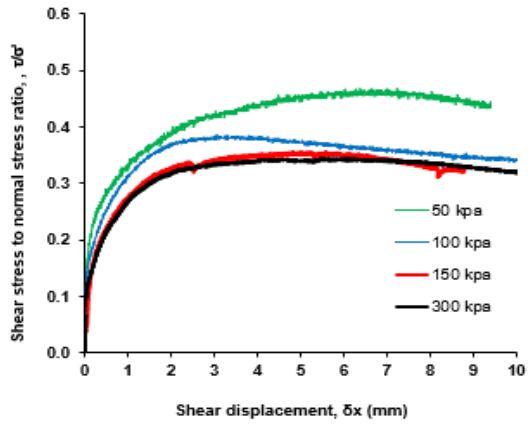
4.4.1. Shear strength behaviour of kaolin-mica composites



(a)



(b)



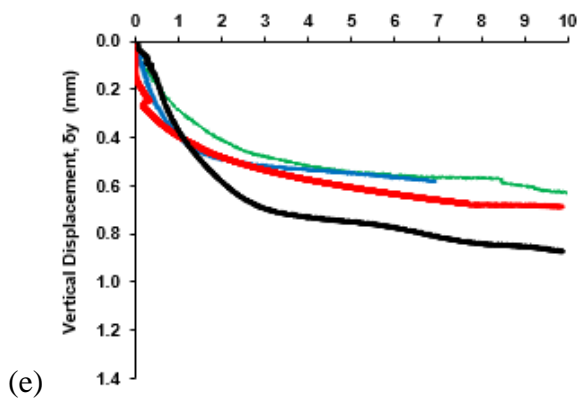
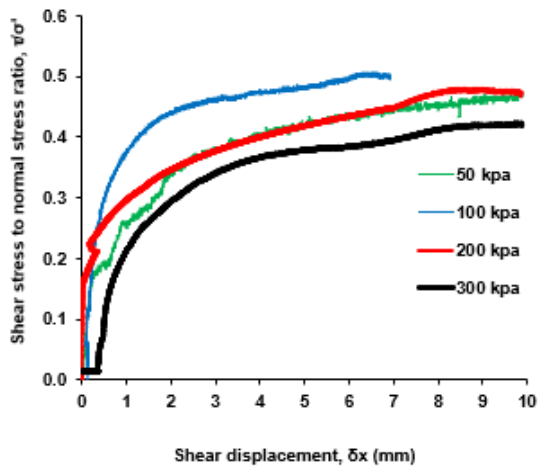
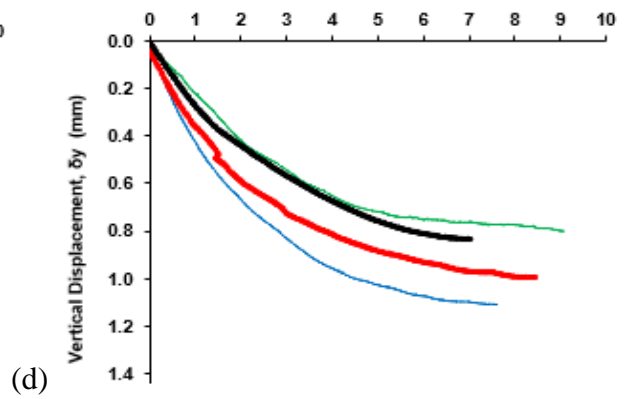
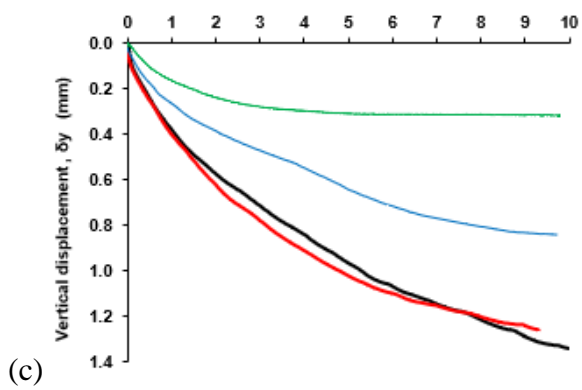
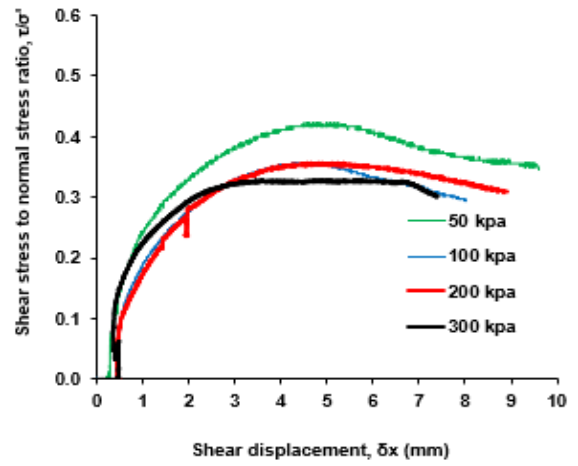
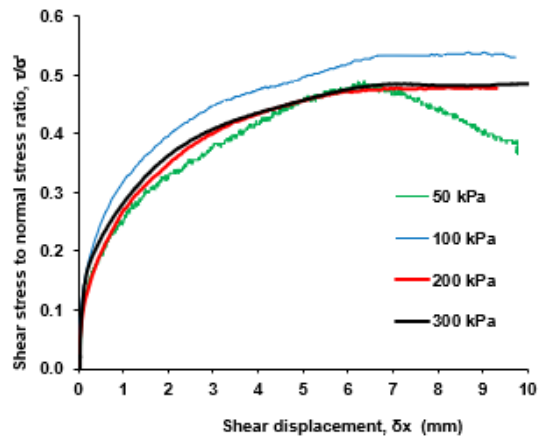
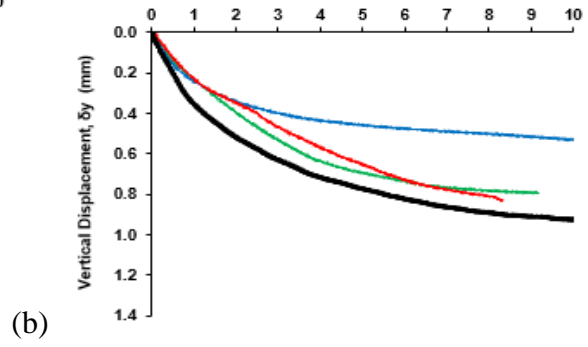
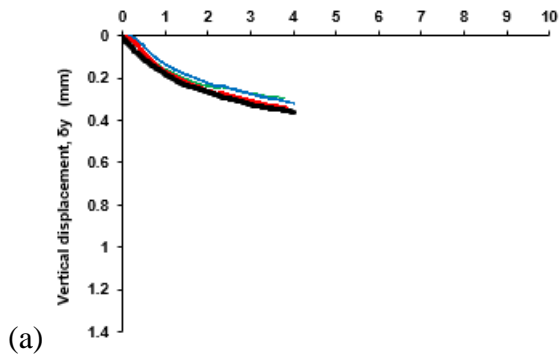
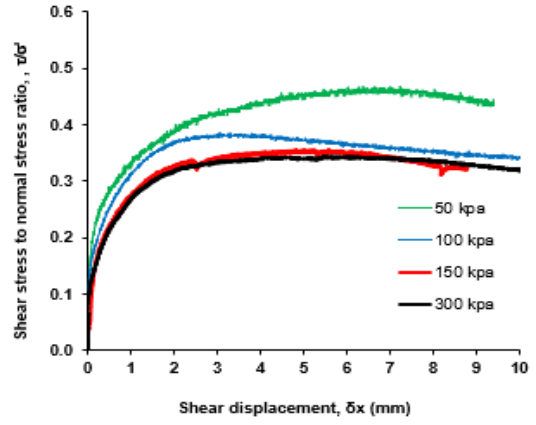
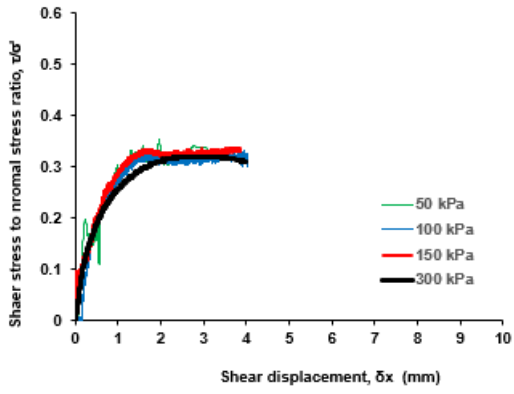


Figure 5 (a, b, c, d, e) shows the results of direct shear tests performed on 100% kaolin, 10% muscovite sand/kaolin composite, 100% muscovite silt, 10% muscovite silt/kaolin composite and 100% muscovite sand, respectively. The kaolin, 10% muscovite sand/kaolin composite and muscovite silt and muscovite sand all exhibit a monotonic increase in shear stress up to the ultimate value and a contractile volumetric behaviour. This is the typical behaviour for the composite. It is worth noting that for both the kaolin and muscovite, the curves, in terms of the shear displacement versus the ratio between shear stress τ and normal effective stress σ' , overlap. This indicates that the failure envelopes in the Mohr-Coulomb plane σ' - τ (Knappett. and Craig, 2012) for both the muscovite and the clay are linear and pass through the origin as shown in Figure 6. The experimental data for muscovite silt and muscovite sand lie almost perfectly along a linear failure envelope, with the exception of the data point associated with muscovite sand at 300 kPa vertical stress (see Figure 6). The angle of shearing resistance for both the muscovite silt and the muscovite sand was found to be $\phi'=25.8^\circ$ while the angle of shearing resistance for kaolin was found to be $\phi'=17.8^\circ$.



(a)

(b)

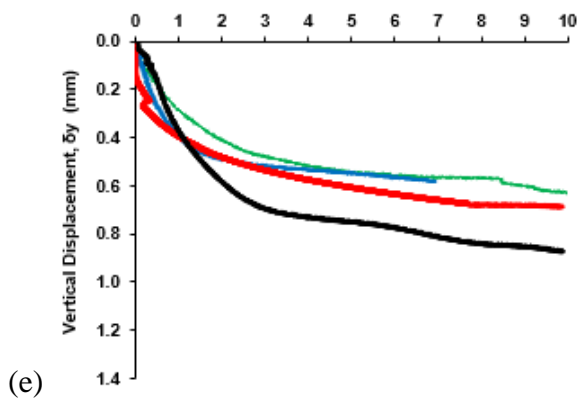
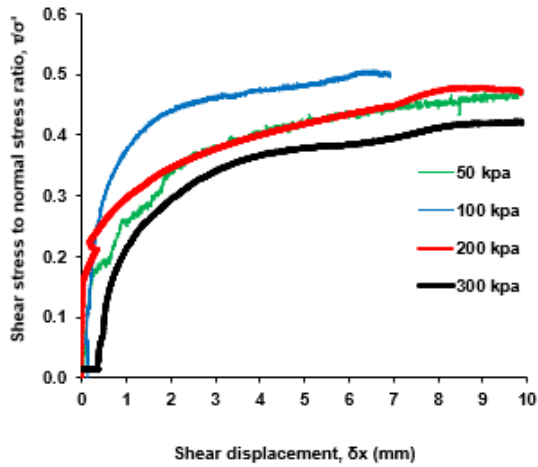
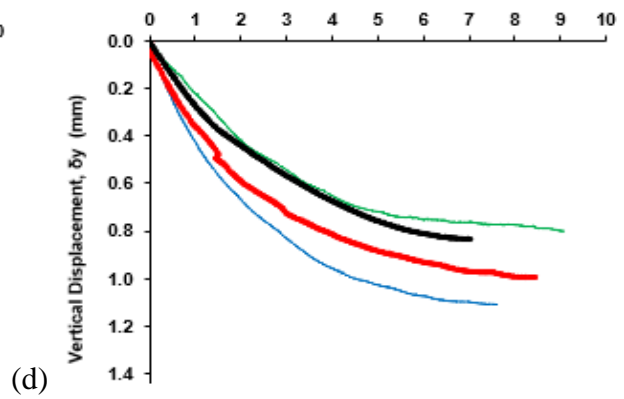
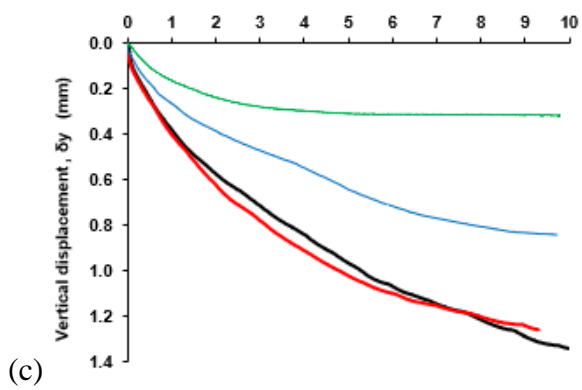
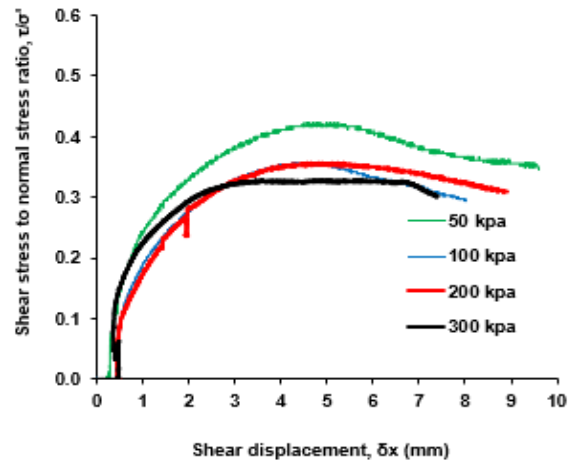
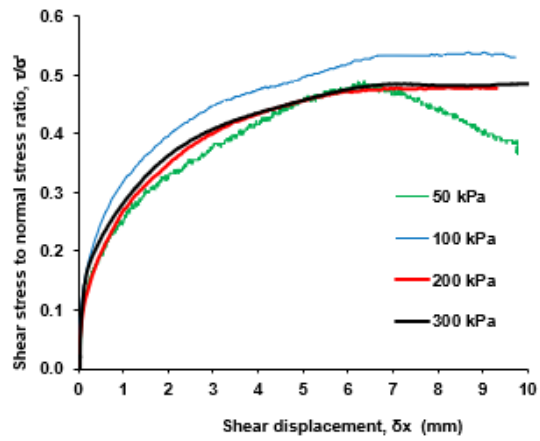


Figure 5. Results of direct shear tests in terms of i) shear stress to normal stress ratio versus shear displacement and (plotted at the top of each Figure) ii) vertical displacement versus shear displacement (plotted at the bottom of each Figure). (a) 100% kaolin (b) 10% muscovite sand kaolin composite (c) 100% muscovite silt (d) 10% muscovite silt kaolin composite (e) 100% muscovite sand

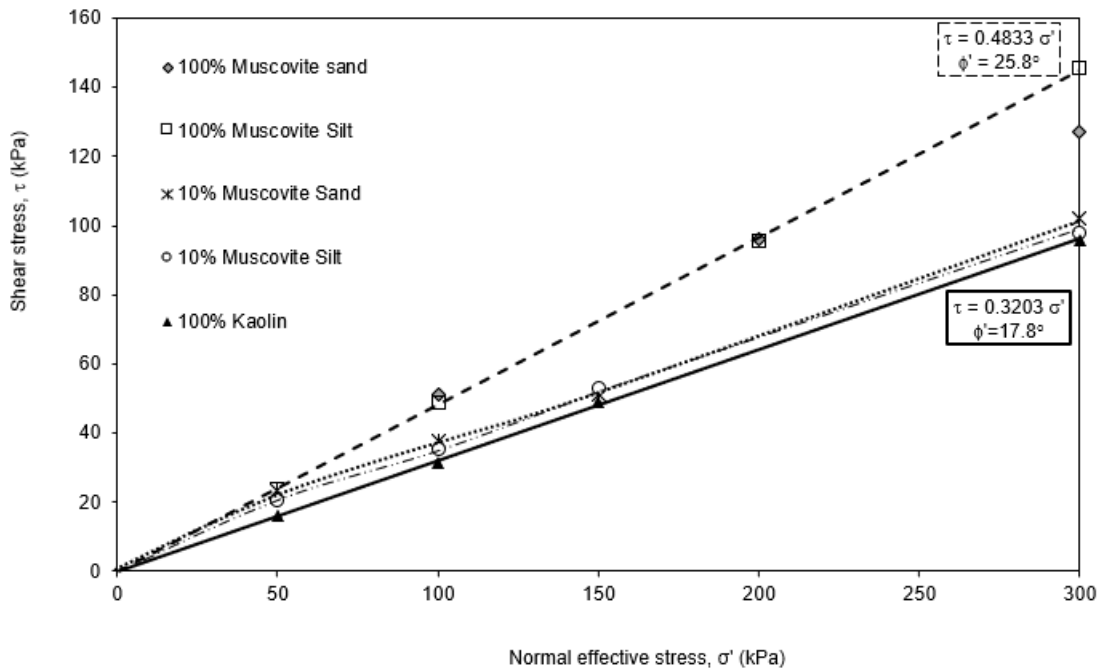


Figure 6. Failure envelope in terms of ultimate shear strength versus normal effective stress of muscovite silt, muscovite sand, kaolin and muscovite/kaolin composite.

To better appreciate the variations in shear strength with increasing normal effective stress, for the various muscovite/kaolin composites, Figure 7 shows the shear stress to normal effective stress ratio vs. the normal effective stress. As expected, the shear strength of the kaolin/ muscovite composites increases toward the value of the shear strength of the muscovite alone as the muscovite fraction increases. However, the most striking aspect of Figure 7 is that a relatively small fraction of muscovite (30%) is sufficient to shift the shear strength to the shear strength of the muscovite alone in the range of low effective normal stresses ($\sigma' \leq 50-100$ kPa). Further, even for smaller muscovite fractions (2.5% and 10%) there is still a significant increase in shear strength at low effective normal stresses. This effect vanishes as the normal effective stress increases ($\sigma' = 200-300$ kPa); at a normal effective stress of 300 kPa, the only

sample that still shows some increase in shear strength is the 30% fraction of sand sized muscovite (Figure 7b).

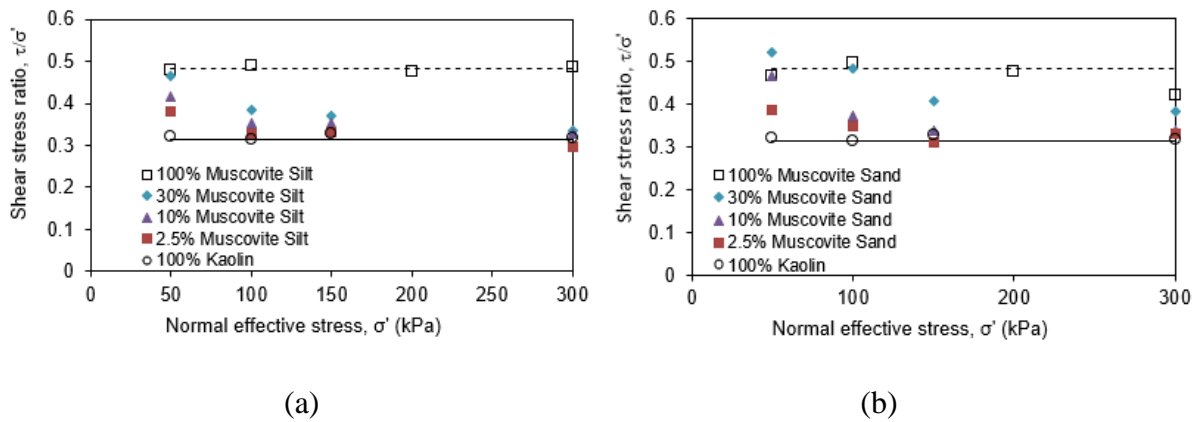


Figure 7. Shear stress to normal effective stress ratio versus normal effective stress. (a) muscovite silt-kaolin composite. (b) muscovite sand-kaolin composite

4.4.2. 1-D compression behaviour of kaolin-mica composites

Figure 8 shows the 1-D compression curves of the clay-muscovite-silt composites at varying proportions from 0% muscovite (100% kaolin) through 2.5%, 10, and 30% muscovite. The compression curves of the kaolin-muscovite silt composites essentially overlap with the compression curve of the kaolin alone, indicating that compression behaviour of the composites is dominated by the clay matrix regardless of the muscovite silt fraction (in the range 0-30%). The compression curve for the muscovite silt alone presents an inflection at around 20 kPa vertical stress before becoming linear beyond 200 kPa vertical stress. The normal compression line of the muscovite silt is clearly located above the normal compression line of the kaolinite, which further corroborates the finding that the compression behaviour of the kaolin-muscovite silt composites are dominated by the clay matrix.

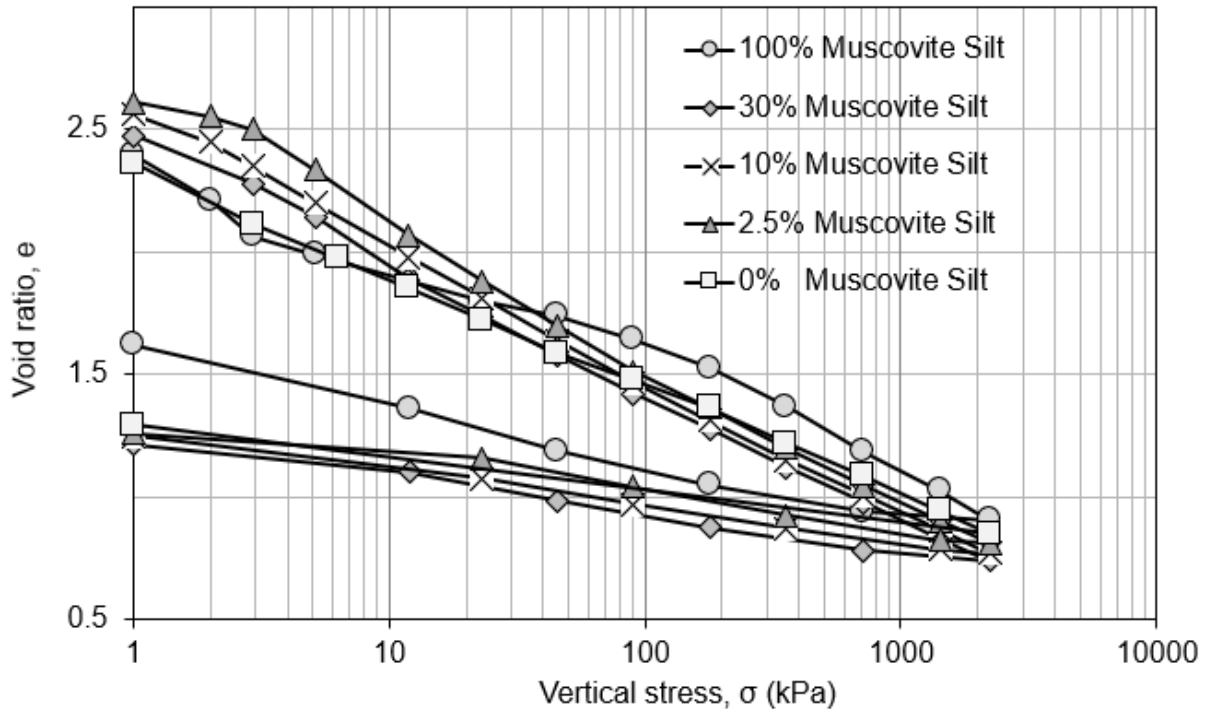


Figure 8. Oedometer compression curve of muscovite silt and kaolin composites

Figure 9 shows similar 1-D compression curves for the clay-muscovite-sand composites. Again, the compression curves of the kaolin-muscovite sand composites essentially overlap with the compression curve of the kaolin alone indicating that compression behaviour of the composites is dominated by the clay matrix.

The compression curve for the muscovite sand alone presents an abnormal initial void ratio. It is not clear whether this is due to an error in the computation of the void ratio change upon the first loading steps due to ‘wall effects’ at the interface between the top surface of the specimen and the loading cap (void ratio change would have been overestimated), or as a result of swelling occurring upon flooding of the oedometer cell (the water content of the initial slurry was the same for all the specimens tested). Unfortunately, the compression test of the muscovite sand alone could not be repeated. Table 2 shows the secant compression index of silt sized muscovite and sand sized muscovite composite obtained for vertical stress values between 100 and 2000 kPa.

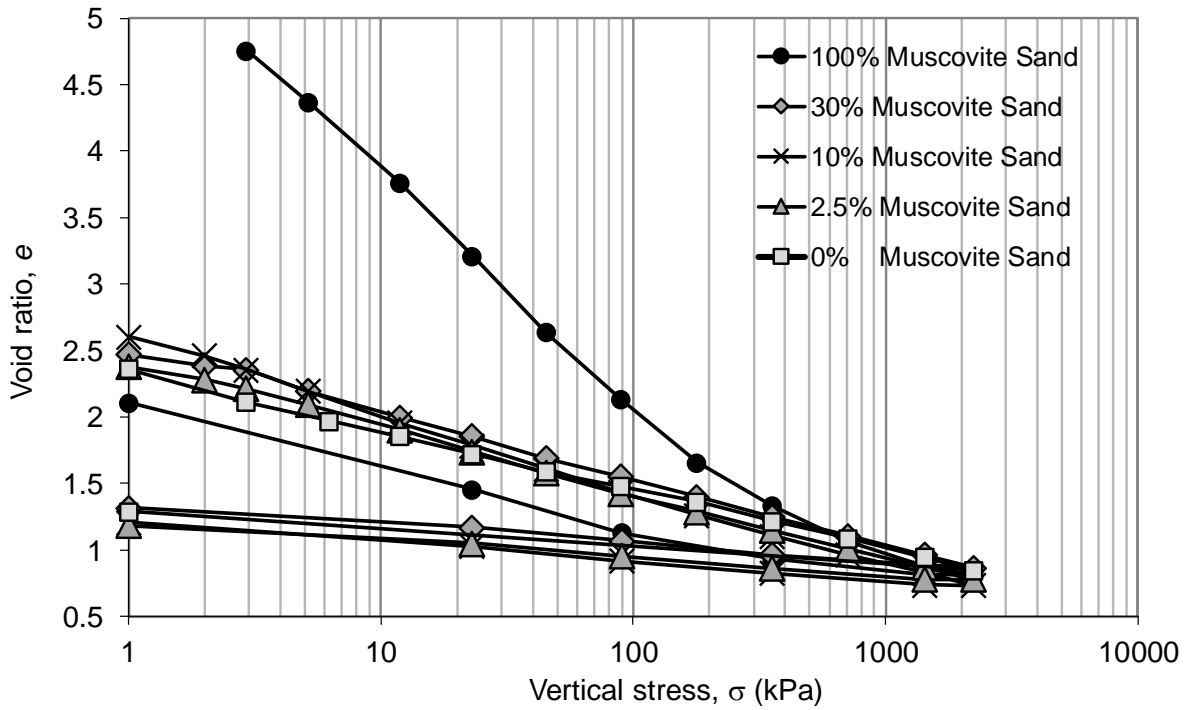


Figure 9. Oedometer compression curve of muscovite sand and kaolin mixture

Table 2: Compression index for sand sized muscovite and silt sized muscovite

	Silt sized muscovite Compression index	Sand sized muscovite Compression Index
0%		
(Kaolin)	0.19	0.19
2.50%	0.21	0.19
10%	0.21	0.21
30%	0.21	0.21
100%	0.22	0.40

It is worthy of note that in this study the Atterberg limits for kaolin alone and not the composite mixtures were measured. In addition, the pH of all composites, shear strength, and oedometer

compression were also measured. I was particularly interested in the shear strength, compressibility, and hydraulic conductivity of the samples in this chapter to enable me to understand the mechanical strength and hydraulic characteristics of the samples. The Atterberg limit is not an intrinsic property of the soil as it changes with the chemistry of the pore water Pedrotti (2016). The samples were prepared at the same moisture content i.e. at 1.5% liquid limit of kaolin and not at 1.5% liquid limit of the respective soil mixture. This was to avoid having different initial moisture contents and hence differences in the initial soil void ratio. In addition, the kaolin exerted significant control on the pH of the composites, as shown in Table 3.

Table 3: pH of kaolin and kaolin mica composites after mixture.

Composite	pH
70% Kaolin/30% Sand sized Muscovite	4.5
90% Kaolin/10% Sand sized Muscovite	4.4
97.5 Kaolin/2.5% Sand sized Muscovite	4.2
70% Kaolin/30% Silt sized Muscovite	4.6
90% Kaolin/10% Silt sized Muscovite	4.5
97.5 Kaolin/2.5% Silt sized Muscovite	4.3
100% Kaolin	4.1

There was no evidence of muscovite particle crushing in either the sand sized muscovite or silt sized muscovite; Figure 10 shows there was no change in the laser diffraction particle size analysis of the specimens before and after compression. It is not surprising that there is no grain crushing after consolidating the mica sample up to 2200 kpa, this implies that the mica is a soil with relatively high elasticity.

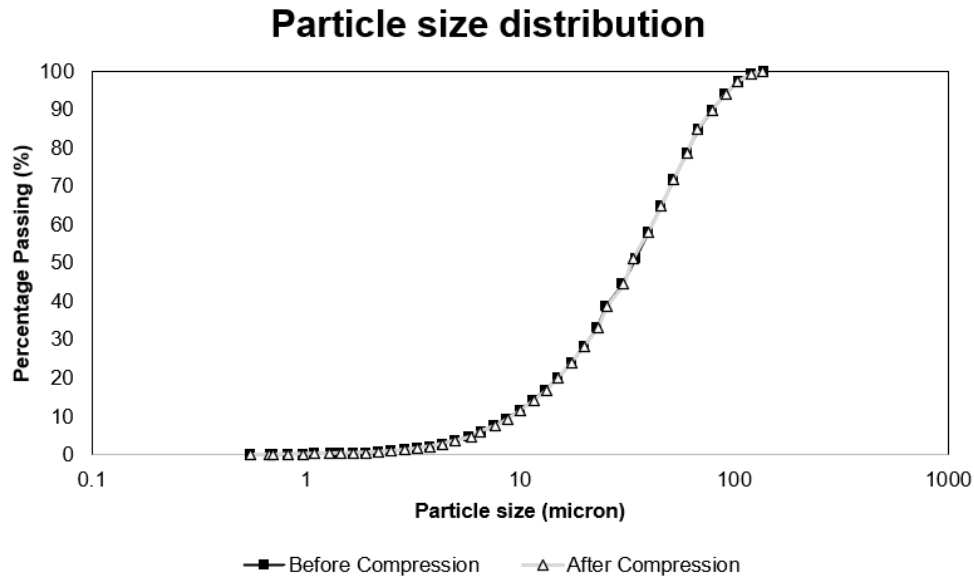
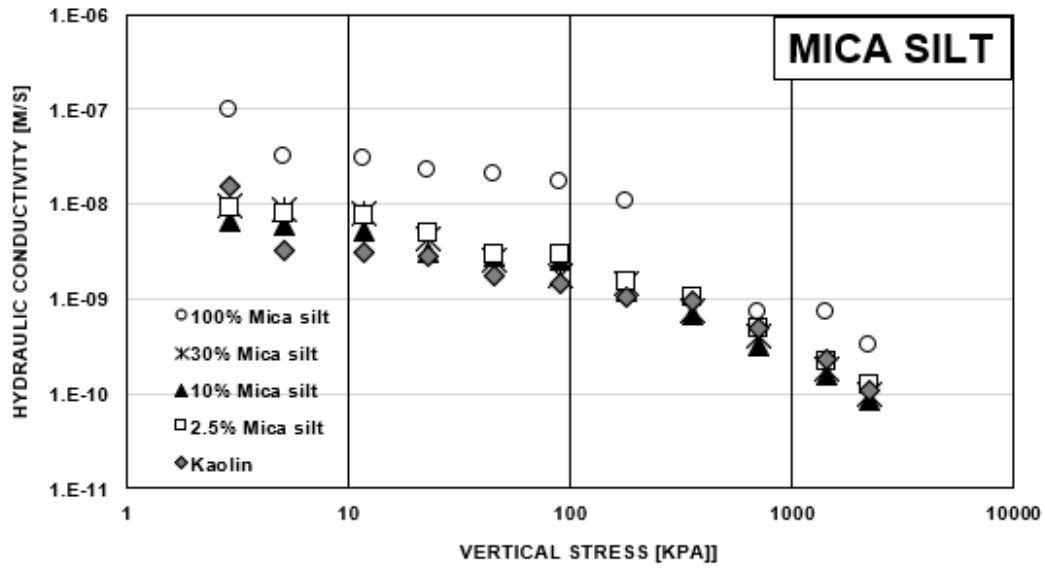


Figure 10: Mica particle size distribution before and after compression

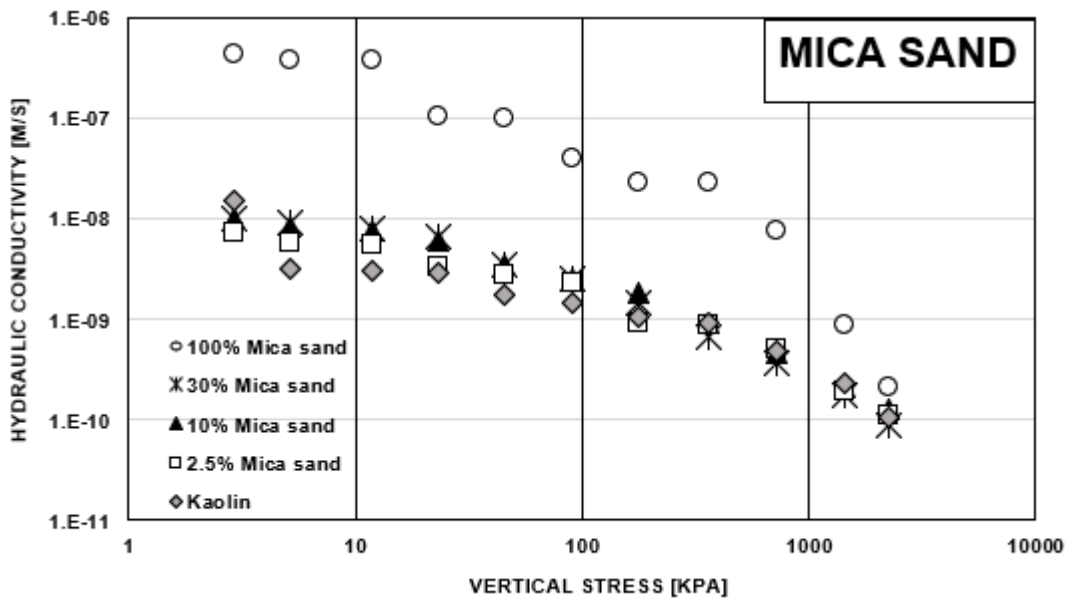
4.4.3. Hydraulic conductivity of kaolin-muscovite composites

The hydraulic conductivity of the kaolin-muscovite composites was derived from the consolidation response upon individual loading steps based on Terzaghi's theory of one-dimensional consolidation (Knappett and Craig, 2012) (Appendix II). As shown by (Martini et al., 2020), the values of hydraulic conductivity inferred from the consolidation data are consistent with the values measured experimentally via standard constant head/falling head hydraulic conductivity tests.

Hydraulic conductivity is plotted against vertical stress for both the muscovite silt composites and the muscovite sand composites in Figure 11. As expected, the hydraulic conductivity decreases as the vertical stress increases and, hence, the void ratio decreases (Figures 11a and 11b). The percentage of mica added (2.5% - 30%) does not significantly affect the hydraulic conductivity of the composite material compared to the clay. Therefore, up to 30% mica, the hydraulic conductivity remains controlled by the finer fraction.



(a)



(b)

Figure 11. Hydraulic conductivity versus vertical stress. (a) kaolin-muscovite silt composites. (b) kaolin-muscovite sand composites.

4.4.4. X-ray CT slices of consolidated and sheared samples

Figures 12a, b show X-ray CT slices of two samples of the sand sized mica mixed with kaolin (30 percent sand sized muscovite) after consolidation to 50 kPa and 300 kPa vertical effective stress respectively. Sand sized muscovite particles appear to be randomly oriented in

both samples, which is a reflection of the process of hand mixing of the composite material in its slurry state.

Figures 12c and d show the same specimens after shearing. The dashed line represents the position of the joint between the bottom and top halves of the shear box. Figure 12c (the sample sheared after compression to 50 kPa) shows preferential orientation of mica particles in the shearing zone whereas Figure 12d (the sample sheared after consolidation to 300 kPa) shows that mica particles remained randomly oriented in the shearing zone.

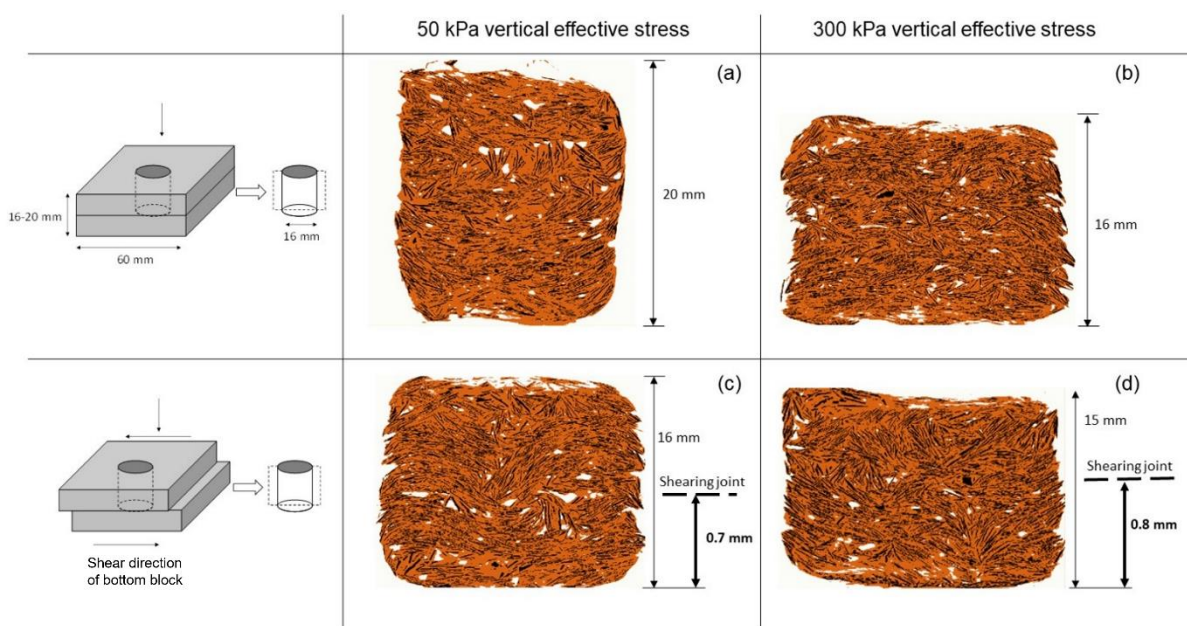


Figure 12: X-ray CT slices of (a) sand sized muscovite (30%) and kaolin (70%) consolidated to 50 kPa (b) sand sized muscovite (30%) and kaolin (70%) consolidated to 300 kPa (c) mica (30%) sand and kaolin (70%) consolidated to 50 kPa and sheared (d) sand sized muscovite and kaolin consolidated to 300 kPa and sheared. The black grains are sand sized muscovite, and the orange grains are kaolin, while the white section is water.

4.5. Discussion

The results from the oedometer tests, in terms of compressibility and hydraulic conductivity of the muscovite/kaolin composites show that behaviour in compression remains dominated by the clay matrix. It was not unexpected that a muscovite fraction up to 30% is not large enough to modify the compressional behaviour, which remains dominated by the clay

matrix. Similarly, for the hydraulic conductivity behaviour, mica particles ‘float’ within the clay matrix and this results in no significant hydraulic conductivity change of the composites (for up to 30% mica) compared to the value for mica alone.

By contrast, the shear strength data are not intuitive and, at the same time, have significant practical relevance. The range of low normal effective stresses where a relatively small fraction of muscovite generates a significant increase in shear strength ($\sigma' \leq 50-100$ kPa) are representative of the range of stresses developing in earth structures such as flood and roadway embankments and in the backfill of retaining structures. As a result, the addition of only 10-30% of muscovite silt or sand to the clay, can significantly enhance the mechanical response of such geostructures.

At a more fundamental level, it is surprising that a relatively small fraction of muscovite can shift the shear strength of kaolin-muscovite mixtures to values close to the ones of the muscovite alone at low normal effective stress. As the compression behaviour of the composite is dominated by the clay matrix, regardless of the muscovite fraction (in the range 0-30%), one would have expected the shear strength to be also dominated by the clay matrix. This is the case at relatively high normal effective stresses ($\sigma' > 100$ kPa) but not at low stresses ($\sigma' \leq 50-100$ kPa).

The kaolinite and the silt/sand mica alone exhibit ultimate shear strength that does not depend on the normal effective stress σ' (Fig. 7a and b). At ultimate (critical) state, it can be assumed that particles in the shearing zone are subjected to ‘turbulent’ mixing (Wood, 2014) and that the ‘macroscopic’ angle of shearing resistance depends on the degree of interlocking that is resisting the sliding and rolling over of particles.

For the case of sand sized muscovite and silt, the interlocking would be greater due to the angularity of mica particles and the nature of the inter-particle contacts. As shown by the X-CT scan in Figure 13, mica particles have a rough surface. This increases the degree of

interlocking at the critical state and, hence, increases the ‘macroscopic’ angle of shearing resistance. This is consistent with the findings of (Cho et al., 2006) who have shown that particle angularity plays a key role in determining the critical state angle of shearing resistance. Experimental data have shown that the angle of shearing resistance of uniform sand can span over a very wide range depending on particle angularity, from 40° in the case of very angular sand particles to 20° for perfectly rounded particles (glass beads) (Alshibli & Cil, 2018). At the same time, the frictional resistance at the inter-particle contact is relatively high being controlled by mechanical interactions (Figure 14a).

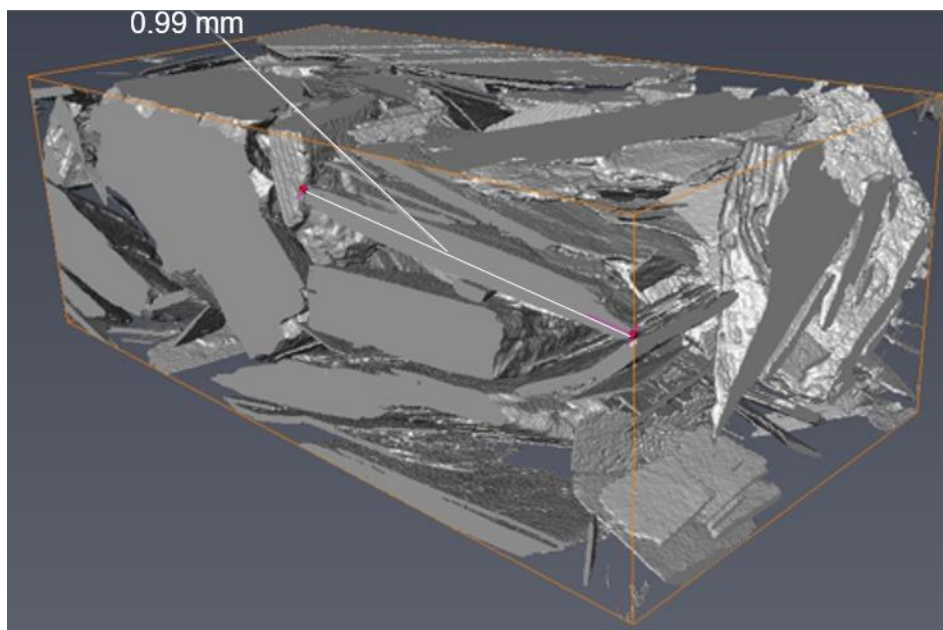


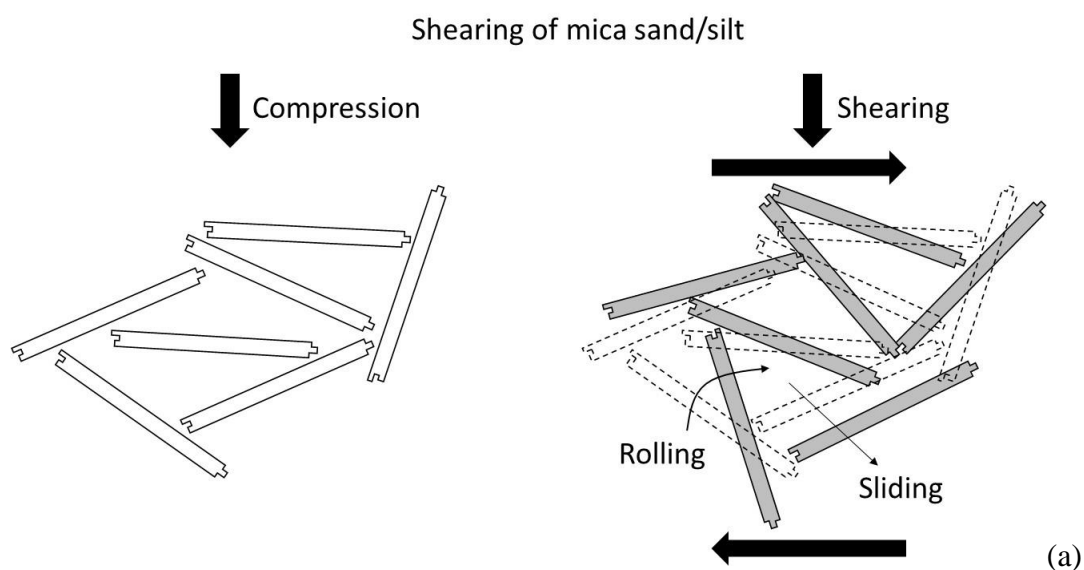
Figure 13 – X-CT image of sand sized muscovite

For the case of kaolinite, it may be that the particles are less angular and, most importantly, the normal stress at the inter-particle contact is diminished by the Coulombian repulsion occurring between the negatively charged particles. This would decrease the inter-particle frictional resistance facilitating particle sliding and rolling eventually leading to a lower macroscopic angle of shearing resistance (Figure 14b).

For the composite material, it is instructive to observe the orientation of the sand mica particles in the shearing zone. At low stress, mica particles highlight a pattern that resembles

ductile shearing in geologically stratified layers, which are first folded and then broken by tectonic forces (Fig. 15a, c). The mica particles contribute to form ‘reinforced’ layers and the shearing process involves a fold-like mechanism rather than a particle-to-particle rolling and sliding. This could explain why the measured friction angle in sand sized muscovite composite at low stresses was observed to be even higher than sand sized muscovite alone (Fig. 7b). It is worth noting that the folding mechanism is a reinforcement mechanism and not a peak strength mechanism since it does not continue at high strain.

At high vertical stress, the mica particles appear to preserve the same random orientation observed after compression (Fig. 15b). It can be speculated that the high vertical stress promotes the development of force chains mainly in the clay matrix and, hence, composite layers do not form upon macroscopic shearing. In this case, the shear band likely forms in the clay matrix (Fig. 15d) and this explains why the measured friction angle at high stresses in the sand sized muscovite composite is observed to be close to the value measured in the kaolinite alone (Fig. 7b).



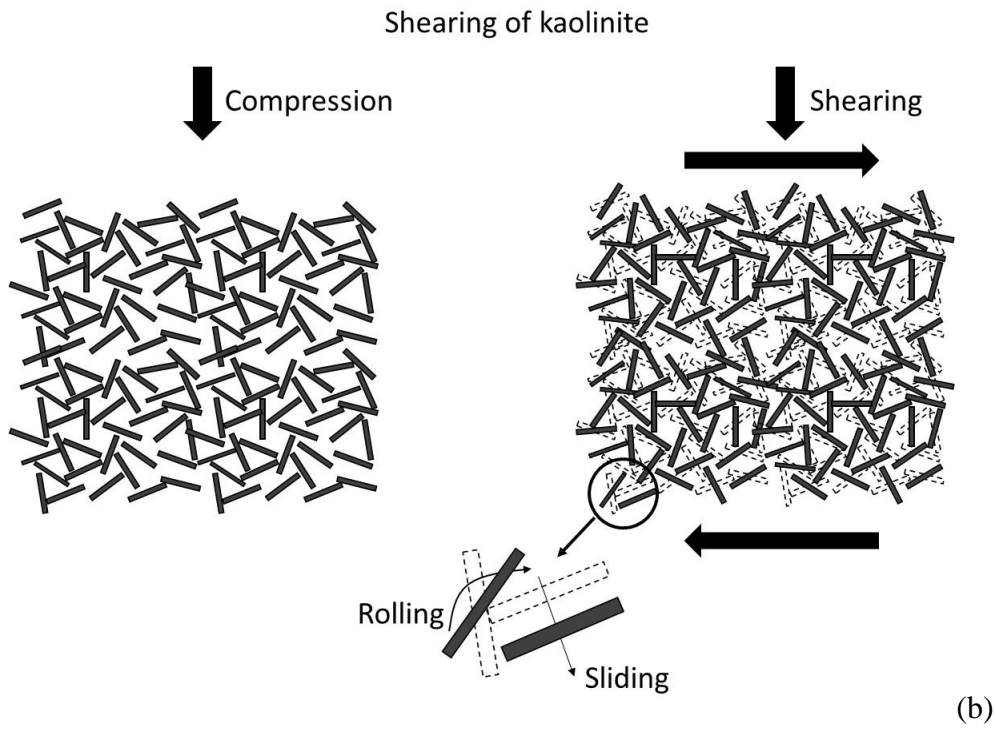


Figure 14. Conceptual model for response in shear of (a) sand/silt sized muscovite; (b) kaolinite

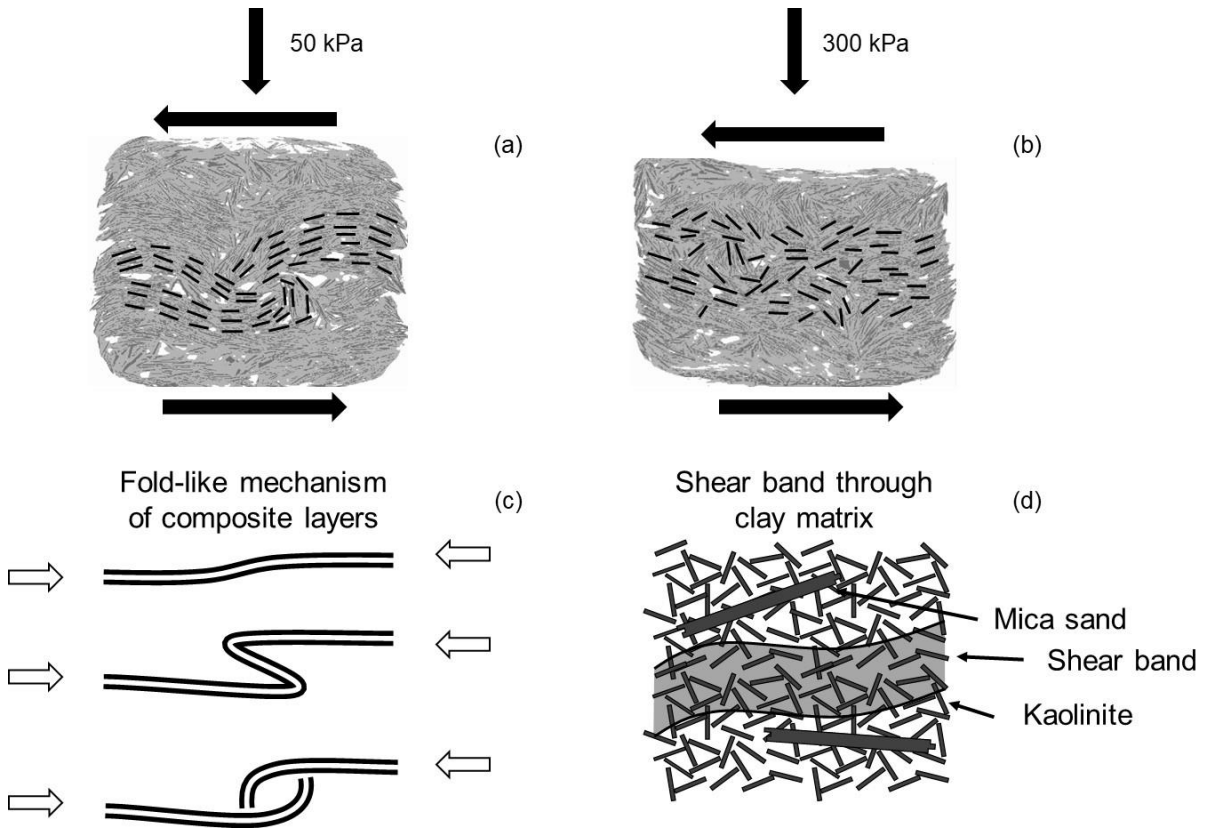


Figure 15. Response in shear of sand sized muscovite/silt and kaolinite composites. (a) preferential orientation of sand sized muscovite particles in the shearing zone at 50 kPa vertical stress. (b) random orientation of sand sized muscovite particles in the shearing zone at 300 kPa vertical stress. (c) Conceptual model for response in shear at low vertical stress. (d) Conceptual model for response in shear at high vertical stress

4.6. 4.6. Conclusions

This paper has evaluated the compressibility, hydraulic conductivity, and shear strength characteristics of muscovite and kaolin composites for their use in low stress geotechnical regimes such as structural fills. Muscovite-kaolin composites were prepared with muscovite contents of 0, 2.5, 10, and 30 wt. %. It was observed that:

- i) by adding both muscovite silt or muscovite sand to kaolin for all the weight percent of muscovite kaolin mixtures tested, compressibility does not change. Up to 30% muscovite sand or muscovite silt, the compressive behaviour is still clay-dominated.
- ii) The addition of muscovite mica (up to 30%) to kaolin does not significantly affect its hydraulic conductivity. Hence a gain in shear strength does not compromise the hydraulic conductivity or compressibility of clay.
- iii) The shear strength characteristics of kaolin are significantly enhanced by the addition of only 2.5-30% of muscovite silt or sand in the low stress regime typical of earth structures such as flood and roadway embankments and retaining structure backfill. Hence, whilst adding up to 30% mica to clay makes no significant difference to the hydraulic conductivity, it does improve the shear strength at low normal stresses.

These findings show that by-product mica could significantly enhance the mechanical properties of marginal clays in low-stress, large-volume building applications such as structural fill. Considering the high cost and carbon footprint (Sargent et al., 2016) of current systems, such as lime, bitumen, cement and fly ash (Coudert et al., 2019; Liebenberg & Visser, 2003; Obuzor et al., 2011; Phummiphan et al., 2016), the addition of by-product mica as an alternative material for mechanical property enhancement in clays could reduce both the cost and

environmental impacts of such applications. Mica-enhanced clay fills could also provide a low-cost, low-energy solution for the bulk of mica-based mine wastes, removing the current requirement for their active management and reducing their impact on the surrounding environment.

4.7. References

- Alshibli, K. A. and Cil, M. B. (2018) ‘Influence of Particle Morphology on the Friction and Dilatancy of Sand’, *Journal of Geotechnical and Geoenvironmental Engineering*, 144(3), p. 04017118. doi: 10.1061/(asce)gt.1943-5606.0001841.
- Ameri, M. and Behnood, A. (2012) ‘Laboratory studies to investigate the properties of CIR mixes containing steel slag as a substitute for virgin aggregates’, *Construction and Building Materials*, 26(1), pp. 475–480. doi: 10.1016/j.conbuildmat.2011.06.047.
- Basak, B. B. (2019) ‘Waste Mica as Alternative Source of Plant-Available Potassium: Evaluation of Agronomic Potential Through Chemical and Biological Methods’, *Natural Resources Research*, 28(3), pp. 953–965. doi: 10.1007/s11053-018-9430-3.
- BS-CODE, 1377-5 (1990) ‘Methods of test for soils for civil engineering purposes. Compressibility, permeability and durability tests’, 3(1).
- BS-CODE, 1377-7 (1990) ‘Methods of test for soils for civil engineering purposes. Shear strength tests (total stress)’, 3(1).
- Burland, J. B. (1990) ‘On the compressibility and shear strength of natural clays’, *Geotechnique*, 40(3), pp. 329–378. doi: 10.1680/geot.1990.40.3.329.
- Cho, G.-C., Dodds, J. and Santamarina, J. C. (2006) ‘Particle Shape Effects on Packing Density, Stiffness, and Strength: Natural and Crushed Sands’, *Journal of Geotechnical and Geoenvironmental Engineering*, 132(5), pp. 591–602. doi: 10.1061/(asce)1090-0241(2006)132:5(591).

- Choi, S.G., Chang, I., Lee, M., Lee, J.H., Han, J.T. and Kwon, T.H., 2020. Review on geotechnical engineering properties of sands treated by microbially induced calcium carbonate precipitation (MICP) and biopolymers. *Construction and Building Materials*, 246, p.118415.. doi: 10.1016/j.conbuildmat.2020.118415.
- Cook, J. R. and Gourley, C. S. (2002) ‘A Framework for the Appropriate Use of Marginal Materials J R Cook C S Gourley’, UK, TRL Ltd, 1, pp. 1–19.
- Coudert, E., Paris, M., Deneele, D., Russo, G. and Tarantino, A., (2019). Use of alkali activated high-calcium fly ash binder for kaolin clay soil stabilisation: Physicochemical evolution. *Construction and Building Materials*, 201, pp.539-552. doi: 10.1016/j.conbuildmat.2018.12.188.
- Galvani, A. (2003) ‘Resistenza a taglio di un argilla non satura ricostituita in laboratorio’, M.Eng., University of Trento.
- Kalinowska-Wichrowska, K., Pawluczuk, E. and Bołtryk, M. (2020) ‘Waste-free technology for recycling concrete rubble’, *Construction and Building Materials*, 234, p. 117407. doi: 10.1016/j.conbuildmat.2019.117407.
- Kibert, C. J. (2001) ‘Policy Instruments for Sustainable Built Environment’, *Journal of Land Use & Environmental Law*, 17. Available at: <https://heinonline.org/HOL/Page?handle=hein.journals/jluenv117&id=385&div=&collection=>.
- Knappett, J & Craig R. F. (2012) *Craig’s Soil Mechanics*. 8th ed. CRC press.
- Liebenberg, J. J. E. and Visser, A. T. (2003) ‘Stabilization and Structural Design of Marginal Materials for Use in Low-Volume Roads’, *Transportation Research Record*, II(1819), pp. 166–172. doi: 10.3141/1819b-21.
- Low, N. L. P. (1980) ‘Formation and properties of glass-mica composite materials’, *Ceramurgia International*, 6(3), pp. 85–90. doi: 10.1016/0390-5519(80)90018-6.

- Mallik, A. (2020) 'Physico-mechanical behaviour of alkali and alkaline earth metal-containing mica glass-ceramics: a comparative evaluation', *Journal of the Korean Ceramic Society*, 57(5), pp. 520–529. doi: 10.1007/s43207-020-00054-9.
- Martini, M., Tarantino, A. and Sloan, A. (2020) 'Suction drain as a low carbon ground improvement technique: Proof-of-concept at the laboratory scale', *Tunnelling and Underground Space Technology*, 99(January), p. 103361. doi: 10.1016/j.tust.2020.103361.
- Moreno, F., Rubio, M. C. and Martinez-Echevarria, M. J. (2012) 'The mechanical performance of dry-process crumb rubber modified hot bituminous mixes: The influence of digestion time and crumb rubber percentage', *Construction and Building Materials*, 26(1), pp. 466–474. doi: 10.1016/j.conbuildmat.2011.06.046.
- Nosrati, A., Addai-Mensah, J. and Skinner, W. (2009) 'pH-mediated interfacial chemistry and particle interactions in aqueous muscovite dispersions', *Chemical Engineering Journal*, 152(2–3), pp. 406–414. doi: 10.1016/j.cej.2009.05.001.
- Obuzor, G. N., Kinuthia, J. M. and Robinson, R. B. (2011) 'Utilisation of lime activated GGBS to reduce the deleterious effect of flooding on stabilised road structural materials: A laboratory simulation', *Engineering Geology*, 122(3–4), pp. 334–338. doi: 10.1016/j.enggeo.2011.06.010.
- Pacheco-Torgal, F., Castro-Gomes, J. and Jalali, S. (2009) 'Tungsten mine waste geopolymeric binder: Preliminary hydration products investigations', *Construction and Building Materials*, 23(1), pp. 200–209. doi: 10.1016/j.conbuildmat.2008.01.003.
- Palumbo-Roe, B., Colman, T., Cameron, D.G., Linley, K. and Gunn, A.G. (2014) 'The nature of waste associated with closed mines in England and Wales', p. 82. Available at: <http://nora.nerc.ac.uk/id/eprint/10083/>.

- Phummiphan, I., Horpibulsuk, S., Sukmak, P., Chinkulkijniwat, A., Arulrajah, A. and Shen, S.L. (2016) 'Stabilisation of marginal lateritic soil using high calcium fly ash-based geopolymer', *Road Materials and Pavement Design*, 17(4), pp. 877–891. doi: 10.1080/14680629.2015.1132632.
- Sargent, P., Hughes, P. N. and Rouainia, M. (2016) 'A new low carbon cementitious binder for stabilising weak ground conditions through deep soil mixing', *Soils and Foundations*, 56(6), pp. 1021–1034. doi: 10.1016/j.sandf.2016.11.007.
- Shishelova, T. and Zhitov, V. (2018) 'Radiation-resistant materials based on mica in the construction industry', *MATEC Web of Conferences*, 212, pp. 1–6. doi: 10.1051/mateconf/201821201012.
- Soleimanbeigi, A. and Edil, T. B. (2015) 'Compressibility of Recycled Materials for Use As Highway Embankment Fill', *Journal of Geotechnical and Geoenvironmental Engineering*, 141(5), p. 04015011. doi: 10.1061/(asce)gt.1943-5606.0001285.
- Wong, C., Pedrotti, M., El Mountassir, G. and Lunn, R.J. (2018) 'A study on the mechanical interaction between soil and colloidal silica gel for ground improvement', *Engineering Geology*, 243(June), pp. 84–100. doi: 10.1016/j.enggeo.2018.06.011.
- Wood, D. M. (2014) *Soil behaviour and critical state soil mechanics*, *Soil Behaviour and Critical State Soil Mechanics*. Cambridge University Press. doi: 10.1017/CBO9781139878272.
- Zografou, A., Heath, A. and Walker, P. (2014) 'China clay waste as aggregate in alkali-activated cement mortars', *Proceedings of the Institution of Civil Engineers - Construction Materials*, 167(6), pp. 312–322. doi: 10.1680/coma.13.00037.

4.8. Appendix I – Determination of void ratio change in oedometer compression.

Upon each loading and unloading step, specimens are allowed to complete primary consolidation. The completion of primary consolidation can be detected only when the secondary consolidation branch of the settlement versus time curve becomes clearly visible. As a result, the change in void ratio accumulated upon a loading or unloading step includes these two components. As shown in Figure 16, the primary consolidation is associated with an increase in effective stress whereas the secondary consolidation occurs at constant effective stress. The secondary consolidation at constant effective stress represents a change in void ratio that should have occurred in the subsequent loading step and should therefore be attributed to the subsequent loading step as shown in Fig. 16.

In other words, the change in void ratio Δe_i upon the i -th step associated with an increase in the effective stress $\Delta \sigma_i$, is given by

$$\Delta e_i = \Delta e_{i,primary} + \Delta e_{i-1,secondary} \quad [1]$$

where $\Delta e_{i,primary}$ is the void ratio change associated with the primary consolidation of the step i and $\Delta e_{i-1,secondary}$ is the void ratio change associated with the secondary consolidation of the previous step $i-1$.

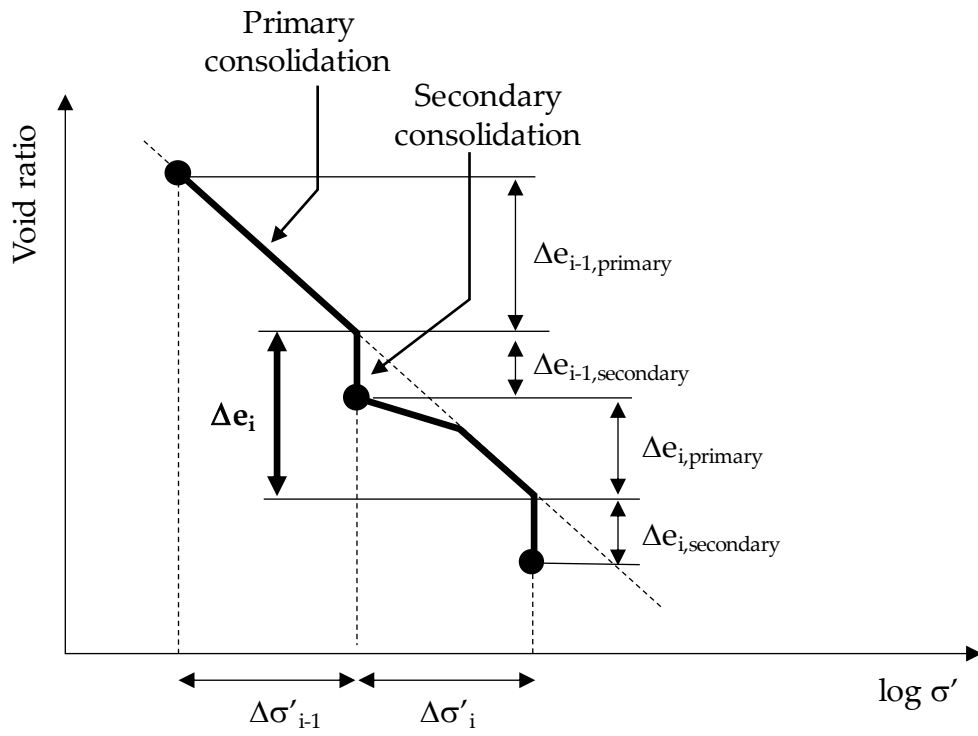


Figure 16. Computation of void ratio change Δe upon associated with an increment in effective stress $\Delta \sigma'$.

4.9. Appendix II – Determination of hydraulic conductivity from oedometer consolidation test

The hydraulic conductivity was determined as follows: The consolidation curve of each loading step was plotted, and the primary and secondary consolidation settlements were identified as shown in Fig. 17. The time t_{50} corresponding to 50% primary consolidation was then identified as shown in Figure 17 and the consolidation coefficient C_v computes as follows:

$$C_v = \frac{0.197 h^2}{t_{50}} \quad [2]$$

where 0.197 is the theoretical time factor corresponding to 50% consolidation and h is the drainage length (a standard oedometer consolidating test has double drainage and, as such, the specimen height is equal to $2h$).

The 1-D secant modulus E_{1D} was the calculated as

$$E_{1D} = \frac{\Delta\sigma_i}{\varepsilon_i} \quad [3]$$

where ε_i is the strain accumulated in the i -th loading step in turn given by:

$$\varepsilon_i = \frac{\Delta e_i}{1 + e_{0,i}} \quad [4]$$

where Δe_i and $e_{0,i}$ are the change in void ratio and the initial void ratio respectively in the i -th step. Finally, the hydraulic conductivity k was calculated as follows:

$$k = \frac{C_v \gamma_w}{E_{1D}} \quad [5]$$

where γ_w is the unit weight of water.

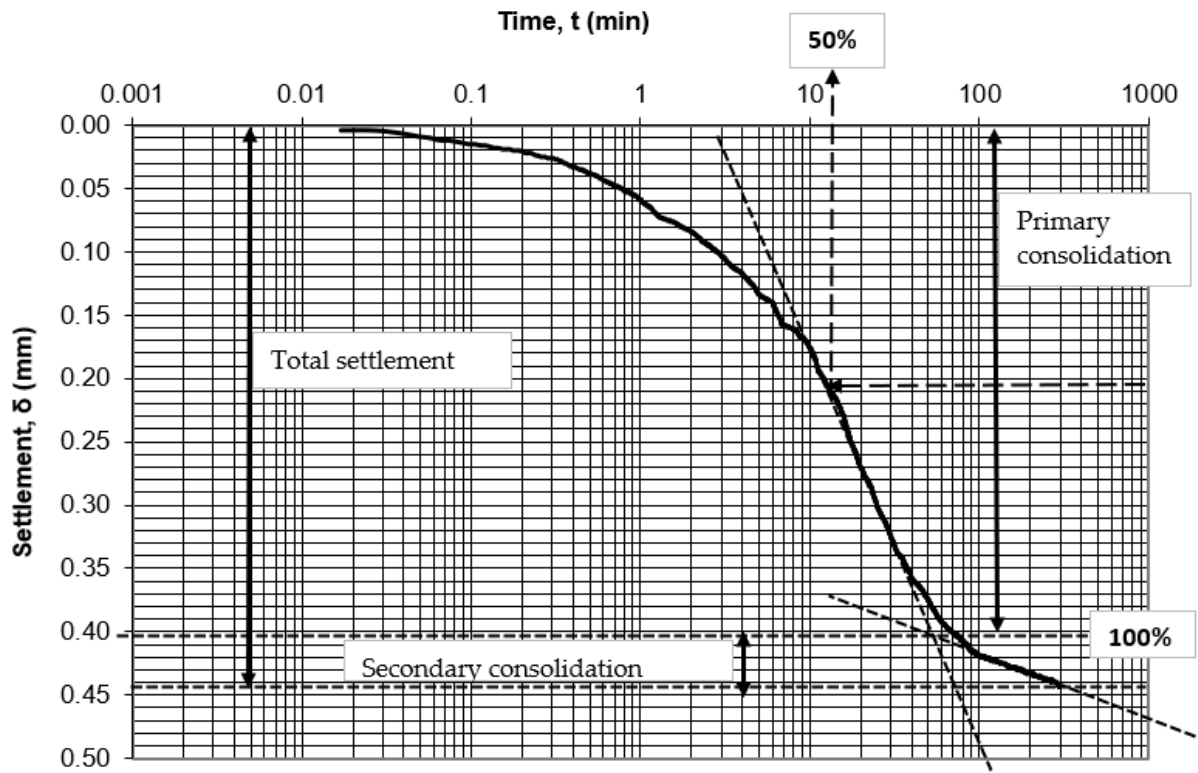


Figure 17. A typical consolidation curve for 2.5% muscovite and 97.5% kaolin at 3kPa loading step showing consolidation phases and analysis of log-time/settlement.

5. An X-ray CT study of miniature clay sample preparation techniques

The same version of this chapter (with slight modification) has been published in: Ibeh C. U., Pedrotti M., Tarantino A., Lunn R. J. (2019) An X-ray CT study of miniature clay sample preparation techniques. *E3S Web of Conferences*, 92. 01004. ISSN 2267-1242. <https://doi.org/10.1051/e3sconf/20199201004>

Abstract.

The quality and reliability of cohesive soil laboratory test data can be significantly affected by sample disturbance during sampling or sample preparation. Sample disturbance may affect key design and modelling parameters such as stiffness, preconsolidation stress, compressibility, and undrained shear strength, and ultimately determine particle mobilization and shear plane development. The use of X-ray computed tomography (X-ray CT) in the study of soil is restricted by the inverse relationship of specimen size and obtainable image resolution. This has led to the testing of miniature specimen sizes which are far less than conventional laboratory sample size in a bid to obtain high resolution images and detailed particle-scale soil properties; however, these miniature soil specimen are more prone to sample disturbance. In this work 2% muscovite was mixed with speswhite kaolin clay as a strain marker for use in X-CT. The clay soil sample was prepared from slurry and either consolidated using an oedometer or a gypsum mould. Specimens obtained from a 7 mm tube sampler were compared to lathe trimmed specimens with a diameter (\emptyset) of 7 mm. Results from X-ray CT imaging were used to study the influence of sampler type on specimen disturbance, by analyzing the muscovite particle orientation of the obtained 3D images. The results show that; for samples subjected to large consolidation stress ($>200\text{kpa}$) lathe trimmed specimens may be subject to lesser disturbance compared to tube sampled specimens.

5.1. Introduction

Laboratory specimen quality is important to obtain reliable and representative soil parameters, however, a great deal of disturbance to the soil specimen may occur during sampling. If the soil specimen loses its original structure, the test-derived soil parameters may be unrepresentative and lead to overly conservative designs (Emdal et al., 2016). Similarly, soil modelling requires input parameters to be as close as possible to the actual experiment data, hence significant sample disturbance should be avoided.

With the proliferation of X-ray Computed Tomography (X-ray CT) in soil mechanics, there is currently no standard guide for the preparation of miniature soil specimen for X-ray CT and there are no specifications for approaches to the preparation of these miniature specimens. Miniature specimens are obtained from large-scale samples prepared with conventional methods, -for example, from a conventional triaxial sample that is 38mm by 72mm-. The deformation of a soil is affected by its initial state, and if a specimen has undergone significant deformation *ab initio*, this may well determine how the sample further deforms. Currently, the testing of miniature soil specimen under the X-ray CT has focused on observing phenomena without really considering the effects of sample preparation and the degree of specimen disturbance. These latter considerations raise a number of questions such as: Is the specimen being tested representative of the original sample? Does the sample preparation approach lead to significant initial sample deformation that affects how particles ultimately behave? How much specimen disturbance does the sampling approach, such as tube sampling or lathe-trimmed block sampling cause to miniature specimens and are these disturbances within acceptable limits for a representative soil?

Traditionally, it is considered adequate to take samples which have a minimum dimension of the order of 5-10 times the maximum particle size of the soil BS-5930 (1981) suggests that

sample sizes should be determined on the basis both of the soil type and the purpose for which the sample is needed. Additional research has shown that sample disturbance may affect estimates of shear strength on soft clays and soil may be so disturbed as to contain zones of potential weakness along which slippage may occur during strength testing, hence the level of disturbance to which the soil is subjected should be acceptable (Lunne et al., 2006).

5.1.1. Miniature soil sample preparation techniques

In the laboratory, remolded miniature specimens can be produced by cutting blocks of soil and then trimming it to the desired shape using a soil lathe, by pushing or driving tubes into a larger sample (see Figure 1a below) or by preparing a soil specimen just to size either using a gypsum mould (see Figure 1b below) or a miniature oedometer. Each of these specimen preparation approaches may impose a certain degree of disturbance on the resulting soil specimen.

Trimmed block sampling is recommended, as it is considered of a better-quality over piston/tube derived samples in conventional geomechanics soil sampling (DeGroot et al. 2005; Emdal et al., 2016). What constitutes an “undisturbed sample” is unknown, as no definitive method exists to obtain a “perfect sample” let alone “a perfect unconventional miniature soil specimen”. Therefore, there is the need to assign a confidence level to sample quality assessment (Amundsen et al. 2015).

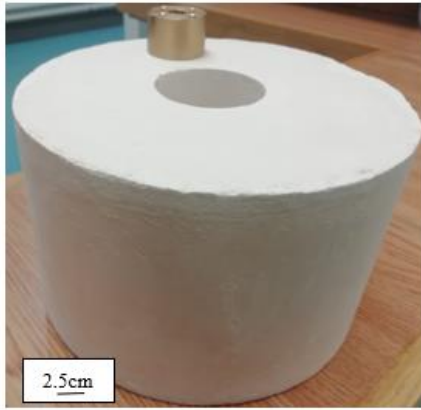
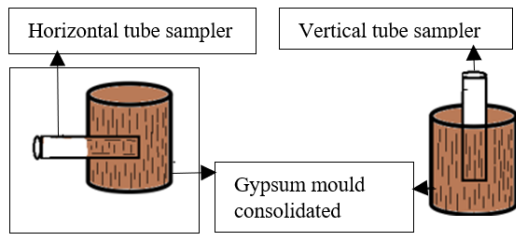


Fig. 1a: Tube sampling configuration (not to scale); b) large Cylindrical hollow gypsum mould for consolidating clay sample.

The aim of this study is to determine and compare the degree of miniature specimen disturbance imposed by different sampling approaches. We used mica particles (fine silt to sand sized) as remolded clay specimen strain markers. This is because X-ray CT resolution is in the order of a few microns, but clay particles are less than 2 microns in size. Particle orientation analysis using stereographic projections and Fisher statistics were used to determine the amount of specimen disturbance. A specially prepared gypsum mould and a conventional oedometer were used to prepare samples with different particle configuration; these were then subsampled using a tube and a lathe.

5.2. Material

Slurries were prepared using speswhite kaolin purchased from IMERY'S Minerals Limited (with a liquid limit of 63 and a particle size range of 0.3 micron to 6 micron and an

average particle size of 0.7 microns) and sand muscovite mica from LKAB minerals LTD (the mica was crushed to a range of particle size between 10 micron and 200 micron and an average size of 90 micron). A firm plastic tube sampler with an inner diameter of 7mm, a metal soil lathe and a specially produced hollow cylindrical gypsum mould were used to prepare the specimens. A mould with inner and outer diameters of 38mm 120 mm was used. The gypsum mould was prepared using conventional ceramic gypsum mould preparation approach.

5.3. Sample Preparation

Two different consolidation methods were adopted: suction induced consolidation using a large gypsum mould, and conventional oedometer consolidation. For the mould sample, after mixing the appropriate amount of kaolin and mica (2% wt mica) with de-aired distilled water (using 4 times the liquid limit of kaolin -252%), a shear- mixer was used to homogenize the slurry for 30 mins. Thereafter, the slurry is consolidated with either of the larger sized or the smaller sized gypsum mould, by pouring the slurry into the mould at intervals (ensuring no space in the mould as it consolidated) until a firm sample is cast (total of about 2hrs for the 38mm sample and about 20minutes for the 7mm sample). After consolidation (to 100kpa), the mould is then lifted leaving behind the sample. The oedometer sample was prepared using 1.5 times the liquid limit of kaolin (96%), consolidated to 2200kpa, unloaded to 200kpa and quickly drained (overconsolidated specimen).

Specimens were either sampled using a miniature tube sampler or, a soil lathe. A total of four specimen types were studied (see Table 1 below):

- i) a vertical tube specimen derived by inserting the tube sampler vertically through the sample consolidated in the large cylindrical gypsum mould (LM-VT),
- ii) a horizontally tube specimen derived by inserting the tube sampler horizontally across the sample consolidated in the large cylindrical gypsum mould (LM-HT),
- iii) a vertical tube specimen derived by inserting the tube sampler vertically through the overconsolidated oedometer sample (OED-VT), and
- iv) a lathe trimmed vertical specimen derived from the oedometer consolidated sample (OED-VL) and

After preparing the lathe trimmed and mould specimens, the specimens were covered with liquid latex to prevent moisture loss during imaging. The tube derived specimens were imaged without extrusion from the tubes so as to have the least possible tube disturbance; the top and bottom of the tubes were sealed with liquid latex before imaging.

5.4. Methodology

In this study, because of the miniature specimen size, we have restricted the evaluation approach to non-destructive testing, specifically the use of X-ray CT (with mica as a strain marker). Particle orientation at the specimen's outer surface (outer- surface thickness defined as 2 times the average marker particle length) was compared to the internal (inner) particle orientation of the specimen, see Figure 2 below.

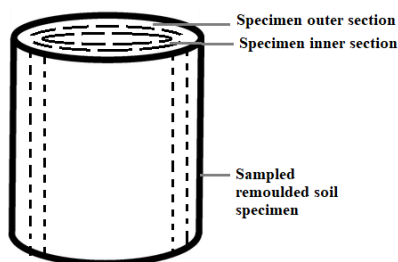

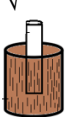
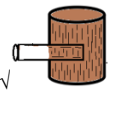


Fig. 2: Typical specimen sections analyzed for disturbance (not to scale)

5.4.1. X-CT imaging

X-ray CT imaging of the samples were performed by means of a Nikon XT H 320 X-Ray CT scanner (at the University of Strathclyde, Advanced Materials Research laboratory). In the present work, the voxel resolution was approximately 5 μm and the scanner settings were energy 150 kV and current 38 μA .

Table 1: description and schematic of specimens studied.

Sample consolidation method	Lathe trimmed block sample	Vertical Tube sample	Horizontal Tube sample	Specimen prepared to size
Oedometer Consolidated	√	√ 	-	-
Large gypsum mould suction induced consolidation sample	-	√ 	√ 	-

The reconstruction was carried out using CT Pro and CT Agent software (Nikon189 Metrology). The visualization and analysis of the CT data was performed with AVIZO 9.0 software. Avizo border kill tool was used to remove all particles touching the sampler border and the particle long-axis orientations were exported to the Stereonet software (Allmendinger et al., 2011; Cardozo & Allmendinger, 2013) for particle distribution and orientation analysis.

5.4.2. Stereographic projection

Contoured stereoplots were used for the presentation and analysis of the mica particle orientations, enabling 3-dimensional data to be plotted in two dimensions. The stereonets were

plotted using the Stereonet software with the orientation of the mica particles plotted as poles to the mica plates.

5.4.3. Spatial statistical analysis (Fisher Spherical distribution).

The Fisher distribution is the basic model for directions distributed unimodally with rotational symmetry and it is the direct generalization for a sphere of the von Misses distribution on the circle (Fisher, 1993). According to (Cardozo & Allmendinger, 2013) the distribution is the standard mean vector calculation such that the direction cosines of all the individual unit vectors are simply added up; the mean length is the length of the resultant vector divided by the number of vectors summed and the reported trend is derived from the resultant vector normalized to a unit vector.

The shape parameter k (or kappa) also known as the dispersion or the concentration factor, is estimated from equation (1):

$$k \approx (N - 1)/(N - R) \text{ for } N \geq 16; \quad [1]$$

the uncertainty intervals are calculated from the equation (2) below:

$$\cos\delta\alpha = 1 - \left(\frac{N - R}{R}\right) \left[\left(\frac{1}{1 - P}\right)^{\frac{1}{N-1}} - 1\right] \quad [2]$$

Where N is the number of observations, P is the probability, and R is the resultant vector length. The larger the value of k , the more the distribution is concentrated towards the equivalent direction cosines. A high k differential means more disturbance: an undisturbed sample will result in the same (or very close) k values for both the inner and the outer sections of the sample.

The hypothesis tested is that the inner specimen particles are distributed more directionally to the mean whole sample direction than the outer specimen particles, that is, that the absolute difference of the k between the specimen outer section and the inner section is smaller for a less disturbed specimen than for a more disturbed specimen. This is expected to be the case if the outer part of the specimen is significantly disturbed in a direction away from the mean specimen direction.

With Δk = absolute difference between the inner and outer section k values

$$H_0: (|\Delta k|_{\text{less disturbed specimen}}) > (|\Delta k|_{\text{more disturbed specimen}})$$

$$H_1: (|\Delta k|_{\text{less disturbed specimen}}) < (|\Delta k|_{\text{more disturbed specimen}})$$

For each of the specimens, 1000 of the larger mica particles in the inner specimen section and 1000 mica particles in the outer specimen section (also the larger particles) were each analyzed for the section's concentration factor k. This was done using an equal area stereographic projection and the Fisher statistics distribution. The larger mica particles were used because of the limitations imposed by the X-CT resolution.

5.5. Results and Discussion

5.5.1. Tube and lathe derived Oedometer overconsolidated specimens

Results of the Fisher spherical distribution analysis of the stereoplots for all of the specimen types tested are presented in Figure 3 below. For the OED -VT, the inner section

particles are aligned more closely to the horizontal, as compared to the particles at the outer section which are oriented vertically (due to the tube sampler effect – see Figure 5c below) and horizontally. In the case of, - the, OED -VL, there are also more vertically oriented particles in the outer section, but the effect is not as in the OED-VT.

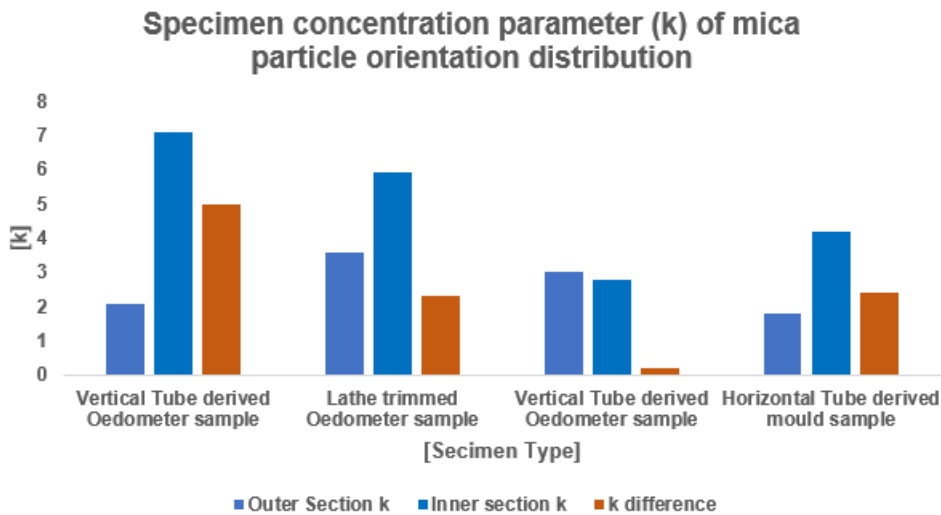


Fig. 3: concentration parameter of mica particle orientation distribution (N-1000; 95% significance)

The k-values for the vertical tube sampled oedometer overconsolidated specimen are 2.1 (outermost section) and 7.1 (inner section) and the difference is 5.0 all at 95% confidence level, while for the lathe trimmed oedometer overconsolidated specimen, the k value for the outer section is 3.6, as compared to 5.9 for the inner section and a difference of 2.3. The k value difference for the vertical tube sampled oedometer overconsolidated specimen (5.0) is higher than the k difference for the lathe trimmed oedometer overconsolidated specimen (2.3). This implies that the vertical tube sampled oedometer overconsolidated specimen experienced significantly more disturbance than the lathe trimmed oedometer overconsolidated specimen. This is despite the sample not being extruded from the tube (which may impose some additional disturbance) and the particles touching the border being removed (using the border kill tool, in Avizo)- from the analysis. The stereoplot for the inner and outer sections of the lathe-trimmed oedometer specimens are shown in Figures 4a and b below.

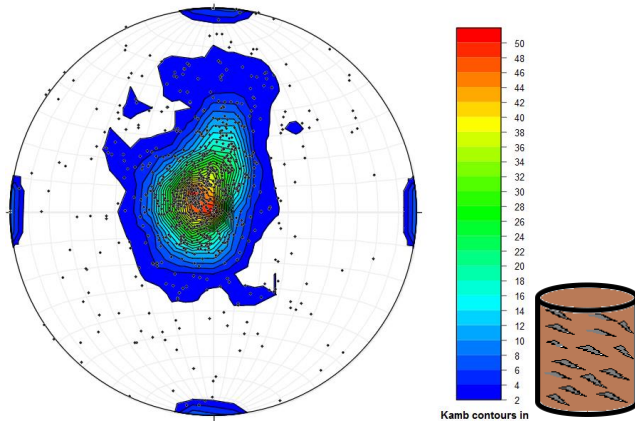


Fig. 4a: Lathe-trimmed oedometer specimen inner section particle pole to mica particles long axes (N=1000)

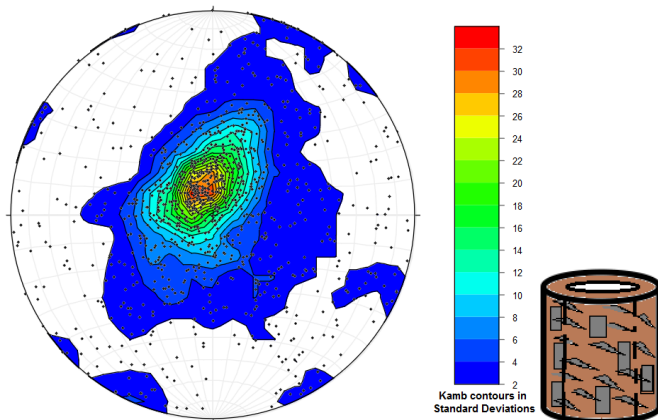


Fig. 4b: Lathe-trimmed oedometer specimen outer section particle pole to mica particles long axes (N=1000)

Figures 5a and b below show a top view of the X-ray CT images of a typical oedometer consolidated specimen cored with a tube sampler, with the edges showing re-oriented mica particles. Figure 5b shows the innermost part of the same cored specimen, with the outermost cylindrical section cut off. The outermost part of the original image shows particle alignment (away from the original specimen) to the walls of the tube sampler. The difference is also visible in Figures 5c and d (side view of same specimen).

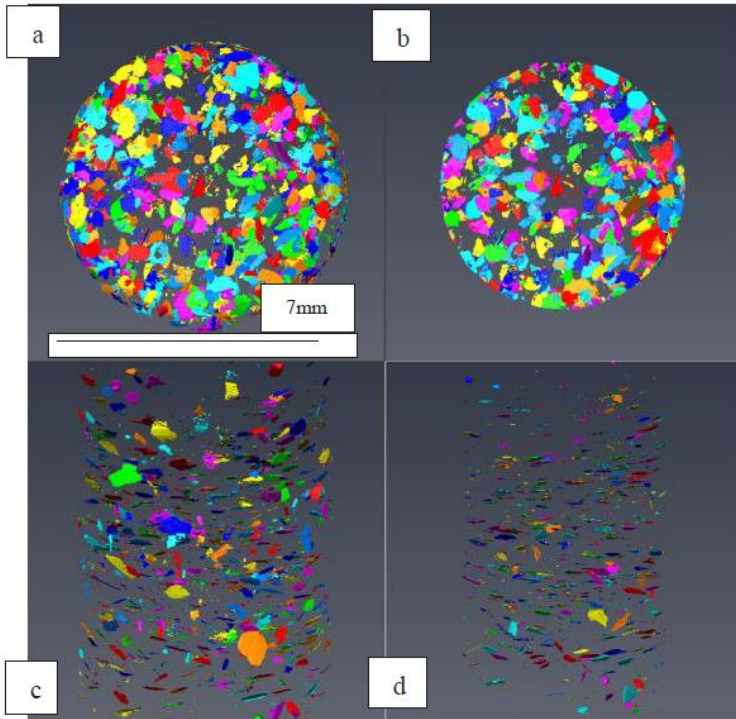


Fig. 5: a) Top view of an oedometer consolidated specimen cored with a tube sampler with the outer surface intact and b) with the outer surface cut off; c) side view of an oedometer consolidated specimen cored with a tube sampler with the outer surface intact and d) with the outer surface cut off.

5.5.2. Mould consolidated specimens (to lower stress)

The vertical and horizontal tube specimen cored from the middle of a cylindrical gypsum mould sample, have k difference values: 0.2 and 2.4 respectively (Figure 4):

$$(|k_{\text{inner}} - k_{\text{outer}}|_{\text{horizontal tube mould specimen}}) > (|k_{\text{inner}} - k_{\text{outer}}|_{\text{vertical tube derived mould specimen}})$$

This implies significantly more disturbance when the specimen was sampled horizontally compared to the specimen sampled vertically. This is actually to be expected, because both the vertical tube sampler and the gypsum mould itself during consolidation, act to orient the particles in alignment with the sides of the mould i.e. vertically. Hence, any sampling disturbance is minimized in the mould prepared sample.

The stereonet representations for the horizontal sampling, which did show significant disturbance, with the gypsum mould are shown in Figures 6a and b below:

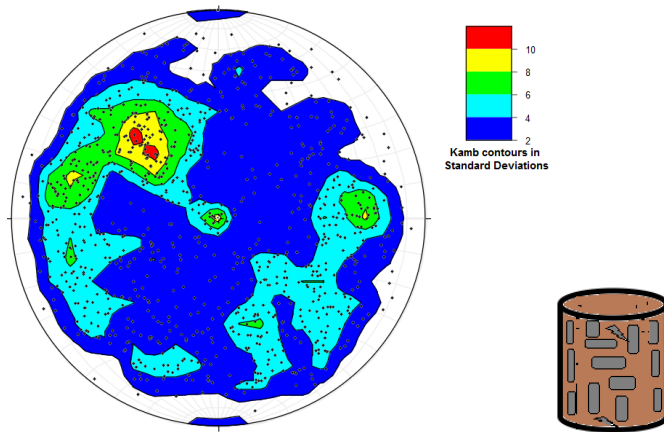


Fig. 6a: Horizontal tube specimen inner section particle pole to planes of the mica particles long axes (N=1000)

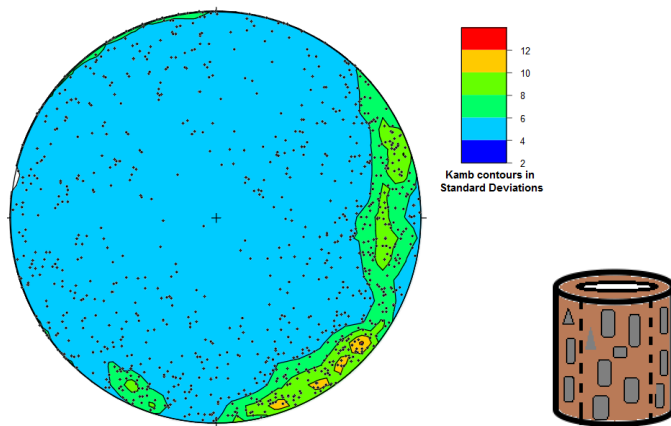


Fig. 6b: Horizontal tube specimen outer section particle pole to planes of the mica particles long axes (N = 1000)

Significant difference in particle orientation are observed. In the inner section, the undisturbed particles tend to be vertically oriented and there is a significant concentration of particles oriented NW-SE on Figure 6a, which is perpendicular to the radial direction in which the horizontal sample was taken. This is because during preparation of the sample, the radial suction forces tend to orient the particles parallel to the face through which drainage is occurring. Figure 6b shows the orientation of particles within the outer section of the horizontal tube sample. Particles here are now almost entirely randomly oriented and hence are clearly disturbed by the sampling process.

5.6. Conclusion

Soil sampling imposes some level of disturbance on soil microstructure, and this may affect soil mechanics test results. Miniature cylindrical remoulded kaolin specimen (containing 2% silt-sand sized mica markers) produced by tube sampling and lathe trimmed sampling were analyzed for sample disturbance. Fisher distribution analysis of the mica particle strain markers, represented as poles to planes plotted on stereonet, showed that lathe trimmed vertical specimens may be subject to lesser disturbance when compared to vertical tube sampled specimens for overconsolidated specimens prepared in an oedometer (possibly because tube sampling in addition to the limitations of a block trimmed sample is also affected by shear distortion). In the case of gypsum mould prepared samples, the radial suction force results in the particles being preferentially radially oriented and parallel to the drainage surface. Consequently, vertical tube sampling produced almost no disturbance. We conclude that mica particles can give valuable information on miniature sample disturbance, which can then be mitigated by design of improved sampling methods.

This research is supported by a University of Strathclyde funded PhD Studentship.

5.7. Reference

- Allmendinger, R. W., Cardozo, N., & Fisher, D. M. (2011). *Structural Geology Algorithms: Vectors and Tensors*: Cambridge, England, Cambridge University Press.
- Amundsen, H.A., Thakur, V. and Emdal, A. (2015). Comparison of two sample quality assessment methods applied to oedometer test results. 6th International Symposium on Deformation Characteristics of Geomaterials, 923–930.
- BS 5930: 1981 - Standard, B., 5930, Code of Practice for Site Investigations. British Standards Institution, London, p.147 (1981)

- Cardozo, N., & Allmendinger, R. W. (2013). Spherical projections with OSXStereonet. *Computers and Geosciences*, 51, 193–205. <https://doi.org/10.1016/j.cageo.2012.07.021>
- DeGroot, D. J., S. E. P. and M. M. L. (2005). Sample disturbance-Soft clays. *Studia Geotechnica et Mechanica*, 27(3–4), 91–105.
- Emdal, A., Gylland, A., Amundsen, H. A., Kåsin, K., & Long, M. (2016). Mini-block sampler. *Journal of Geotechnical Engineering*, 53(8), 1235–1245.
- Fisher, N.I., Lewis, T. and Embleton, B. J. (1993). *Statistical analysis of spherical data*. Cambridge University Press.
- Lunne, T., Berre, T., Andersen, K. H., Strandvik, S., & Sjørsen, M. (2006). Effects of sample disturbance and consolidation procedures on measured shear strength of soft marine Norwegian clays. *Canadian Geotechnical Journal*, 43(7), 726–750. <https://doi.org/10.1139/T06-040>

6. PLATYMATCH- A particle-matching algorithm for the analysis of platy particle kinematics using X-ray Computed Tomography

The same version of this chapter (with slight modification) has been published in: Ibeh, C.U., Pedrotti, M., Tarantino, A. and Lunn, R.J., 2021. PLATYMATCH–A particle-matching algorithm for the analysis of platy particle kinematics using X-ray Computed Tomography. *Computers and Geotechnics*, 138, p.104367.

Abstract

Particle scale mechanisms influence the mechanical behaviour of geomaterials. A better understanding of soil micromechanics will help develop more accurate constitutive models and, by extension, safer and more economic geotechnical design. Sand-grained soils have been widely studied at the particle scale using X-ray Computed tomography and this has revealed important micromechanical behaviour of sands. Clays are least understood and studied at the particle scale. As technology rapidly progresses, to understand clay kinematics, a particle kinematic algorithm to match plate shaped (platy) particles will be required. Current algorithms developed for the matching of quartz and carbonate sand particles may not be suitable, since particle attributes that are strong discriminators of round particles may be less unique on platy particles, due to their extremely small c-axis and the reduced image resolution associated with their smaller size. This study presents particle tracking of kaolin sample using mica markers and provides a platy soil particle matching algorithm for evaluating platy particle kinematics. After testing a range of alternative particle attributes, it was observed that a combination of

particle major axis length, intermediate axis length, and perimeter was a good discriminant of the platy mica particles studied. On this basis, we developed PLATYMATCH, an optimised platy particle matching algorithm that considers a minimised combined normalised error of unique particle attributes within a defined search volume space. The algorithm was implemented such that particle attributes were compared in parallel, rather than sequentially, to avoid filtering out a potential particle match based on a single non-unique attribute. PLATYMATCH was then successfully validated using a compressed mica soil sample.

Keywords: PLATYMATCH, X-ray Computer tomography (X-CT), mica, clay, particle matching, algorithm

6.1. Introduction

An increasing body of research shows that the particle scale properties of soil importantly influence the mechanical behaviour of granular materials. Unlike clays, sand-grained soils have been widely studied at the particle scale and this has revealed important micromechanical behaviours including the change of sand grain morphology due to fracture mechanisms (Zhao et al., 2015), the decrease of dilatant behaviour with the suppression of peak shear strength in sand mixed with tyre chips (Chevalier et al. 2019), and the observation of pre-peak initiation of strain localisation in sand using X-ray computer tomography (X-ray CT), (Andò et al., 2012). Despite clay soils exhibiting relatively more complex behaviour compared to sands, clays are less understood and studied at the particle scale. This is because clay particles are very small – with size in the order of microns/sub-microns and thickness in the order of tenths/hundredths of nanometres, they are platy in shape, and they exhibit physico-chemical interactions in addition to mechanical interactions. An improved understanding of clay micromechanics could inform macroscopic constitutive models (Alonso et al., 2010; Cetin & Gökoğlu, 2013; Hattab et al., 2014; C. Ibeh et al., 2019; Lin et al., 2021; Pedrotti & Tarantino, 2018, 2019; Sridharan et al., 1974) enabling greater accuracy of predictions and, by extension, safer and more economic geotechnical design.

To better understand soil discrete mechanics, X-ray CT imaging techniques have been used to capture the particle scale attributes of soils subjected to different types of loading over time (mechanical, thermal, hydraulic, etc.). The X-ray CT data provides detailed 3D images of microscopically deformed geomaterials (Yuan Chen et al., 2021; Haldrup et al., 2008; Karatza et al., 2019; Nielsen et al., 2003; Reijonen et al., 2020; Takemura, 2004; Taylor et al., 2015; Viggiani et al., 2004). This technique could provide localized strain measurements. To determine particle motion, the analysis of such images usually requires particle matching between pre- and post-deformation scans, i.e. before and after loading. Two approaches are

commonly used for this analysis. Discrete digital image correlation - Discrete DIC (Andò et al., 2012; Hall et al., 2010) recognises grains based on their image (numerous voxel grey-scale information) which can be further analysed using full field strain measurement with the main limitation of being computationally expensive (Andò et al., 2012). Alternatively, particle before and after loading are matched using simple morphological particle attributes. Even if only a fraction of particles is matched, this approach enables the effective determination of sample kinematics with the advantage of being less computationally expensive (Andò et al., 2012).

A summary of key particle matching approaches to-date for granular materials is presented in Table 1. (Fu et al., 2008) implemented a particle matching algorithm to match crushed limestone particles (average size of $127\mu\text{m}$), using expected particle position reference and volume as matching parameters. They assumed that the sample deformed as a continuum and hence the algorithm searches for a particle in the initial sample scan with the closest location to where the particle should be in the second scan 2 (after loading). They then used the particle volume as an additional parameter if there was more than one particle in that location. This search approach may, however, break-down when searching for particles in a shear band (where particles could move in an unpredictable manner). Andò *et al.*, (2012) developed a particle matching algorithm -ID Track and used it to match carbonate and quartz sand (average size of $400\mu\text{m}$ and imaged at $15\mu\text{m}$ voxel size). ID Track searches for particles in two passes with the first pass using only volume difference and the second pass using both volume difference and difference of displacement of neighbouring particles. Particles with the closest attribute to the one under consideration are matched. Their assumption is that grains will tend to displace like their neighbours but also noted that this may cause problems when a neighbourhood overlaps a developed shear band. They used only one particle attribute as a matching parameter, i.e. volume, which would clearly present a challenge for particles where

the volume may be poorly variable. Cheng and Wang, (2018) also implemented an algorithm similar to ID-Track to match quartz sand with an average size of 500 μm and imaged at 6.5 μm voxel size, but rather than using volume as the matching parameter, they used surface area instead producing similar results. Druckrey and Alshibli, (2014) implemented an algorithm to match quartz sand particles with an average size of 700 μm and 10.85 μm voxel size that compared particles between scans using multiple particle attributes: Volume (number of voxels included in the particle), Area (Area of the object boundary), Feret length (the distance between two parallel planes tangent to the particle on the maximum extent direction - maximum Feret diameter), and Feret width (the distance between two parallel planes tangent to the particle on the minimum extent direction -minimum Feret diameter). These attributes were considered in series (sequentially), and as such, a particle must be within a set tolerance for the first attribute to be considered using the second, then similarly for the third and fourth. Table 1 presents details of the samples studied, the imaging condition and the algorithm implementation approach used. The Table also contains details of the sample studied and the particle matching algorithm implemented.

Table 1: available matching algorithm and their implementation

Author	(Fu et al., 2008)	(Andò et al., 2012)	(Druckrey & Alshibli, 2014)	(Cheng & Wang, 2018a)	This Study	
1	Material Tested and size	Crushed Limestone	Calcareous and quarzitic Sand	Quarzitic sand	Sand	Mica
2	Sample-size (Diameter X Height)	103 mm X 100 mm	11mm X 22 mm	19.5mm X 20.2mm	8mm X 16 mm	10mm X 20mm
3	Average Particle size	127 μm	400 μm	700 μm	500 μm	70 μm
4	Voxel size	-	15 μm	10.85 μm	6.5 μm	10 μm
5	Average ratio of particle major axis to voxel size		27	65	77	7
6	Average ratio of particle minor axis to voxel size		27	65	77	1
7	Particle segmentation approach	-	Watershed segmentation	Watershed segmentation	-	Machine learning trainable Weka
8	Search box used	No	Yes	Yes	Yes	Yes
9	Particle attribute used for matching.	Particle proximity	Particle position and particle volume	Particle position with sequential filtering of particle attributes: Volume, Surface area; Feret width and Feret lengths	Particle position and Area or Volume	Particle position with normalised parallel filtering of particle attributes: Major and intermediate

10 Matching criteria	Direct comparison	Iterative comparison	Sequential comparison	Iterative comparison	axis length and perimeter. Parallel comparison
----------------------	-------------------	----------------------	-----------------------	----------------------	---

The aim of the research presented here is to understand how to match relatively small platy particles (silt sized muscovite) as a guide to better understanding clay particle kinematics. We studied this by first using the available matching algorithm by Druckrey and Alshibli, (2014) which was originally developed for matching round sand particles. Applying the algorithm, we observed some challenges due to the platy shape, lesser image resolution (as a result of the smaller particle size) and associated geometry peculiarities. We then developed and validated PLATYMATCH (available at <https://github.com/Christopher-Ibeh/PLATYMATCH>), an optimised platy particle matching algorithm, taking into consideration the lessons learnt from implementing the code (Druckrey & Alshibli, 2014). In the future, PLATYMATCH can be used to further the understanding of the kinematics of plate shaped particles. For the example presented here of tracking platy mica particles, embedded in clay, it could provide new information on the evolution of strain localisation, since unlike tracking round particles, tracking plate-shaped particles provides information on particle rotation, as well as particle displacement.

6.2. Material and sample preparation

We tested soil samples (silt sized muscovite) with a significantly smaller particle size to voxel size ratio compared to the samples tested by the works listed in Table 1. The number of mica particles per unit volume was decreased by embedding the silt sized muscovite (1.5% by weight) in kaolin (98.5% by weight) to reduce any particle segmentation error that may emanate from particles sticking face-to-face.

Ground muscovite mica passing through sieve size 400-micron and Speswhite kaolin with a liquid limit (LL) of 0.64 and a plastic limit (PL) of 0.32, were used for the tests. The grain size distribution of the Kaolin shows it is composed of 80% clay-sized particles and 20%

silt-sized particles. After mixing the appropriate amount of mica (1.5% by weight) and kaolin (98.5% by weight) with de-aired distilled water using 1.5 times the liquid limit of kaolin (96%), the resultant slurry was consolidated in a modified oedometer cell (40mm ring height see Figure 1a) to 2200kpa, then unloaded under drained conditions to 200kpa and finally quickly unloaded (quasi-undrained unloading). This procedure was adopted to create overconsolidated samples (OCR=11). When unloading the sample, the last 200 kPa were unloaded under undrained conditions to generate suction and hence some apparent cohesion and facilitate the trimming of the specimen. Samples were trimmed to 20mm height and 10mm diameter using a miniature soil lathe (see Figure 1b). After preparing the lathe-trimmed specimen, the specimen was covered with a cling film to minimise moisture loss during imaging.

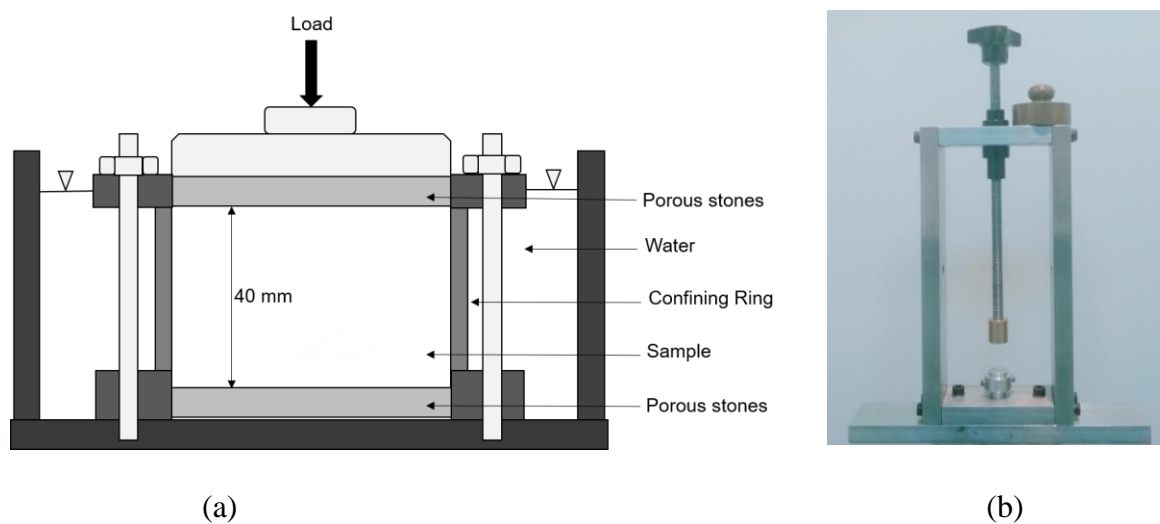


Figure 1: a) Modified oedometer cell b) Lathe used to trim soil samples.

6.3. Experimental Procedure

Three tests were performed using the lathe trimmed oedometer consolidated sample: a rotation test, a replacement test, and a compression test. For the rotation test, the sample was scanned and a section (2.9mm x 10mm) was digitally extracted from the scanned sample and

artificially rotated by 5 degrees (see Figure 3a and c). The original extracted section (without rotation) and the rotated image were then segmented and analysed. For the replacement test, the first scanned sample was re-scanned (i.e. the sample scanned, removed from the imaging stage, placed back on the imaging stage, and then rescanned), segmented, and the particle kinematics evaluated. Finally, the re-scanned sample was subjected to 8% uniaxial compression (using a plastic plunger loaded from bottom up) and the compressed sample scanned. By way of example, details of the third test are presented in Figure 2 and Table 2.

Images from the tests were processed as follows. First, we tried to match the mica particles in the compressed sample (compression test) using the matching code by Druckrey and Alshibli, (2014) to evaluate the particle kinematics. The Druckrey and Alshibli, (2014) approach was not originally designed for platy particles. We then adapted their approach by taking into consideration, the peculiar nature of platy particles as part of the image processing and particle matching workflow.

Secondly, we used the new PLATYMATCH approach. PLATYMATCH was initially applied to the rotation test to understand the effect of image remeshing due to rotation on particle attributes and for the evaluation of the best particle attribute for matching platy particles. It was then applied to the replacement test to evaluate the error associated with rescanning and image processing and finally applied to the compression test analysis (same test sample previously processed using the code by Druckrey and Alshibli, (2014)).

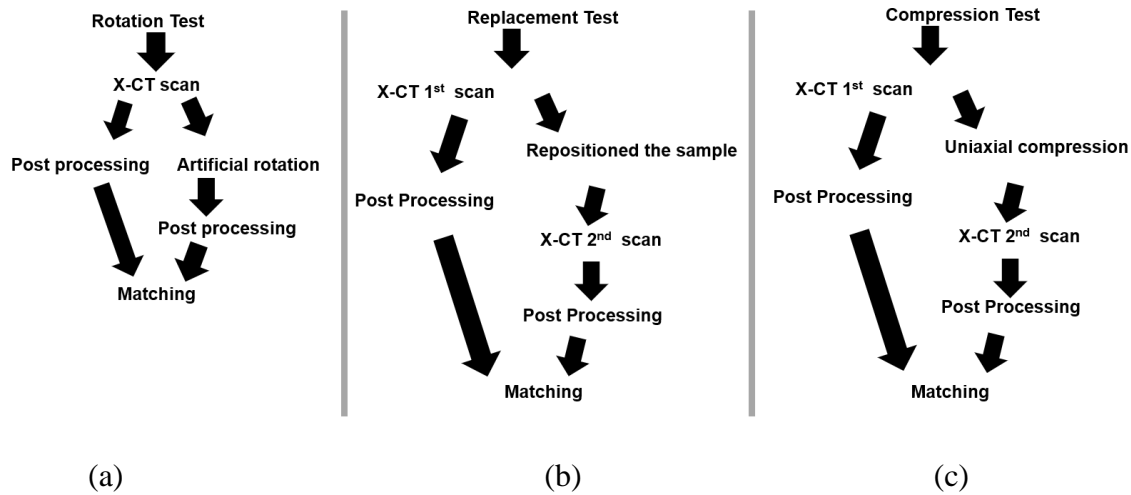


Figure 2: The samples scanned and analysed: a) sub-section of a digitally extracted section of a main scan, artificially rotated by 5 degrees; b) The main sample scanned, removed from the imaging stage, replace and rescanned c) The rescanned sample subjected to 8% axial strain and scanned.

Table 2: Description of the samples for the three tests conducted.

S/N	Image size	Sample size	Test
I	Sub-section of a digitally extracted section of a main scan, artificially rotated by 5 degrees	2.9mm height by 10 mm diameter	To understand of the effect of image remeshing due to rotation on particle attributes and evaluation of the best particle attribute for matching platy particles
II	Sample scanned, removed from the imaging stage, placed back on the imaging stage, and then rescanned	20mm height by 10 mm diameter	Evaluation of the error associated with rescanning and image processing.

III	Sample scanned, subjected to 8% axial strain and re-scanned	20mm height by 10 mm diameter	Validation of the matching code for a deformed sample
-----	---	-------------------------------	---

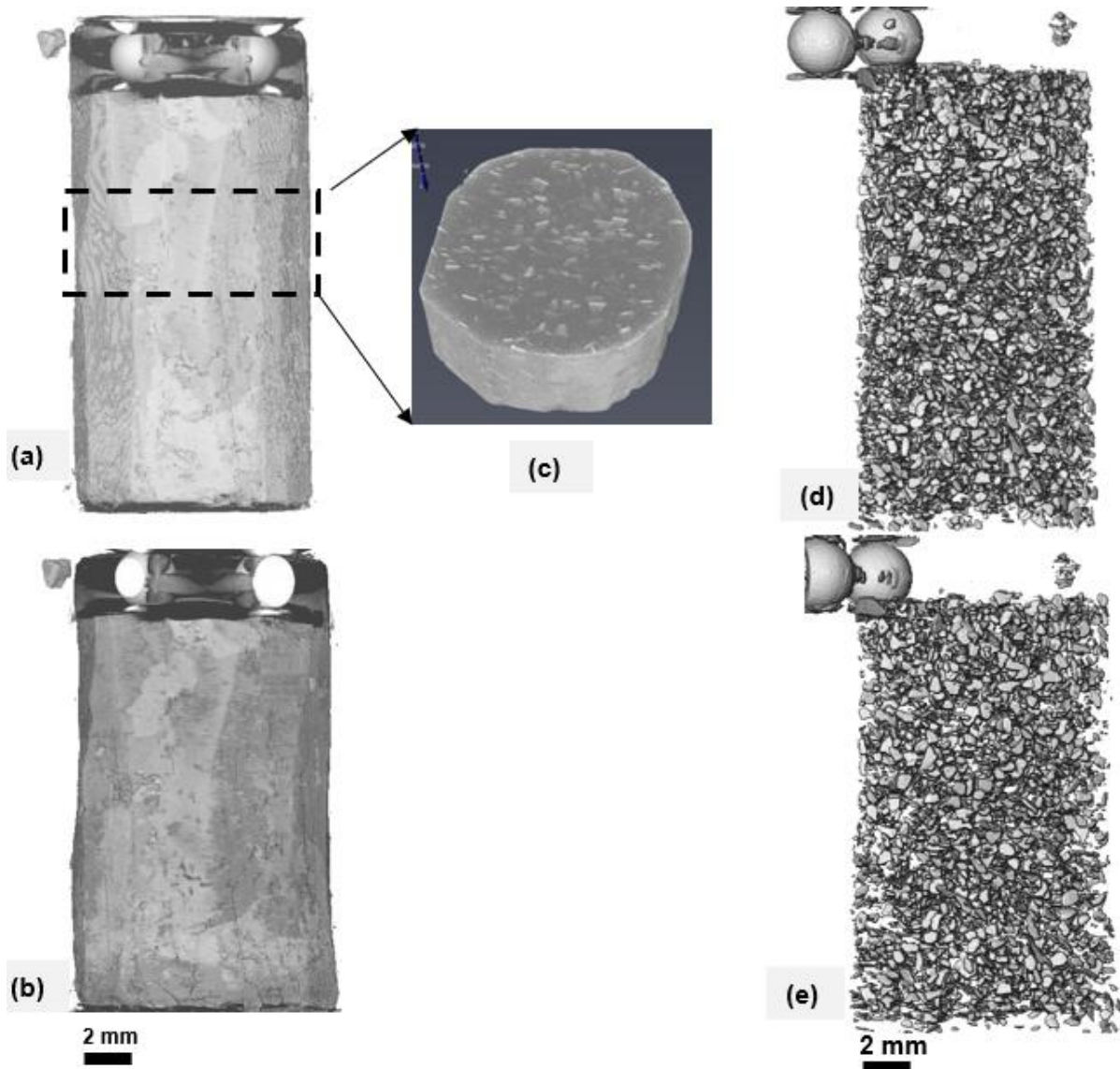


Figure 3: 3D renderings of the tomography a) sample before compression b) Sample after compression c) Artificially extracted sub section of the main sample d) segmented sample before compression e) segmented sample after compression.

6.3.1. *Image Acquisition and processing*

The scans were acquired in-situ in the XTH320 NICON X-ray scanner at the University of Strathclyde, which allows for 360-degree rotation of the sample. The voxel size of the 3D tomographic image is $10\ \mu\text{m} \times 10\ \mu\text{m} \times 10\ \mu\text{m}$. X-ray energy of 160 kV and power 9.8 W and exposure time of 1 second were used to image the samples. Each scan was reconstructed using X-TEC commercial software and then processed using ImageJ software (<https://imagej.net>) and Avizo-9 software (<https://www.fei.com/software/amira-avizo/>). To allow for later registration, a metallic spherical ball (500 μm) was placed on the bottom side of the sample during scanning and used as a sample reference marker. In the compression test, the sample was imaged with the compressed end down and the stationary end up.

6.3.2. *Thresholding and Image classification*

The scans were first filtered using a non-local means filter (Kumar, 2013) because it preserved the mica particle edges, smoothed out the kaolin matrix to one constituent and enhanced the contrasts between the mica and kaolin. Following a conventional image processing approach, the image components were classified using absolute thresholding of the greyscale histogram after greyscale normalisation. See Figure 20 in the Appendix for the grey scale histogram of the imaged sample. Each mica particle was then labelled using the interactive thresholding and label analysis tools in Avizo. The kaolin particles and mica particles have specific gravity that are very close (~ 2.7 and 2.8 respectively), there is no clearly defined bimodal distribution in the greyscale histogram.

6.3.3. *Particle Property Measurement*

Particle properties required for implementing the matching algorithm by Druckrey and Alshibli, (2014) were extracted. These properties included: position (x, y and z coordinates of

the barycentre respectively), orientation (angles φ and θ for the minor and major axes of the particle, see Figure 4) and specific attributes: area, volume, Feret length and width (the distance between two parallel tangents of the particle on the maximum and minimum extent direction respectively). The attributes are those considered for particle matching, while the position and orientation data are used for particle kinematics (translation and rotation) and particle search regions. Additional geometry attributes derivable using Avizo were also extracted, they include particle perimeter (sum of particle edge length), major, intermediate, and minor axis lengths (these are derived as ExtentMax1, ExtentMax2 and ExtentMax3 in Avizo and correspond to particle extents calculated in the direction of the smallest, intermediate and largest eigenvectors of the moment of inertia covariance matrix respectively).

The major [minor] axis is defined as the extent of the data in the direction of the smallest [largest] eigenvector of the covariance matrix (of the moments of inertia). It indicates the extent of the bounding box of the shape oriented along the corresponding eigenvector, with respect to the barycentre. The axis orientation in the x-y plane, θ , ranges between -180° and $+180^\circ$. The φ angle formed by the particle axis with the z-axis (as shown in Figure 4) ranges between 0 and 90° .

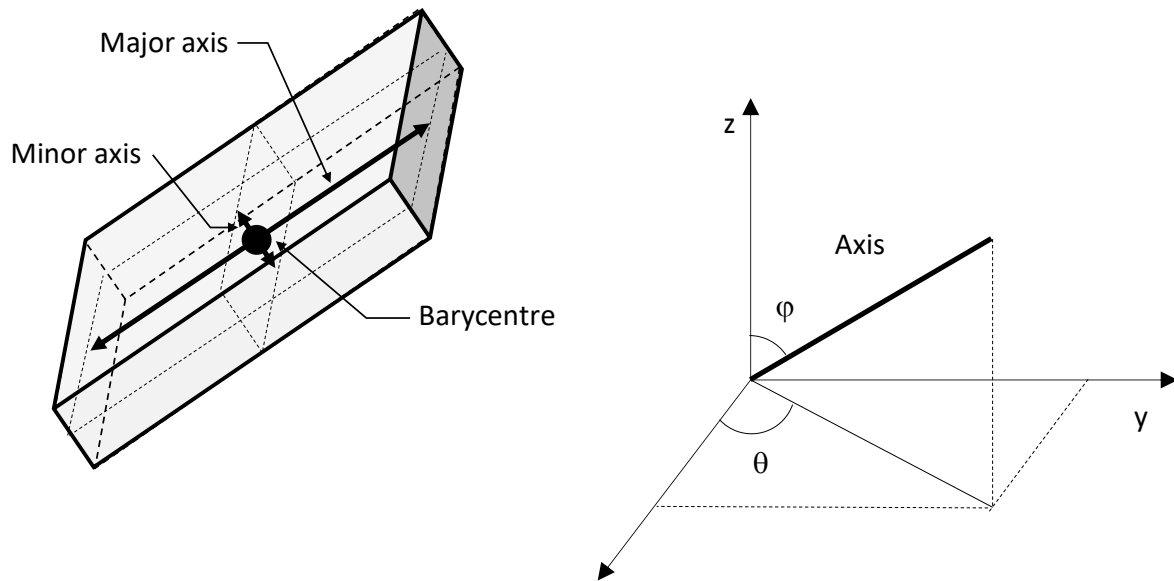


Figure 4: Orientation φ and θ of particle major and minor axes

6.4. Implementation of matching algorithm by Druckrey and Alshibli, (2014)

The algorithm proceeds by first isolating a sub-section around each of the particle centroids in the first image (a cube centred on the particle centroid). The particle under consideration (in scan 1) is then searched for within the defined cubic sub-section in the second scan using a first particle morphology attribute (within a percentage error tolerance). A particle is not analysed if no particles were found in the following image within the defined sub-section. The sub-volume was then searched for particles within 5% the volume of the particle in the first image, and these particles are searched for particles within 5% surface area, followed by 5% length and finally 5% width of the particle in the first image. If more than one particle in the second image matches the search criteria for all attributes examined in series, the particle with the lowest error in the first attribute is matched. Thereafter the particle kinematics (displacement and rotation) are computed. The parameters used by this matching algorithm include: the size of the cubic search box centred on the particle centroid (chosen as a factor of the maximum imposed displacement. For example, 1.1 times the maximum macroscopic

displacement observed, equal to $1.4 \times 1.1 \text{ mm} = 1.54 \text{ mm}$ in the test discussed in the paper.), the matching attributes (volume, surface area, Feret length and width) and the matching attribute tolerance (5% according to Druckrey and Alshibli, (2014)).

6.4.1. Initial Results for the compression test using algorithm by Druckrey and Alshibli, (2014)

The matching was performed using the algorithm by Druckrey and Alshibli, (2014) and resulted in only four particle matches despite increasing the percentage of acceptable attribute error to 50%. To understand the problem, we first evaluated the effectiveness of the particle segmentation by conventional thresholding. Since the pre- and post-scans contain the same particles (if the particles do not significantly bend), we expect the statistical distributions of the various attributes to be the same for both scans. Figure 5 shows a comparison of the particle attribute distributions for particle volume and major axis length, with the distribution of scan 2 (compressed sample) superimposed on scan 1 (sample before compression). A comparison of particle attributes between the initial and final scans shows a different number of particles. Nowhere near as many particles are identified, presumably because they are poorly segmented. These observations indicate that the scans are poorly classified using a conventional thresholding approach.

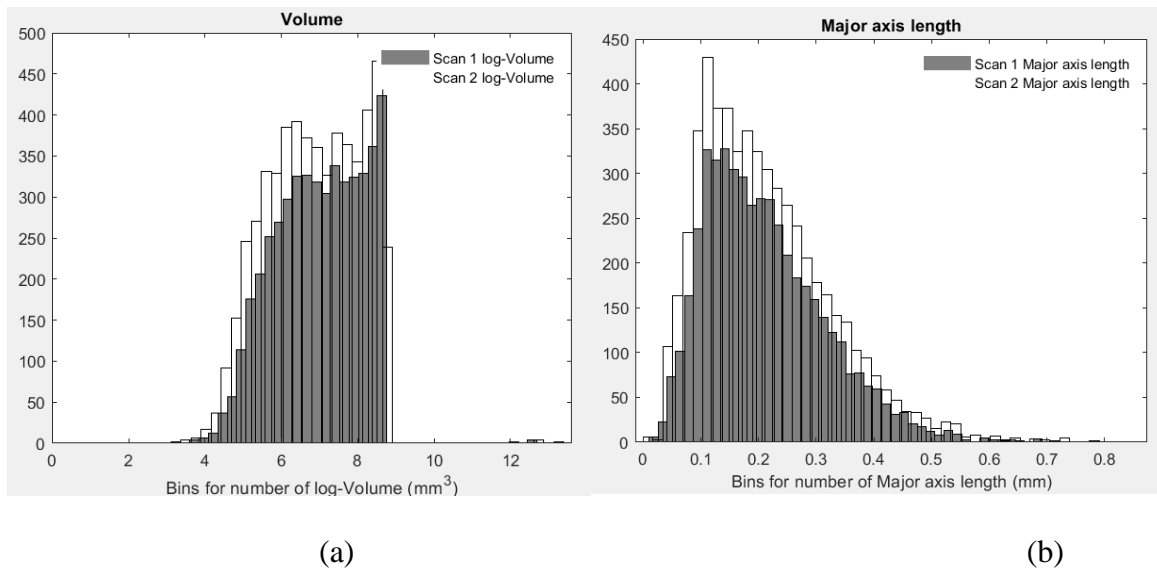
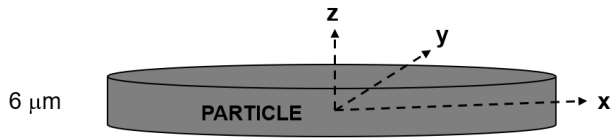
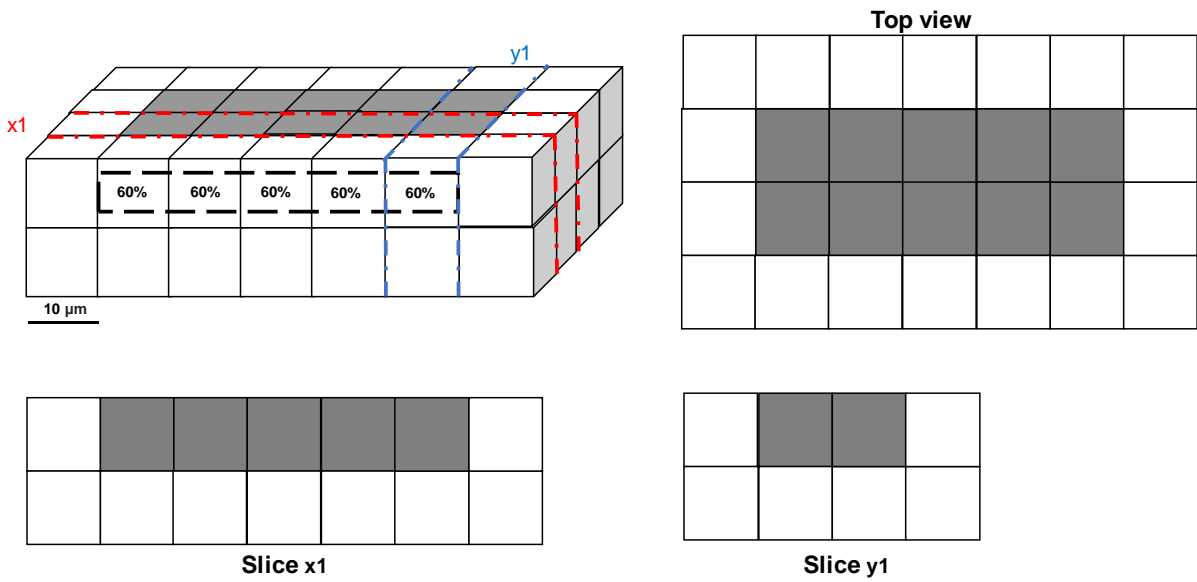


Figure 5: Conventional thresholding segmentation result particle attribute histogram distribution for scan 1 and scan 2 a) Volume, b) Major axis length.

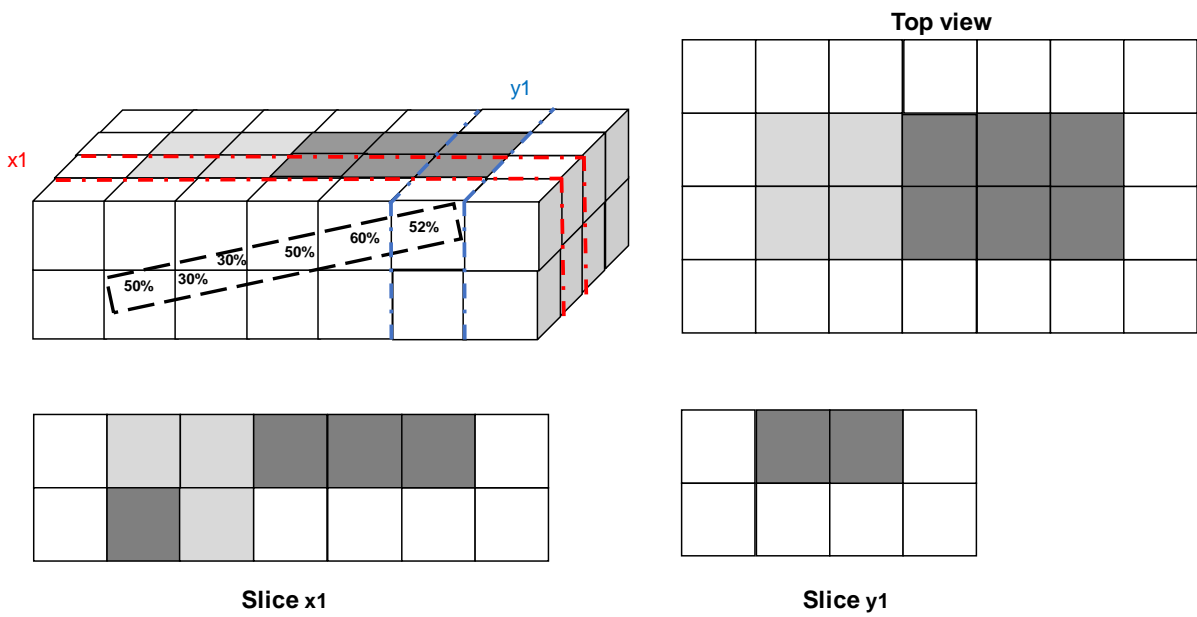
Platy particles have a large specific surface area (ratio of external surface area to volume) and are highly non-spherical. Their small size and high specific surface area imply that, they contain far fewer voxels in comparison to round sand particles represented by the same voxel size and, hence, are liable to incur a larger particle segmentation error. For example, the tiny C-axis associated with the platy shape may give rise to artificial splitting of particles upon rotation. This is demonstrated in Figures 6 a, b and c; if the threshold for considering a voxel as belonging to a particle is 50% then upon rotation of the particle (represented by dark grey voxels) the particle will artificially split. Figures 6d and 6e show two images, before rotation and after rotation, of voxels from the same particle, selected from the scan in Figure 3. The circle highlights where the particle has split into three after rotation (shown by the change in voxel colour from blue to yellow/green, as each segmented particle is plotted in a distinct colour).



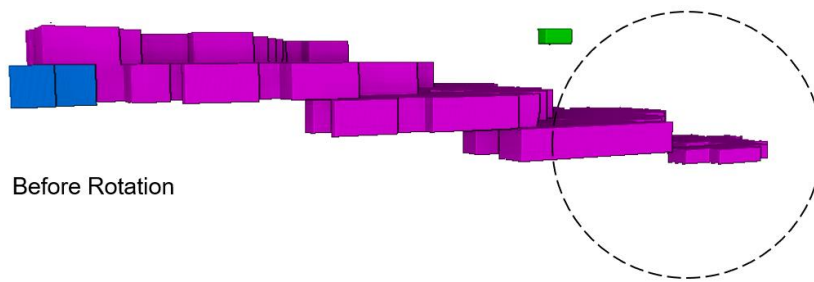
(a)



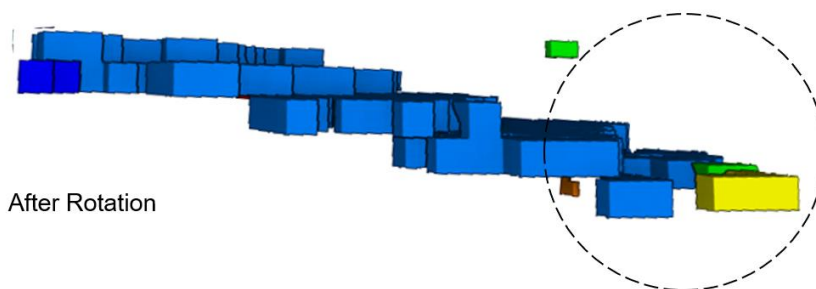
(b)



(c)



(d)



(e)

Figure 6 (a) Platy particle (b) horizontal platy particle represented as voxels with the top view, slice- $x1$ and slice- $y1$ (c) same platy particle is slightly rotated and becomes artificially split into 2 because the 2nd voxel is below the 50% threshold for considering voxels as part of the particle, with the top view, slice $x1$ and slice $y1$ (d) intact particle before rotation (e) particle split after rotation (see the circular section with broken lines).

As shown in Table 1, while the average number of voxels representing particle length of previous studies is at least 27 voxels, for a silt sized muscovite, it can be as small as 4 voxels. This is even worse for the platy silt sized muscovite particle C-axis, which may be as low as just 1 or 2 voxels. By comparison, in round sand particles there is only a slight reduction in the number of voxels representing the minor axis dimension compared to the major axis dimension. The limited achievable resolution and the small size of the platy particle C-axis dimension result in a large margin of error in the image segmentation. For a given particle, slight segmentation errors may result in a large difference in particles attributes between an initial

scan and subsequent scans thus giving rise to erroneous match. There is therefore the need for a better segmentation approach for the platy particles.

To improve particle segmentation, we used the Trainable WEKA machine learning segmentation (TWS) tool (Arganda-Carreras et al., 2017), a machine learning segmentation tool that has been applied successfully by researchers to discriminate other thin objects such as fibres (Karamov et al., 2020; Madra et al., 2014) TWS is open source code that combines the advantages of human knowledge, intensity and the spatial relationship of voxels with machine learning for an improved accuracy of the labelled region. It leverages a limited number of manual annotations to train a classifier and segment the remaining data automatically (Arganda-Carreras et al., 2017). To give an objective classification of each scan, the TWS model was trained using a combination of the sub- sections of the two scans to be compared. The process proceeded as follows: First, the images to be classified were filtered (in this case, using a non-local means filter). Then, a section of each filtered image was cut and imported into TWS and combined. The pixels were classified as either being kaolin, mica or the background – see Figure 18, Appendix 1. This set of labelled input pixels were then used as a training set for the classifier and the trained model was used to classify the whole sample image. Figure 19 (Appendix 1) shows the distribution of the mica particles intermediate length after TWS was used, which was consistent with the image resolution.

Figure 7 below shows the difference between a mica particle segmented using the conventional segmentation technique (thresholding) and using the TWS. It is clear that due to the thin nature of the platy particles, the conventional technique has a tendency to split the particles into multiple smaller plates whereas this problem was minimised using the TWS technique.

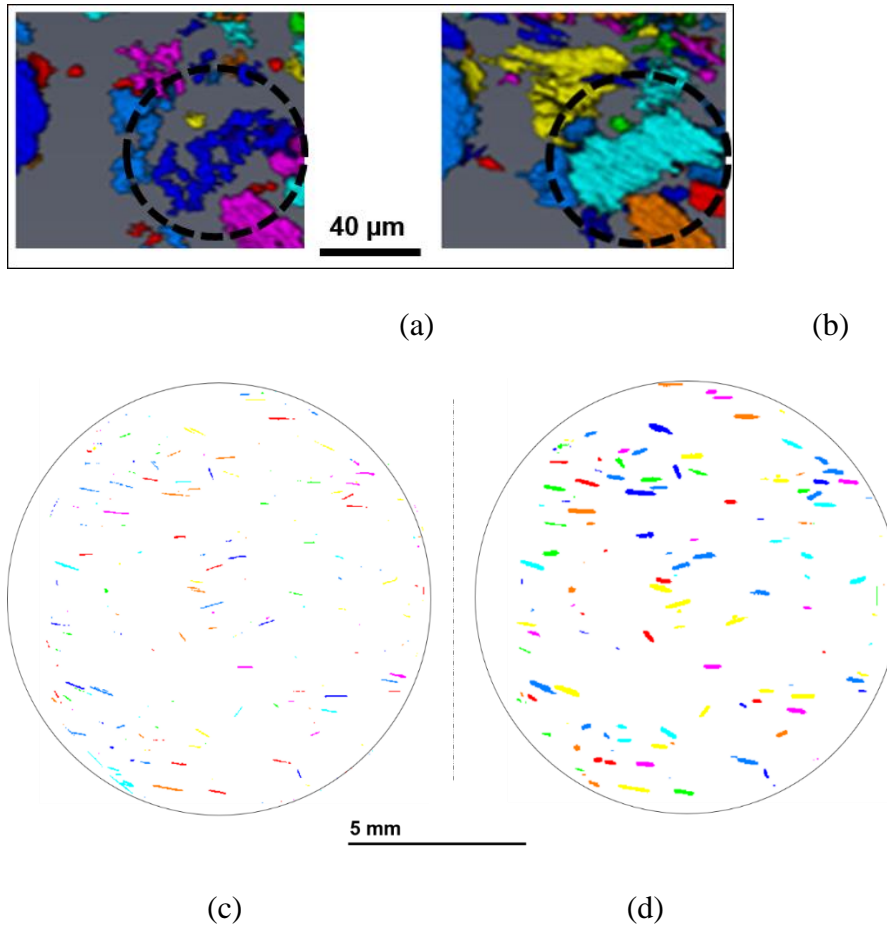


Figure 7: Image segmentation performed on sub-sample image volume using (a) absolute thresholding (b) TWS (c) 2D images of a sample classified using absolute thresholding (d) 2D images of a sample classified using TWS,

Figure 8 shows the pre- and post-deformation scan distributions for the same particle attributes as in Figure 5 (Volume and Major axis length) but using the TWS technique. The results are considerably improved, with very similar total particle numbers and attribute distributions between the two scans.

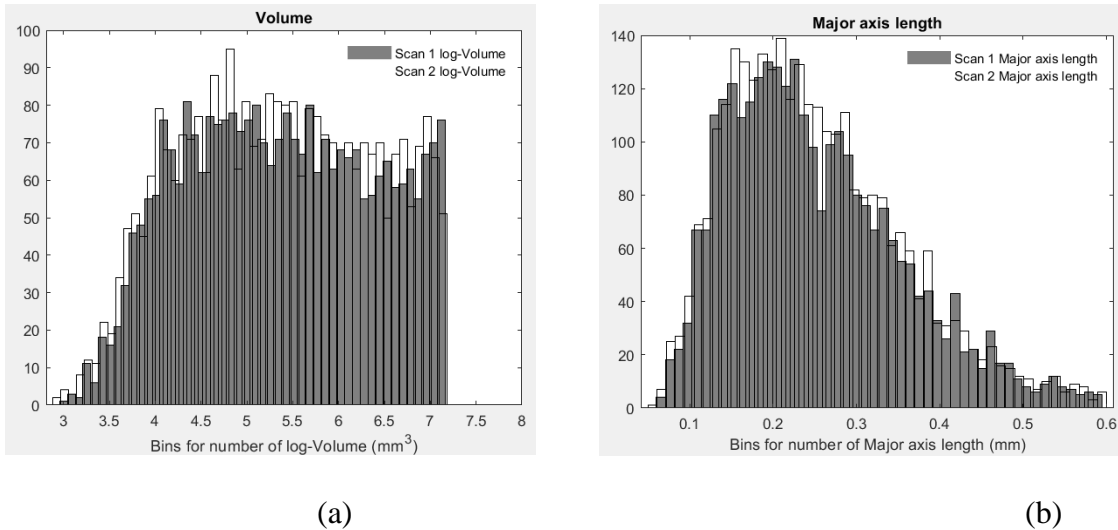
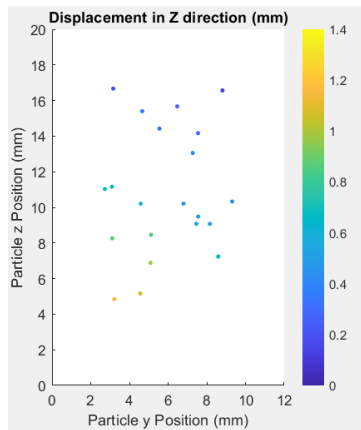


Figure 8: TWS segmentation result for Particle attribute histogram distribution for scan 1 and scan 2 a) Volume, b) Major axis length.

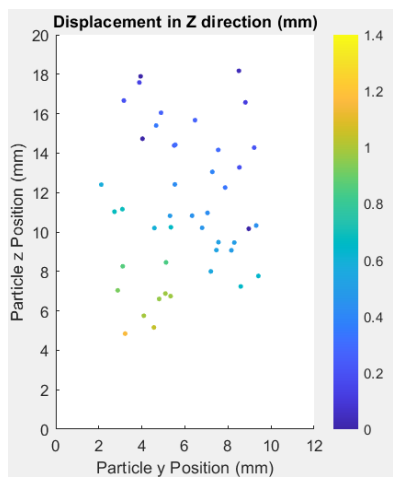
Using the TWS particle segmentation method, particles of the initial sample scan and the loaded sample scan were then re-matched using the algorithm of Druckrey and Alshibli, (2014). Again, the parameters used by this matching algorithm include: the search box centred on the particle centroid (different search box sizes were run to get the best search box size), the matching particle attributes volume, surface area, feret length, and feret width. Various scenarios considering different search box sizes and particle attribute error tolerance were run to achieve the best possible appropriately matched particles. Matching attribute tolerance errors of 2%, 5%, 7% and 10% respectively were considered.

With a 2% attribute error tolerance, no particle was matched. Figures 9 a, b and c show plots of particle y-zposition against particle z-displacement, for attribute error tolerances of 5%, 7% and 10% respectively. It can be observed that with increasing error tolerance, more particles are matched, but as expected this also results in increasing numbers of wrongly matched particles. An increase in attribute error tolerance to 20% resulted in numerous erroneous matches. Although the match gives an overview of the sense of movement of the

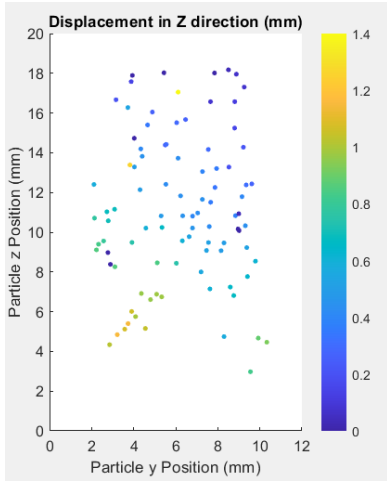
particles (which is from bottom up, as the sample was scanned with the stationary end at the top), the number of particles matched in the test with 10% error tolerance was 95, which represents 4% of the total number of particles segmented.



(a)



(b)



(c)

Figure 9: Result of particle matching using the algorithm by Druckrey and Alshibli, (2014) a) Particle z-axis displacement with a 5% error tolerance, b) Particle z-axis displacement with a 7% error tolerance c) Particle z-axis displacement with a 10% error tolerance.

Figure 9 highlights the need to determine and evaluate unique platy particle attributes that can adequately match a larger number of particles with a low error tolerance. To investigate which particle attributes might be the most effective, the statistics of each attribute were compared between scans. Since both scans contain the same particles, the standard deviations of each particle attribute should be the same. Table 3 shows the normalised difference of the standard deviations (as a percentage) for each particle attribute. The Minor axis length gives the largest normalised difference, followed by Volume, Feret Width, Area, Intermediate axis length, Perimeter, Feret Length and the Major axis length. Although Feret length gives a low normalised difference, it is not a robust attribute for platy particles, since under some loading conditions platy particles may flex, hence this parameter was not examined further.

$$\left(\frac{Sd_1 - Sd_2}{Sd_2} \right) \times 100 \quad [1]$$

Where Sd_1 is the scan 1 standard deviation of the attribute under consideration and Sd_2 is its scan 2 standard deviation.

Table 3: Percentage normalised difference of standard deviation of particle attributes before and after sample compression.

ATTRIBUTE	% Normalised difference
Minor axis Length	8.7719
Volume	6.7568
Feret Width	5.8236
Area	3.4331
Intermediate axis Length	1.7595
Perimeter	1.1205
Feret Length	0.1954
Major axis Length	0.0963

6.5. PLATYMATCH Framework

The approach of Druckrey and Alshibli, (2014) was adapted to match plate-shaped particles. To minimise the issues associated with any remaining segmentation errors, the particle match was optimised based on the calculation of a combined ‘attribute error statistics’, as opposed to the approach based on the assessment of each attribute error in a sequential fashion, which can lead to potential particle matches to be overlooked (particles that do not match the first attribute of the sequence are discarded and not considered anymore when the second attribute is examined and so on). Second, the process was optimised by determining the combination of particle attributes that best discriminates individual particles and hence maximises the number of particles matches that can be reliably obtained.

Figure 10 shows the workflow for PLATYMATCH. The code implements a least square error optimization workflow in MATLAB to match particles from one scan to another with a given error tolerance. The PLATYMATCH workflow is adaptable to different particle geometries, but the relevant attributes will differ for different particle geometries, for example,

in the case of ‘needle-like’ fibres, the fibre diameter and fibre length may prove discriminatory particle attributes. The workflow proceeds as follows.

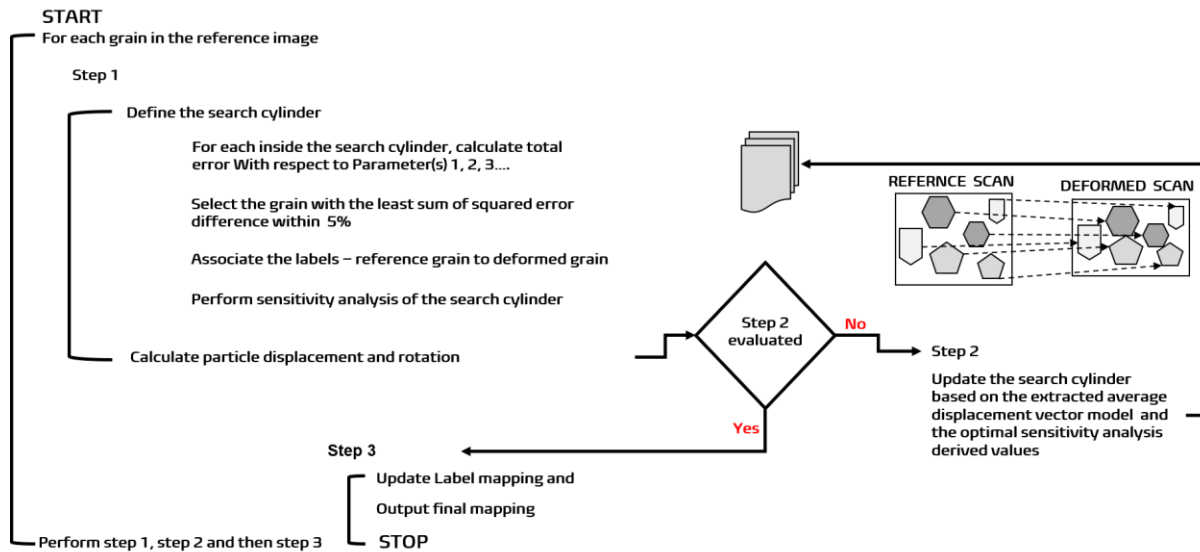


Figure 10: PLATYMATCH workflow

First, we define x_{ik} as the value of the k^{th} attribute for particle number i in scan 1, where $k=1, \dots, q$ and q is the total number of attributes. So for example, if we used volume, area and perimeter, $q=3$ and x_{i1} , x_{i2} and x_{i3} would be the values of volume, area and perimeter respectively for particle i scan 1.

Particles are then matched as follows. For each particle i in scan 1, where $i=1, \dots, n$ and n is the total number of particles in scan 1, a search cylinder is defined in scan 2, the centre of which is the coordinate of the barycentre of particle i in scan 1. If each cylinder in scan 2 contains m particles, then in order to find the best particle match for particle i , PLATYMATCH calculates the sum of the normalised square differences in the particle attribute values, Δ_{ij} , for each possible matching particle $j = 1, \dots, m_i$ in the search cylinder in scan 2:

$$\Lambda_{ij} = \sum_{k=1}^q \left[\frac{\sqrt{(x_{ik}^2 - x_{jk}^2)}}{x_{ik}} \right] \quad [2]$$

Then, particle j_{match} is the matched particle if

$$\Lambda_{ij_{match}} = \min_{j=1, \dots, m_i} \{\Lambda_{ij}\} \quad [3]$$

and $\Lambda_{ij_{match}} <$ user defined error threshold. If $\Lambda_{ij_{match}} >$ the error threshold then the particle match is discarded and no match for particle i is achieved.

Particle displacement is calculated as the Euclidian distance between particle initial and final position.

$$Displacement = \sqrt{(X_1 - X_2)^2 + (Y_1 - Y_2)^2 + (Z_1 - Z_2)^2} \quad [4]$$

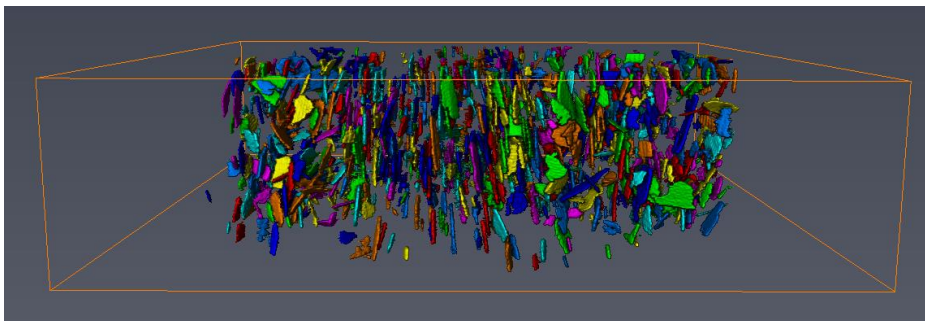
6.6. PLATYMATCH Implementations

PLATYMATCH was evaluated using three tests. The first ‘Rotation’ test was conducted to understand which particle attribute produced the largest number of adequately matched particles, whilst maintaining a satisfactorily low error tolerance. The second ‘Replacement’ test was conducted to evaluate the effect of sample image processing on particle matches. Finally, the code was used to match the particles and analyse the particle kinematics of the Compression test presented earlier.

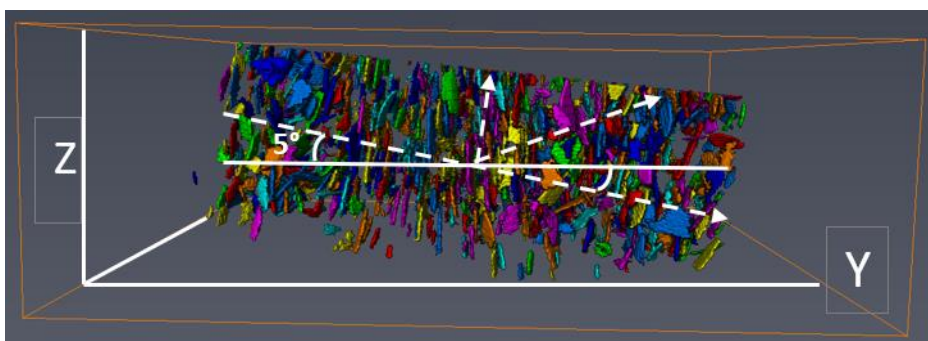
6.6.1. Evaluation of particle matching attributes using the artificially rotated sample (Rotation Test) – Attribute Analysis.

In this test, the sample was reconstructed, processed to identify the particles, and the particles attributes extracted for 'scan 1'. The scan was then artificially rotated by 5 degrees along the y-z- plane (within Avizo), then re-processed and the new particle attributes obtained for 'scan 2'. Figure 11 shows the segmented sample before and after rotation.

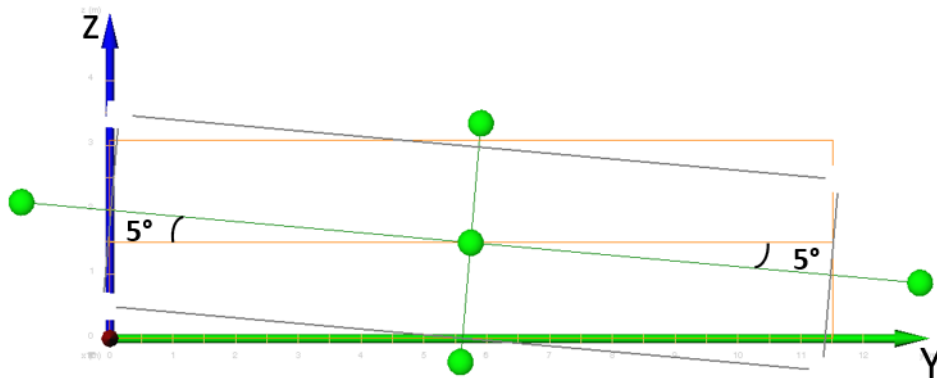
The uniqueness of the attributes with respect to the platy nature of mica particles were evaluated to determine which attribute or attributes may be more suited for matching the platy particles considering the platy nature of the particles and their relatively small *c*-axis compared to the resolution of the X-CT. The use of derived attributes (attributes resulting from mathematical combination of basic morphological attributes- primary attributes) instead of primary attributes may present some challenges due to larger error and uncertainty in their values. Hence it is proposed that using primary attributes that are not functions of the minor axis (*c*-axis) length and do not change significantly with sample deformation will be a more unique identifiers, enabling effective platy particle matching across scans.



(a)



(b)



(c)

Figure 11: a) sample after image processing and segmentation but before rotation b) sample after 5 degrees rotation along the y-z plane c) sample sense of rotation, the orange line indicates the initial sample boundary and the grey line indicate the sample boundary after the 5 percent rotation.

To understand the particle attribute or attribute combination that give the best match, each attribute was used individually in turn to match the particles between the two scans. Particle attributes used were volume, perimeter, area, major axis length, and intermediate axis length, minor axis length, Feret length and Feret width. Attributes that appeared to give an accurate match were then tested in combination to find the optimum combination of attributes for accurately matching of platy particles.

Results are given in Figure 12 and are expressed as the standard error in the z-coordinate displacement values, which are imposed by the 5° rotation and therefore known. No single attribute gave a z-displacement error of less than 1% between scans. The least error was achieved using an attribute combination of the Major axis length, the Intermediate axis length, and the Perimeter.

Detailed results from combining these three attributes are shown Figure 13a to c. Figure 13a compares the imposed and computed z-displacements showing a satisfactory agreement. Figure 13b clearly shows the rotational trajectory of each matched particle (the view is taken

along the axis of rotation). Figure 13c shows the statistical distribution of the z-displacement error (difference between imposed and computed displacement) in terms of empirical cumulative distribution. This is characterised by a mean of 0.3 μm and a standard deviation =3.0 μm . The Figures also show the normal cumulative and frequency distributions associated with these values of mean and standard deviation, which shows that the error is essentially normally distributed. Errors are likely to be a result of small changes in the voxels used to describe a particle between scans that result in slight changes to the particle segmentation. This can cause the centre of inertia of a particle to be located in a slightly different position within the particle between scans, thus resulting in a small displacement error.

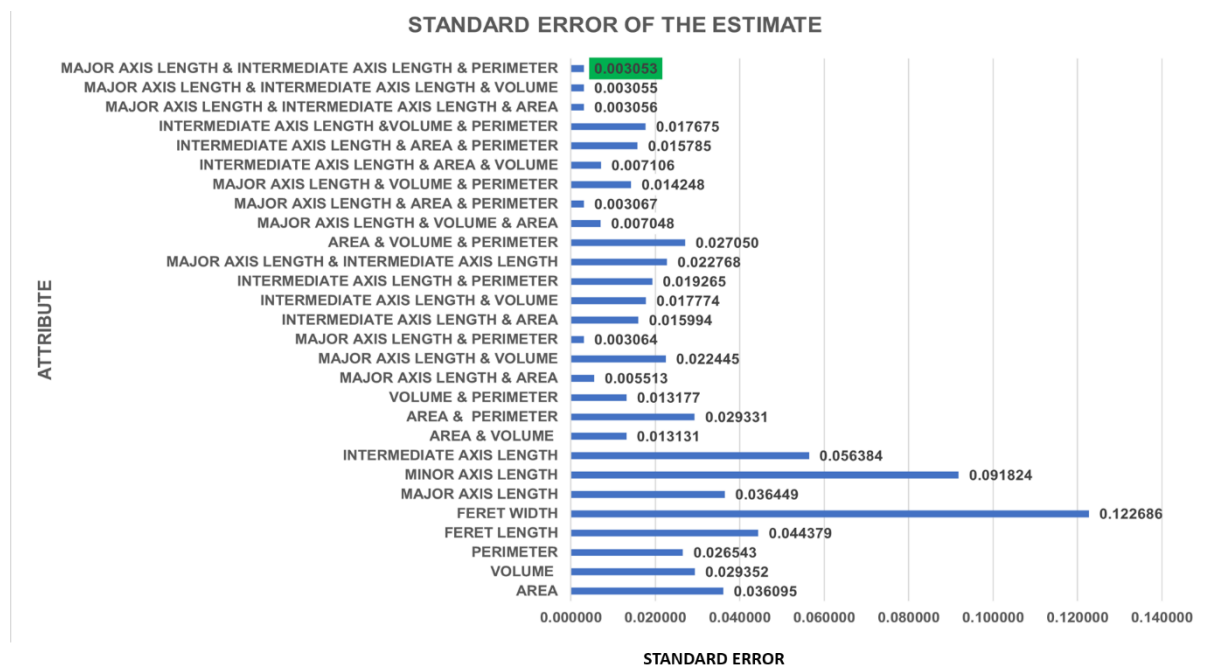
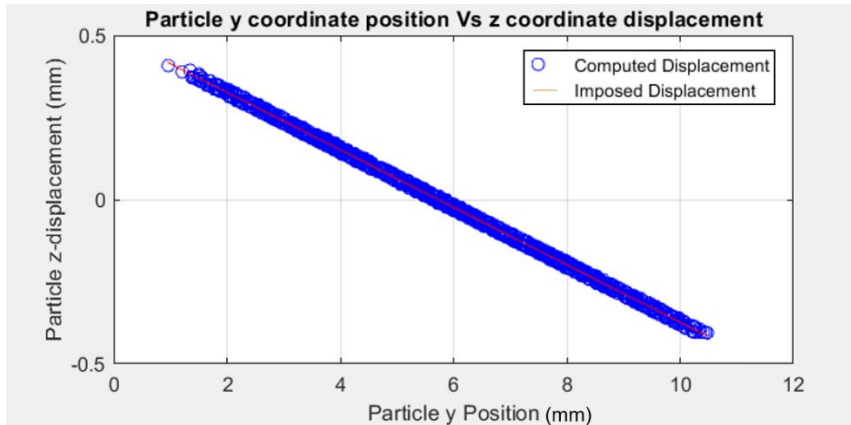
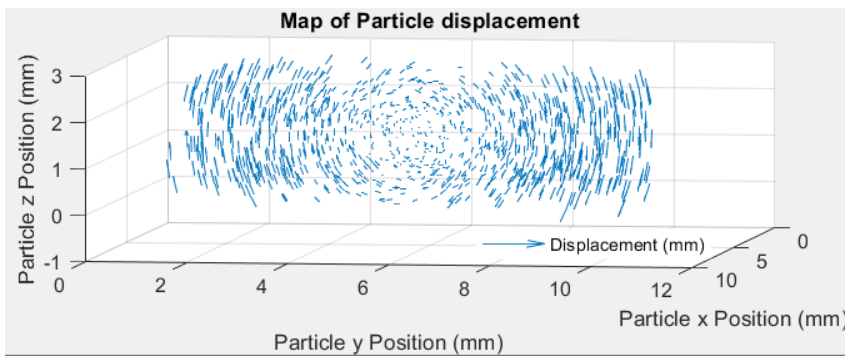


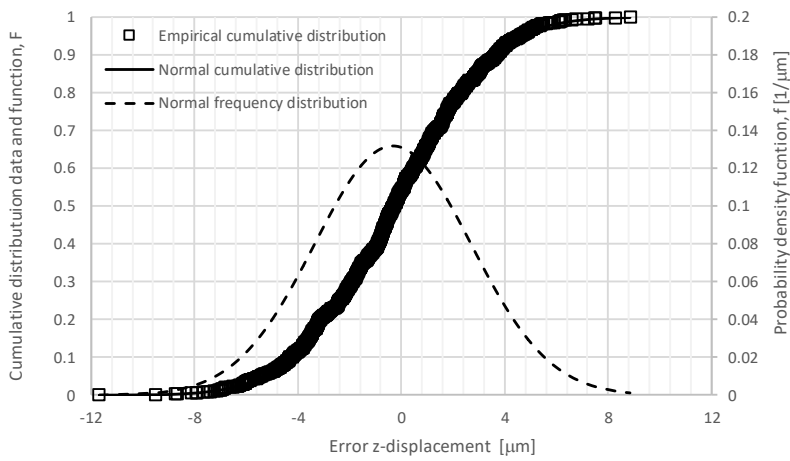
Figure 12: Standard error of Z-coordinate displacement using matched particles for all attribute and attribute combinations, with a combination of major axis length and perimeter giving the least standard error of the estimate



(a)



(b)



(c)

Figure 13: Sample artificially rotated 5° in the y-z plane and unregistered matched to the original sample (without rotation) using Major axis length, and Perimeter as PLATYMATCH search attributes. a) particle y position against z- coordinate displacement; b) displacement vectors; c) Cumulative and frequency distribution of the z-coordinate displacement (mean=0.3 μm and standard deviation=3.0 μm)

6.6.2. *Evaluation of particle matching accuracy, using a sample that was scanned, removed, and replaced and re-scanned (Replacement Test).*

In the Replacement Test, particles have not been displaced (there is no rotation or translation of the image so they should remain virtually in the same location between the two scans). The differences between the two scans should only depend on the ability to align the two scans (i.e., to accurately co-locate the ‘marker’ steel spheres that were inserted into the sample). The two scans were processed, registered and then the particles matched using PLATYMATCH. The matching was performed using Major axis length, Intermediate axis length and Perimeter as PLATYMATCH search attributes and a 5% error tolerance.

Figure 14 shows the statistical distribution of the z-displacements in terms of empirical cumulative distribution. This is characterised by a mean of 3.4 μm and a standard deviation =5.1 μm. The Figures also show the normal cumulative and frequency distributions associated with these values of mean and standard deviation, which shows that the error is essentially normally distributed. The result is consistent with an expected displacement of zero; the scan resolution was at 10 micrometres, hence a z-coordinate displacement cumulative and frequency distribution with a mean of 3.4 μm and standard deviation of 5.1 μm is within the resolution of the scan.

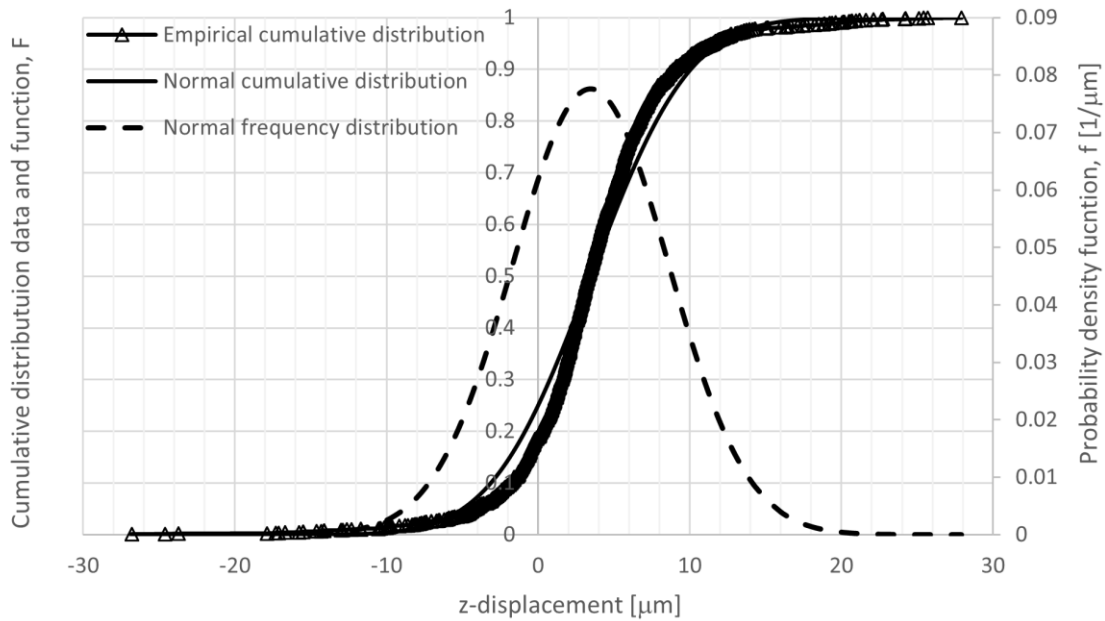


Figure 14: Cumulative and frequency distribution of the z-coordinate displacement (mean=3.4 μm and standard deviation=5.1 μm) .

6.6.3. Particle tracking after unconfined uniaxial compression (Compression Test)

To validate the matching code on a genuine tracking problem, the sample subjected to 8% uniaxial strain, was analysed for particle kinematics. The sample was scanned with the fixed end at the top and the compressed end at the bottom and thus was expected to show higher axial deformation at the bottom compared to the top where motion is restricted. The axial deformation recorded at the bottom by the XCT scan is also expected to be less than the imposed deformation, since the sample experienced some rebound when it was unloaded and removed from the loading frame, prior to the second scan. Since the sample was laterally confined by a rubber membrane, radial deformation was expected to occur with higher values at the bottom (which was being compressed) compared to the top (which is fixed). The sample profile in the x-z and y-z planes before and after compression are shown in Figure 15 and confirms that the sample was deforming in both axial and radial directions.

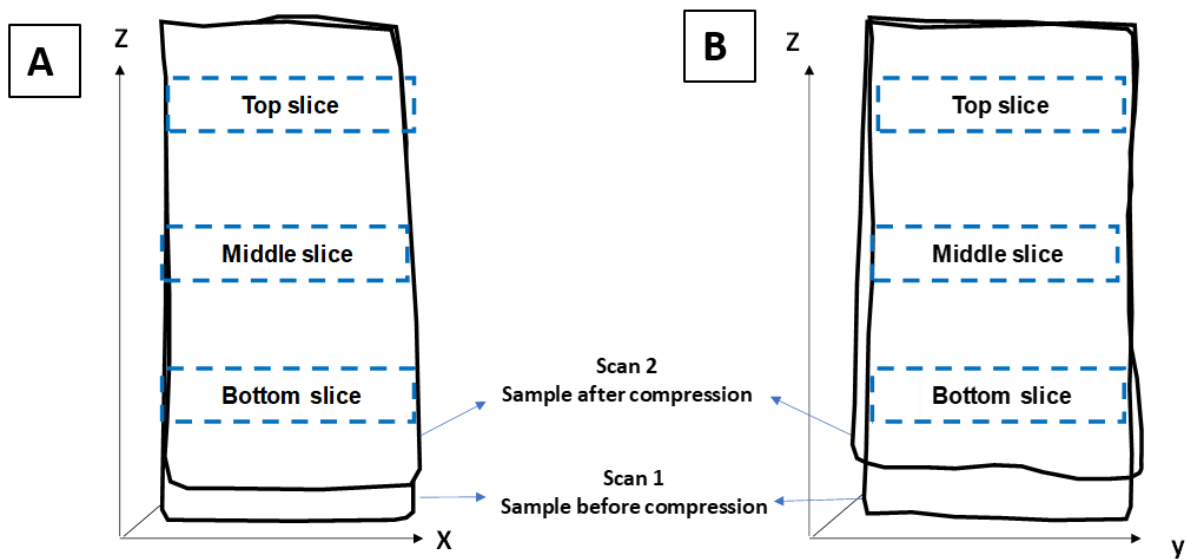


Figure 15: Kinematic analysis of clay sample subjected to 8% axial compression a) particle displacement map along the z-y plane b) Particle displacement vector map in the x-z plane.

Mica particles before and after uniaxial compression were matched to evaluate particle kinematics. As in the previous analysis, Major axis length, Intermediate axis length and Perimeter were used to match the particles with PLATYMATCH. The number of particles matched in the test was 1035, which represents 40% of the total number of particles segmented. The slightly low percentage of particles matched may be due to the relatively large (8%) displacement step applied in the uniaxial compression test, however, as discussed below they are sufficient to accurately capture the sample displacement.

Figures 16 show results of the particle displacements for the sample subjected to an 8% axial strain, with Figure 16a showing the displacement map along the z-y plane and Figure 16b showing the particle displacement vectors in the x-z plane. As expected, the particle trajectory distances reduce from a maximum 1.4 mm at the bottom of the image to zero at the top.

Interestingly, the result in Figure 16b show that the sample does not deform in a homogeneous manner. The displacement vectors are not all parallel to the z-axis, i.e., the

displacement vectors have a horizontal component. This is consistent with the profiles shown in Fig. 15. To explore the displacements in the x-y plane, three slices were considered as shown in Fig. 15. The horizontal component of the displacement of the mica particles contained within these three slices are shown in Fig. 17. The sample is subjected to a slight torsional deformation. When this torsional deformation is discounted, the remaining displacement is radial, which is consistent with the sample profiles shown in Fig. 15.

In the interpretation of the tracking results presented here for uniaxial compression, particle kinematics were only analysed in terms of displacements of their barycentre. However, because particles are platy, analysis of particle orientation may give interesting insights into shear strains, as compared to spherical particles. This may allow a greater understanding of concepts such as initiation and propagation of strain localisation and dilation.

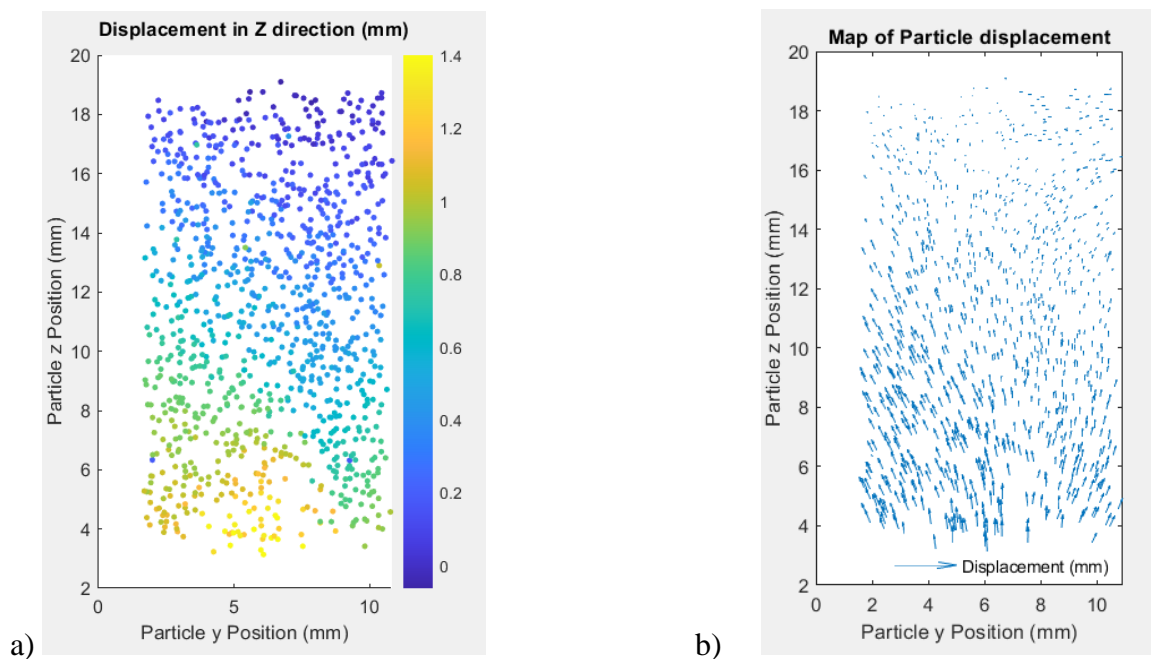
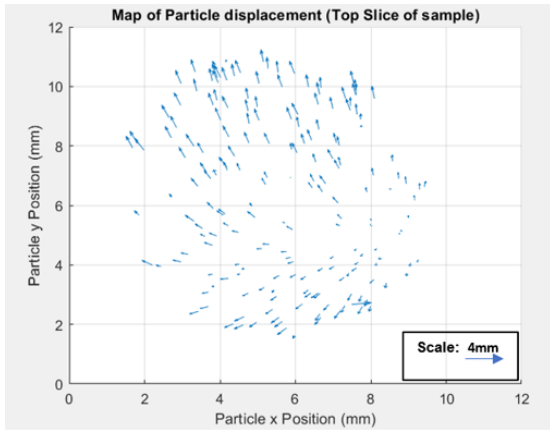
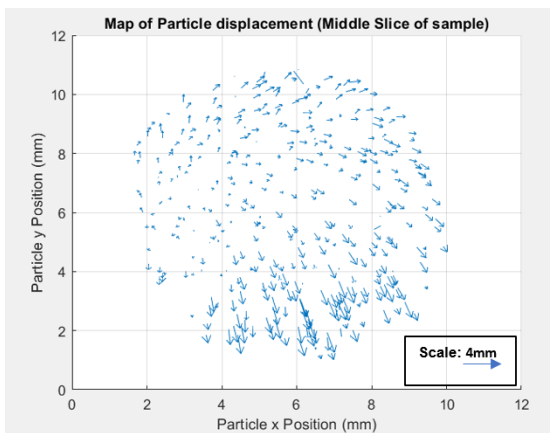


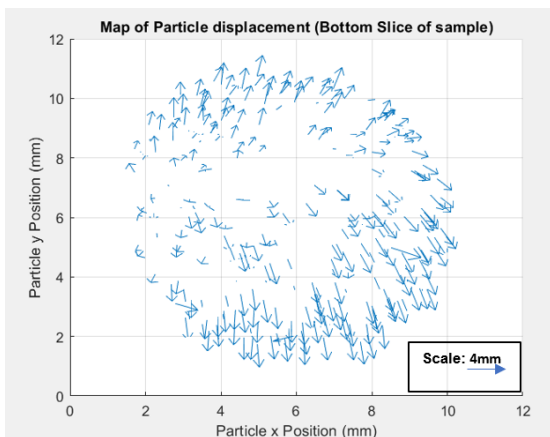
Figure 16: Kinematic analysis of clay sample subjected to 8% axial compression a) particle displacement map along the z-y plane b) Particle displacement vector map in the x-z plane.



(a)



(b)



(c)

Figure 17: Horizontal slice of displacement vectors of compressed sample at the a) top section b) middle section and c) bottom section. (Note that the scale of the displacement vector – arrows, is magnified by a factor of 4).

6.7. Conclusion

This study evaluates, for the first time, kinematic analysis of platy soil particles through individual particle matching. Particles were first matched using an existing algorithm successfully developed for matching round sand particles. Some challenges were observed due to the small size and platy nature of mica. Attributes such as: Feret width, Feret length, minor axis length, which may be unique for round sand particles were observed to be significantly less unique to the platy particles studied. This was due to their tiny c-axis and smaller overall size, which resulted in a poorer image resolution and segmentation errors.

We adapted the matching code by Druckrey and Alshibli, (2014) (which was originally designed for matching sand particles) by incorporating attributes and workflows that are best suited for platy particles to form a matching algorithm – PLATYMATCH. We evaluated platy silt sized muscovite particle attributes to identify unique attributes successful at matching platy particles. PLATYMATCH considers a minimised combined normalised error of parameters of particles within a defined search volume space. Parameters of the algorithm are: location and size of the search volume space, the selected combination of particle geometric attributes and the error tolerance.

The code was tested using a clay sample with mica particle markers subjected to uniaxial compression. The following conclusions were drawn:

- i) Correctly implemented, a voxel training machine learning algorithm gave optimal segmentation results compared to threshold segmentation and hence enhanced particle matching. For objective comparison using the machine learning segmentation, it was important to train the machine learning algorithm using both ‘before’ and ‘after’ scans.
- ii) A combination of particle attributes: major and intermediate axis length and perimeter gave the best particle match, when compared to other particle attributes. Due to the larger errors in

segmentation found on platy particles, the particle attributes should be compared in parallel, rather than sequentially, which avoided filtering out good particle matches based on a single attribute and resulted in a greater number of correctly matched particles.

iii) PLATYMATCH can effectively match platy particles when consecutive scans are adequately registered and particles within scans are adequately segmented.

6.8. Acknowledgements

The publication of this work was made possible through support from the University of Strathclyde Research Studentship. We also acknowledge the support of Mr Derek McNee in assembling the modified oedometer cell and soil Lathe designed in this study.

6.9. Data Availability Statement

Some or all data, models, or code that support the findings of this study are available from the corresponding author upon reasonable request.

6.10. References

- Alonso, E.E., Pereira, J.M., Vaunat, J. and Olivella, S. (2010) ‘A microstructurally based effective stress for unsaturated soils’, *Geotechnique*, 60(12), pp. 913–925. doi: 10.1680/geot.8.P.002.
- Andò, E., Hall, S.A., Viggiani, G., Desrues, J. and Bésuelle, P. (2012) ‘Grain-scale experimental investigation of localised deformation in sand: A discrete particle tracking approach’, *Acta Geotechnica*, 7(1), pp. 1–13. doi: 10.1007/s11440-011-0151-6.
- Arganda-Carreras, I., Kaynig, V., Rueden, C., Eliceiri, K.W., Schindelin, J., Cardona, A. and Sebastian Seung, H. (2017) ‘Trainable Weka Segmentation: A machine learning tool for microscopy pixel classification’, *Bioinformatics*, 33(15), pp. 2424–2426. doi: 10.1093/bioinformatics/btx180.
- Cetin, H. and Gökoğlu, A. (2013) ‘Soil structure changes during drained and undrained triaxial shear of a clayey soil’, *Soils and Foundations*, 53(5), pp. 628–638. doi: 10.1016/j.sandf.2013.08.002.

- Chen, Y., Ma, G., Zhou, W., Wei, D., Zhao, Q., Zou, Y. and Grasselli, G. (2021) 'An enhanced tool for probing the microscopic behavior of granular materials based on X-ray micro-CT and FDEM', *Computers and Geotechnics*, 132(December 2020), p. 103974. doi: 10.1016/j.compgeo.2020.103974.
- Cheng, Z. and Wang, J. (2018) 'A particle-tracking method for experimental investigation of kinematics of sand particles under triaxial compression', *Powder Technology*, 328(September), pp. 436–451. doi: 10.1016/j.powtec.2017.12.071.
- Chevalier, B., Tsutsumi, Y. and Otani, J. (2019) 'Direct Shear Behavior of a Mixture of Sand and Tire Chips Using X-ray Computed Tomography and Discrete Element Method', *International Journal of Geosynthetics and Ground Engineering*, 5(2), pp. 1–12. doi: 10.1007/s40891-019-0160-3.
- Druckrey, A. M. and Alshibli, K. A. (2014) '3D Behavior of Sand Particles Using X-Ray Synchrotron Micro-Tomography', pp. 2814–2821. doi: 10.1061/9780784413272.272.
- Fu, Y., Wang, L., Tumay, M.T. and Li, Q. (2008) 'Quantification and Simulation of Particle Kinematics and Local Strains in Granular Materials Using X-Ray Tomography Imaging and Discrete-Element Method', *Journal of Engineering Mechanics*, 134(2), pp. 143–154. doi: 10.1061/(asce)0733-9399(2008)134:2(143).
- Haldrup, K., Nielsen, S. F. and Wert, J. A. (2008) 'A general methodology for full-field plastic strain measurements using X-ray absorption tomography and internal markers', *Experimental Mechanics*, 48(2), pp. 199–211. doi: 10.1007/s11340-007-9079-z.
- Hall, S.A., Bornert, M., Desrues, J., Pannier, Y., Lenoir, N., Viggiani, G. and Bésuelle, P. (2010) 'Discrete and continuum analysis of localised deformation in sand using X-ray μ CT and volumetric digital image correlation', *Geotechnique*, 60(5), pp. 315–322. doi: 10.1680/geot.2010.60.5.315.

- Hattab, M., Hammad, T., Fleureau, J.M. and Hicher, P.Y. (2014) 'Behaviour of a sensitive marine sediment: Microstructural investigation', *Geotechnique*, 64(1), pp. 89–90. doi: 10.1680/geot.13.D.02.
- Ibeh, C., Pedrotti, M., Tarantino, A. and Lunn, R. J. (2019) 'An x-ray CT study of miniature clay sample preparation techniques', in *E3S Web of Conferences*. doi: 10.1051/e3sconf/20199201004.
- Karamov, R., Martulli, L.M., Kerschbaum, M., Sergeichev, I., Swolfs, Y. and Lomov, S.V. (2020) 'Micro-CT based structure tensor analysis of fibre orientation in random fibre composites versus high-fidelity fibre identification methods', *Composite Structures*, 235(June 2019), p. 111818. doi: 10.1016/j.compstruct.2019.111818.
- Karatza, Z., Andò, E., Papanicolopoulos, S.A., Viggiani, G. and Ooi, J.Y. (2019) 'Effect of particle morphology and contacts on particle breakage in a granular assembly studied using X-ray tomography', *Granular Matter*, 21(3), pp. 1–13. doi: 10.1007/s10035-019-0898-2.
- Lin, Z.Y., Wang, Y.S., Tang, C.S., Cheng, Q., Zeng, H., Liu, C. and Shi, B. (2021) 'Discrete element modelling of desiccation cracking in thin clay layer under different basal boundary conditions', *Computers and Geotechnics*, 130(December 2020), p. 103931. doi: 10.1016/j.compgeo.2020.103931.
- Madra, A., Hajj, N. El and Benzeggagh, M. (2014) 'X-ray microtomography applications for quantitative and qualitative analysis of porosity in woven glass fiber reinforced thermoplastic', *Composites Science and Technology*, 95, pp. 50–58. doi: 10.1016/j.compscitech.2014.02.009.
- Nielsen, S.F., Poulsen, H.F., Beckmann, F., Thorning, C. and Wert, J.A. (2003) 'Measurements of plastic displacement gradient components in three dimensions using marker particles

- and synchrotron X-ray absorption microtomography’, *Acta Materialia*, 51(8), pp. 2407–2415. doi: 10.1016/S1359-6454(03)00053-3.
- Pedrotti, M. and Tarantino, A. (2018) ‘An experimental investigation into the micromechanics of non-active clays’, *Geotechnique*, 68(8), pp. 666–683. doi: 10.1680/jgeot.16.P.245.
- Pedrotti, M. and Tarantino, A. (2019) ‘A conceptual constitutive model unifying slurried (saturated), compacted (unsaturated) and dry states’, *Geotechnique*, 69(3), pp. 217–233. doi: 10.1680/jgeot.17.P.133.
- Reijonen, H. M., Kuva, J. and Heikkilä, P. (2020) ‘Benefits of applying X-ray computed tomography in bentonite based material research focussed on geological disposal of radioactive waste’, *Environmental Science and Pollution Research*, 27(31), pp. 38407–38421. doi: 10.1007/s11356-020-08151-2.
- Shreyamsha Kumar, B. K. (2013) ‘Image denoising based on non-local means filter and its method noise thresholding’, *Signal, Image and Video Processing*, 7(6), pp. 1211–1227. doi: 10.1007/s11760-012-0389-y.
- Sridharan, A., Venkatappa Rao, G. and De, P. K. (1974) ‘Mechanisms Controlling Volume Change Of Saturated Clays and the Role of the Effective Stress Concept’, *Geotechnique*, 24(3), pp. 447–449. doi: 10.1680/geot.1974.24.3.447.
- Takemura, T. (2004) ‘Microstructure observation in deformed geomaterials using microfocus X-ray computed tomography’, *X-ray CT for Geomaterials; Soils, Concrete, Rocks*, pp. 299–304.
- Taylor, H. F., O’Sullivan, C. and Sim, W. W. (2015) ‘A new method to identify void constrictions in micro-CT images of sand’, *Computers and Geotechnics*, 69, pp. 279–290. doi: 10.1016/j.compgeo.2015.05.012.
- Viggiani, G., Lenoir, N., Bésuelle, P., Di Michiel, M., Marelllo, S., Desrues, J. and Kretschmer, M. (2004) ‘Utilisation de la microtomographie rayon X pour l’étude de

la localisation des déformations dans les géomatériaux argileux sous sollicitation axisymétrique’, *Comptes Rendus - Mécanique*, 332(10), pp. 819–826. doi: 10.1016/j.crme.2004.05.006.

Zhao, B., Wang, J., Coop, M.R., Viggiani, G. and Jiang, M. (2015) ‘An investigation of single sand particle fracture using x-ray micro-tomography’, *Geotechnique*, 65(8), pp. 625–641. doi: 10.1680/geot.4.P.157.

6.11. Appendix 1

Trainable WEKA Segmentation approach

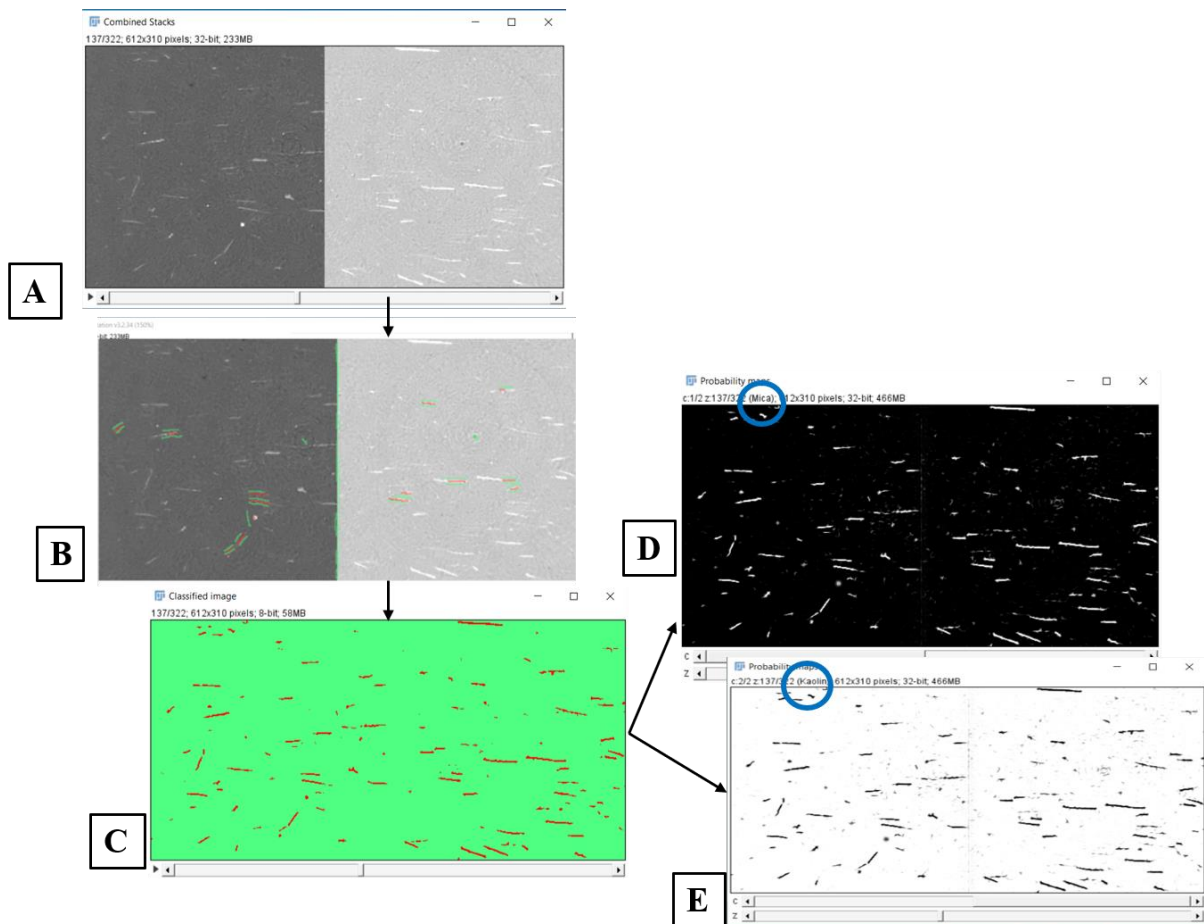


Figure 18 a) Stacks of CT images used for pixel training, b) pixel training of the stacked image c) the stacked CT image classified using TWS d) Mica particles (white section), e) Kaolin (white section).

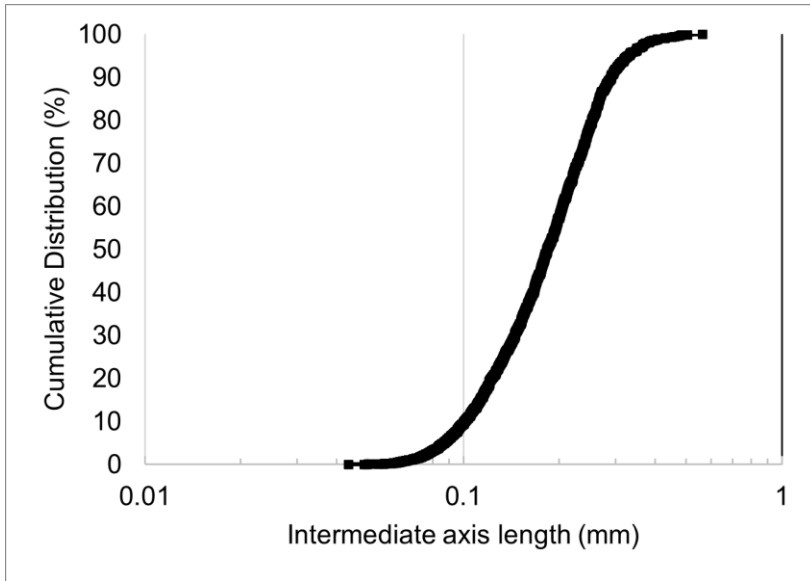


Figure 19: Mica particle cumulative particle intermediate axis length distribution plot.

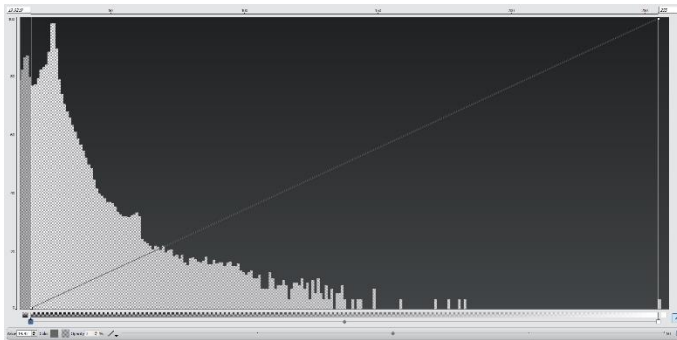


Figure 20: sample grey scale histogram of the imaged sample.

7. Investigating strain localisation in clay using “platy” mica particles and X-ray Computed tomography

Abstract

Mass movements in clay deposits result in damage to infrastructures and buildings with significant social, economic, and environmental consequences. These processes are characterised by strain localisation, a complex process to investigate experimentally and model. Most strain localisation studies of soft clay rely on either the tracking of patterns drawn on clay surface or using natural inclusions to generate adequate texture and enable Digital Volume Correlation of X-Ray Computed Tomography 3D images. This chapter presents a novel versatile approach for 3D detection of shear strain localisation in clay based on the use of platy mica particles embedded in the clay matrix. Mica particles can serve the same purpose as the natural inclusions to produce the texture required for DVC. At the same time, mica particles offer the chance of investigating strain localisation via a number of complementary approaches (displacement and rotation field and orientation map). A miniature triaxial cell, instrumented with a tensiometer to enable us understand pore pressure regimes as the clay sample is sheared was built and validated. An analysis and evaluation of mica marker particle kinematics (displacement and rotation) was carried out for additional insight on the initiation and propagation of strain localisation in kaolin. To the authors' knowledge, this is the first study of soft clay to show 4-D clay particle (mica in this case) rotation within a shear band. The study reveals that we can detect strain localisation in kaolin using mica markers and X-CT prior to the peak shear strength.

Key words: Strain Localisation, X-ray Computed Tomography, Miniature triaxial cell, Mica markers, Kaolin.

7.1. Introduction

Mass movements in clay deposits result in damage to infrastructures and buildings with significant social, economic, and environmental consequences (Yulong Chen et al., 2020; Huang & Dai, 2014; Liu et al., 2018; Pritchard et al., 2014). A common feature of geomaterial instability process is that they most often involve multi-physical and non-linear processes at several length scales, this makes it challenging to predict them accurately. In addition, these processes are often characterized by strain localization, a sudden nonhomogeneous deformation phenomenon (ALERT, 2016). Strain localization is a complex process to investigate experimentally and to model.

Strain localisation can occur in all types of geomaterial (soils, rocks, concrete, etc.) but strain localisation in clays is particularly worrisome because clay is characterised by low shear strength. This makes it important to better understand and better predict strain localisation phenomena in clay. Examples of failures in clay include: the Blue clay slope Spineto landslide system in Italy (Di Maio, C. and Vassallo, 2011); the Agulu-Nanka landslide in west Africa (Ibeh, 2020); Black Ven mudslide complex in Dorset, UK (Chandler, J.H. and Brunsten, 1995); and mudslide in Southern California (Ren et al. 2011). Shear bands may form as a symmetric conjugate bands, asymmetric conjugate bands or a single band. The formation of either of these may be attributed to conditions such as sample layering, uneven loading, and sample morphology (height to diameter ratio). A special type of shear band is known as a kink band. Kink bands are formed by strain localisation and have the following characteristics: i) the deformation band is misoriented from the rest of the sample ii) there is approximately

uniform misorientation across the width of the band and iii) the relationship between the boundary of the deformation band (β) and the rotation of the materials within the deformation band (ϕ) is about $\phi = 2\beta$ (Nizolek et al. 2017).

Shear strain localisation has been investigated by drawing a mesh on the sample surface and tracking the displacement of the mesh nodes. The strain field was then derived from the gradients of the displacement field assumed to be continuous (Sachan & Penumadu, 2007). The resolution of the strain field depends on the spacing of the mesh nodes and shear bands with thickness smaller than the node spacing might be difficult to capture.

Digital Image Correlation (DIC) has also been used to map the shear strain field. Sample surface is stained to produce an artificial texture and the surface is subdivided in pixel subsets. Each pixel subset is cross-correlated in the images before and after deformation to derive the displacement field of the centres of the pixel subsets. The displacement field is then interpolated to generate the strain field (Zhang et al. 2005; Kim et al 2017; Thakur et al. 2018; Kwak et al., 2020). The main limitation of this approach is that soil deformation is only observed at the sample boundary.

An extension of the DIC is the Digital Volume Correlation (DVC) based on 3D images acquired via X-ray Computed Tomography. The applications presented by Viggiani et al. (2013) and Birmpilis et al. (2017) have relied on natural inclusions (calcite inclusions or quartz silt particles respectively) to generate the speckle pattern required for the DVC. This approach has allowed detection of strain localisation patterns forming and evolving through loading.

This chapter presents a novel versatile approach for 3D detection of shear strain localisation in clay based on the use of mica particles embedded in the clay matrix. Mica particles can serve the same purpose as the natural inclusions to produce the texture required for DVC. At the same time, mica particles offer the chance of investigating strain localisation via a number of complementary approaches that can effectively complement the DVC method.

A displacement field can be derived by tracking the displacement of individual mica particles, which can be potentially compared to the displacement field inferred from the DVC. In addition, the platy shape of the mica particles allows enriching the dataset with information associated with the orientation and rotation of the particles possibly revealing mechanisms that the displacement field (inferred from either DVC or particle tracking) cannot highlight.

For this purpose, a miniature triaxial cell was built and instrumented with a high capacity tensiometer, to allow for measurement of the clay pore-water pressure during undrained shear test. Several samples of Speswhite kaolin having different mica particle alignment were first sheared and then scanned post-mortem with X-ray CT. Finally, an analysis of the kinematics (displacement, rotation, and orientation) of mica markers within the kaolin samples is presented to show the potential of this approach of investigating mechanisms of strain localisation in clay.

7.2. X-ray Computed Tomography

On an X-ray CT system, X-ray are produced through a source with the sample to be imaged placed at a distance from the source. In carrying out X-ray imaging, X-ray radiographic projections of the sample are first recorded at several angular points through the X-ray CT stage rotation. The acquired attenuation signatures are reconstructed through tomographic reconstruction which consists of linear integration of attenuation, using reconstruction techniques such as filtered back propagation (Singh et al., 2010). The images are then filtered to remove/suppress noise (unwanted signal) prior to segmentation. Thereafter, elements of the X-ray CT image are differentiated through a technique known as segmentation (which divides an image into regions or categories, which correspond to different objects or parts of objects). The segmented images are then used to analyse sample properties. In this study, sample to be

imaged is placed in a miniature triaxial cell (described below) which sits on the X-ray CT rotating stage.

7.3. Miniature Triaxial cell apparatus

7.3.1. Schematic of triaxial apparatus

A miniature triaxial cell (Figure 1) was designed such that its radial effective stress is generated by suction in the clay sample and as such there is no need for a confining fluid around the sample as in conventional triaxial cell design. Different confining pressure can be tested by preparing samples at different initial suctions. With this design, the sample being imaged can be brought closer to the X-ray source for resolution as high as 3 μm , however for this study, we used a sample size with a diameter the size of a High-Capacity Tensiometer (HCT) (Tarantino & Mongiovì, 2001) and with this set-up we achieved a resolution of 10 μm .

The cell is composed of six elements arranged in series: an actuator, a button load cell, a ball bearing, a steel rod, the sample, and a HCT (see Figure 1a for the equipment set-up and Figure 1b for the triaxial cell description). A displacement transducer is used to monitor the vertical displacement of the specimen. An upward vertical displacement is imposed on the sample from the bottom through a precision actuator (see part labelled 9 in Figure 1a). The actuator is housed within the cell frame and is controlled using an X-MCB1 Zabber controller and Zabber open-source software (see appendix 1) through which the rate of displacement is modulated. The vertical load is measured by a button compression load sensor (Omega LC302 – 100 N sensor) with a capacity of 100 N and 19 mm diameter (see part 7 of Figure 1). The button load sensor is housed within a metallic hollow cylinder in series with the actuator and the sample. To avoid bending moment, the load cell button is in contact with a smooth steel ball that maintains point contact with the mounting base directly on top. The steel ball, load

cell housing and the soil mounting base are all temporarily enclosed within a specially designed split mould which is removed just before the start of sample compression test. Above the ball bearing is a steel rod upon which the sample to be tested sits. The rod also acts as a base for latex membrane covering the sample and for the O-ring holding the latex membrane in place, ensuring that the sample is air and watertight. The high capacity tensiometer is in contact with the top of the sample and seats in a ball bearing housing at the top and it enables suction measurement up to 1500 kPa and serve as a base upon which the top part of the latex membrane sits as well as the base for the top O-ring, latches. A dedicated frame was built to load the cell as shown in Figure 1b. Additional details of the miniature triaxial cell apparatus and the test procedures are given in the appendix 1.

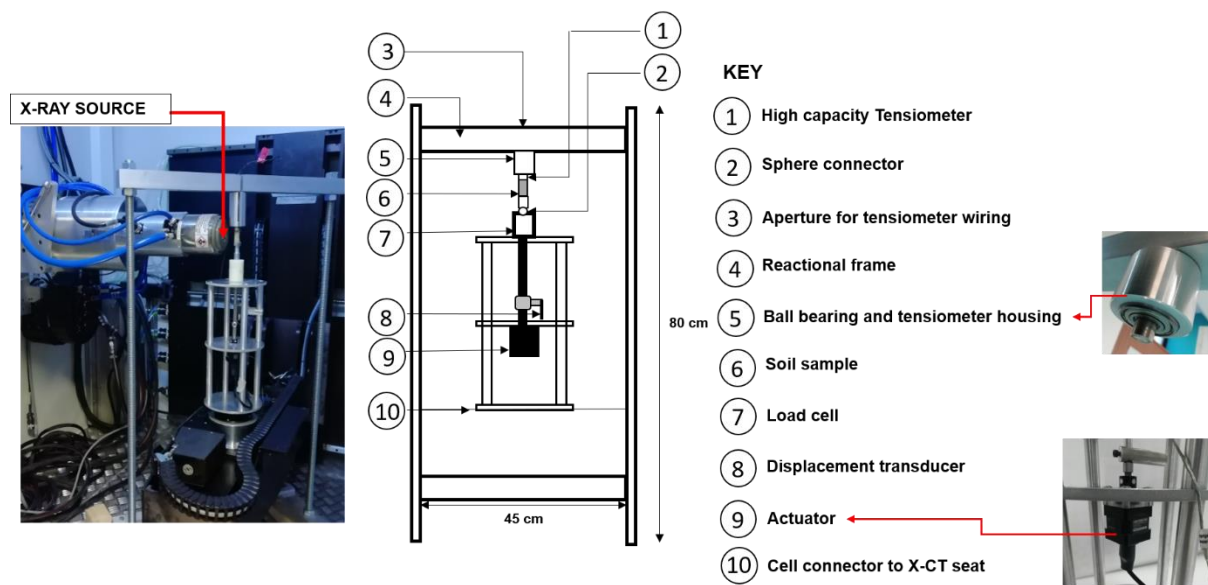


Figure 1a: Miniature Triaxial cell set-up schematic.

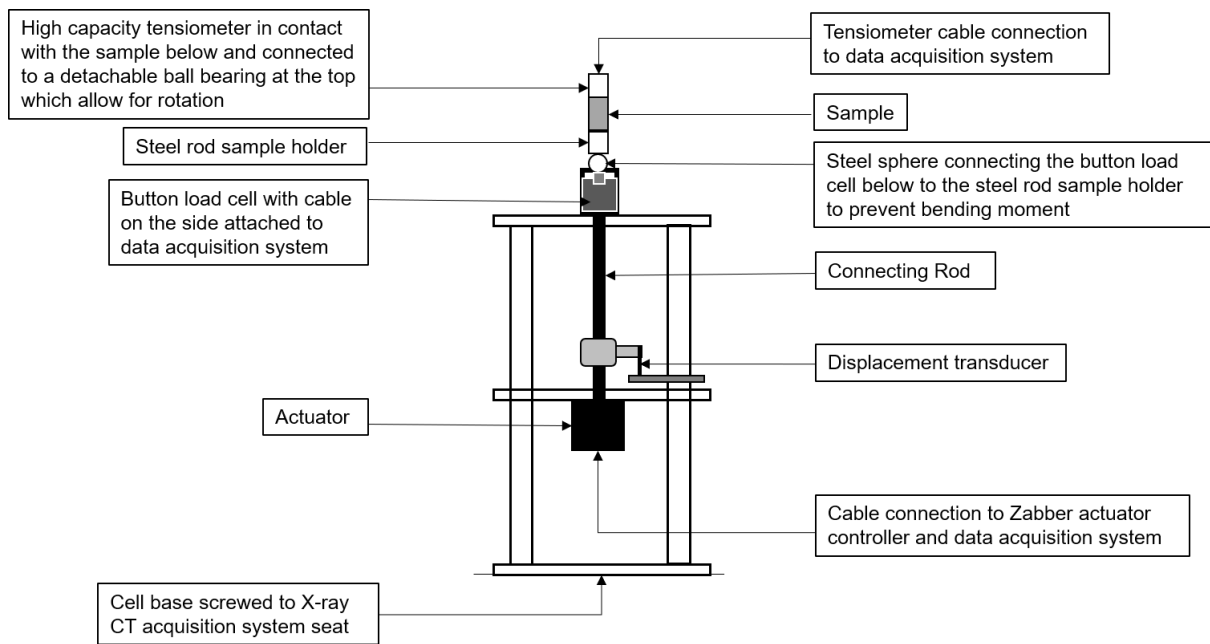


Figure 1b: Miniature triaxial cell

Table 1 presents the apparatus sensor’s full-scale range and resolution. Table 1 presents details of the sensors in the miniature triaxial cell. The linear actuator (NA14B16-T4-MC04 purchased from Zaber Technologies Inc) has 16 mm travel, 180 N maximum continuous thrust, 0.09525 μm resolution and 0.000058 mm/s minimum speed.

Table 1: Description of equipment sensor full scale range and resolution

Features	Full scale range	Resolution/Accuracy
Tensiometer	Up to -1500kPa	1.5 kPa (0.5% full scale output FSO)
Displacement Transducer	0 - 10cm	0.001 μm
Loadcell	0 to 100N	$\pm 0.5\%$ FSO linearity,
Actuator resolution	Up to 16mm	0.09525 μm

The miniature triaxial cell is limited in the following ways:

- i) the equipment is not instrumented with controls for cell and back pressure, and the equipment is currently not suitable for conducting either a drained triaxial test or a flow test. Modification of the test cell would be possible if these tests were required in the future.

- ii) The equipment is currently designed to allow for stepwise X-ray CT scan at increasing strain levels. However, due to creep in the clay, obtaining effective scans of the sample under load would require a redesign of the loading frame.
- iii) The instrumented high capacity tensiometer measures bulk sample pore-pressure distribution and not local pore pressure distribution. At present, no triaxial cell (conventional or miniature) is currently able to provide a spatial distribution of the pore pressure within clay samples. As part of future research, the author is working on the development of techniques for evaluating the spatial distribution of suction within clay samples.

7.4. Miniature Triaxial Test

7.4.1. Materials and sample preparation:

As shown in Table 2, six samples were sheared with the miniature triaxial cell. The first two samples were prepared with 100% Speswhite kaolin and the other 4 samples contained 98.5% kaolin and 1.5% mica by weight. The mica has an equivalent average grain size of about 30 μm determined through laser diffraction analysis and the kaolin is characterised by an 80% clay-fraction (fraction < 2 micrometer) and a 20% silt-fraction. The samples were reconstituted from slurry (1.5 the liquid limit of Speswhite kaolin) and consolidated in an oedometer cell. To allow for a final sample height of 30 mm, the height of the oedometer cell was increased to 40 mm as described in chapter 6. Samples were first consolidated to 2200kPa and then unloaded under drained conditions to 200kPa in the oedometer. From 200kPa the samples were unloaded under quasi-undrained conditions. For this last step, in order to minimise sample's rebound, the oedometer reservoir was emptied prior and then unloaded as fast as possible. Soil specimen were then trimmed using a miniature lathe machine as described by Ibeh et al., (2019).

All trimmed samples were cylindrically shaped with size of 20 mm height and 10 mm diameter and covered with cling film and sealed in a plastic bag to ensure that the water content did not change. One sample (0H) was trimmed so that the cylinder long axis was aligned with the loading direction in the oedometer (see Figure 2). The other samples were trimmed in the direction orthogonal to the loading direction (see Table 2). The rationale behind the different trimming orientation is that samples trimmed in a direction parallel to the oedometer loading direction are expected to have mainly horizontal mica particles, whereas sample trimmed in the orthogonal to the loading direction are expected to have vertical mica particles (Figure 2).

Table 2: Description of samples tested.

S/N	ID (H represent horizontal and V, vertical particles)	Kaolin weight %	Mica weight %	Vertical stress/strain	Sample trimming direction with respect to oedometer loading direction	X-ray Image
1	0H	100	0		Parallel	No
2	0V	100	0		Perpendicular	No
3	1MV	98.5	1.5		Orthogonal	Yes
4	2MV	98.5	1.5		Orthogonal	Yes
5	3MV	98.5	1.5		Orthogonal	Yes
6	4MV	98.5	1.5		Orthogonal	Yes

7.4.2. Testing procedure:

The triaxial compression tests on the over-consolidated samples were performed with the miniature cell described above. For all samples, shear was performed at a compression rate of 0.5µm/s (2.16%/day). During the shear, axial deformation and negative pore-water pressure were continuously measured. Samples “0” (OH and OV) were sheared up to failure to produce a ‘baseline’ stress-strain curve. Samples 1MV, 2MV, 3MV and 4MV were sheared to 4.5% strain, to 5.5% strain, to 6% strain and to 10% strain level respectively (see Figure 3).

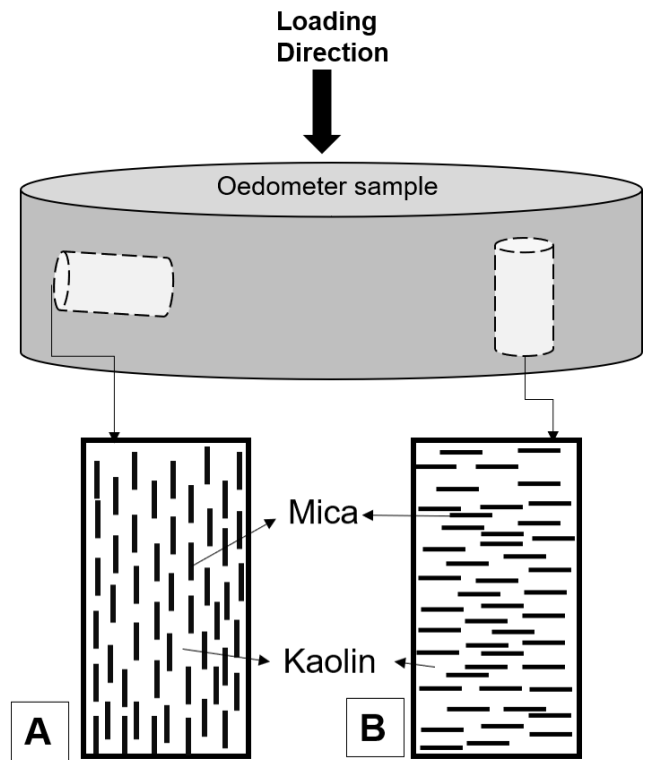


Figure 2: Mica particle orientation within kaolin a) Sampled perpendicular to the oedometer loading direction (particles vertically aligned) and b) Sampled parallel to the oedometer loading direction (particles horizontally aligned).

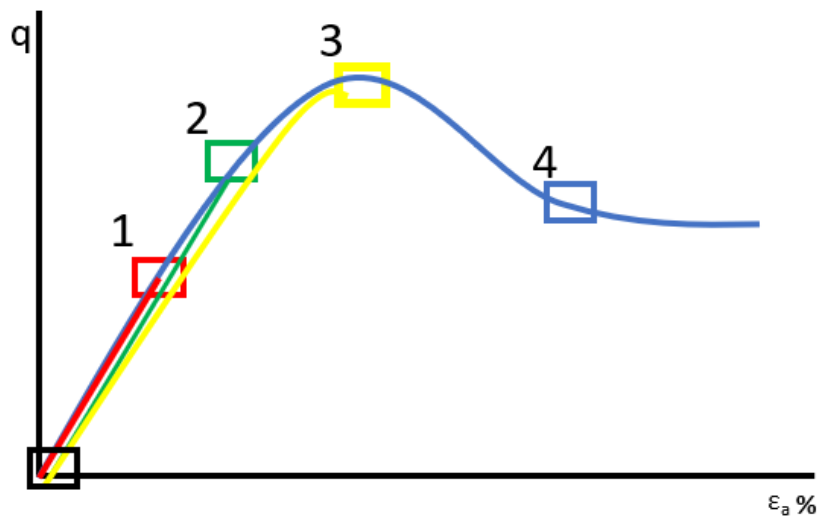


Figure 3: Scan steps for the four samples imaged. Blue curve is associated with sample '0'.

Samples “0” were not imaged. Sample 1MV, 2MV, 3MV and 4MV were imaged using X-ray CT at the University of Strathclyde with NIKON XTH transmission source, focal Spot Size of 1micron, detector size of 2000 x 2000 and detector Pixel size of 200 μm . A voxel size of 10 μm was used to image the samples, with X-ray energy of 160 kV, power - 9.8 W and exposure time of 1 second. A scan of each sample took about 50 min. The samples were scanned before and after compression (under unloaded conditions). It is worthy of note that the 4 experiments are stopped at different points along the curve, as shown in Figure 3. The variations in the angle of failure, especially for sample 4, is a consequence of difference in the initial conditions of the samples and is discussed in the following sections (in sample 4, the mica fabric within the clay material is slightly curved).

7.4.3. Particle Matching

PLATYMATCH, a ‘platy’ particle matching algorithm developed by (Ibeh et al. 2021c) was used for the mica particle matching. The X-CT images were first reconstructed to obtain a 3D grey-scale image, processed using non-local means filter to enhance mica and kaolin discrimination. The image was segmented in Image J using WEKA machine learning algorithm: and the mica particles identified. Mica particle attributes were then calculated in AVIZO. Same particles in the initial scan and the subsequent scan after compression were then matched using the PLATYMATCH code. The code implements a least square error optimization workflow in MATLAB to match particles from one scan to another with a given error tolerance. The parameters used for the matching included i) the particle matching attributes (major axis length, intermediate axis length and Perimeter and the particle x, y, z coordinates), ii) the search cylinder (diameter and height), and iii) an error tolerance (5%).

The algorithm outputs matched particles with their corresponding attributes and the three displacement coordinates. The orientation is then characterised as shown below for further analysis.

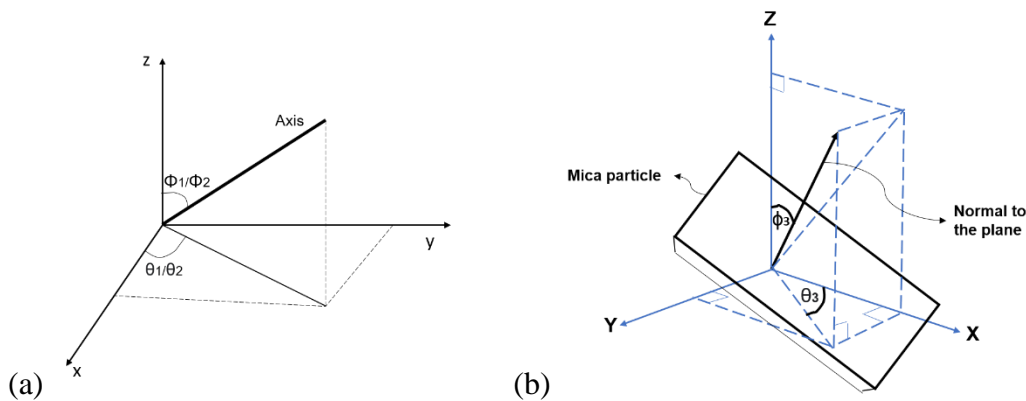
7.4.4. Particle orientation

The particle orientation was characterised in terms of dip and strike (Figure 4c) which were derived as follows. For each segmented particle, AVIZO returned the orientation of the major and intermediate axes (denoted with 1 and 2) in terms of angles ϕ and θ (Figure 4a). The normal to the plane characterised by the angles ϕ_3 and θ_3 (Figure 4b) was calculated as:

$$\cos(\phi_3) = \sin(\phi_1) * \sin(\phi_2) * \sin(\theta_2 - \theta_1) \quad [1]$$

$$\tan \theta_3 = \frac{\cos \phi_1 \sin \phi_2 \cos \theta_2 - \cos \phi_2 \sin \phi_1 \cos \theta_1}{\sin \phi_1 \sin \theta_1 \cos \phi_2 - \sin \phi_2 \cos \phi_1 \sin \theta_2} \quad [2]$$

These two equations were derived by first calculating the unit vectors in the direction of major and intermediate axes (1 and 2) and then considering the dot product between these vectors. Finally, the dip to the plane was calculated by subtracting ϕ_3 from 90° and the strike by adding 90 to θ_3 (dip ranges from -90° to a $+90^\circ$).



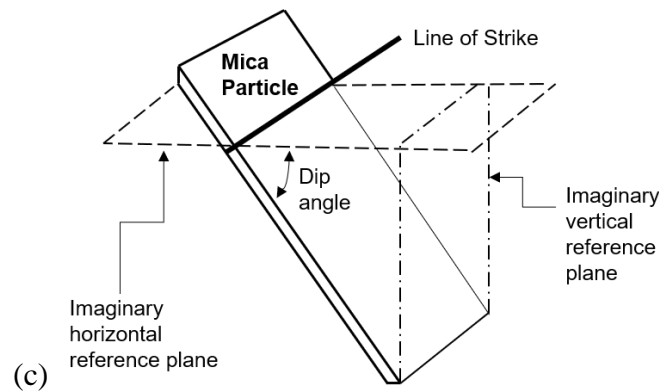


Figure 4: a) Angles formed by the major and intermedia axes. b) Angles ϕ_3 and θ_3 formed by the normal to the plane c) particle strike and dip d) Pole to plane angles

The particle rotation was calculated as the difference in the particle initial and final orientation (change in dip). A rotation convention such that clockwise rotation is negative and anti-clockwise rotation is positive was used. Plots of particle initial and final orientation (in terms of dip and strike) particle rotation as well as particle displacement were analysed in conjunction with the segmented X-ray CT image. The particle kinematics was then used to evaluate the initiation and propagation of strain localisation in the clay samples.

7.5. Test result and discussion

7.5.1. Triaxial test on kaolin samples

Figure 5 shows the axial stress (Figure 5b) and the pore-water pressure (Figure 5b) against axial strain for samples 0H and 0V. Both samples show a ‘dilatant’ behaviour as the suction is first decreasing up to an axial strain of about 2% and 3% for samples 0V and 0H respectively and then increasing again. Test results for sample 0H shows an increase in axial stress up to peak followed by a reduction as expected for an over-consolidated sample. The peak stress is barely noticeable for sample 0V.

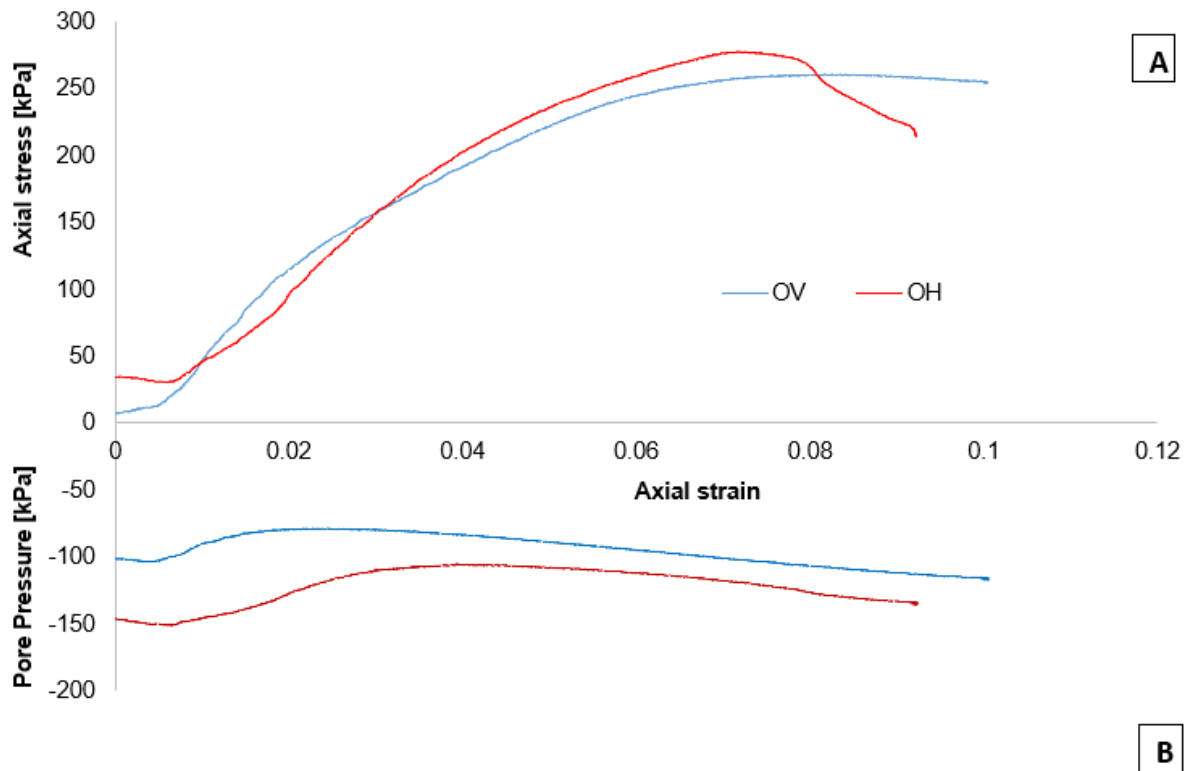


Figure 5: Plot of axial stress (A) and pore pressure (B) against axial strain. Sample OH – major principal stress direction in triaxial test parallel to major principal stress direction during consolidation (horizontal mica particles). Sample OV – major principal stress direction in triaxial test orthogonal to major principal stress direction during consolidation (vertical mica particles)

In Figure 6, the stress path (deviatoric stress q vs isotropic effective stress p') is reported for the two samples. The Critical State Line (CLS) obtained by Murray & Tarantino (2019) from conventional CU triaxial tests on the same speswhite kaolin clay is also shown in the Figure. The stress path of sample OH, despite not reaching an ultimate state as shown in Figure 5a, appears to converge towards the critical state line suggesting that the mini-triaxial cell produced satisfactory triaxial measurements.

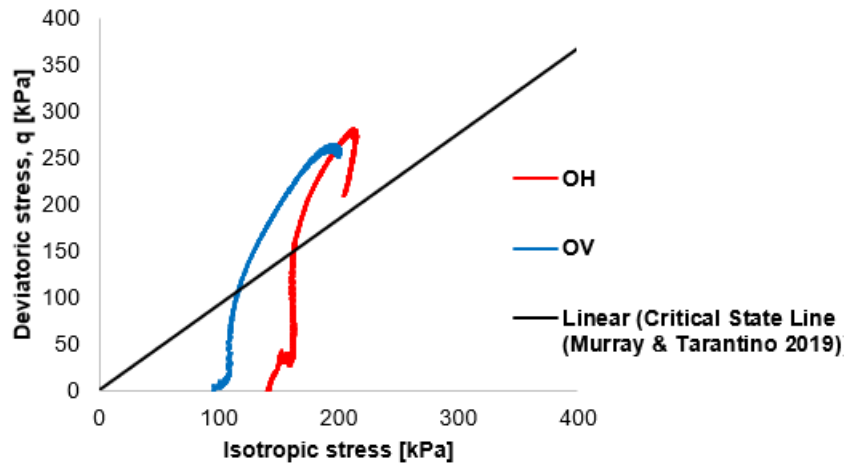
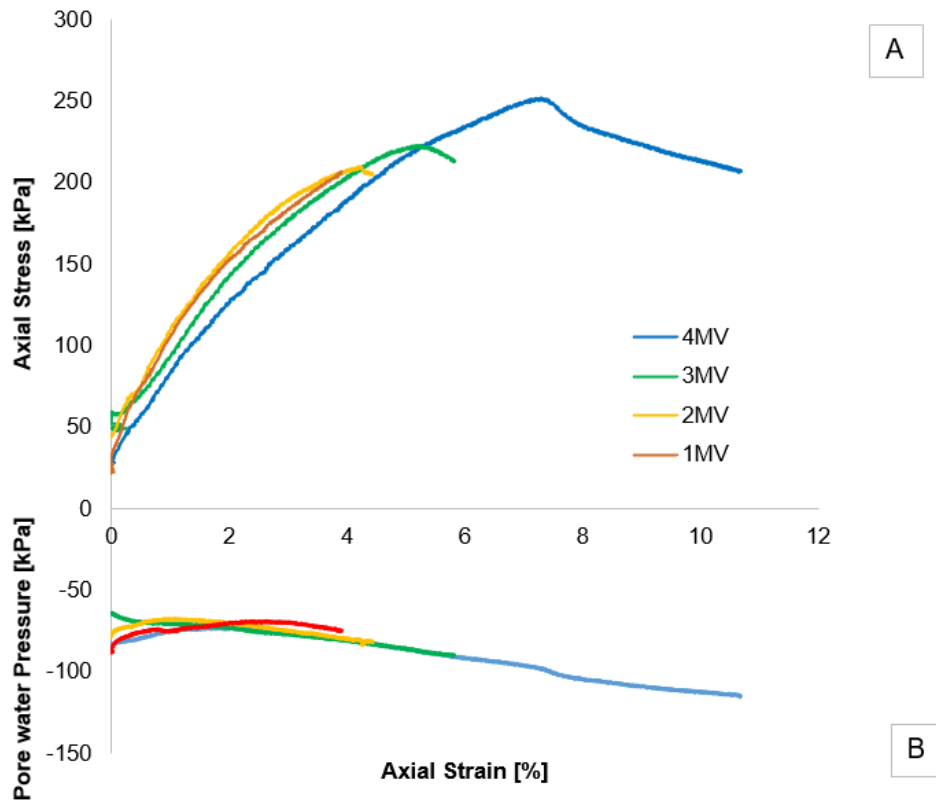


Figure 6: Stress paths and for sample OV and OH.

7.5.2. Triaxial test on kaolin with mica markers

Results of triaxial compression of the four kaolin samples with 1.5% wt mica sheared to different stages are shown in Figure 7a and b. It can be observed that the four samples follow the same shear stress path. Similarly, the $p' - q$ plot shows that the samples align to the same strength envelope (Figure 7c).



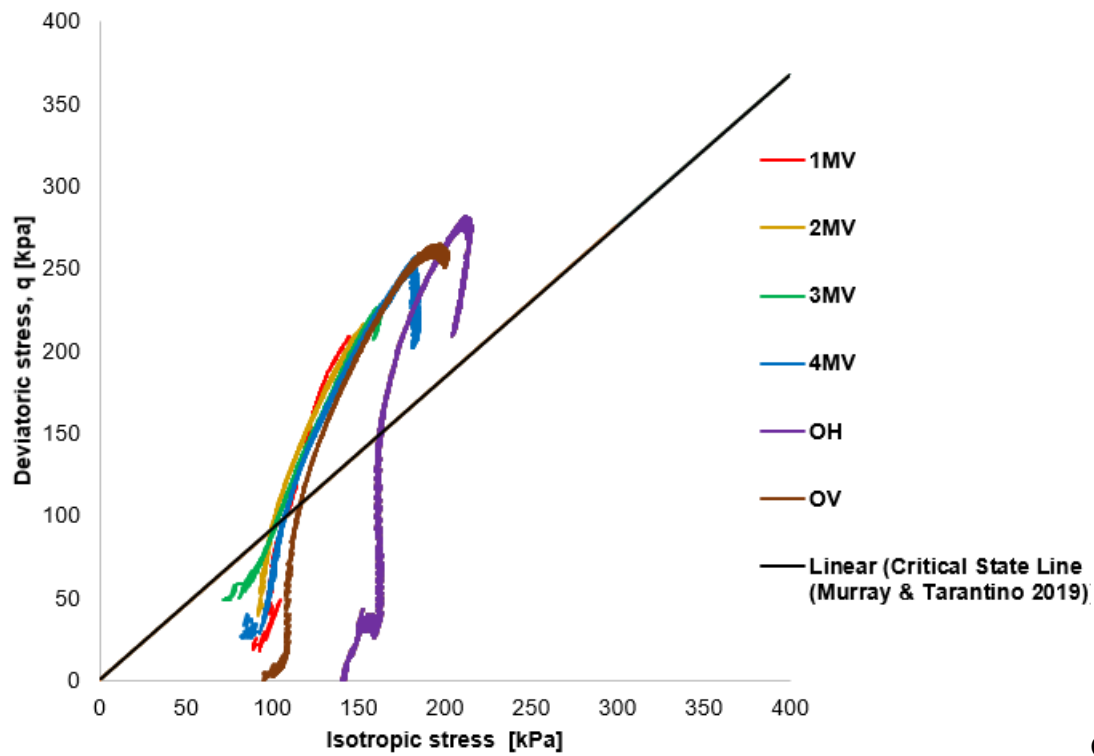


Figure 7: a) plot of axial stress against axial strain for the 4 sheared samples and b) plot of pore water pressure and axial strain for the four samples c) p' - q plots of kaolin samples with mica and sheared to different strain levels with the critical state line for kaolin from Murray and Tarantino (2019).

It is worthy of note that the addition of silt sized muscovite particle markers to kaolin may jeopardise the response of the clay. Ibeh et al., (2021b) showed that, depending on water chemistry, silt sized muscovite may exhibit dispersive or non-dispersive behaviour, and this is similar to the behaviour of kaolin (Pedrotti & Tarantino, 2018). It is therefore important to check that the mica is not altering the behaviour of the kaolin. Direct shear test and oedometer tests by Ibeh et al. (2021b) showed that the addition of up to 30% muscovite sand sized muscovite or silt does not affect the hydraulic conductivity or compressibility of kaolin. However, the shear strength was affected in the low stress (<100 kPa normal stress) but not at relatively high normal stresses. It was therefore assumed that the 2.5% fraction of mica would have not affected the triaxial response in the range of isotropic effective stresses greater than 100 kPa.

The triaxial test in Figure 7 showed that the kaolin without mica and the kaolin with 1.5% mica returned similar peak and end-of-test deviator stress confirming that the mica marker content under the shearing conditions explored in Figure 7 did not affect the behaviour of the kaolin. Hence, we can evaluate kaolin behaviour using the adequate amount of mica marker and at the shear condition without compromising the kaolin behaviour.

7.6. Particle kinematic analysis

Results of the particle matching and kinematic analysis using PLATYMATCH on four samples of kaolin with mica markers, sheared to four different strain levels with the miniature triaxial cell, are presented below.

7.6.1. Particle Displacement

In Figure 8 the displacement of the matched particles is shown for each sample. In Figure 8a, b, c and d, the segmented images of each sample before shearing are shown. For ease of visualization, only the segmented mica particles images are presented. In Figure 8e, f, g and h the direction of the particle displacement for sample 1MV, 2MV, 3MV and 4MV are shown respectively. To aid visualization of the different directions, the arrows were represented with two different colours depending on their x direction. In Figure 8 i, j, k and l the magnitudes of the particle displacement are shown.

It is worthy of mention that samples were compressed from the bottom upwards such that axial displacement is least at the top of the sample and highest at the bottom of the sample. For sample 1MV the displacement magnitude map (8i) shows that the particle displacement at the upper and lower boundary are consistent with the physical boundaries imposed during the test. At the upper boundary, the average displacement was zero and at the lower boundary the average displacement was about 1.5 mm. Similarly, at this initial compression stage, the

displacement appears to be distributed in a continuous way, all vectors point upward. The displacement magnitude map (Figure 8i) also shows a similar trend. The empty sections in the displacement vector correspond to sections of the sample with fewer mica particles as can be observed in the segmented particles image. However, the displacement direction plot (Figure 8e) shows two rigid blocks, one in red and the other in blue. Divergent particle motion is initiated in the clay sample already at this early stage, when axial strain is still small. A similar particle translation behaviour as that described above is seen to occur for sample 2MV subjected to 5.5% strain which is also before the peak shear strength. The particle displacement vector field shows a similar trend to 1MV: the particle displacement is from bottom up as expected, the displacement direction shows two particle blocks moving in two general directions as shown by the blue lines and the red arrows in Figure 8f. Sample 3MV was sheared close to the peak (6% strain). It can be observed again that while the displacement magnitude map (8g) shows progressive increase in displacement from the bottom to the top of the sample, the displacement direction is such that there is a trend of difference in the displacement direction across the sample. Sample 4MV (compressed beyond the peak shear strength to 10% shear strain) shows some additional unique features. It can be observed that the mica samples show two discontinuities in the displacement field suggesting localised deformation. Figure 8h and i show the particle displacement direction and magnitude respectively and both clearly capture the zone of discontinuity. It is good to note that the displacement map shows that the top right section of the kink (localised deformation) is a block, holding against an upwards moving bottom block, and motion resulting in a local re-orientation of particles. More so, a section at the bottom of the displacement direction map (Figure 8h) shows a displacement sense that is in a direction, conjugate to the deformation band. It will be expected that if shearing had continued the zone will probably have also shown intense particle rotation.

From the displacement calculated with the matched particle, a continuum mechanics analysis could be carried out to map the volumetric and deviatoric strain of the sample. A summary of the deviatoric strain for samples 3MV and 4MV are reported in Appendix II.

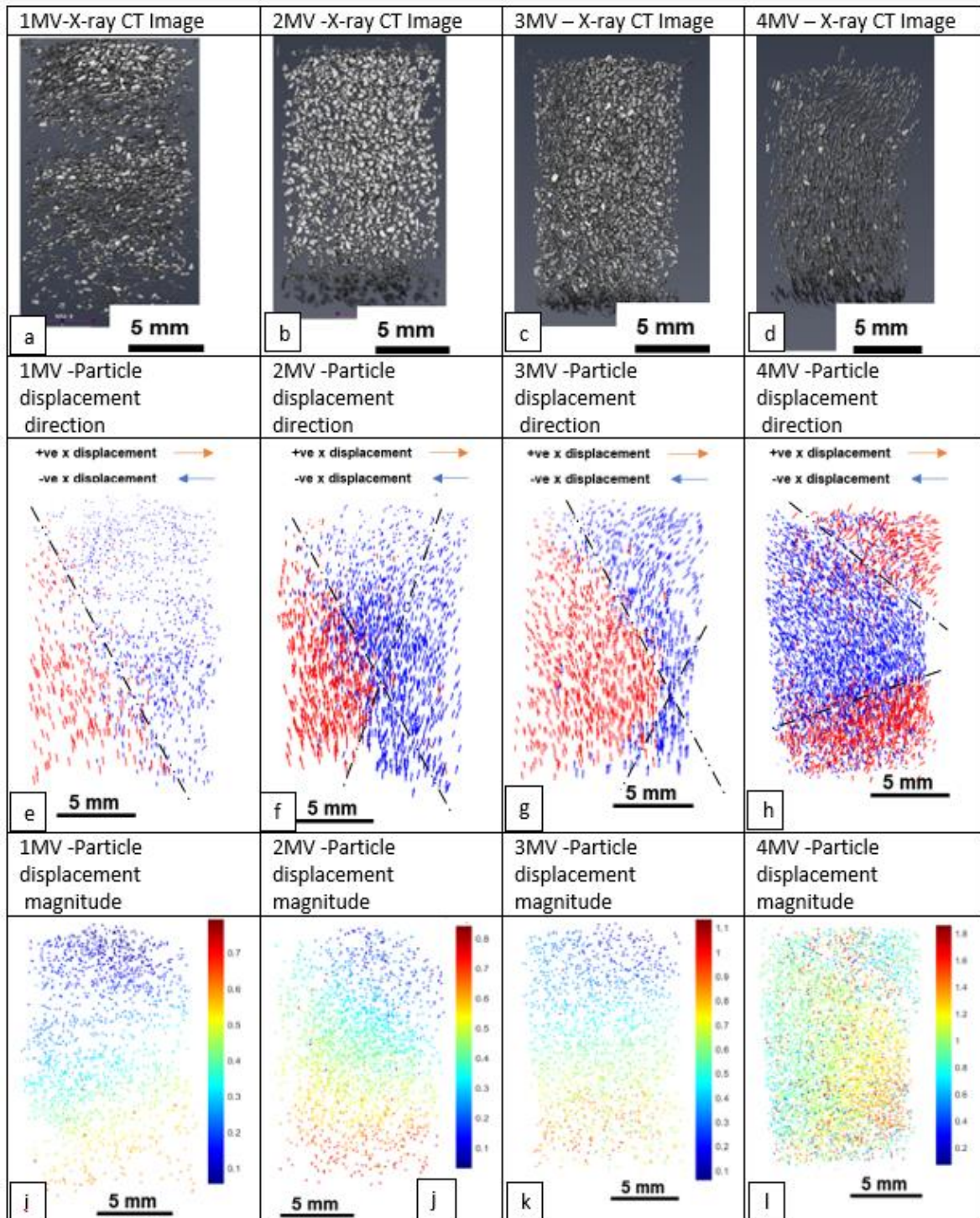
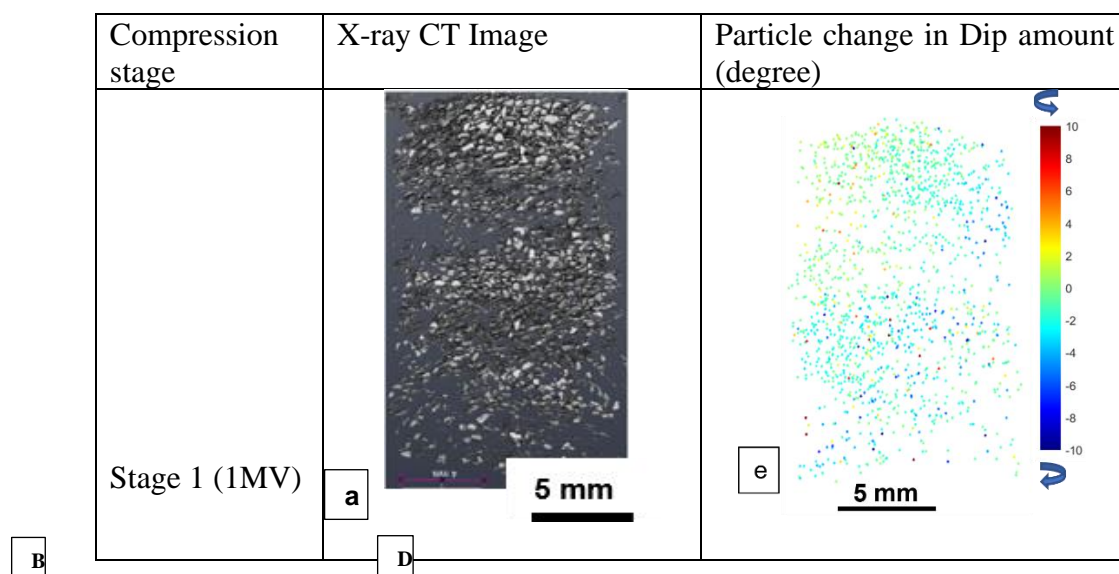


Figure 8: Step 1 a) Segmented sample image before shear showing mica particles for a) sample 1, b) sample 2 c) sample 3 d) sample 4. Partilce displacement direction for e) sample 1, f) sample 2 g) sample 3 h) sample 4 and Particle displacement magnitude for j) sample 1, j) sample 2 k) sample 3 and l) sample 4

7.6.2. Particle Rotation

Figures 9a, b, c and d show the segmented images of mica particles after compression for samples 1MV, 2MV, 3MV and 4MV respectively. Figure 9d uniquely show a zone of localised deformation. Figure 9e is the change in dip amount between successive scans of sample 1MV before and after compression. It shows a relatively uniform particle rotation. In the same manner, sample 2MV (Figure 9f) shows the change in particle dip amount with a faint alignment of particles in a trend similar to that observed in the displacement direction plot. Figure 9g shows the change in dip amount of sample 3MV, it shows a zone of relatively higher rotation. The zone of relatively higher rotation evidences an area of localised rotation pattern possibly associated with the thickness of the shear band. Figure 9h shows the rotation map for sample 4MV with a larger zone of relatively higher zone of intense rotation compared to that of sample 3MV.




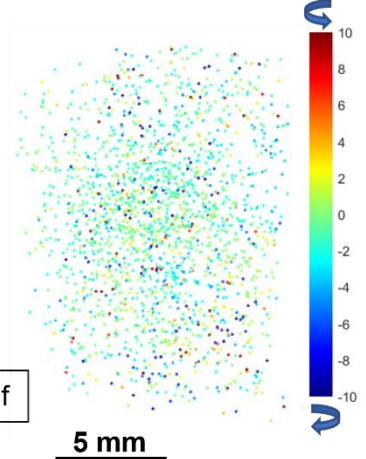

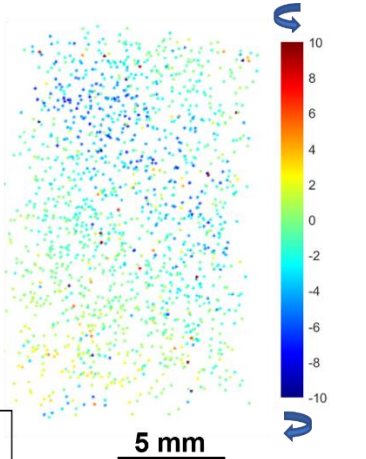

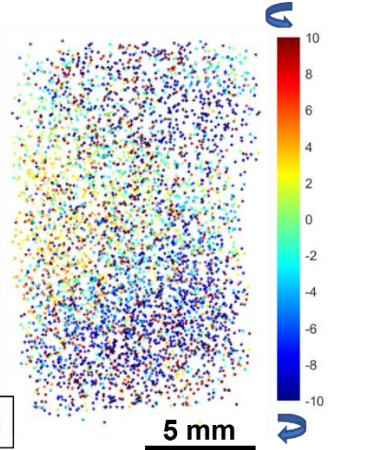
Stage 2 (2MV)	 <p data-bbox="730 607 815 651">5 mm</p> <p data-bbox="518 656 544 696">b</p>	 <p data-bbox="1002 618 1086 663">5 mm</p> <p data-bbox="917 566 943 607">f</p>
Compression Stage	X-ray CT Image	Particle change in Dip amount (degree)
Stage 3 (3MV)	 <p data-bbox="730 1265 815 1310">5 mm</p> <p data-bbox="518 1314 544 1355">c</p>	 <p data-bbox="1066 1276 1150 1321">5 mm</p> <p data-bbox="917 1270 943 1310">g</p>
Stage 4 (4MV)	 <p data-bbox="730 1839 815 1883">5 mm</p> <p data-bbox="518 1888 544 1928">d</p>	 <p data-bbox="1086 1850 1171 1895">5 mm</p> <p data-bbox="917 1843 943 1883">h</p>

Figure 9: Step 1 a) Segmented sample image after shear showing mica particles for a) sample 1 b) sample 2 c) sample 3 d) sample 4 and particle change in dip amount for e) sample 1, f) sample 2 g) sample 3 h) sample 4. Note: all change in dip amount is zoomed to +/- 10 degrees for better visualisation.

7.6.3. Particle Orientation

The particle orientation map for sample 4MV before and after compression are shown in Figures 10c and d respectively with their corresponding images in Figures 10a and b respectively. The analysis on the particle orientation does not need any particle matching and this is only possible because of the platy nature of the particles used. The particle orientation before compression (Figure 10c) and after compression (Figure 10d) clearly show some difference, while the particle before compression is generally vertically oriented, the particles after shearing show a zone of particle orientation deviating from the general vertical orientation of other part of the sample. The particle orientation after compression (Figure 10d) show a zone of localised orientation which is consistent with the zone of intense deformation in the scan image (Figure 10d). Similarly, figure 10e shows histogram of muscovite particles absolute dip amount before and after shear and figure 10f shows histogram of muscovite particles absolute dip amount before and after shear but with the after-shear histogram containing mica particles within 1 mm of the shear band axis. It can be observed that most of the particles within the localised zone are dipping ~45 degrees compared to areas outside the shear zone which are mainly vertical.

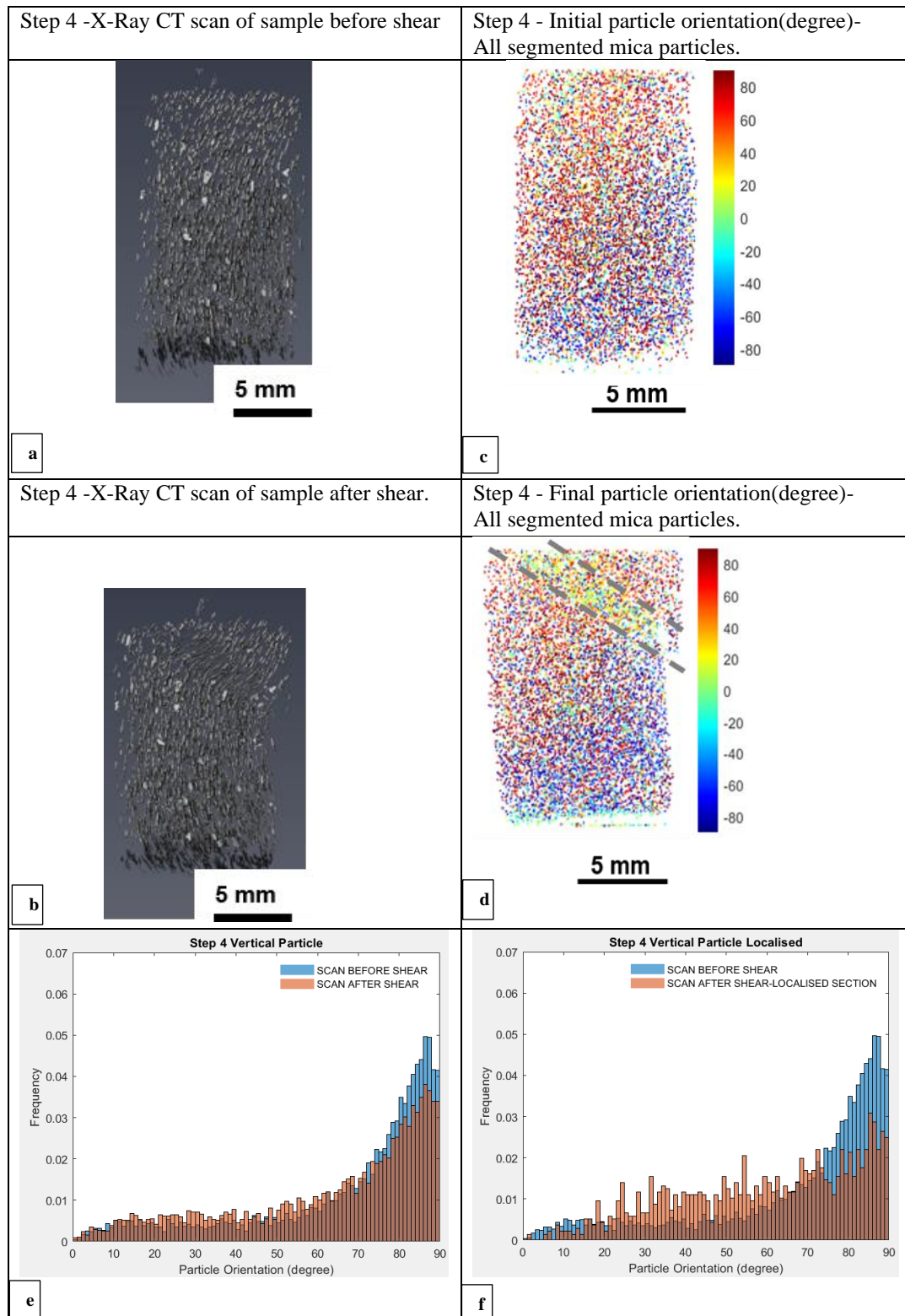


Figure 10: Step 4 a) image of segmented sample image before shear showing mica particles b) image of segmented sample image after shear showing mica particles c) map of particle orientation before compression d) map of particle orientation after compression e) histogram of muscovite particle absolute dip amount before and after compression f) histogram of muscovite particle absolute dip

amount before compression and after compression (containing only particles within 1mm to the localised section)

According to limit analysis, if the friction angle of the clay is 23° , the failure should occur along a plane having an inclination of about $56^\circ (45 + \frac{\varphi'}{2})$ with respect to the horizontal. The shear band individuated both by the analysis of the particle displacement direction (Figure 8g), and by the analysis of the deviatoric strain (Figure 7c) returns an inclination value of about 58° . In addition, a closer observation of the displacement and rotation map at the peak, shows that shear band at the peak concentrated into about 6 mica particles thickness as can be seen in the rotation map in step 3 (Figure 9g). Post peak, the shear band also show a thickness of about 8 mica particles. Figure 11a and b show sections of sample 4MV before and after compression respectively, with the after-scan image showing a section of localised deformation (highlighted with a red rectangle with broken lines in Figure 11b). The use of platy particles clearly shows particle rotation due to their angular nature which allows for orientation to be more easily measured. It is worth noting that the thickness of the shear bands in these strain volumes may be exaggerated with respect to real size. This is due to the lower limit to resolvable thickness dictated by the dimensions of mica (d_{50} of $30 \mu\text{m}$), whereas clay particle matrix in the sample have size in the order of $2 \mu\text{m}$. However, this discrete observation supports the theoretical idealisation of a shear band as a region of localised deformation bounded by weak discontinuities. Figure 11c show the full sample image containing the shear band.

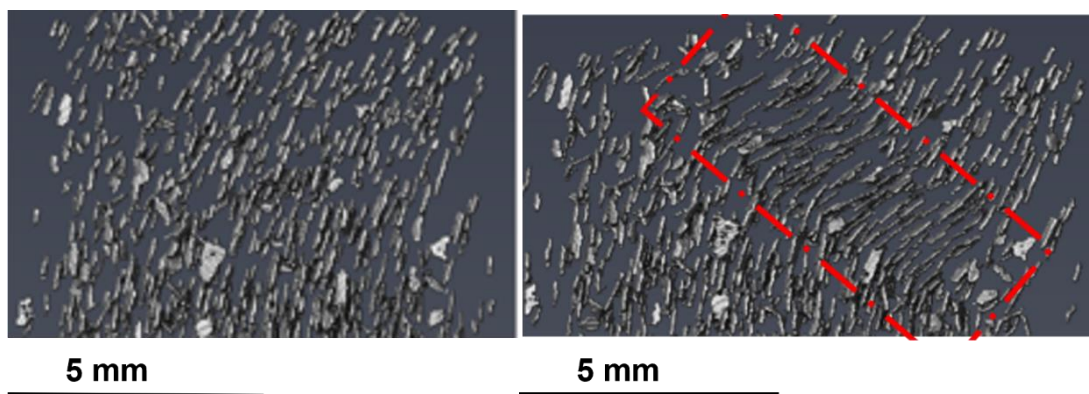




Figure 11: Shear band formation: mica marker configuration, a) before shear b) after shear c) image of sample 4MV after scan

Sample 4MV failed with a localisation plane inclination of ~ 35 degree to the horizontal, this is shallower than the expected angle based on the limit state. The shape of the shear-band in 4MV is like a classical kink band. There are several theoretical reasons why this may have formed: i) the rapid sample shear rate, ii) the sample morphology – sample height \gg sample diameter, iii) the presence of anisotropy or layering within the sample (Biot et al. 1961), iv) causing uneven sample loading, v) an indentation on one side of the sample or a high sample body roughness, vi) a curved structure within the materials within the sample, and vii) the un-lubricated top and bottom for the triaxial cell sample holder. Rapid shearing or anisotropy within the sample seems unlikely, because a similarly prepared sample with mica markers sheared at a faster rate (Ibeh et al 2021c) did not show kink-like banding. Similarly, sample morphology, indentation on the side of the sample and uneven sample loading, are also not likely to be the reason because the sample was prepared with a diameter two times the sample height, without visible indentation on the side of the sample and was loaded evenly using a steel sphere ball to avoid the application of a bending moment. The un-lubricated sample holder at the top and bottom may also not be the reason for the kink-like band considering that sample

3MV, which was sheared with the same cell, did not show a band with shallow angle to the horizontal as occurs in a kink band. The most likely cause of the kink-like band formation is the pre-existing curved structure of the materials within the sample, which is visible in the initial sample 4MV scan prior to shearing. This finding emphasises the dependence of shear band morphology on the initial condition of the clay sample.

7.7. Inferring mechanisms of initiation and propagation of strain localisation

In Figure 12a and b, the evolution of the strain localisation is shown. While Figure 12a show the clay sample strain localisation conceptual model along a compression curve, Figure 12b show a more detailed description of the conceptual model. At the pre peak initial compression stages, the samples showed some shear deformation as can be seen in Figures 12a and b (I and II). Divergent particle motion is initiated in the clay sample already prior to the deviatoric stress peak. The particle motion is a divergent motion of two blocks of particles, and the intersection between the blocks is the most likely zone of first rupture if the samples were sheared to failure.

Strain localisation was visible for stress state corresponding to the occurrence of peak shear strength (III in Figure 12b). This was captured as preferential increase in rotation of particles along a zone. The visible localised rotation at the peak shows that strain localisation is accompanied by mica particle rotation. Beyond the peak, the zone of localised strain increases in size and the localisation is much more visible. Apart from the main zone of localisation towards the top of the sample at stage IV (beyond the peak) there is also a developing localisation band at the bottom of the sample having a different orientation to the one formed at the top of the sample.

The width of the zone of particle rotation both at the peak and post peak shear strength seems to suggest that the size of the microstructure of strain localization in soft clay is larger than the size of a clay particle. However, this might be due to the size of the marker itself, and

further analyses are needed to better evaluate this. This also further shows that it will take shearing to relatively larger displacement after the peak to get a perfect alignment of particles to the localised zone direction (see Figure 12 showing the conceptual model of clay particle configuration). To the authors knowledge, this is the first study of soft clay to show 4-D clay particle (mica in this case) rotation within a shear band. It has been shown here that particle displacement magnitude may not reveal strain localisation early enough, but particle displacement direction reveals failure surface even before the peak shear strength.

The kinematics analysis shows some insight into the initiation and propagation of strain localisation in kaolin: prior to the stress peak, the shear strain appears to start localising with some mild particle divergent motion leading to the formation of two rigid blocks. At the peak, there appears a thick shear band with an area of relatively intense particle rotation and divergent particle displacement and post peak, the shear band is essentially thicker. The development of shear bands initiates during the pre-peak regime in triaxial experiments, as detected through particle displacement direction and rotation. Platy clay particles (mica in this case) within overconsolidated clay samples undergo translation and rotation and there is the potential to capture the growth of a shear band from pre peak shear, through the peak and post peak shear strength.

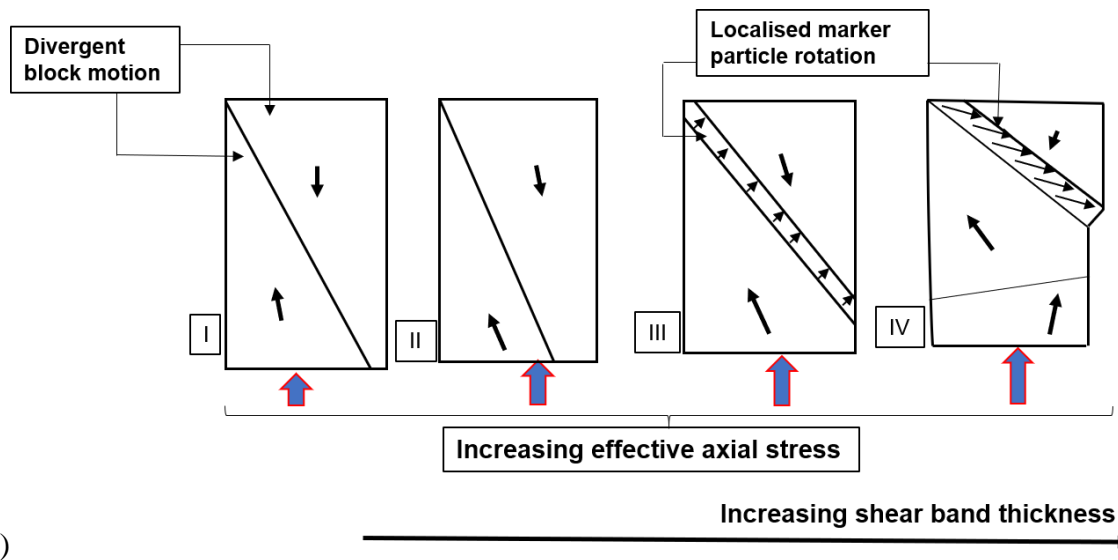
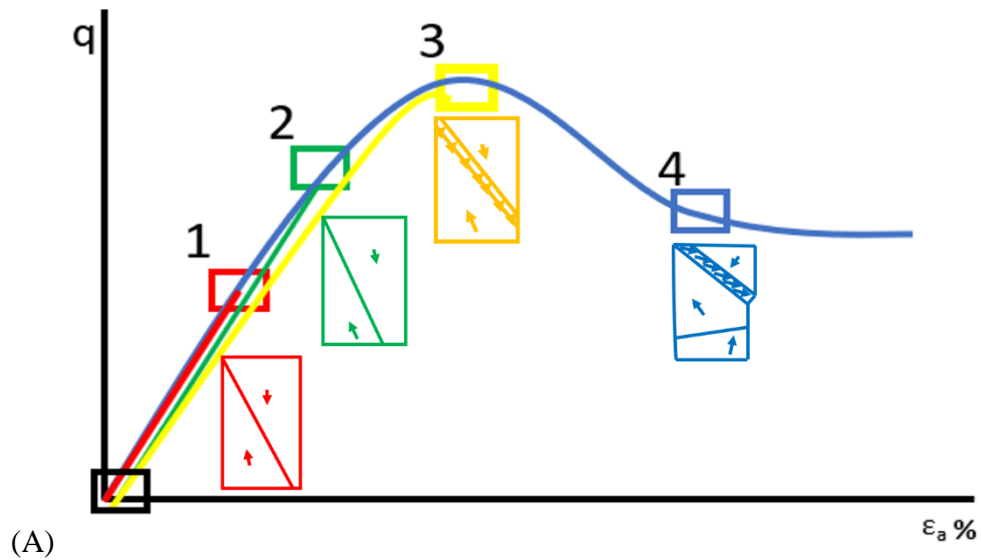


Figure 12: Conceptual model of strain localisation evolution a) along a clay sample compression curve b) from sample I (1MV) through to sample iv (4MV).

Overall, analysis of the direction of particle motion is more indicative of localisation than the magnitude of particle displacement. The displacement direction also reveals a similar pattern of localisation emergence as indicated by the rotation map. A major observation is that while the displacement direction map shows the trend of localisation early enough, it does not however give a clear indication of the thickness of the shear band. The particle rotation gives

an indication of the shear band thickness at the peak shear strength. The localisation zone for the 3MV sample was with an angle of 42-58 ° to the horizontal.

This application of particle tracking to the x-ray CT images of kaolin clay with platy particle marker (mica) demonstrates that platy silt sized particles, provides a means to effectively detect (within a given accuracy) localized deformation in clays. The result of this experimental approach provides insight into progressive structural changes of soft soil deformation mechanisms at different loading steps. This also shows that platy particle kinematic analysis of 3D images from x-ray tomography can reveal patterns of deformation that could not be observed using only the grey scale images (especially when samples do not involve significant volume change and as such deformation is hidden). This is a valuable approach in strengthening and improving the existing constitutive models for clays, which currently are only based on boundary measurements.

7.8. Conclusion

This study presented an evaluation of the evolution of strain localization in clay upon CU triaxial test. Mica particles were used as markers for X-ray CT to analyse the localisation of strain upon shearing. First, the design and specifications for a new miniature triaxial compression apparatus and procedures for its use were presented. Subsequently, the miniature triaxial cell was adequately validated by comparing triaxial compression of speswhite kaolin clay using the new apparatus to similar test performed with conventional triaxial cell. Further, evaluation of the shear strength of kaolin compared to kaolin/mica mixture was carried out. It was observed that there was no significant difference in shear strength between the two samples and as such the small mica fraction did not appear to affect kaolin behaviour.

Finally, an exploration of the kinematics of the mica particle markers within kaolin sample was evaluated for an insight into the initiation and localisation of strain in kaolin. The samples

were subjected to triaxial compression with X-ray imaging carried out before and after compression at four different strain levels. The tests were conducted using different samples for each strain level. The following were observed:

- i) At the start of compression (axial strain before peak strength) platy particles move in blocks of distinct opposing direction shown by the mica particle displacement direction map. This divergent displacement is in response to accommodate imposed loading and gives an indication of the initiation of strain localisation.
- ii) Platy mica markers in kaolin samples undergo translation and rotation at the peak strength within a localised zone. The mica marker particles capture kaolin clay sample kinematics from pre peak up to the peak and post peak shear strength.
- iii) Analysis of the direction of mica marker particle motion is more indicative of localisation in clay, at a much earlier stage than the peak strength and particle rotation is more indicative of localisation zone thickness, and this is more visible from the peak strength.
- iv) For an over-consolidated kaolin sheared to the peak stress, the zone of localisation is much larger than clay size and there is the potential to capture the growth of a shear band in kaolin using mica markers.

7.9. Reference

- ALERT. (2016). ALERT Doctoral School 2016 Modelling of instabilities and bifurcation in Geomechanics. Alert School Book.
- Biot, M.A., 1961. Theory of folding of stratified viscoelastic media and its implications in tectonics and orogenesis. Geological Society of America Bulletin, 72(11), pp.1595-1620
- Birmpilis, G., Dijkstra, J., Tudisco, E., & Hall, S. (2017). In-situ study of deformation mechanisms of soft clay using X-ray Computed Tomography and Digital Volumetric Correlation. June.
- Chandler, J.H. and Brunsten, D. (1995). Steady state behaviour of the Black Ven mudslide: the application of archival analytical photogrammetry to studies of landform change. Earth Surface Processes and Landforms, 20(3), 255–275.
- Chen, Y., Withanage, K. R., Uchimura, T., Mao, W., & Nie, W. (2020). Shear deformation and failure of unsaturated sandy soils in surface layers of slopes during rainwater infiltration. Measurement: Journal of the International Measurement Confederation, 149, 107001. <https://doi.org/10.1016/j.measurement.2019.107001>
- Di Maio, C. and Vassallo, R. (2011). Geotechnical characterization of a landslide in a Blue Clay slope. 8(1), 17–32.
- Huang, Y., & Dai, Z. (2014). Large deformation and failure simulations for geo-disasters using smoothed particle hydrodynamics method. Engineering Geology, 168, 86–97. <https://doi.org/10.1016/j.enggeo.2013.10.022>
- Ibeh, C. U., Pedrotti, M., Tarantino, A., & Lunn, R. (2019). An x-ray CT study of miniature clay sample preparation techniques. E3S Web of Conferences, 92. <https://doi.org/10.1051/e3sconf/20199201004>

- Ibeh, C. U., Pedrotti, M., Tarantino, A., & Lunn, R. J. (2021a). On the utilization of mica waste: The pore-fluid chemistry of mica soils and its implication for erosion susceptibility. *Geoderma*, 403, 115256. <https://doi.org/10.1016/j.geoderma.2021.115256>
- Ibeh C. U., Tarantino A., Pedrotti M., Lunn R. J. (2021b). An experimental investigation into the use of mica as a material for the stabilisation of marginal clays in construction. *Construction and Building Materials* 299 (123971). <https://doi.org/10.1016/j.conbuildmat.2021.123971>
- Ibeh C. U., Pedrotti M., Tarantino A., Lunn R. J. (2021c). PLATYMATCH- A particle-matching algorithm for the analysis of platy particle kinematics using X-ray Computed Tomography. *Computers and Geotechnics*.
- Ibeh, C. U. (2020). Effect of changing groundwater level on shallow landslide at the basin scale: A case study in the Odo basin of south eastern Nigeria. *Journal of African Earth Sciences*, 165(August 2019), 103773. <https://doi.org/10.1016/j.jafrearsci.2020.103773>
- Kim, J.; Woo, S.I.; Chung, C.-K. Assessment of non-uniform deformation during consolidation with lateral drainage using Particle Image Velocimetry (PIV). *KSCE J. Civ. Eng.*2017,22, 520–531.
- Kwak, T. Y., Park, K. H., Kim, J., Chung, C. K., & Baek, S. H. (2020). Shear band characterization of clayey soils with particle image velocimetry. *Applied Sciences (Switzerland)*, 10(3). <https://doi.org/10.3390/app10031139>
- Liu, J., Gao, G., Wang, S., Jiao, L., Wu, X., & Fu, B. (2018). The effects of vegetation on runoff and soil loss: Multidimensional structure analysis and scale characteristics. *Journal of Geographical Sciences*, 28(1), 59–78. <https://doi.org/10.1007/s11442-018-1459-z>

- Murray, I., & Tarantino, A. (2019). Mechanisms of failure in saturated and unsaturated clayey geomaterials subjected to (total) tensile stress. *Geotechnique*, 69(8), 701–712. <https://doi.org/10.1680/jgeot.17.P.252>.
- Nizolek, T.J., Begley, M.R., McCabe, R.J., Avallone, J.T., Mara, N.A., Beyerlein, I.J. and Pollock, T.M., 2017. Strain fields induced by kink band propagation in Cu-Nb nanolaminate composites. *Acta Materialia*, 133, pp.303-315.
- Pedrotti, M., & Tarantino, A. (2018). An experimental investigation into the micromechanics of non-active clays. *Geotechnique*, 68(8), 666–683. <https://doi.org/10.1680/jgeot.16.P.245>
- Pritchard, O. G., Hallett, S. H., & Farewell, T. S. (2014). Soil impacts on UK infrastructure: Current and future climate. *Proceedings of the Institution of Civil Engineers: Engineering Sustainability*, 167(4), 170–184. <https://doi.org/10.1680/ensu.13.00035>
- Ren, D., Fu, R., Leslie, L.M. and Dickinson, R. E. (2011). Modeling the mudslide aftermath of the 2007 Southern California Wildfires. *Natural Hazards*, 57(2), 327–343.
- Ridley A. M. and Burland B. J. (1993). A new instrument for the measurement of soil moisture suction. *Geotechnique*, 43(2), 321–324.
- Sachan, A., & Penumadu, D. (2007). Strain localization in solid cylindrical clay specimens using Digital Image Analysis (DIA) technique. *Soils and Foundations*, 47(1), 67–78. <https://doi.org/10.3208/sandf.47.67>
- Singh, G., Biswas, D. R., & Marwaha, T. S. (2010). Mobilization of potassium from waste mica by plant growth promoting rhizobacteria and its assimilation by maize (*Zea mays*) and wheat (*Triticum aestivum* L.): A hydroponics study under phytotron growth chamber. *Journal of Plant Nutrition*, 33(8), 1236–1251. <https://doi.org/10.1080/01904161003765760>

- Tarantino, A., & Mongiovì, L. (2001). Experimental procedures and cavitation mechanisms in tensiometer measurements. In *Unsaturated Soil Concepts and Their Application in Geotechnical Practice* (pp. 189–210). Springer Netherlands. https://doi.org/10.1007/978-94-015-9775-3_1
- Thakur, V., Nordal, S., Viggiani, G. and Charrier, P., 2018. Shear bands in undrained plane strain compression of Norwegian quick clays. *Canadian Geotechnical Journal*, 55(1), pp.45-56. [dx.doi.org/10.1139/cgj-2016-0443](https://doi.org/10.1139/cgj-2016-0443)
- Viggiani, G., Bésuelle, P., & Desrues, J. (2013). X-ray Micro tomography as a Tool for Studying Localized Damage / Deformation in Clay Rock. *Proceedings of the NEA Clay Club Workshop on Clay Characterisation from Nanoscopic to Microscopic Resolution*, 91–98.
- Zhang, Y.; Tan, T.; Leung, C. Application of particle imaging velocimetry (PIV) in centrifuge testing of uniform clay. *Int. J. Phys. Model. Geotech.*2005,5, 15–26.

7.10. Appendix 1

Main Features of the miniature triaxial cell

7.10.1. Pore -water pressure measurement device (Tensiometer)

The tensiometer component of the cell is used in undrained compression test to provide reliable and continuous pore pressure measurement of the soil sample. Figure 13 below shows a sketch of the tensiometer adapted from Ridley and Burland, 1993. Customized 4.9 cm diameter stainless steel inserts were designed and fabricated to house the tensiometer and a ball bearing that enable the cell rotation. The tensiometer is designed inhouse (see (Tarantino & Mongiovi, 2001) and it is composed of a water reservoir, a high air entry ceramic disk (1.5MPa) and an integral strain gauge diaphragm. The ball bearing has deep groove with sealed ends. It has a 20 mm inner diameter and 47 mm outer diameter. The tensiometer is inserted into the ball bearing middle opening, where it sits securely, and the ball bearing in turn sits securely in the steel insert as shown in Figure 1 in the main text.

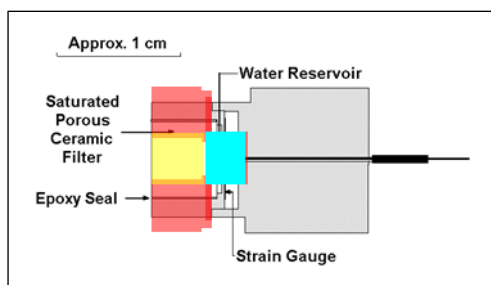


Figure 13: Sketch of high capacity tensiometer for pore pressure measurement (Ridley and Burland 1993) and image of the tensiometer

7.10.1.1. Tensiometer Calibration

Dead weight calibration device was used to calibrate the tensiometers by applying known pressure with the tensiometers positioned in a saturation chamber. The tensiometer calibration data was derived for positive pressures and calibration consisted of two pressure increase and

decrease cycles between 0 and 3000 kPa in steps of 50 or 100 kPa similar to the calibration approach applied by Tarantino & Mongiovì (2001). Negative pore water pressures were determined by extrapolating the calibration curve to the negative range, assuming a symmetric response of the measurement diaphragm. The predicted error standard deviation using the tensiometer calibration curve is 0.4 kPa. Other sensor components of the apparatus were calibrated and accordingly. Figure 14 show images of the calibration device set up.

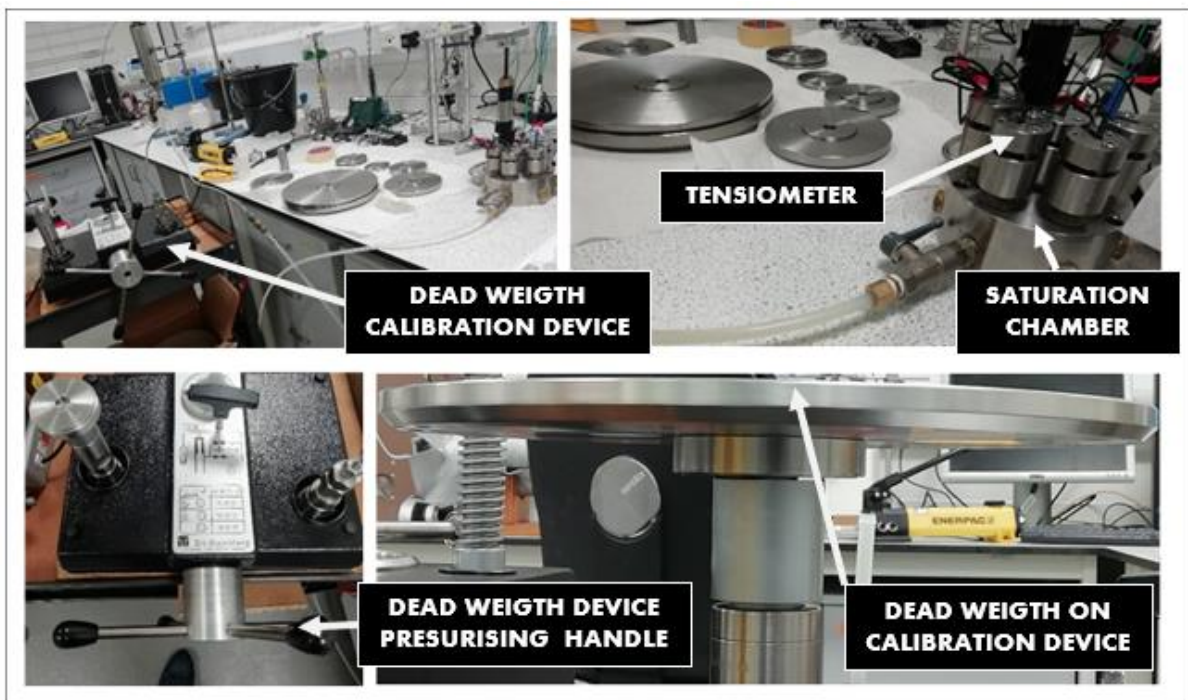


Figure 14: Tensiometer calibration device set up.

7.10.1.2. Tensiometer calibration check

Tensiometers are prone to cavitation and insufficiently saturated porous ceramic is believed to produce anomalous tensiometer response and as such there is the need to ensure adequate tensiometer saturation and measurement reliability (Tarantino & Mongiovì, 2001). This is especially important because the miniature triaxial cell design only allow for one tensiometer, as such the tensiometer to be used in the miniature device must be efficiently prepared to record

adequate readings. According to Tarantino & Mongiovì (2001) the following are adequate indicators of tensiometer porous ceramic saturation: consistent change in calibration parameters, the time required for equalisation after removal from saturation chamber and response of the tensiometer upon rapid drop in pressure. If any of these indicators were inconsistent, the tensiometer must be re-saturated after triggering cavitation. To ensure that the porous ceramic was adequately saturated and that the available tensiometers were responding appropriately and suitable for measurement, three tensiometer checks were carried out: i) check on possible change in the slope of the calibration line; ii) response of tensiometer upon rapid drop in pressure (in two cycles) to about -800 to -1000 kPa and iii) response of tensiometer to cavitation and constant tensiometer reading over time.

Possible change in the slope of calibration line were first checked before using the tensiometer for measurement. The best way to check the change in calibration line slope is to repeatedly calibrate it and compare the slope but considering that a new calibration would be unpractical because the calibration process lasts for several hours there has to be an alternative approach. Hence an indirect and swift approach is used as suggested by (Tarantino & Mongiovì, 2001), by modifying the pressure using a screw piston in the saturation chamber, housing all the tensiometer being tested and then comparing the change in pressure recorded by the tensiometers, which is expected to be the same if the calibration curve did not change, otherwise the tensiometer is re-calibrated.

To ensure that the tensiometer is measuring the right values, after equilibrating on free water, the tensiometer porous stone was wiped and allowed to dry out until a water pressure of about -800 to -1000 was reached and immediately replaced in free water, with the pressure before and after drying out recorded. This cycle is repeated (second rebound) and the pressure after placing back the tensiometer in free water is compared to the tensiometer reading before drying to check if the water pressure regained the same initial value. Good saturation is

indicated by a return to zero kPa (0 to -10kPa acceptable for the first cycle) when put back into free water, when cavitation has not occurred and provided that the difference between the second cycle rebound and the first rebound is negligible. Figure 15a, b & d show three tensiometer response check, tensiometer A (Ta), tensiometer B (Tb) and tensiometer C (Tc), the responses were within 0 and 10kPa.

Saturation of the porous ceramic was also checked by ensuring that the pressure reading returned to about – 100 kPa upon cavitation. Figure 15b, c & e show that the three tensiometers checked returned to about -100kPa upon cavitation. The tensiometer was also checked throughout the experimental procedure and especially before measurement.

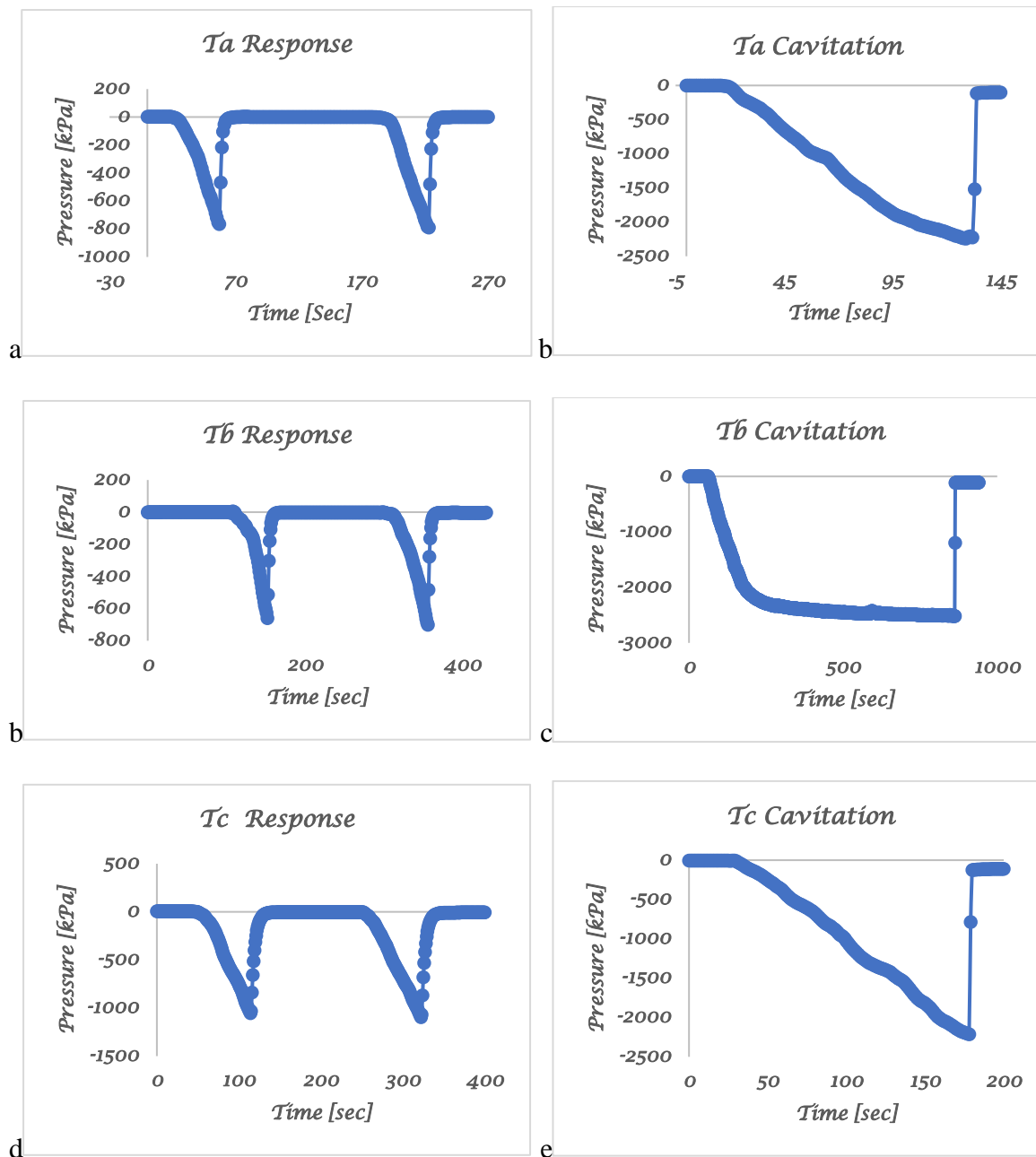


Figure 15: a) tensiometer 1 response check calibration b) tensiometer 1 cavitation check, c) tensiometer 2 response check calibration d) tensiometer 2 cavitation check, e) tensiometer 3 response check calibration f) tensiometer 3 cavitation check

7.10.2. Latex Membrane

The latex membrane enclosing soil sample provides restraining effect. It protects soil sample from evaporating or drying out. O rings were used to hold the latex to the top and bottom of the cell sample pedestal. Latex membrane in conventional triaxial cell is known to

contribute to the soil resistance offered against compression. This resistance must be corrected for by subtracting it from the measured stress at failure. The nature of deformation (plastic or brittle) determines the correction to be applied. For plastic deformation (typified by soil barrelling) the membrane correction (C_M) is given by:

$$C_M = \frac{0.4M\varepsilon(100-\varepsilon)}{D} \text{ KN/m}^2$$

where ε = specimen axial strain; M= the compression modulus of the membrane material in N/mm width (which is equal to the extension modulus) and D is the initial Diameter in mm. For brittle failure, the sample fail along a slip surface and the membrane distorts in a different way from plastic deformation. For stiff clay, membrane correction is negligible.

7.10.3. External Stress Application/Control System (Actuator and controller)

External compression force was applied and controlled using the Zabber NA series electronic linear actuator -NA14B16-T4, NEMA size 14, 16 mm travel, and 180 N maximum continuous thrust (Figure 16a). The actuator was controlled with an X-MCB1 series stepper motor controller (Figure 16b).

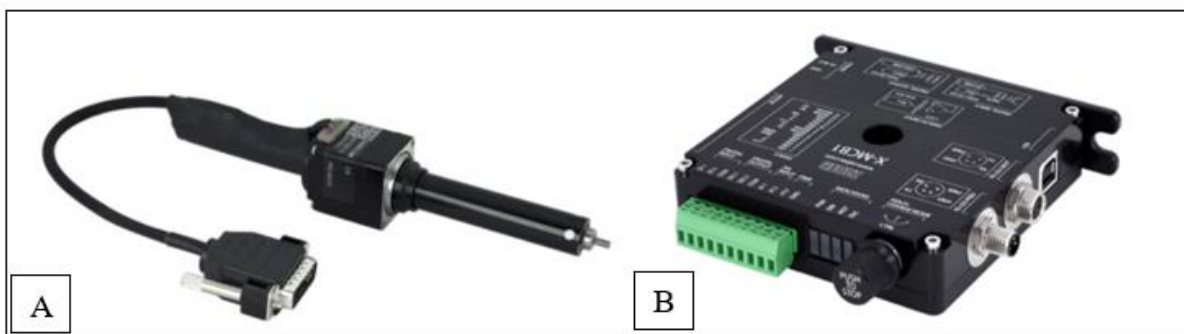


Figure 16: a) Actuator and b) controller for soil compression within the miniature triaxial cell

7.10.4. Load cell and displacement transducer

The miniature triaxial cell (Figure 17a and b) consists of a button load cell for compression load measurement with a measuring load range of 0 to 100N, an accuracy of 0.5% and a resolution of 6.36 kPa. Figure 3b below show the displacement transducer in the cell; it has a travel length of 2 cm and a micro step size of 0.047625 μm .

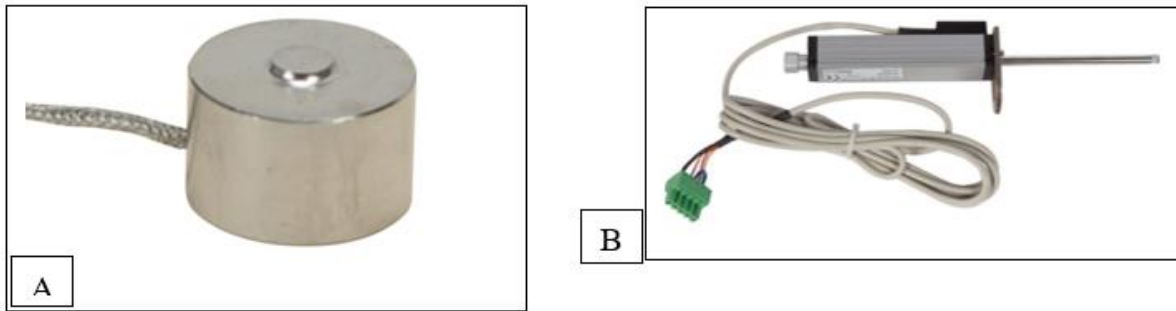


Figure 17: a) load cell and b) displacement transducer

7.10.5. Data acquisition/Process Control System

Figure 18 shows a schematic diagram of the data acquisition system used for the miniature triaxial-cell. Data logging is done automatically using personal computer and this require the instrumentation to provide electrical signals from each component of the triaxial set up. All sensors of the miniature triaxial cell except the linear actuator are connected to National Instrument (NI) data acquisition system; the linear actuator is separately connected to a controller which runs with an open-source software from Zaber technologies. The sensors are connected to the appropriate NI C-series I/O sensor type module which provide the required excitation voltage, signal processing and signal measurement. The modules are embedded in a 6-slot chassis which is connected to a PC. The computer program that controls the miniature triaxial cell is a custom written MATLAB code with graphic user interface (GUI) enabling data logging and test control.

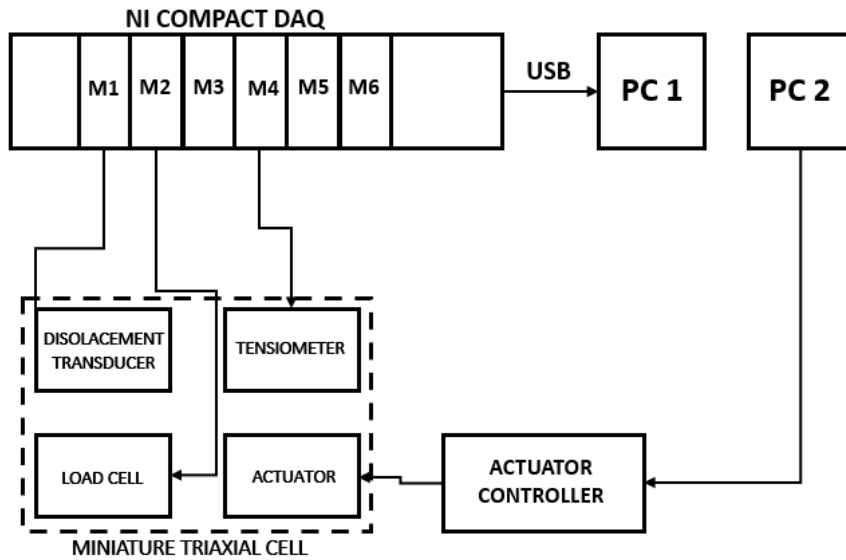


Figure 18: schematic diagram of the data acquisition system used for the miniature triaxial-cell. M1 to M6 indicates NI C-series module 1 to 6, housed within a chassis.

7.10.6. Test Apparatus use procedure

The miniature device allows for undrained compression strength measurement of over consolidated clay sample. The cell may be adapted in the future to allow for testing of soil of larger or smaller sample size with minimal modification. The cell operation procedure are as follows:

Step 1: Soil sample mounting

In preparation for the test, the cell acquisition system is connected and switched on and the tensiometer is removed from its saturation chamber and put in free de-aired water. The loadcell, smooth steel ball and sample mounting base split housing are installed and the sample to be tested is put inside a latex membrane using a 1mm plastic miniature membrane stretcher, designed specifically for this test (Figure 19). The membrane stretcher is designed similar to conventional membrane stretches such that, with the latex membrane stretched, the top and bottom end of the latex is rolled inside-out, and O-rings are rolled on to the ends of the stretcher. An air orifice on the body of the membrane stretcher is used to suck air out of the interface between the latex membrane and the membrane stretcher, ensuring that the latex membrane is

adequately stretched to accommodate the soil sample to be tested. With the latex membrane wide open within the membrane stretcher, the soil sample is placed inside the latex membrane. The sample is then placed on top of the miniature triaxial cell pedestal and the excess latex membrane rolled down to the bottom cylindrical pedestal, held in place with the bottom O-ring.

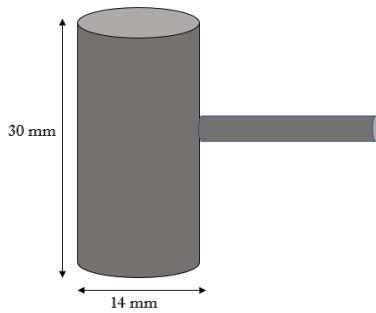


Figure 19: Latex membrane stretcher.

Step 2: Tensiometer deployment

The tensiometer is then put into the ball bearing ring housing and an earlier prepared pea sized kaolin paste with the consistency of a slurry is put on the tensiometer face to allow for hydraulic connection to the sample. The tensiometer is then put on the sample with the top excess latex membrane on the membrane stretcher rolled up to the tensiometer and the O-ring also rolled up to secure the membrane in place and ensure air and water tight sample. The tensiometer reading is then allowed to equilibrate before loading starts.

Step 3: Compression test and X-ray CT scan

The plastic split mould (housing the loadcell, smooth steel ball and sample mounting base) is removed and with the sample adequately in place, the actuator is put on with a specified displacement velocity. As the test proceeds, all the sensor measurement (displacement transducer, tensiometer and loadcell) are monitored through the acquisition graphic user interface. Progressively, the sample may be compressed to pre-defined levels.

Step 4: Moisture content measurement and Data Interpretation

At the end of the compression test and possible X-ray CT scan, the tensiometer is removed from the sample top and put back to free de-aired water for onward cleaning and re-saturation. This is then followed by test data interpretation.

7.11. Appendix II

Strain plots of samples 3MV and 4MV show zones of localised deformation as evidenced by the distinct bright colour concentration in both sample Figures 20a and b.

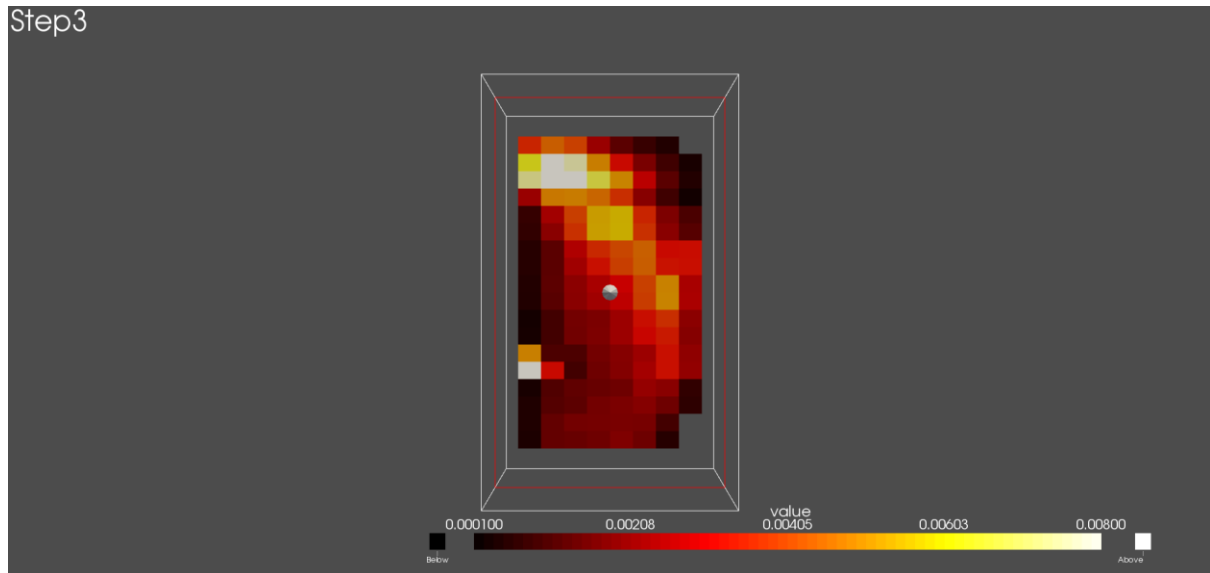


Figure 20a strain plot of sample compressed to the peak strength. The shear strain plot shows that there is a concentration of strain diagonally across the sample, this is consistent with the particle displacement direction plot and the rotation map.

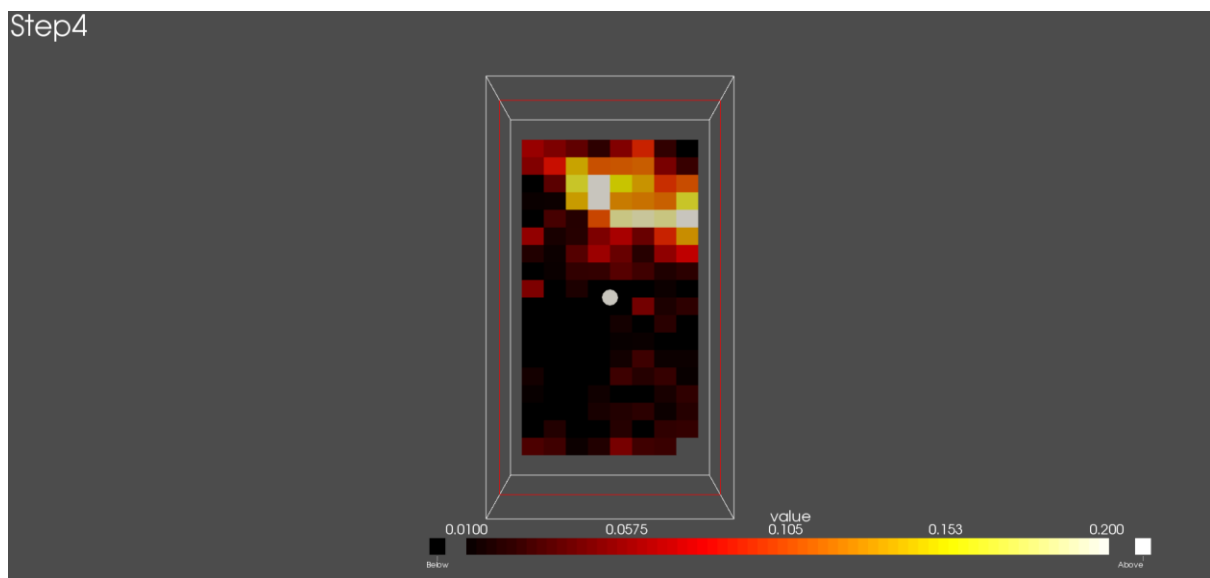


Figure 20b strain plot of sample compressed to the peak strength. The shear strain plot shows that there is a concentration of strain diagonally across the sample, this is consistent with the particle displacement direction plot and the rotation map.

8. Conclusion and Recommendation

8.1. Introduction

As a first step in a larger systematic research campaign investigating the potential use of mica markers for understanding the initiation and propagation of strain localisation in kaolin, this thesis has focussed on gaining an in-depth understanding of the chemical and mechanical characteristics of mica and the strain localisation upon shear using mica markers and X-ray computed tomography. The specific objectives of this research were:

- 1) To characterize mica chemically (in terms of its particle interaction and erodibility in different pore-fluid pH and electrolyte concentration) and mechanically (in terms of compressibility, shear strength, and hydraulic conductivity).
- 2) To determine the best approach for sampling miniature clay sample with minimum disturbance.
- 3) To develop a miniature triaxial cell suitable for X-ray Computed Tomography (X-ray CT) imaging of clay with markers and with an inbuilt High-Capacity Tensiometer for hydro-mechanical measurement.
- 4) To develop, implement and validate a particle matching algorithm to quantify particle kinematics -displacement and rotation- of plate-shaped particles using X-ray -CT data.
- 5) To develop a conceptual understanding of the initiation and propagation of strain localisation in kaolin by using X-ray CT and mica markers.

The key findings related to each of the objectives listed above are presented in each section below and the contributions to existing knowledge are briefly highlighted. The final section of this chapter concludes with a list of proposed areas for future research towards the development of a more effective constitutive model for clays.

8.1.1. Chemical and mechanical characterisation of mica

This is the first study to investigate the mechanical and chemical behaviour of mica/kaolin mixture. Moreover, it is the first study to evaluate the erodibility of mica in different pore-water chemistry environment. The investigation was done to characterise mica compressibility, shear strength, hydraulic conductivity, particle interaction and erodibility in different pore fluid pH and electrolyte concentration, for an understanding on the effect of mica on the chemistry and mechanical behaviour of kaolin. The results from Chapter 3 showed that the particle configuration of mica particles consistently varies with the pore water chemistry (dispersive to non - dispersive configuration), regardless of whether the samples being tested were sediments in suspension or compacted samples. This is a similar behaviour obtainable with kaolin. Results from chapter 4 showed that by adding both muscovite silt or muscovite sand to kaolin for all the weight percent of muscovite/kaolin mixtures tested (muscovite contents of 0, 2.5, 10, and 30 % by weight), the compressibility does not change and for up to 30% muscovite sand or muscovite silt, the compressive behaviour is still kaolin-dominated. Similarly, oedometer tests showed that the addition of up to 30% muscovite sand sized muscovite or silt does not affect the hydraulic conductivity or compressibility of kaolin however direct shear test showed that the shear strength was affected at low normal stresses (≤ 100 kPa) but not at relatively higher normal stresses. Provided the macroscopic response of kaolin compared to the kaolin and mica mixture are the same, we can assume that the behaviour of kaolin is not affected. This was further investigated in chapter 7 by comparing triaxial test result of kaolin sample with 1.5% by wt of mica to that of kaolin alone both sheared to failure. Prior to this, we investigated the approaches to prepare miniature clay soil sample with the least possible disturbance.

8.1.2. Influence of sampling method on disturbance of kaolin microstructure

The influence of soil sampling method on the level of disturbance on soil microstructure was investigated as part of evaluating the best approach to prepare miniature clay soil sample with the least possible disturbance. Miniature cylindrical remoulded kaolin specimens (containing 2% silt-sand sized mica markers) produced by tube sampling and lathe trimmed sampling were analysed for sample disturbance.

Fisher distribution analysis of the mica particle strain markers, represented as poles to planes plotted on stereonets, showed that lathe trimmed vertical specimens may be subject to lesser disturbance when compared to vertical tube sampled specimens for overconsolidated specimens prepared in an oedometer. This is possibly because tube sampling generates shear distortion. Chapter 5 results further showed that for samples prepared with gypsum mould, radial suction force (generated by the gypsum mould) resulted in the particles being preferentially radially oriented and parallel to the mould drainage surface.

This is the first research to use X-ray computed tomography and mica particle marker to show the effect of miniature clay sampling disturbance and this provided insight for improved sampling methods (how to better prepare clay samples for minimal disturbance). This was taken further by developing an algorithm for plate shaped particle matching upon compression.

8.1.3. Platy particle matching Code

The possibility of matching silt sized plate shaped (platy) particles was investigated using matching code that have successfully been used for sand. Some challenges were observed with using the code for platy particles as it was not originally designed for platy particles. The matching code by Druckery and Alshibli 2014 was adapted for platy particle matching to create a new platy particle matching algorithm - PLATYMATCH.

After X-ray CT imaging and image processing, platy silt sized muscovite particle attributes were evaluated to identify unique attributes that may be useful for matching platy particles. PLATYMATCH considers a minimised combined normalised error of parameters of particles within a defined search volume space. Parameters of the algorithm are location and size of the search volume space, the selected combination of particle geometric attributes and the error tolerance. Attributes such as: Feret width, Feret length, minor axis length, which may be unique for rotund sand particles were observed to be significantly less unique to the platy particles studied. This was due to their tiny c-axis and smaller overall size, which resulted in a poorer image resolution and segmentation errors. A combination of particle attributes: major and minor axis length and perimeter gave the best particle match, when compared to other particle attributes.

This research presented for the first time, kinematic analysis of platy soil particles through individual particle matching. PLATYMATCH can effectively match plate shaped particles when consecutive scans are adequately registered and particles within scans are adequately segmented. Furthermore, miniature triaxial test were carried out on kaolin with mica markers using a newly designed miniature triaxial device (described in the next chapter) and PLATYMATCH to evaluate the marker particle kinematics.

8.1.4. Miniature triaxial cell with an in-built High Capacity Tensiometer

A novel miniature triaxial cell instrumented with a High-Capacity Tensiometer was developed for pore-water pressure (positive and negative) measurement enabling triaxial compression of relatively soft clay with total and effective stress path evaluation. The miniature cell is designed such that it does not require a confining cell which may limit resolution achievable in X-ray CT.

The new miniature triaxial cell was adequately validated separately prior to use with an X-ray scanner system by comparing triaxial compression of speswhite kaolin clay using the new apparatus to similar test performed with conventional triaxial cell. The result showed good agreement with similar test using the same speswhite kaolin. The equipment was further used to conduct triaxial compression test of kaolin clay within laboratory X-ray computed tomography machine.

8.1.5. Strain localisation investigated using mica markers and X-ray CT

It is worthy of note that the addition of silt sized muscovite particle markers to kaolin may jeopardise clay behaviour. Provided the macroscopic response of kaolin alone compared to kaolin and mica remains the same, we can assume that the behaviour of kaolin is not affected. Four samples of kaolin with 1.5% by wt of mica were sheared to different axial strain levels, two before the peak shear strength, one close to peak shear strength and one beyond the peak shear strength. The behaviour of the kaolin with mica marker sample sheared to failure was compared to that of kaolin sample without mica sheared to failure. The triaxial test showed that the kaolin without mica and the kaolin with 1.5% mica give the same peak and end-of-test shear strength, thus there is no significant difference between the shear strength behaviour of the kaolin and the kaolin/mica mixture which suggests that the mica marker content at the shear conditions tested did not affect the behaviour of the kaolin. Hence, we could evaluate kaolin behaviour using tested the mica marker and at the shear condition without compromising the kaolin behaviour.

The initiation and propagation of strain localisation in kaolin was studied using mica marker and X-ray CT. Kinematic analysis of mica particle markers within the kaolin sample with vertical particle configuration was carried out. The four kaolin samples with mica markers were subjected to triaxial compression with X-ray scans done before and after compression.

The result showed that platy clay particles markers (mica in this case) in kaolin samples undergo translation and rotation of particles at the peak strength within a localised zone. The mica marker particles capture kaolin clay sample localised deformation from pre peak up to the peak and post peak shear strength. At the start of compression (axial strain before peak strength) platy particles move in blocks of distinct opposing direction shown by the mica particle displacement direction map. This divergent displacement is in response to accommodate imposed loading and gives an indication of the initiation of strain localisation.

Analysis of the direction of mica marker particle motion is more indicative of localisation in clay, at a much earlier stage than the peak strength and particle rotation is more indicative of localisation zone thickness, and this is more visible from the peak strength. For an over-consolidated kaolin sheared to the peak stress, the zone of localisation is much larger than clay size and there is the potential to capture the growth of a shear band in kaolin using mica markers. A conceptual model of the initiation and propagation of strain localisation in kaolin was also presented.

8.2. Proposed Future areas

This thesis has opened diverse future research areas in the geotechnics community, particularly in the study of clay micromechanics. The findings of this research work on understanding the micromechanics of clay for enhanced clay constitutive models for better prediction and improvement of soft clay. It thus presents diverse questions which require in depth investigation. Below is a list of suggested topics, based on lessons learnt from this research, for future extension of this work:

1. These experimental results can be extended to modelling the failure behaviour of clayey soil using numerical simulations for validation purpose, for example using Discrete element modelling (DEM). It will be interesting to use output from this research for

discrete element modelling of clay micromechanical behaviour. This could involve importing the acquired images in this study into a DEM platform and carrying out similar tests conducted in this study to compare results from DEM with same acquired image and test conditions to the results obtained in this study.

2. Further development of PLATYMATCH using machine learning deep learning methods such as neural networks to improve the matching of particles especially in strain localised zones.
3. Although, this study included a macroscopic evaluation of the effect of mica addition to kaolin strength characteristics and the similarity of mica pore fluid chemistry effect and that of kaolin, the contribution of the mica particles in the initiation of shear localisation - in kaolin is not fully understood. Differential local stiffness in the direction of loading, as well as longer flow paths around the mica particles could trigger shear distortions and localisation pattern which may not perfectly represent the smaller clay particle behaviour. As part of future studies, there is therefore the need to develop approaches that may be used to visualize and characterise clay sized clay, without inclusions to enable a comparison of the result obtained in this study.
4. This study used one type of clay (Speswhite kaolinite) that has both low plasticity and low compressibility. Caution should be exercised when predicting the failure behaviour in different soil (e.g., highly compressible, or collapsible soil), whose shearing characteristics may be considerably different from those of the tested soil. As part of future studies, it will be interesting to evaluate how platy particles translate and rotate as well as how pore pressure is distributed in other clay types such as bentonitic clays and collapsible soils. The applicability of the results of this study should, thus, be verified for other types of clayey soil that exhibit significantly different plasticity or compressibility.

5. In terms of the miniature triaxial cell equipment, considering the observed heterogeneous pore pressure distribution within the clay sample as it undergoes shearing, future equipment design should consider an approach to determining pore pressure distribution in clay as a single tensiometer does not capture the spatial pore pressure distribution within the clay sample as it is compressed. In addition, because the time dependent mechanical response (i.e., pore pressure dissipation and creep preventing instant deformation) in the clay sample, it was challenging to obtain accurate reconstructions from raw X-ray CT radiographs, when the miniature triaxial cell top restraining frame is in place. There is the need to modify the miniature triaxial cell such that no top restraining frame will be required such that during X-CT acquisition, the sample will ideally be kept stable without the slightest of additional deformations. This with undrained condition (preventing water outflow from the sample) and the use of sufficiently short acquisition time as used in this study would help ensure that continuous loading of the same sample without unloading is tested.
6. Considering that particle configuration within the shear zone, just beyond peak shear strength, is an opposing preferential alignment, such as to counteract the imposed shear force. Additional test involving relatively larger displacement to understand clay particle configuration at ultimate shear strength will be interesting to better understand particle configuration at ultimate shear strength.
7. There is also the scope for developing soil sample X-ray CT image bank with the condition with which they were imaged. Such image bank can be normalised and trained using machine learning approaches for incremental understanding of soil micro mechanics.

8. The result from this research and the above-described further research will be invaluable for enriching double scale constitutive models which takes into consideration, both micro scale physics and macro scale simplified physics. In turn, such constitutive model can be used to better predict failure behaviour and guide reinforcement at actual sites with soft clay ground.

“The larger the island of knowledge, the longer the shoreline of wonder.”

— Ralph W. Sockman (1889 – 1970)

*“If I have seen further than others, it is by standing upon the shoulders of
giants”.*

—Isaac Newton (1643 – 1727)